Response of FRP-Retrofitted Reinforced Concrete Panels to Blast Loading

By

Ahmed Fahmy Farag Tolba, M. Eng.

A thesis submitted to the
Faculty of Graduate Studies and Research
in partial fulfillment of the requirements for the degree of

Doctor of Philosophy

Department of Civil and Environmental Engineering
Carleton University, Ottawa, Canada
December 2001

The Doctor of Philosophy in Civil Engineering is a joint program with the University of Ottawa, administered by the Ottawa-Carleton Institute for Civil Engineering.

The undersigned recommend to the Faculty of Graduate Studies and Research acceptance of the thesis

Response of FRP-Retrofitted Reinforced Concrete Panels to Blast Loading

Submitted by

Ahmed Fahmy Farag Tolba
B.Sc. Military Technical College
M.Sc. Military Technical College

In partial fulfillment of the requirements for the degree of

Doctor of Philosophy

Professor A.G. Razaqpur, Thesis Supervisor

Professor T. Katsabanis, External Examiner

Professor Wayne J. Parker, Chair, Civil and Environmental Engineering

Carleton University
December 2001

Abstract

This study deals with the structural response and ultimate resistance of reinforced concrete panels retrofitted with externally bonded fibre reinforced polymer (FRP) sheets and laminates. Eighteen 1000 × 1000 × 70 mm reinforced concrete panels were made of 40 MPa concrete. Each panel was reinforced with two orthogonal layers of top and bottom steel mesh reinforcement, with an average reinforcement ration of 0.003 and yield strength of 400 MPa. Five of the panels were used as control and were not retrofitted with any FRP. Four panels were identically retrofitted with four 500 mm wide unidirectional glass FRP (GFRP) sheets, with two sheets applied in a cross shape to the top surface and the other two sheets similarly applied to the bottom surface. The sheets were bonded to the concrete by means of epoxy. The FRP sheets covered the middle half of the panels. Five other panels were similarly retrofitted with uni-directional carbon (CFRP) sheets. The remaining four panels were retrofitted with CFRP laminate strips. The strips were 80 mm wide and were applied diagonally, akin to X-brace, to the bottom and top surfaces of each panel. Four of the control panels and twelve of the FRP retrofitted panels were subjected to various blast pressures, emanating from 13.4, 22.4 or 33.4-kg of ANFO explosive at a standoff distance of 3 m. The blast wave characteristics, including incident and reflected pressures and impulses were measured and recorded. The central deflection and strains in the reinforcing steel and the concrete/FRP surfaces were also measured and recorded. The post-blast damage and mode of failure of each panel were observed, and panels that were not completely damaged were subsequently statically tested to find their residual strength.

The test data and observations revealed that the panels retrofitted with either the GFRP or the CFRP sheets had higher blast resistance and they generally performed better than the control panels, but the panels with the CFRP laminates did not perform better than the control panels. The relative performance of the GFRP and CFRP sheet retrofitted panels was the same, despite the fact that the CFRP has both higher strength and modulus.

Theoretical analysis of the test data showed that the software CONWEP can predict the blast wave parameters relatively accurately and is a useful tool for estimating blast loads on structures. The dynamic analysis of the panels was performed using a closed-form solution. When the flexural rigidity of reinforced concrete at different load levels was properly considered, the closed-form solution was able to predict the observed response of the panels reasonably well. However, using elastic properties of the panels and assuming uncracked sections, grossly over-estimated the blast moments acting on the panels. Overall, the analytical solution was found adequate for the purpose of the current study.

Acknowledgments

The author wishes to express his thanks to Professor A. G. Razaqpur, under whose supervision this research work was carried out, for his understanding and encouragement.

My thanks are extended to the following professors, who at early stages of my work commented on my thesis proposal: Professors A. O. Abd El Halim, D. T. Lau, and J. L. Humar, of the Civil and Environmental Engineering Department at Carleton University, Professor P. V. Straznicky, of the Mechanical and Aerospace Department, Carleton University, Professor N. J. Gardner, the University of Ottawa, and Mr. E. Contestabile, head of explosive applications, the Canadian Explosive Research Laboratories (CERL).

The blast experiments of this work would not have been possible without the professional guidance of the CERL personnel: Messrs B. Von Rosen, R. Guilbeault, and D. Wilson. The help of the staff of the Civil Engineering Laboratories at Carleton University during the static tests is also acknowledged.

Assistance of Master Builders Canada by providing the Carbon fibre sheets and strips, and of Watson Engineering, USA by providing the Glass fabric is highly acknowledged.

The financial assistance received from the Egyptian Government, and the Faculty of Graduate Studies and Research at Carleton University, is gratefully appreciated.

Finally, I am very thankful to my wife Naglaa, my family and friends for their continued support and love during my study.

Table of Contents

List of Figures

List of Tables

List of Symbols

P_o	Ambient atmospheric pressure
P_{so}	Positive peak side-on (incident) overpressure
P_{so}^-	Negative peak under pressure
P_r	Reflected pressure
P_d	Dynamic pressure
t_A, t_c	Time of arrival and Clearing time
t_o, t'_o	Positive and Negative phase duration
α	Dimensionless decay coefficient of blast wave
θ	Decay coefficient (msec)
I_r	Positive reflected impulse
U_s	Velocity of the blast wave front
u_s	Wind speed
P_d	Maximum dynamic pressure
Z	Scaled distance
Q_x	Mass specific energy of an explosive
R	Standoff distance
W	Mass of the TNT equivalent charge
W_r	Weight of the reference explosive
d_1 and d_2	Diameters of spherical explosive charges
t_{Ar}, t_{or}	Time of arrival and Positive phase duration of the reference explosive
τ_{sc}	Scaled time
λ	Explosives yield factor
F_D	Drag force
C_D	Drag coefficient
Y	Explosive yield
γ	Specific heat ratio
C_o	Speed of sound in settled atmosphere
a_o	Speed of sound at ambient conditions
M_s	Mach number
r_h	Specific heat of air

ρ_s	Air density behind the shock front
C_f, C_r, C_t	Drag coefficients of the structure's front face, rear face and roof, respectively
T_{so} and T_r	Durations of incident and reflected pulses for internal explosions
P_{qs}	Peak quasi-static pressure resulted from gas explosion
i_g	Gas impulse
V	Volume of the structure
A_{sur}	Total inside wall surface area of the structure
α_e	Ratio of vent area to wall surface area
H	Depth of the soil layer
C_p	Seismic velocity of soil
V_v, D_v, A_v	Maximum vertical velocity, displacement and acceleration (ground motions) at the ground surface due to ground shock, respectively
V_H, D_H, A_H	Maximum horizontal velocity, displacement and acceleration (ground motions) at the ground surface due to ground shock, respectively
$D_{V_{rock}}$, $D_{V_{soil}}$	Maximum vertical displacement at the ground surface for rock and soil
$D_{h_{rock}}$, $D_{h_{soil}}$	Maximum horizontal displacement at the ground surface for rock and soil
V_h	Maximum vertical and horizontal velocities for all ground media
A_v, A_h	Maximum vertical and horizontal accelerations for all ground media
R, M	Structural resistance and mass
K	Spring constant
F	External applied force
T	(1) Natural period of vibration of the structure
ω	Natural circular frequency of vibration of the structure
x, $\dot{x}$, $\ddot{x}$	Displacement, velocity, and acceleration of a structural system
δ_{max}	Maximum structural displacement
ε_s	Static strain rate
$\dot{\varepsilon}$	High strain rate
ε	Strain
f_{ts}, f_{rd}	Static and dynamic tensile strength of concrete, respectively
c	Depth of neutral axis, or concrete cover
d_b	Bar diameter
d_c	Concrete cover measured from the centroid of tension reinforcement to the extreme tension fibre

	extreme tension fibre
f'_c	Compressive strength of concrete
f_r	Modulus of rupture
h	Depth of the cross-section (plate thickness)
y_t	Neutral axis depth
y_c	Distance between the neutral axis in the cracked transformed section and the extreme compression fibre.
A_s	Area of flexural reinforcement (steel)
A'_s	Area of compression reinforcement
C	Resultant force in compression zone of concrete
C_c	Compressive force in concrete
E_c	Modulus of elasticity of concrete
E_s	Modulus of elasticity of steel
I	Moment of inertia
I_{cr}	Moment of inertia of cracked section
I_{eff}	Effective moment of inertia
I_{gross}	Moment of inertia of gross section
L	Total panel span
M_a	Applied moment
M_{cr}, M_{ult}	Moment at cracking and Ultimate moment
M_r	Moment of resistance
T	(2) Tensile force in reinforcement
a, b	Side dimensions of a rectangular flat plate
q_o	Load intensity
w	Mid-span total deflection of a rectangular plate
D	Flexural rigidity
v	Poison's ratio
α, β_1	Rectangular stress block parameters
K, U	Kinetic energy and Strain energy
W_e	Work done by the external loads
σ_{max}	Peak bending stress
n	Modular ratio

Chapter 1

INTRODUCTION

1.1 General

In recent years there have been rapid developments in the manufacture of conventional and non-conventional destructive weapons. The detonation of modern explosive materials threatens target structures with severe loading conditions. Damage effect due to terrorist attacks is an ever-present threat to existing military and civil defence structures. In addition, major catastrophes resulting from aircraft crashes, petro-chemical explosions, nuclear leakage, and earthquakes result in large dynamic loads, greater than the original design loads, of many structures. Due to the threat from such extreme loading conditions, efforts have been made during the past three decades to develop methods of structural analysis and design to resist blast loads. These efforts have led to the publication of some guidelines for the analysis and design of blast-resistant reinforced concrete and steel structures, such as the U. S. manual TM 5-1300. Although these guidelines are widely used to design military fortifications and civil defence buildings, none of them provide any basis for retrofitting means that can be used to increase the blast-resistance capacity of existing structures or for repair of blast damaged structures.

FRP composites are currently used in civil applications to extend the structural integrity of deteriorated structures or to increase the load bearing capacity and ductility of existing buildings and bridges. In addition, seismic retrofitting for masonry structures, shear walls and structural joints is also deemed to be an important field for the application of externally bonded FRP composites. FRP composites have high strength, high-energy absorption capacity and are lightweight. In addition, their elastic modulus/strength ratio is much lower than that of steel. This means that a small quantity of FRP can significantly increase the resistance of a structural member to resist tensile loads and bending moments, but their effect on the member stiffness would typically be insignificant.

In the design of structures to resist blast loads, there are two important considerations; prevention of structure's catastrophic failure and reduction of projectiles due to spalling and fragmentation that ensue from the destruction of the structural and non-structural components of a building after exposure to blast loads. Control of deflection, crack width and other serviceability related performance criteria are not generally a major consideration in blast resistant design. Consequently, due to the transient nature of blast loads and the known properties of FRP composites, externally bonded FRP sheets and laminates are expected to offer an effective and practical method for increasing the blast-resistance capacity of existing reinforced concrete buildings and other structures. Furthermore, the flexible nature of FRP sheets and fabrics, their thinness and light-weight and the ease with which they can be bonded (glued) to most surfaces render them very attractive for retrofit purposes because they do not alter in any significant way the original weight or geometry of a structure. But this expectation needs to be verified through suitable investigation and research as pursued in this thesis.

1.2 Motivation of the Study

Some limited research work has been sponsored by the U. S. Army Corps of Engineers and other private corporations to assess the feasibility of using externally bonded FRP composites to retrofit existing reinforced concrete structures in order to increase their blast-resistance capacity (Crawford *et al.*, 1997). However, due to the military nature of such research work and their high cost, most of the results remain classified and are not available in the public domain. Also, due to the high cost of experimentation, most of the published studies have focused on the analytical modeling of the problem. This has resulted in a paucity of relevant literature and insufficient experimental data that can be used to develop design guidelines for reinforced concrete structures subjected to blast loads. Therefore, there is an increasing need to perform more experimental investigations aimed at the civilian application of FRP composites for the purpose of retrofitting of existing reinforced concrete structures to increase their blast resistance.

Traditionally, structures subjected to blast loads have been either of a military nature or part of the civil defence infrastructure. However, the current ease of access to explosives and know-how, facilitated in large part by the modern communication revolution, has enlarged the categories of existing structures that may be threatened by terrorist attacks. Consequently, to overcome the lack of published data in the field of blast loading effects and the dynamic response of FRP retrofitted reinforced concrete structures to blast loading, the current research work is concerned with increasing the blast-resistance capacity of existing reinforced concrete structural elements. In particular, the response of scaled flat square panels retrofitted with externally bonded FRP composite sheets and strips will be investigated.

1.3 Objectives

The main objective of the current research program is to experimentally and analytically investigate the effectiveness of FRP composites to increase the blast-resistance capacity of existing reinforced concrete panels. This objective is viewed within the wider context of developing an efficient and cost effective retrofitting scheme that can be easily applied to target structures through externally bonding FRP composites to their outer and/or inner surfaces. In addition to increasing the structural integrity, the proposed retrofitting scheme is envisaged to maintain the original architectural features and structural dimensions, to obtain a high strength/weight ratio and to reduce damage resulting from fragmentation projectiles.

The tasks involved to reach the above objective can be summarized as follows:

- Introduce the basic definitions and the main characteristics of the blast loading that result from different explosion sources. Special attention needs to be given to the free-air (external) detonation of various high explosive charges at fixed standoff distance.
- Review the experimental blast methodologies and the measuring techniques used both in the field and in laboratory testing.
- Study the analytical models and codes that can be used to estimate the blast loads resulting from different explosion sources.
- Evaluate the blast loading effects on target structures and analyze the dynamic response of blast-loaded reinforced concrete structural elements.

- Review current strengthening techniques involving externally bonded FRP composites and their application to existing blast-loaded structures.
- Design an experimental program to study the response of FRP-retrofitted reinforced concrete panels subjected to increasing levels of blast load.
- Propose and utilize a new field set-up for testing small-dimension targets against blast loading.
- Measure the blast wave parameters and the panels response, including pressure, impulse and deformations during the test.
- Analyze the test data to determine the effectiveness of the FRP for the purpose of increasing the blast resistance of reinforced concrete structures.
- Compare the experimental results with appropriate analytical and/or numerical predictions, with a view to examine the generality of the current test results.
- Draw appropriate conclusions and make recommendations for future work.

1.4 Scope of the Research

The experimental focus of the current research work will be the free-air detonation of high explosive charges and the blast loads resulting from such explosions, with particular emphasis on the effects of these loads on the dynamic response of FRP retrofitted reinforced concrete panels. The explosive charges will be suspended at a fixed standoff distance from the target panels. The experimental study is limited to reinforced concrete panels of dimensions 1000 × 1000 × 70 mm. For the assessment of the feasibility of using FRP composites in resisting air blast loading, concrete panels having the same compressive strength and internal reinforcement configurations will be strengthened using different commercially available FRP materials. The three FRP composites applied to both surfaces of the panels are: glass fibre reinforced polymer (GFRP) sheets, carbon fibre reinforced polymer (CFRP) sheets and CFRP laminate strips.

The analytical phase of the study involves a closed-form solution to the equation of motion of the target plates, with suitable modifications to allow for concrete cracking and other non-linearities. The aim is to predict the structural dynamic response of simply supported flat plates subjected to blast loads. The analytical results will be compared with the experimental data, in order to judge the validity of the assumptions used in the analysis. In order to simplify the analysis, only the out-of-plane pressure loads will be considered. Furthermore, in the analysis it will be assumed that the FRP-retrofitting layers are fully anchored to the concrete surface and that the failure of the FRP layers is initiated by the tensile stresses generated by the propagating shock waves.

1.5 Outlines of the Thesis

Chapter 2 presents a literature review of blast phenomenon including the basic characteristics of blast waves resulting from various explosion sources, the interaction of blast waves with target structures, the effects of air blast loads resulting from external explosions, internal explosions and ground shocks, and finally the dynamic response of structural elements, with special attention to limits of structural response. Chapter 3 provides an overview of the structural response to explosive effects, the techniques available in the open literature to define structural damage, and the analysis techniques used to evaluate the dynamic response of structures subjected to blast loading. In addition, the effect of strain rate on the dynamic strength of concrete, reinforcing steel, reinforced concrete and FRP composites is highlighted, and the available information regarding the use of externally bonded FRP composites to enhance the blast-resistance capacity of existing structures is reviewed. The extensive experimental program, including both the blast and the static testing phases, is described in Chapter 4, and test results are presented and analyzed in Chapter 5. The analytical study, including results of the closed-form solution and comparison between the experimental results and predictions of the analytical study, are detailed in Chapter 6. Research summary, conclusions of both phases of the study and recommendations for future work are given in Chapter 7.

Chapter 2

BLAST PHENOMENON: TERMINOLOGY, EVALUATION AND EFFECTS

2.1 Introduction

The analysis and design of reinforced concrete structures subjected to blast loads require a detailed understanding of blast phenomena and the dynamic response of various structural elements. In the dynamic analysis of blast-loaded structures, difficulties may arise due to the non-linear inelastic material behaviour, high strain rate effect, the time dependent finite deformations and the uncertainties of the blast wave measurements. This has led to a number of assumptions and approximations to simplify the analysis. Many of these simplifying approaches have provided fairly reasonable predictions for design purposes. Due to the nature of this field of study, much of the literature is classified for security reasons. Therefore, it is not intended that this chapter serve as a complete source of information about blast loading effects, instead a limited discussion of the topic is presented.

2.2 Historical Background

The history of modern explosives begins with nitroglycerine (NG), discovered by the Italian scientist Ascario Sobrero in 1846. Following that and as a result of more than a decade of a relentless effort, Immanuel Nobel developed in 1862 a simple and safe method for the industrial manufacture of nitroglycerine. In 1863 his son, Alfred Nobel, invented the first ignition wooden capsule and introduced liquid nitroglycerine in rock blasting. Two years later, he brought out the detonator consisting of metal capsule loaded with primary explosive such as mercury fulminate. To overcome the severe accidents associated with the use of nitroglycerine as a liquid explosive, Alfred Nobel continued his effort to improve the safety in handling and using liquid explosives. As a result, he produced in 1875 dynamites by adding ammonium nitrate (AN) and combustible material. Another step forward was taken by Nowckhoff in 1905, by introducing the low-freezing NG, which remains liquid in cold weather. Other forms of explosives such as ANFO (AN + Fuel Oil) and slurry explosives began to be used in the USA army by the end of 1950s. For more details, refer to Johansson and Persson (1970) and Baker (1973).

2.3 Explosions and Blast Phenomenon

An explosion is defined as a large-scale, rapid and sudden release of energy (Baker, 1973). Explosions can be categorized on the basis of their nature as physical, nuclear or chemical events. In physical explosions, energy may be released from the catastrophic failure of a cylinder of compressed gas, volcanic eruptions or even mixing of two liquids at different temperatures. In a nuclear explosion, energy is released from the formation of

different atomic nuclei by the redistribution of the protons and neutrons within the interacting nuclei, whereas the rapid oxidation of fuel elements (carbon and hydrogen atoms) is the main source of energy in the case of chemical explosions.

Explosive materials can be classified according to their physical state as solids, liquids or gases. Solid explosives are mainly high explosives for which blast effects are best known. They can also be classified on the basis of their sensitivity to ignition as secondary or primary explosive. The latter is one that can be easily detonated by simple ignition from a spark, flame or impact. Materials such as mercury fulminate and lead azide are primary explosives. Secondary explosives detonate creating blast (shock) waves, which result in damage to the surroundings. Examples include trinitrotoluene (TNT) and ANFO.

2.3.1 Explosion process

The detonation of a condensed high explosive generates hot gases under pressure up to 300 kilo bar and a temperature of about 3000~4000 C°. The hot gas expands forcing out the volume it occupies. As a consequence, a layer of compressed air (blast wave) forms in front of this gas volume containing most of the energy released by the explosion. Blast wave instantaneously increases to a value of pressure above the ambient atmospheric pressure. This is referred to as the side-on overpressure that decays as the shock wave expands outward from the explosion source. After a short time, the pressure behind the front may drop below the ambient pressure (see Figure 2.1). During such a negative phase, a partial vacuum is created and air is sucked in. This is also accompanied by high suction winds that carry the debris for long distances away from the explosion source.

As the blast wave resulting from an airburst leaves the explosion point, it travels as an incident wave until it strikes some object of density greater than that of the normal atmosphere. Upon striking such an object, a reflected wave travels back towards the point of explosion. The reflected overpressure, and its front velocity, is much greater in magnitude than the incident pressure (see Kinney and Graham, 1985 for more details).

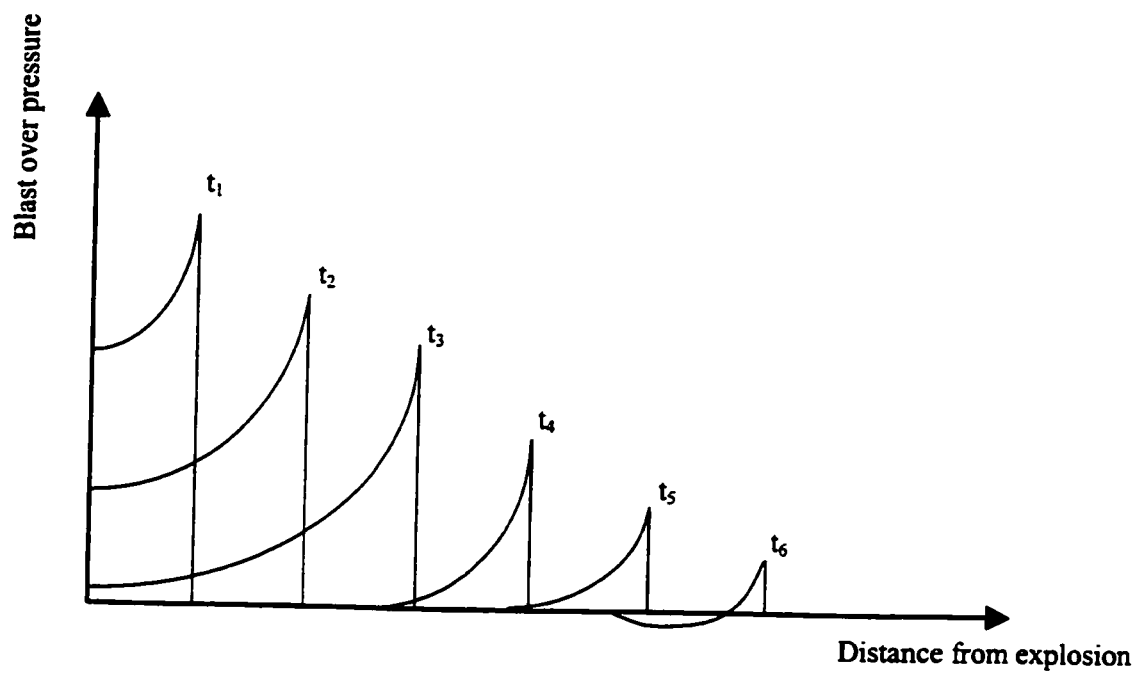

Figure 2.1: Variation of blast pressure with distance from centre of explosions at various times (Rogers, 1959)

2.3.2 Regular and Mach reflection

The angle of incidence, α_I, of the blast wave on the surface of a target structure defines the type of blast loading that will affect the structure. When the incident blast wave front travels at velocity U_s parallel to the structure surface, it makes an angle α_I equal zero with the reflection surface or the ground. Regular reflection occurs for α_I from 0° up to approximately 40° of air (refer to Figure 2.2, a). When the angle α_I equals 90°, there is no reflection and the target is loaded by the peak static overpressure (side-on pressure).

Mach reflection takes place for α_I between 40° and 90°. It is a complex process and is sometimes described as a 'spurt-type' effect where the incident wave skims off the reflecting surface rather than bouncing on it (Mays and Smith, 1995). Mach reflection occurs at a point some distance from the point of explosion where the reflected wave catches up with the incident wave, producing a third wave called the Mach stem. The three waves meet together at a point known as the "Triple Point", which describes a reflection path as the wave front moves forward. The process of wave reflections resulting from an air explosion is illustrated in Figure 2.2 (b). Structures located below the triple point reflection path shown in Figure 2.2 (b) will experience a single vertical shock Mach stem propagating parallel to the ground, whereas those above the path will be under the effect of both the incident and reflected waves. Below the path, as in the case of surface bursts, the shock wave moves on the ground surface with a vertical front near the ground. The importance of Mach stem arises when an explosive charge detonates at some height above the ground and also in case of internal explosions where the angles of incidence of the blast waves on the internal surfaces of the structure may vary over a wide range (Baker *et al.*, 1983).

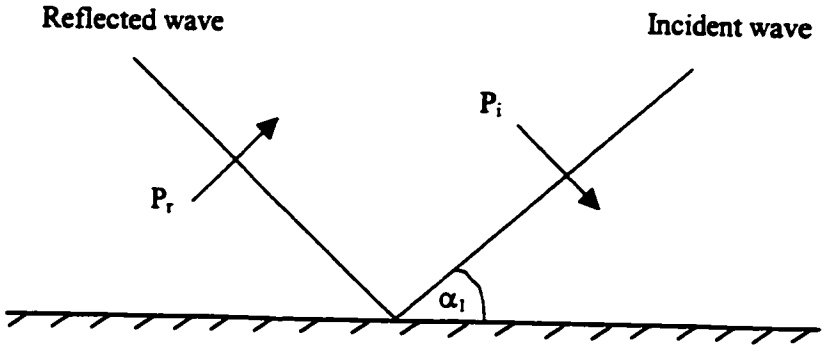

(a) Regular reflection

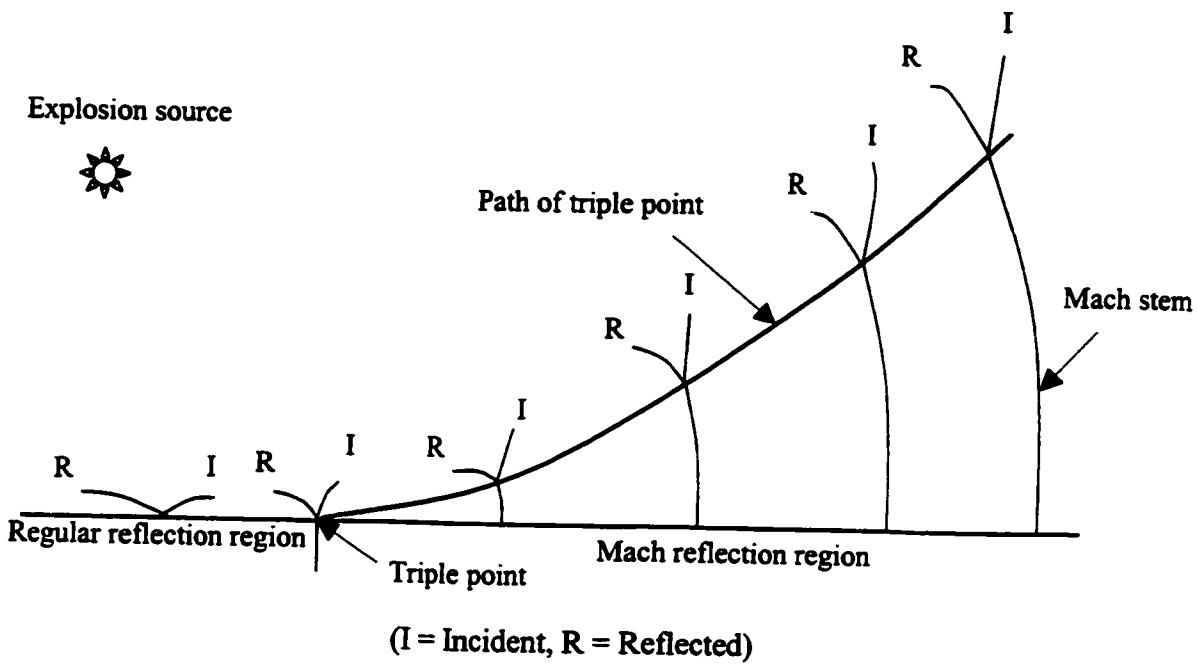

(b) Mach reflection

Figure 2.2: Regular and Mach reflection (Baker, 1973)

2.3.3 Ideal blast wave

The observed characteristics of air blast waves are found to be affected by the physical properties of the explosion source. Nevertheless, at a certain distance from the explosion centre and regardless of the source, all blast waves have almost the same configurations. Figure 2.3 shows a typical blast pressure profile as measured using a pressure transducer positioned at a sufficient distance from the source. At an arrival time of t_A after the explosion, pressure at that position suddenly increases to a peak value of overpressure, P_{so}, over the ambient pressure, P_o. The pressure then decays to ambient in time t_o, till it reaches a partial vacuum of peak under pressure P_{so}^-, and eventually returns to ambient in time $t_o + t_o^-$. The quantity P_{so} is usually referred to as the peak side-on overpressure, or merely peak over pressure (TM 5-1300, 1990).

Throughout the pressure-time profile, two main phases can be observed; portion above ambient is called positive phase of duration t_o, while that below ambient is called negative phase of duration, t_o^-. The negative phase is of a longer duration and a lower intensity than the positive duration, thus its blast wave parameters are always ignored. On the other hand, blast wave parameters associated with positive phase such as shock front velocity, wind velocity, peak overpressure, duration and dynamic pressure are of primary importance and always reported in blast studies. The overpressure decay is governed by the decay coefficient, θ, in msec. Baker (1973) suggested a mathematical form to describe the pressure decay in terms of the dimensionless decay coefficient, α, and time t measured from instant of the shock front arrival as follows

$$P_{so}(t) = P_{so}\left(1 - \frac{t}{t_o}\right) e^{\frac{-\alpha t}{t_o}} \tag{2.1}$$

where α equal to t_o/θ.

The positive specific impulse per unit area can be obtained by the time integration of the positive phase stated in Equation. 2.1:

$$i_{so} = \int_{t_A}^{t_A+t_o} P_{so}(t)\,dt \tag{2.2, a}$$

$$= P_{so}\, t_o \left[\frac{1}{\alpha} - \frac{1}{\alpha^2}\left(1 - e^{-\alpha}\right)\right] \tag{2.2, b}$$

Newmark (1953) suggested that the overpressure-time curves could be represented by triangular equivalents, which have the same initial peak overpressure but have different durations depending on the expected time of maximum structural response.

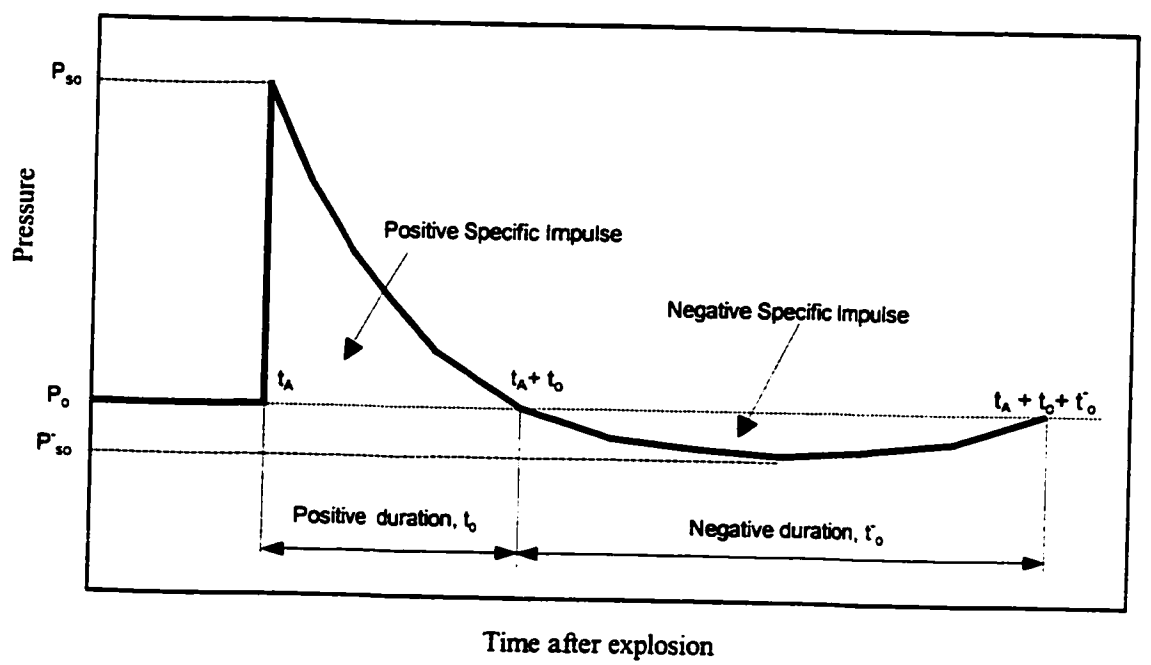

Figure 2.3: Typical pressure-time profile of blast wave in free air (TM 5-1300, 1990)

2.3.4 Blast wave front parameters

Blast wave front parameters are of particular importance to be evaluated. The analytical expressions for these quantities have been introduced in a number of references (see for example, Brode, 1955, Baker, 1973, and Smith and Hetherington, 1994). Brode (1955) proposed analytical forms for some of the most important blast wave parameters for an airburst of a high explosive material. The velocity of the wave front, U_s, the maximum dynamic pressure, P_d, and the peak static overpressure are given, respectively, as

$$U_s = \sqrt{\frac{6P_{so} + 7P_o}{7P_o}}\, a_o \tag{2.3}$$

$$P_d = \frac{5P_{so}^{\ 2}}{2(P_{so} + 7P_o)} \tag{2.4}$$

$$P_{so} = \frac{6.7}{Z^3} + 1 \qquad (P_{so} > 10 \text{ bar}) \tag{2.5, a}$$

$$P_{so} = \frac{0.975}{Z} + \frac{1.455}{Z^2} + \frac{5.85}{Z^3} - 0.019 \qquad (0.1 < P_{so} < 10 \text{ bar}) \tag{2.5, b}$$

where P_{so} is the peak overpressure at the wave front, P_o is the ambient air pressure in bars and a_o is the speed of sound in air expressed in m/s at ambient pressure. Here Z is the scaled distance, and will be discussed later.

The use of TNT as the 'reference' explosive in defining Z is universal, and the majority of blast effects in practice are introduced in terms of the output of an equivalent spherical charge of TNT explosive. A number of approaches have been introduced to convert the actual mass of the charge into a TNT equivalent mass. Baker *et al.*, (1983) introduced a simplified method of achieving that by multiplying the explosive mass by a conversion factor based on its relative specific energy and that of TNT. Table 2.1 shows conversion

factors for a number of common high explosives. From Table 2.1 it can be seen that a 100 kg charge of Compound B converts to 114.8 Kg of TNT since the ratio of the specific energies is 5190/4520, which equal to1.148.

Table 2.1: Conversion factors for common explosives (Baker *et al.*, 1983)

Explosive	Mass specific energy Q_x (kJ/kg)	TNT equivalent (Q_x/Q_{TNT})
Compound B (60% RDX 40% TNT)	5190	1.148
RDX (Cyclonite)	5360	1.185
HMX	5680	1.256
Nitroglycerine (liquid)	6700	1.481
TNT	4520	1.000
Blasting Gelatine	4520	1.000
60 % Nitroglycerine dynamite	2710	0.600
Semtex	5660	1.250
ANFO	3028	0.670

2.3.5 Blast wave scaling laws

The characteristics of blast waves resulting from an explosion depend mainly on the physical properties of the source and the medium that blast waves propagate through. To create reference blast experiments, some controlled explosions have been conducted under ideal conditions. To relate other explosions with non-ideal conditions to the reference explosions, blast scaling laws can be employed. The most widely used approach to blast wave scaling is that formulated by Hopkinson, which is commonly described as the cube-root scaling law. This law states that: "if two structural systems, identically similar except in size, be subjected to blast loading from two explosive charges whose weights are in proportion to the cube of the ratio of the linear dimensions of the two structures, then the behaviour of the two structural systems will be identically similar with the distortions scaling as the ratio of the linear dimensions" Hopkinson (1915). Thus, the scaled distance, Z, is defined as

$$Z = \frac{R}{W^{\frac{1}{3}}} \tag{2.6}$$

where R is the standoff distance from the centre of the spherical explosive charge in meters and W is the charge mass expressed in kilograms of TNT.

Applying the scaling laws for two charges of masses W_1 and W_2 of the same explosive material, and having diameters d_1 and d_2, respectively, yields

$$\frac{d_1}{d_2} = \left(\frac{W_1}{W_2}\right)^{\frac{1}{3}} \tag{2.7}$$

Scaling may also be extended to the time parameters. For a time t, the scaled time τ_{sc} is

$$\tau_{sc} = \frac{t}{W^{\frac{1}{3}}} \tag{2.8}$$

Baker *et al.*, (1991) introduced the so-called explosive yield factor, λ, defined as

$$\lambda = \left(\frac{W}{W_r}\right)^{\frac{1}{3}} \tag{2.9}$$

where W_r is the weight of the reference explosive. It is now easy to express the time of arrival, t_A, and the positive duration, t_o, in terms of the corresponding reference time values (t_{Ar}, t_{or}), viz.

$$t_A = \lambda t_{Ar} \tag{2.10}$$

$$t_o = \lambda t_{or} \tag{2.11}$$

The decay coefficient, θ, and the peak side-on overpressure, P_{so}, are not scaled, but the values used are those that correspond to the scaled distance (Baker *et al.*, 1991)

2.4 Blast Wave-Structure Interaction

The blast wave phenomena were discussed in the preceding section. The structural behaviour of an object or structure exposed to such a wave may be analyzed by dealing with two main issues. Firstly, blast-loading effects, i.e., forces that result from the action of the blast pressure; secondly, the structural response, or the expected damage criteria associated with such loading effects. It is of importance, before proceeding, to discuss the interaction of the blast waves with target structures. This might be quite complicated in the case of complex structural configurations. However, it is possible to consider some equivalent simplified geometry. Accordingly, in analyzing the dynamic response to blast loading, two types of target structures can be considered: *diffraction-type* and *drag-type* structures. As these names imply, the former would be affected mainly by diffraction (engulfing) loading and the latter by drag loading. It should be emphasized, however, that actual buildings will respond to both types of loading and the distinction is made primarily to simplify the analysis. The structural response will depend upon the size, shape and weight of the target, how firmly it is attached to the ground, and also on existence of openings in each face of the structure.

2.4.1 Diffraction effect

The current discussion is focused on infinite reflecting surfaces, which do not allow diffraction to occur. In case of finite target structures, three scenarios of blast wave-structure interaction can be recognized. The first occurs when a large-scale blast wave hits large buildings having a moderately small window and door area and fairly strong exterior reinforced concrete walls: Here the target is engulfed and crushed by the blast

wave. This might be associated also with a translational force tending to move the whole structure laterally (drag force). Yet, due to the size and nature of the structure, this would not likely happen. This is referred to as *diffraction loading*, and examples of structures of this type are multi-storey reinforced concrete buildings and wood-frame buildings. The second scenario occurs when a large-scale blast wave interacts with small structures such as a vehicle. Due to the size of the target in this case, there will be more or less equal engulfing overpressure acting on all parts of the target. In addition, the effect of translational force will be more significant resulting in damage and causing the target to move. Finally, the detonation of small charges would likely produce blast loads that affect structural elements in various ways according to their location with respect to the load applied. This may consequently require a separate analysis for each member.

For the first and second scenarios, the effects of diffraction loads and drag loads are illustrated in Figure 2.4 (a) through (e), which show the squashing and dynamic pressure variation at significant times on the structure. In Figure 2.4 (a) the blast wave front is seen approaching the structure with the direction of motion perpendicular to the face of the structure exposed to the blast. In Figure 2.4 (b), the front face of the target experiences a peak reflected pressure of value, P_r, at a time t_2. As the pressure wave passes on top and around the target sides, the reflected pressure will decay within a time interval (t_c-t_2), where $t_c = 3S/U_s$. Here, S is the smaller of half of the structure breadth or the structure height, and U_s is the blast wave front velocity. The pressure continues to decay until reaches the so called the stagnation pressure, P_{stag}. The diffraction loads on the rear face of the structure are shown in Figure 2.4 (c). The drag force, F_D, on the front and rear faces of the structure are shown in Figures 2.4 (d) and (e), respectively and can

be given in terms of the general drag coefficient, C_D, and the area loaded, A, as ($F_D = C_D \times P_d \times A$), where P_d is the maximum dynamic pressure. The pressure differential between the front and the rear faces will have a maximum value when the blast wave has not yet surrounded the structure. Such pressure will produce a lateral force tending to cause the structure to deflect usually in the direction of the blast wave propagation. If the structure is oriented at an angle to the blast wave, the pressure would be exerted on two faces of the structure, instead of one, but the general scenario of the blast wave would be similar to that just described.

2.4.2 Drag (dynamic pressure) effect

As the wave front moves forward from the source, the reflected pressure on the structure front face drops rapidly. A drag force (dynamic pressure) caused by the transient winds behind the blast wave front will be formed and the front face of the structure will be subjected to its effect. The dynamic pressure at a face of a structure is much less than the wave front overpressure. However, the drag loading on a structure persists for a longer period of time compared to the diffraction loading. It is of interest to mention that the drag pressure is responsible for carrying the structural and non-structural debris away from the explosion site. So, it is common to see the debris hundreds of meters away from the explosion source. Typical drag-type structures are smoke stacks, telephone poles, electric transmission towers, and truss bridges. In these cases, diffraction of blast wave around the structure requires such a short time that its effect can be neglected, and the structural behaviour is dominated by the drag loading. Also, both the drag loading and its positive phase duration will affect the extent of damage to the structural elements.

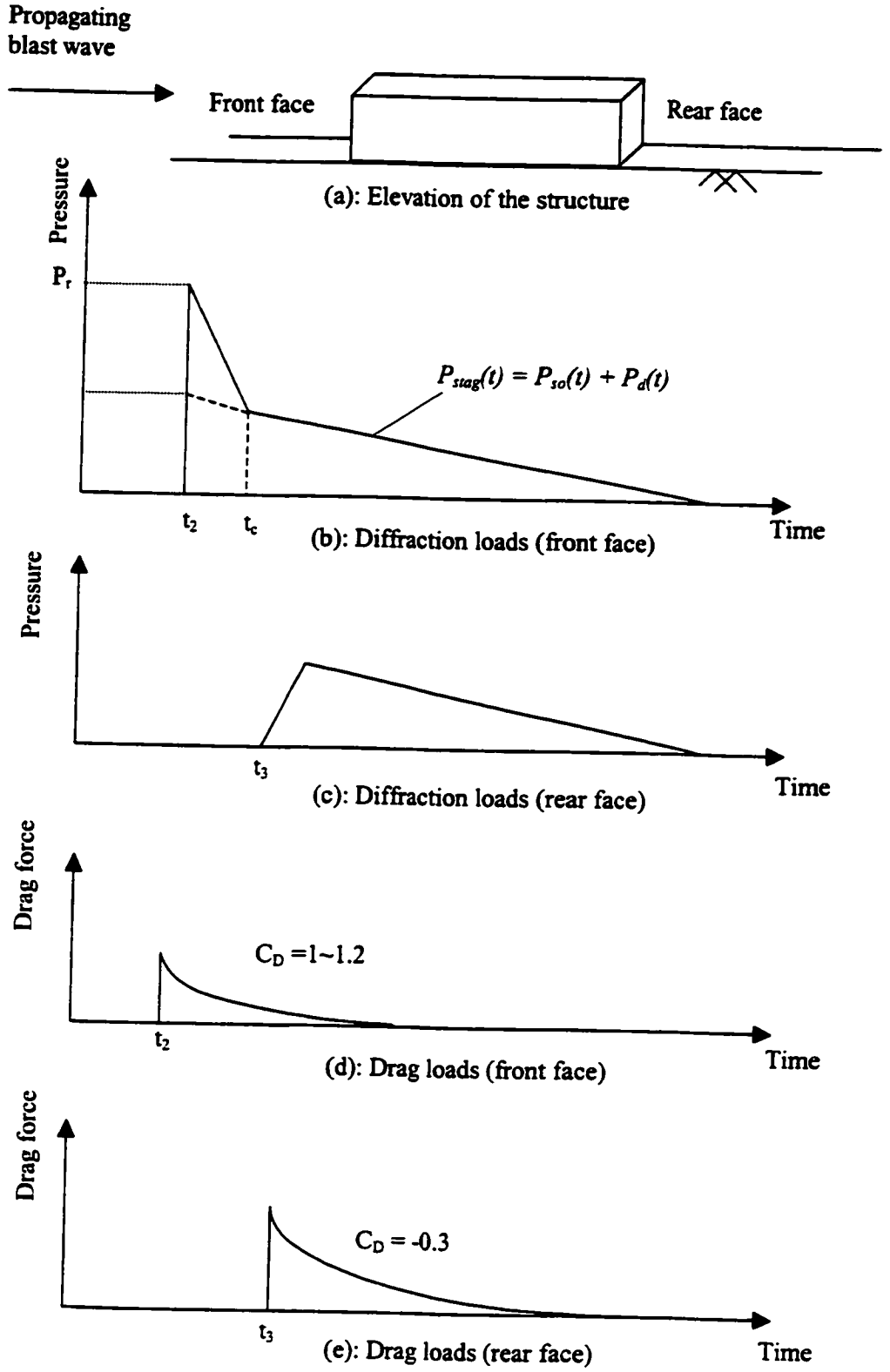

Figure 2.4: Diffraction effect of blast loading on large structures (Smith and Hetherington, 1994)

2.5 Effect of External Explosions

Above ground structures can be affected by blast loads resulting from the external detonation of atomic warheads, or conventional high explosives. The detailed description of the nuclear air-blast phenomena is outside the scope of this study and can be found in Agbabian (1985), and Glasstone and Dolan (1977). The detonation of external high explosive charges results in three loading components; overpressure, reflected pressure and dynamic pressure. However, the magnitude and distribution of such loading components depend mainly on the type and weight of the explosive material, its location relative to the target and the interaction between the pressure waves and structure (TM 5-1300, 1990). The overpressure is the instantaneous increase in pressure at the instant of explosion that can be measured in the free air outside the structure. Upon striking an object, the propagating blast wave creates a reflected pressure wave. The dynamic pressure is associated with suction waves causing drag and lift on surrounding objects. This section deals with the modeling of air-blast loading due to external explosions of conventional high explosives in order to predict blast loading parameters.

2.5.1 Prediction of the side-on overpressure

Blast wave parameters for conventional high explosive materials have been the focus of a number of studies during the 1950's and 1960's. Newmark and Hansen (1961) introduced a relationship to calculate the maximum blast overpressure, P_{so}, in bars, for a high explosive charge detonates at the ground surface as

$$P_{so} = 6784\,\frac{W}{R^3} + 93\left(\frac{W}{R^3}\right)^{\frac{1}{2}} \tag{2.12}$$

where R is the distance in meters between the point of measurements and the explosion source, and W is the total detonation energy measured in equivalent weight of tons of TNT. Another expression of the peak overpressure in kPa is introduced by Mills (1987), in which W is expressed as the equivalent charge weight in kilograms of TNT, and Z is the scaled distance defined in Equation 2.6

$$P_{so} = \frac{1772}{Z^3} - \frac{114}{Z^2} + \frac{108}{Z} \tag{2.13}$$

In recent work by Crawford and Karagozian (1995), equations are given to solve for the peak overpressure, P_{so}, in psi and the positive duration, t_o, in seconds

$$\frac{P_{so}}{P_o} = \frac{40.4\,x^2 + 810}{\left[\left(1+434\,x^2\right)\left(9.77\,x^2\right)\left(1-0.55\,x^2\right)\right]^{\frac{1}{2}}} \tag{2.14}$$

$$\frac{t_o}{Y^{1/3}} = \frac{990 + 4.65\times10^5 x^{10}}{\left(1+125\times10^3 x^3\right)\left(1+6.1x^6\right)} \times \frac{1}{\left(1+0.02x^2\right)^{\frac{1}{2}}} \tag{2.15}$$

where in Equation 2.15, Y is the explosive yield in Kilotons of TNT, and x is the distance in meters on the ground surface between the point of measurements and the explosion source, while in Equation 2.14, P_o is the ambient atmospheric pressure in psi.

2.5.2 Prediction of reflected pressures

Upon striking an object in its path, the propagating incident pressure wave reflects (travels back) through the shocked medium generating a reflected pressure wave, which is two to eight times as great as the incident overpressure. Mays and Smith (1995) derived the equation for reflected pressure, P_r, in terms of the peak side-on (incident) overpressure, P_{so}, and the dynamic pressure given by Equation (2.4) as

$$P_r = 2P_{so} + (\gamma + 1)P_d \tag{2.16}$$

in which γ is defined as the specific heat ratio, and equals 1.4 assuming that air behaves as an ideal gas. Substituting P_d from Equation 2.4 into the above equation gives

$$P_r = 2P_{so}\left[\frac{7P_o + 4P_{so}}{7P_o + P_{so}}\right] \tag{2.17}$$

If nonideal gas effects were included, the ratio between the reflected and incident pressure would reach 14. Newmark (1972) suggested an empirical modification given by

$$P_r = P_{so}(1.5 + 4\log_{10} P_{so}) \tag{2.18}$$

A relationship between the reflected pressure and impulse proposed by Baker *et al.*, (1983), in which a similarity between time profiles for the two is assumed, that may lead to a rough estimation for reflected impulse, i_r. If the side-on (incident) impulse is known, then

$$\frac{i_r}{i_s} = \frac{P_r}{P_{so}} \tag{2.19}$$

For design purposes, reflected overpressure can be idealized by an equivalent triangular pulse of maximum peak pressure P_r, and maximum time duration t_o, which yields

$$i_r = \frac{1}{2}P_r\, t_o \tag{2.20}$$

2.5.3 Prediction of the dynamic pressures

As mentioned earlier, the transient winds that follow the wave front can severely affect target structures. This depends to a great extent on the structural configurations and on the dynamic pressure value, which is defined by the velocity of the shock front, peak wind velocity and the density of air behind the shock front (Baker 1973, and Kinney and Graham, 1985). The shock front velocity, U_s, is given as

$$U_s = C_o M_s \tag{2.21}$$

in which C_o is the speed of sound in settled atmosphere, and M_s is the Mach number for the corresponding peak overpressure given in terms of the specific heat of air, r_h, by

$$M_s = \left[1 + \left(\frac{r_h + 1}{2r_h}\right)\frac{P_{so}}{P_o}\right]^{\frac{1}{2}} \tag{2.22}$$

Knowing the shock front velocity, the wind speed, u_s, is given as

$$u_s = \frac{2}{1 + r_h}\left[\frac{U_s^{\,2} - C_o^{\,2}}{U_s}\right] \tag{2.23}$$

Another expression for the wind speed in terms of the peak overpressure and the ambient pressure is given by (TM 5-1300, 1990)

$$u_s = \frac{C_o P_{so}}{r_h P_o}\left[1 + \left(\frac{r_h + 1}{2r_h}\right)\frac{P_{so}}{P_o}\right]^{\frac{-1}{2}} \tag{2.24}$$

This leads to the expression for the air density behind the shock front, ρ_s, which is

$$\rho_s = \rho_o\left[\frac{(\gamma + 1)P_{so} + 2\gamma P_o}{(\gamma - 1)P_{so} + 2\gamma P_o}\right] \tag{2.25}$$

The dynamic pressure, P_d, then can be defined as

$$P_d = \frac{P_{so}^2}{2\gamma P_o + (\gamma - 1)P_{so}} \tag{2.26}$$

For ideal gas conditions where $\gamma = 1.4$, Equation (2.26) yields

$$P_d = 2.5\left[\frac{P_{so}^2}{7P_o + P_{so}}\right] \tag{2.27}$$

2.5.4 Blast wave external loading on structures

For an above ground rigid target structure with assumed infinite dimensions, the front face experiences a pressure that varies with time in the manner shown in Figure 2.5. Upon striking the target front face, the pressure will simultaneously increase to the peak reflected pressure, P_r, and then decay to a value equal to the side-on overpressure plus the dynamic pressure. This pressure decay occurs in a clearing time, t_c, which is defined in terms of the shock front velocity U_s as

$$t_c = \frac{3S}{U_s} \tag{2.28}$$

where S is equal to the height of the structure or one-half the structure width, whichever is less. During this decay period, the maximum pressure is given (TM 5-1300, 1990) by

$$P_{face} = P_{so} + C_f P_d \tag{2.29}$$

where C_f is the front face drag coefficient, and can be considered 1.2. In Figure 2.5, the times t_i' and t_i are known as the *fictitious durations*.

The rear face of the structure is not expected to experience any pressure until the shock wave crosses the side length. This takes the shock front a time t_r equal to the length of the

structure, L, in the direction of the wave propagation divided by the shock front velocity, U_s. The pressure loading on the rear face of an above ground structure is shown in Figure 2.6, in which the maximum experienced rear pressure at time t_r is equal to the value

$$P_{rear} = P_{so} - C_r P_d \qquad (2.30, a)$$

where C_r is the rear face drag coefficient, which ranges between 0.5 for low pressures and 0.3 for high pressures and can be taken as 0.4 (TM 5-1300, 1990). The quantity $C_r P_d$, in Equation 2.30 (a) is referred to as the drag pressure. Also, the pressure in Equation 2.30 (a) requires a time t_{rb} to reach a maximum on the rear face of the structure, where

$$t_{rb} = \frac{L + 5S}{U_s} \qquad (2.30, b)$$

It is of importance to mention here that the structure as a whole is subjected to a net transverse loading equal to the difference between the front and rear loadings.

The roof of the structure is subjected to a pressure equal to the overpressure minus a drag pressure, and is given in (Newmark and Hansen 1961) as

$$P_{roof} = P_{so} - C_t P_d \qquad (2.31)$$

where C_t is the drag coefficient for the roof and can be taken equal to the same as the rear coefficient, C_r, as 0.3~0.5. The negative drag pressure, $C_t P_d$, results from the suction associated with the airflow around the structure. The pressure loading on the roof can be idealized as a triangular load of peak pressure value P_{so}, and a rise time, $t_{r_{roof}}$, that equals

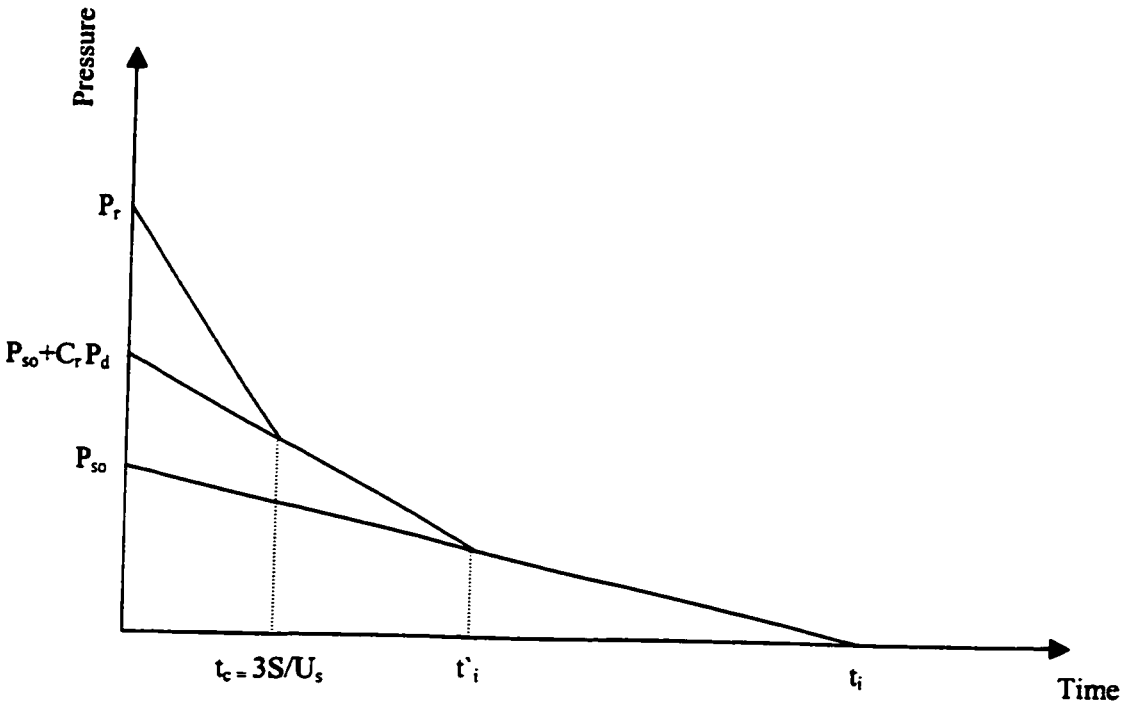

Figure 2.5: External blast loading on front face of structure (Newmark, 1972)

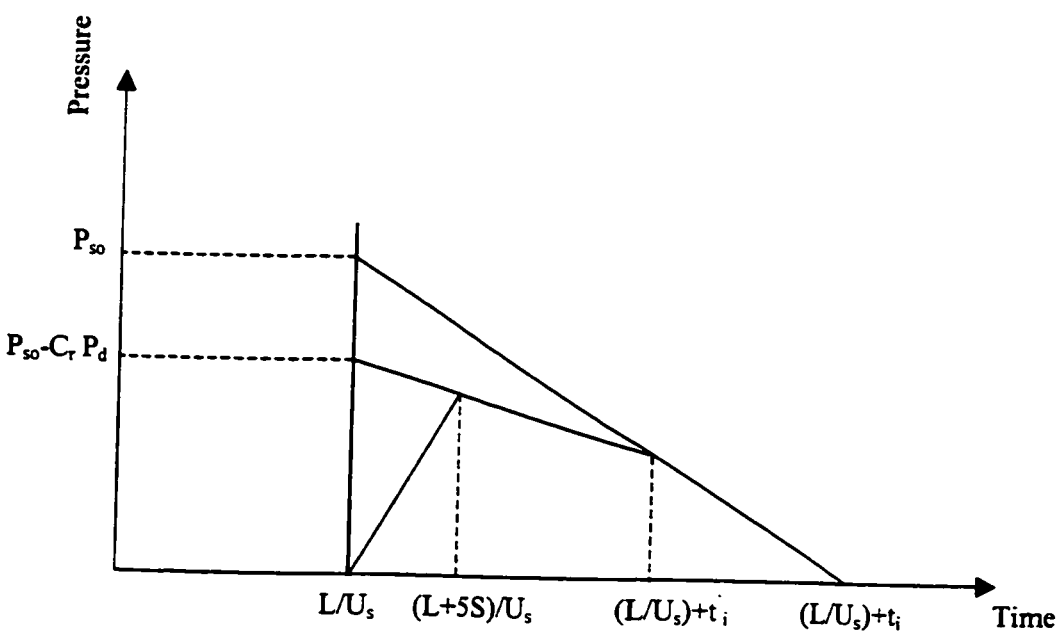

Figure 2.6: External blast loading on rear face of structure (Newmark, 1972)

$$t_{r_{roof}} = t_{rf} + \frac{L}{U_s} \tag{2.32, a}$$

and the duration of the equivalent pulse is equal to

$$t_{ds} = t_{r_{roof}} + t_i \tag{2.32, b}$$

In case of very deep structures, where it takes the shock wave a relatively long time to cross from front to rear, the basic characteristics of the front wave may differ from that of the rear face. It is recommended that in such cases two separate pressure-time histories are calculated for the front and the rear faces.

2.6 Effect of Internal Explosions

Internal explosions likely produce complex pressure loading profiles as a result of the resulting two loading phases. The first results from the blast overpressure reflection and, due to the confinement provided by the structure, re-reflection will occur. Depending on the degree of confinement of the structure, the confined effects of the resulting pressures may cause different degrees of damage to the structure. On the basis of the confinement effect, target structures can be described as either vented or un-vented. The latter must be stronger to resist a specific explosion yield than a vented structure where some of the explosion energy would be dissipated by breaking of window glass or fragile partitions.

2.6.1 Shock wave loading

When an explosion occurs within a structure, it is possible to predict the initial reflected shock wave parameters (pressure and impulse) using either the mathematical expressions

given in Equations 2.16 through 2.20 or charts provided in standard references (see Baker, 1973). The re-reflected blast waves produce a non-uniform distribution of dynamic loads on all the internal surfaces, which is generally more difficult to estimate. However, it is possible to simplify the analysis by approximating the incident and reflected pressure pulses (P_{so} and P_r) to triangular shapes with a pressure-time history given by

$$P_{so}(t) = P_{so}\left(1 - \frac{t}{T_{so}}\right) \tag{2.33}$$

$$P_r(t) = P_r\left(1 - \frac{t}{T_r}\right) \tag{2.34}$$

The durations of these pressure pulses, T_{so} and T_r, are adjusted to correlate these pulses to the actual ones, and can be given as

$$T_{so} = \frac{2\,i_{so}}{P_{so}} \tag{2.35}$$

$$T_r = \frac{2\,i_r}{P_r} \tag{2.36}$$

The effect of the re-reflected pressure waves can be ignored in calculating the final blast loading exerted on structure surfaces. This is because of the reduction in pressure value that happens after each re-reflection phase. Baker *et al.*, (1983) estimated this reduction as one half of the initial pressure pulse. They also suggested, in the same reference, that the pressure loads resulting from all the re-reflection phases could increase those loads due to the initial pulse by a factor of 75 %. Thus, re-reflected pulse durations calculated in Equations 2.35 and 2.36 are to be multiplied by a factor of 1.75. The approximations mentioned above lead to an idealized triangle pressure-time history of maximum peak pressure and pulse duration P_r and t_r, respectively, as in Figure 2.7.

2.6.2 Gas pressure loading

After a certain time from the instance of explosion, blast waves start decaying, and gas pressure develops. The architectural features of the structure (governing volume and area of vents) influence the gas pressure magnitude. Such gas pressures commonly last for a long period of time, and are referred to as quasi-static pressures. A typical pressure-time profile for an internal blast loading of a partially vented structure is shown in Figure 2.8, in which an approximation of the quasi-static pressure is given. Two main parameters are of interest, the peak quasi-static pressure, P_{qs}, and the time t_b at which the pressure returns to ambient (datum time). This time is referred to as the blow down time. An approximation is given by Baker *et al.*, (1983) to describe the pressure-time profile as

$$p(t) = \left(P_{qs} + P_o\right) e^{-2.13\tau} \tag{2.37}$$

where P_o is the ambient pressure and

$$\tau = \frac{\alpha_e A_{sur} t_b a_o}{V} \tag{2.38}$$

where α_e is the ratio of the vent area to wall area, A_{sur} is the total inside surface area of the structure, V is the structure volume and a_o is the speed of sound at ambient conditions. The area under the quasi-static pressure profile is termed the gas impulse, i_g, which, for a positive duration t_o and $P_1 = P_{qs} + P_o$, equals

$$i_g = \int_0^{t_o} \left[P(t) - P_o\right] dt = \frac{P_1}{C}\left[1 - e^{Ct_o}\right] - P_o t_o \tag{2.39}$$

$$C = \frac{2.13\, \alpha_e A_{sur} a_o}{V} \tag{2.40}$$

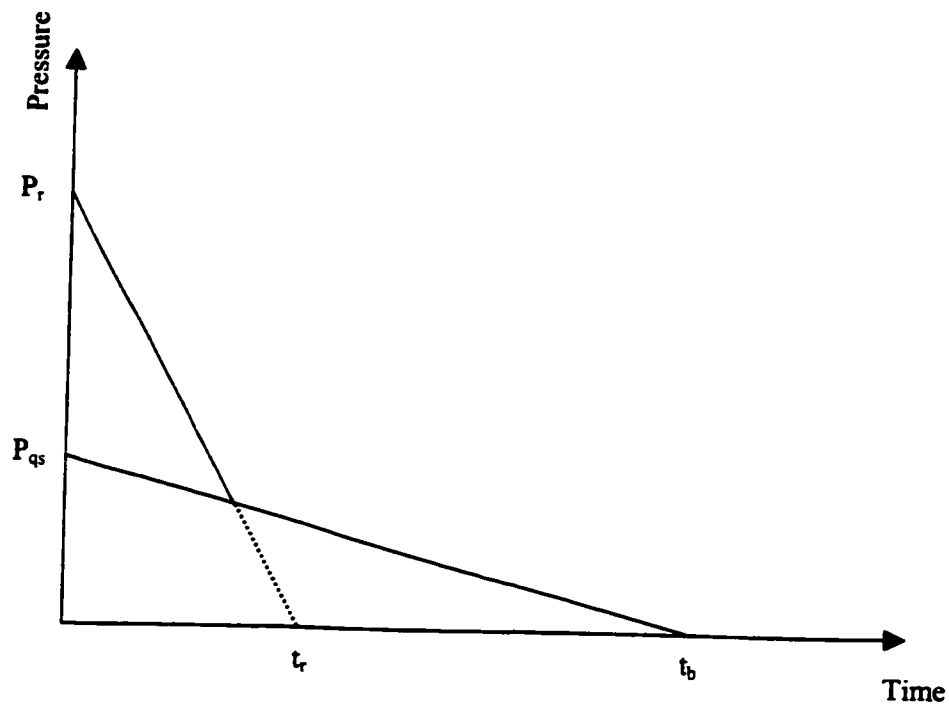

Figure 2.7: An idealized internal pressure loading on inner surface of a structure (Baker *et al.*, 1983)

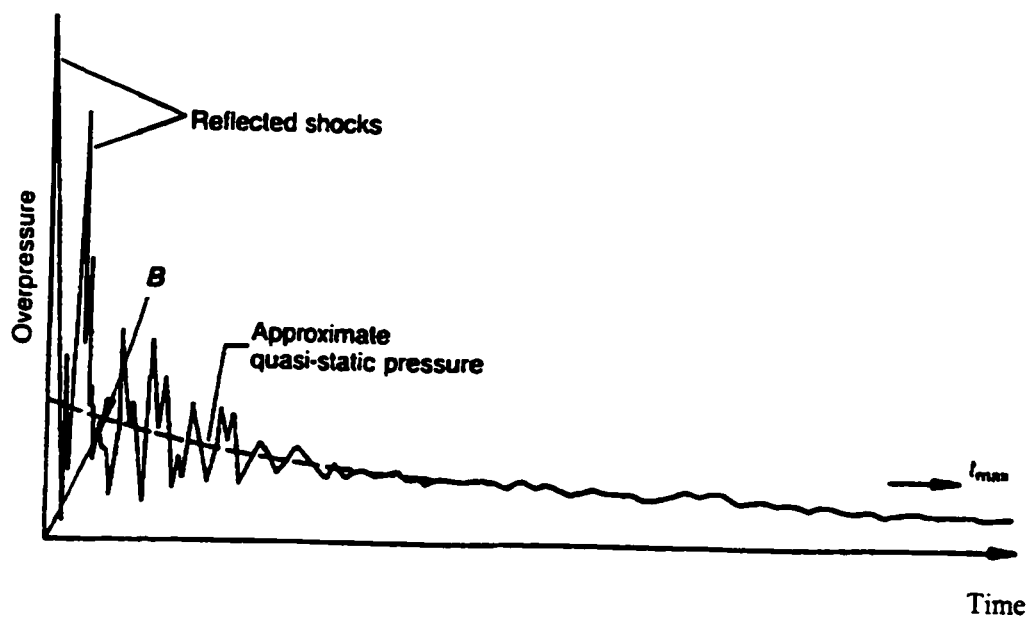

Figure 2.8: Pressure-time history of an internal explosion (Smith and Hetherington, 1994)

2.7 Effect of Ground Shocks

Above ground or shallow-buried structures can be subjected to ground shock resulting from the detonation of explosive charges that are on/or close to ground surface. The energy imparted to the ground by the explosion is the main source of ground shock. A part of this energy is directly transmitted through the ground as *direct-induced* ground shock, while part is transmitted through the air as *air-induced* ground shock. Air-induced ground shock results when the air-blast wave compresses the ground surface and sends a stress pulse into the ground under-layers. Generally, motion due to air-induced ground is maximum at the ground surface and attenuates with depth (TM 5-1300, 1990). The direct-induced shock results from the direct transmission of explosive energy through the ground. For a point of interest on the ground surface, the net experienced ground shock results from a combination of both the air-induced and direct-induced shocks.

2.7.1 Loads from air-induced ground shock

To overcome complications of predicting actual ground motion, one-dimensional wave propagation theory has been employed to quantify the maximum displacement, velocity and acceleration in terms of the already known blast wave parameters (Newmark, 1972 and TM 5-1300, 1990). The maximum vertical velocity at the ground surface, V_v, is expressed in terms of the peak incident overpressure, P_{so}, as

$$V_V = \frac{P_{so}}{\rho C_p} \tag{2.41}$$

where ρ and C_p are, respectively, the mass density and the wave seismic velocity in the soil. Expressing P_{so} in MPa, a mean value of V_v in m/s is introduced as

$$V_V = 1.5\ P_{so} \qquad \text{(m/s)} \tag{2.42}$$

Integrating the vertical velocity in Equation 2.41 with time, results in the maximum vertical displacement at the ground surface, D_v

$$D_V = \frac{i_s}{1000\ \rho\ C_p} \tag{2.43}$$

Accounting for the depth of soil layers, an empirical formula is given by (TM 5-1300) to estimate the vertical displacement in meters so that

$$D_V = 0.09\, W^{\frac{1}{6}}\, (H/50)^{0.6}\, (P_{so})^{\frac{2}{3}} \tag{2.44}$$

where W is the explosion yield in 10^9 kg, and H is the depth of the soil layer in meters. The peak vertical acceleration of the ground surface, A_v, in m/s^2 assuming a linear velocity increase of one millisecond is given approximately as

$$A_V = 150\ P_s\ g \tag{2.45}$$

in which g is the gravitational constant equal to 9.81 m/sec^2 and P_{so} is in MPa. The non-linearity during the rise time is taken into consideration by increasing A_v by 20 %. The maximum horizontal ground motions, D_H, V_H, and A_H, are expressed in terms of the above obtained vertical values and the shock front velocity, U_s, as follows

$$D_H = D_V \tan\left[\sin^{-1}\left(C_p / 12{,}000\ U_s\right)\right] \tag{2.46}$$

$$V_H = V_V \tan\left[\sin^{-1}\left(C_p / 12{,}000\ U_s\right)\right] \tag{2.47}$$

$$A_H = A_V \tan\left[\sin^{-1}\left(C_p / 12{,}000\ U_s\right)\right] \tag{2.48}$$

For (C_p/12,000U_s) greater >1, horizontal and vertical motions are equal (TM 5-1300).

2.7.2 Loads from direct-induced ground shock

As a result of the direct transmission of the explosion energy, the ground surface experiences vertical and horizontal motions. Some empirical equations were derived (TM 5-1300 1983) to predict the direct-induced ground motions in three different ground media; dry soil, saturated soil and rock media. The peak vertical displacement in m/s at the ground surface for rock, $D_{V_{rock}}$ and dry soil, $D_{V_{soil}}$ are given as

$$D_{V_{rock}} = \frac{0.025\ R^{\frac{1}{3}}\ W^{\frac{1}{3}}}{Z^{1/3}} \tag{2.49}$$

$$D_{V_{soil}} = \frac{0.017 R^{\frac{1}{3}}\ W^{\frac{1}{3}}}{Z^{2.3}} \tag{2.50}$$

The maximum horizontal displacement for rock, $D_{h_{rock}}$, and for soil, $D_{h_{soil}}$, are given by

$$D_{h_{rock}} = 0.5 D_V \tag{2.51}$$

$$D_{h_{soil}} = D_V \tag{2.52}$$

For all ground media, the peak vertical, V_V, and horizontal, V_h, velocities are

$$V_V = \frac{150}{Z^{1.5}} \tag{2.53}$$

$$V_h = V_{Vd} \tag{2.54}$$

The maximum vertical acceleration, A_v, in m/s^2 for all ground media is given by

$$A_V = \frac{10000}{W^{\frac{1}{8}}\ Z^2} \tag{2.55}$$

The horizontal and vertical accelerations are equal for wet soil and rock media.

2.8 Structural Response to Blast loading

The structural response to blast loads has been, since the end of World War II, the focus of a huge number of experimental and theoretical studies. This has significantly contributed not only to the field of blast effects but also to the field of structural dynamics in general. Also, this has resulted in a number of design codes and guidelines for blast-resistance design. One of the earlier works in this field has been introduced by Biggs (1964), which provided the basis for the 1990 design manual TM 5-1300 'Structures to resist the effects of accidental explosions'. The design code was prepared by the joint departments of US Army, Navy, and Air Force to provide design criteria for protective structures to resist the effects of accidental explosions. The following discussion relies on the above-mentioned manual, and presents the principles of dynamic response of structural elements under the effect of blast loads and the analysis techniques used in response evaluation.

2.8.1 General considerations

In analyzing the dynamic response of blast-loaded structures, the final deformed state is the main concern of the designer rather than the details of the displacement-time history of the structure. Complexity may arise, in conducting such analysis, due to the nature of the problem, which involves the effect of high strain rates, the non-linear inelastic material behaviour, the uncertainties of blast load calculations and the time-dependent deformations. Therefore, to simplify the analysis, a number of assumptions related to the response of structures and the loads has been proposed and widely accepted (Task Committee on Blast Resistance Design, 1997). To establish the principles of this analysis,

the structure is idealized as a single degree of freedom system and the link between the positive duration of the blast load and the natural period of vibration of the structure is established. This leads to blast load idealization and simplifies the classification of the blast loading regimes. Simply, the analysis strives to evaluate the response of an idealized single degree of freedom structural system to an idealized blast loading function.

2.8.2 Elastic SDOF systems

Structural systems can be idealized either as a multi-degree of freedom (MDOF) or single degree of freedom (SDOF). The simplest discretization of transient problems is by means of the SDOF approach. The actual structure can be replaced by an equivalent system of one concentrated mass and one weightless spring representing the resistance of the structure against deformation. Such an idealized system is illustrated in Figure 2.9 (a). The structural mass, M, is under the effect of an external force, F, and the structural resistance, R, is expressed in terms of the vertical displacement, x, and the spring constant, K.

The blast load can also be idealized as a triangular pulse having a peak force F and positive phase duration t_o (see Figure 2.9, b). The forcing function is given as

$$F(t) = F\left(1 - \frac{t}{t_o}\right) \tag{2.56}$$

An impulse, I, will be delivered to the target structure by the blast wave. The impulse here is approximated as the area under the force-time curve, and is given by

$$I = \frac{1}{2} F t_0 \tag{2.57}$$

The equation of motion of the un-damped elastic SDOF system for a time ranging from 0 to t_o is given by Biggs (1964) as

$$M\ddot{x} + Kx = F\left(1 - \frac{t}{t_o}\right) \tag{2.58}$$

Confining the structural response to times less than the positive phase duration, the general solution can be written as

$$x(t) = \frac{F}{K}(1 - \cos\omega t) + \frac{F}{Kt_o}\left(\frac{\sin\omega t}{\omega} - t\right) \tag{2.59}$$

In which ω is the natural circular frequency of vibration of the structure, and is given by

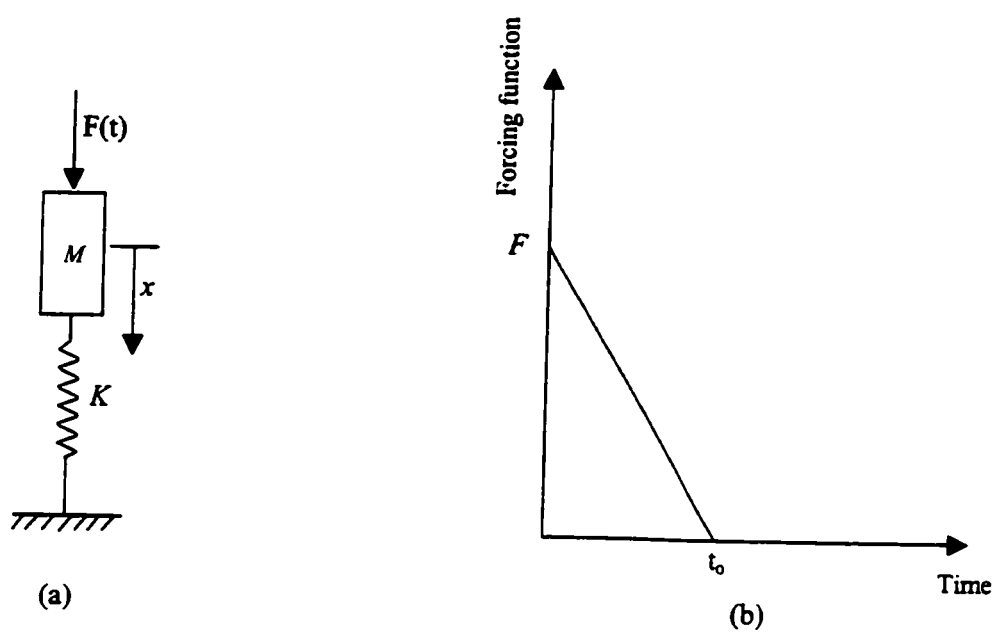

Figure 2.9: Idealization of (a) Structural system as a SDOF and (b) Blast loading

$$\omega = \left(\frac{K}{M}\right)^{\frac{1}{2}} \tag{2.60}$$

Differentiating Equation 2.59 with respect to time t, gives the structural velocity as

$$\dot{x} = \frac{dx}{dt} = \left[\omega \sin \omega t + \frac{1}{t_o}(\cos \omega t - 1)\right]\frac{F}{K} \tag{2.61}$$

Interest is focused here on the maximum structural displacement, δ_{max}, which occurs at time, t_m. This can be evaluated by setting dx/dt in Equation 2.61 equal to zero, i.e., when the structural velocity is zero. Thus, a general solution can be given as

$$\omega t_m = f(\omega t_o) \tag{2.62}$$

This has a similar form as the maximum dynamic displacement, x_{dyn}.

$$\frac{x_{dyn}}{F/K} = \Psi(\omega t_o) = \Psi'\left(\frac{t}{T}\right) \tag{2.63}$$

where Ψ and Ψ' are functions of ωt_o and t_o/T, respectively, and T is the natural period of vibration of the structure. Relating the static displacement to the dynamic one, introduces an expression for the dynamic load factor (*DLF*) or the dynamic increase factor (*DIF*), which can be defined as

$$DLF = \frac{x_{dyn}}{x_{st}} \tag{2.64}$$

2.8.3 Limits of the structural response

It was found (Pan and Watson, 1998 and Beshara, 1994-a) that structural response to blast loading is significantly influenced by the ratio of the positive phase duration, t_o, to the natural period of vibration of the structure, T, known as the duration ratio, t_o/T. The

structural response to blast loading can be identified in terms of t_o/T, as

t_o/T is very small (< 0.1) $\rightarrow \omega t_o < 0.4 \rightarrow$ impulsive loading regime (2.65, a)

t_o/T is very long (> 6) $\rightarrow \omega t_o > 40 \rightarrow$ quasi-static loading regime (2.65, b)

$t_o/T \cong 1 \rightarrow 0.4 < \omega t_o < 40 \rightarrow$ dynamic loading regime (2.65, c)

The three loading regimes are depicted in Figure 2.10, in which the structural resistance is referred to as *R(t)*. First, consider the case of a short time t_o with respect to *T*, Figure 2.10 (a). The load has finished acting before the structure has had time to respond or to reach its full resistance. Deformation occurs at time greater than t_o, which means that displacement is a function of impulse, stiffness and mass. This is referred to as impulsive loading regime. Most above ground concrete structures respond to such impulsive loading, where pressure is applied transiently, even before the start of the structural response. In this study we are interested in this loading regime only.

Next, consider the case of the dynamic loading regime (Figure 2.10, b), where t_o is almost equal to *T*. The situation here is more complex and the equation of motion of the structure requires complete solution. It is generally recommended (Duranovic and Watson 1994) to avoid structures whose *T* is close to t_o.

Finally, when t_o is much larger than *T*, Figure 2.10 (c), the applied load remains constant whilst the structure attains its maximum deflection. In this case, the maximum displacement that the structure can attain is a function of the peak blast pressure. Figure 2.10 (c) illustrates typical structural response to a gas explosion, where the structure is seen to reach its maximum displacement before the blast load has significantly decayed. Such loading is referred to as quasi-static loading regime.

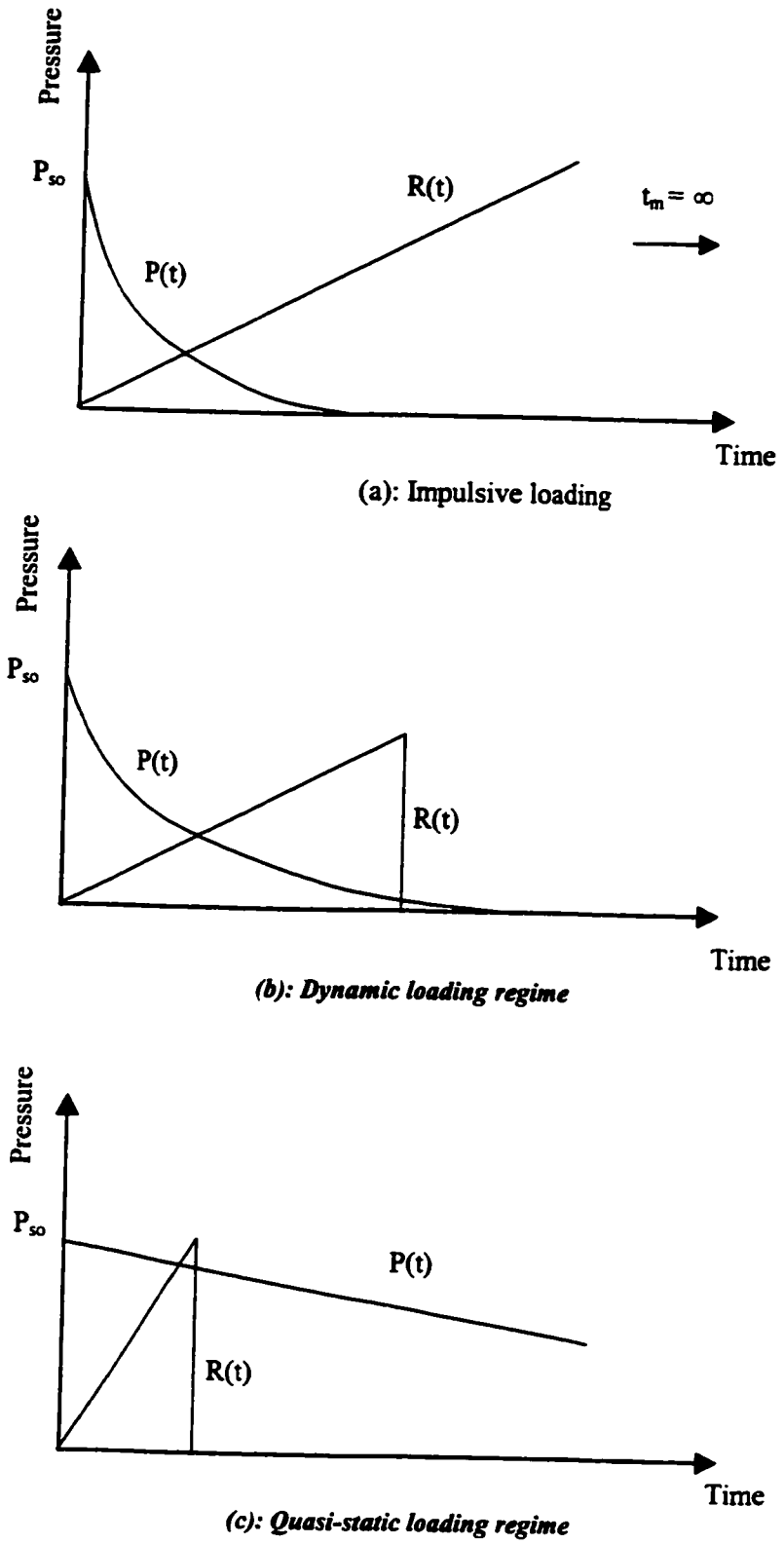

Figure 2.10: Blast loading regimes (Watson, A. J. 1994)

Chapter 3

DAMAGE CRITERIA AND STRAIN RATE EFFECTS

3.1 Introduction

Blast loads typically produce very high strain rates in the range of $10^2 \sim 10^4\ s^{-1}$. This high straining (loading) rate would alter the dynamic mechanical properties of target structures and, accordingly, the expected damage mechanisms for various structural elements.

This chapter provides an overview of the structural responses associated with explosive effects, the methods found in the open literature to define structural damage, and the analysis techniques used to evaluate the dynamic response of structures subjected to blast loading. In addition, an exploration of the new measures used in increasing the blast resistance capacity of existing structures, with special attention to the role of FRP composites in this field will be embarked on. Finally, the effect of strain rate on the dynamic strength of concrete, reinforcing steel, reinforced concrete and FRP composites is highlighted.

3.2 Failure Modes of Blast-Loaded Structures

Blast loading effects on structural members may produce both local and global responses associated with different failure modes. The type of structural response depends mainly on the loading rate, the orientation of the target with respect to the direction of the blast wave propagation, and boundary conditions. The general failure modes associated with blast loading can be flexure, direct shear or punching shear. Local responses are characterized by localized breaching and spalling, and generally result from the close-in effects of explosions, while global responses are typically manifested as flexural failure. The forgoing discussion gives an idea about the expected dynamic structural behaviour and the associated failure modes under the effect of air blast loading.

3.2.1 Global structural behaviour

The global response of structural elements is generally a consequence of transverse (out-of-plane) loads with long exposure time (quasi-static loading), and is always associated with global membrane (bending) and shear responses (Crawford and Karagozian, 1995). Therefore, the global response of above-ground reinforced concrete structures subjected to blast loading is referred to as membrane/bending failure as illustrated in Figure 3.1 (a).

The second global failure mode to be considered is shear failure. It has been found that under the effect of both static and dynamic loads, four types of shear failure can be identified: diagonal tension, diagonal compression, punching shear, and direct (dynamic) shear (Woodson, 1993). The first two types are common in reinforced concrete elements under static loads while punching shear is associated with local shear failure, e.g. the familiar case is column punching through flat slabs. These shear response mechanisms

have relatively minor structural effect in case of blast loading and can be neglected. Figure 3.1 (b) illustrates global shear failure of reinforced concrete slabs.

The fourth type of shear failure is direct (dynamic) shear. This failure mode is primarily associated with transient short duration dynamic loads that result from blast effects, and it depends mainly on the intensity of the pressure waves. The associated shear force is many times higher than the shear force associated with flexural failure modes. The high shear stresses may lead to a direct global shear failure and it may occur very early (within a few milliseconds of shock wave arrival to the facing structure's surface) even prior to any significant bending deformations. Such failure modes are thoroughly discussed as experimental observations in Toutlemonde and Boulay (1993-a & b) and Watson (1993).

3.2.2 Localized structural behaviour

The close-in effect of explosion may cause localized shear or flexural failure in the closest structural elements. This depends mainly on the distance between the explosion centre and the target, and the relative strength/ductility of the structural elements. The localized shear failure takes place in forms of localized punching and spalling, which produces low and high-speed fragments. The localized bending and shear failure modes are schematically depicted in Figures 3.1 (c), and (d), respectively. The punching effect is frequently referred to as breaching, which is well known in high velocity impact applications and the case of explosions close to the surface of structural members. Breaching failures are typically accompanied by spalling and scabbing of concrete covers as well as fragments and debris. Figures 3.2 and 3.3, respectively, illustrate spalling and scabbing failure modes under the close-in effect of explosive charges.

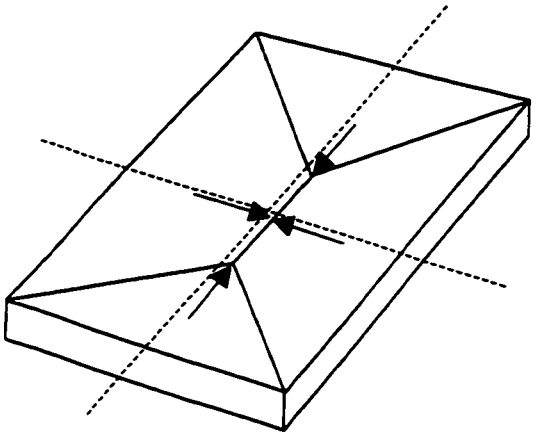

(a): Global bending failure

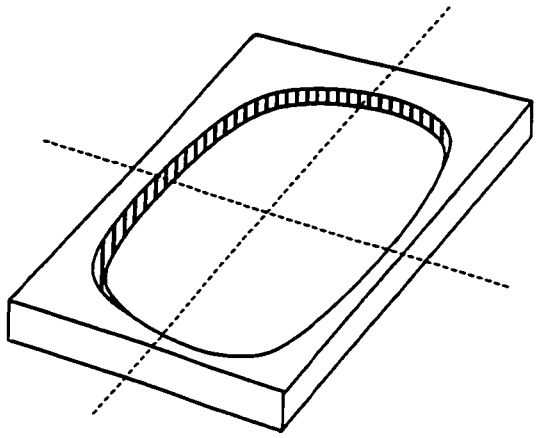

(b): Global shear failure

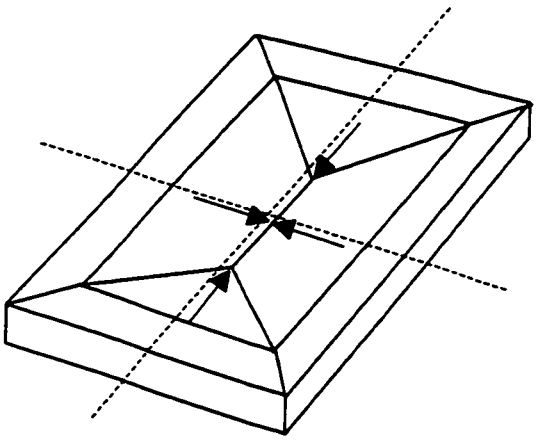

(c): Local bending failure

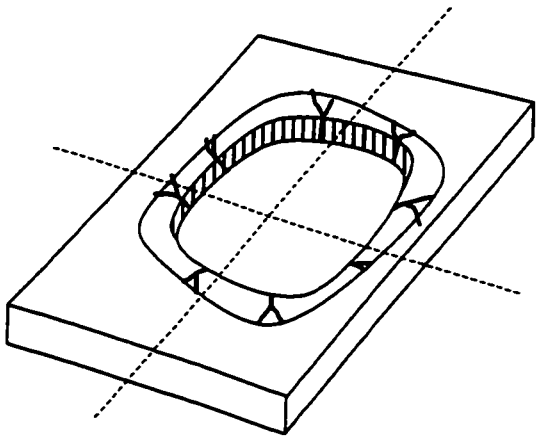

(d): Local shear (breaching) failure

Figure 3.1: Principal failure mechanisms for slabs

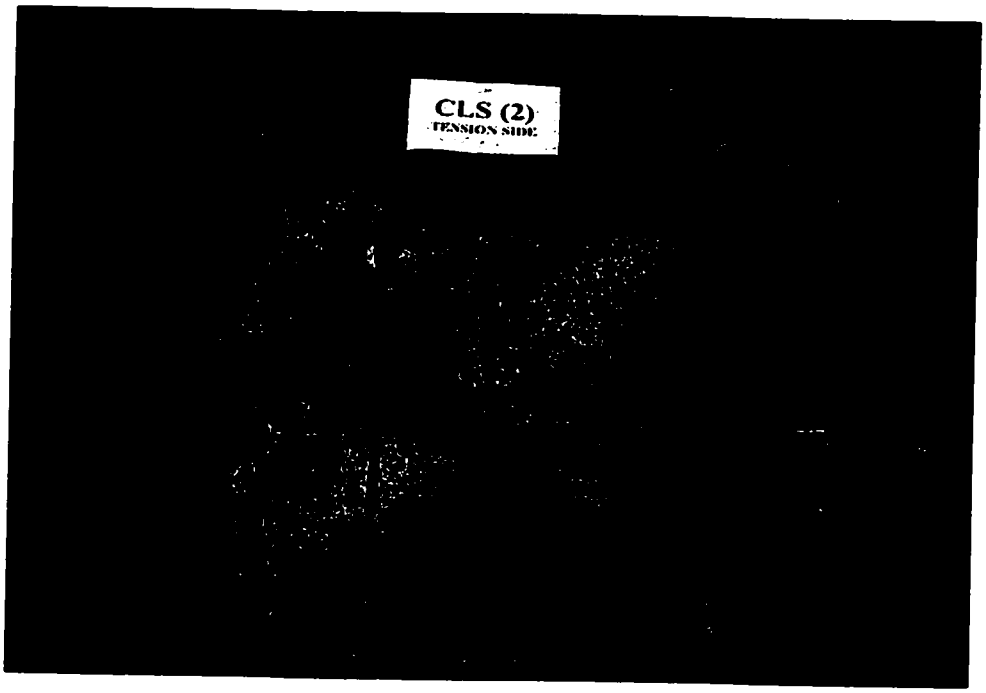

Figure 3.2: Spalling effect of close-in explosions (opposite surface to load direction) (Photograph by Ahmed Tolba)

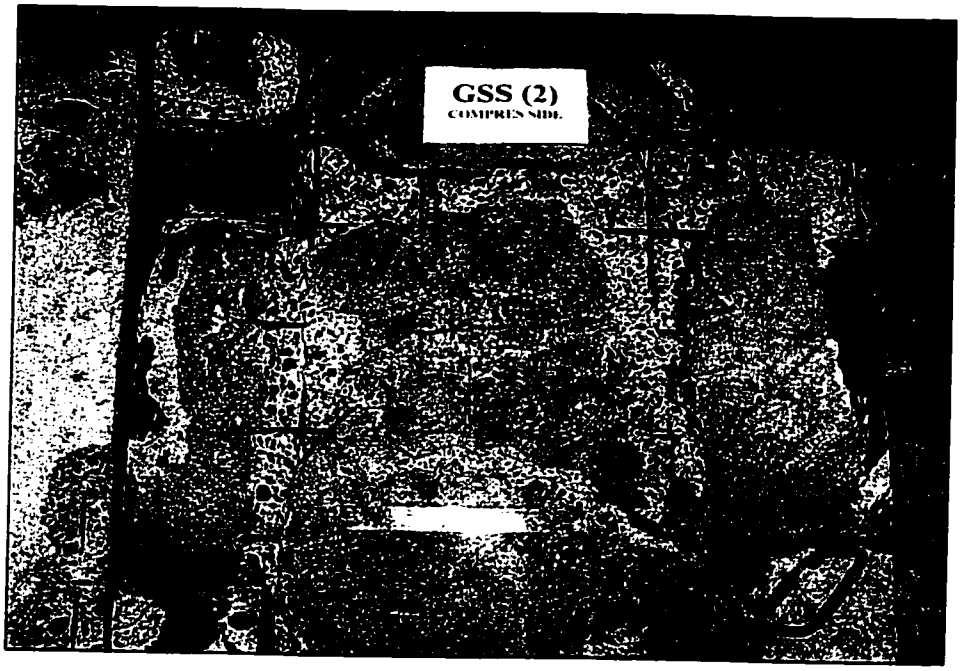

Figure 3.3: Scabbing effect of close-in explosions (surface facing the load direction) (Photograph by Ahmed Tolba)

3.3 Damage Criteria

The detonation of explosive charges in the vicinity of a structure may cause severe structural damage because of blast wave, fragments and ground shock. In the literature there are a number of theories that attempt to predict the structural damage to above ground and buried structures subjected to blast loads. The following is a brief overview of the existing methods used to evaluate both global and local damage criteria of structures.

3.3.1 Global damage criteria

Structural resistance of reinforced concrete elements to a particular type of damage is strongly related to their ductility, and the rate at which load is applied. There are a variety of damage indices that can be used to predict the damage level of a loaded structure. Ductility ratio, μ, provides a metric for bending response and is defined as the ratio of maximum deflection, δ_{max}, at a given load to elastic deflection, δ_e (Jones, 1967). Thus,

$$\mu = \frac{\delta_{max}}{\delta_e} \tag{3.1}$$

This definition may cause some difficulties since δ_e is needed in order to calculate μ, and δ_e varies with the structural properties such as geometry, material characteristics, reinforcement ratio, etc. Moreover, historically ductility has been used in design to establish an upper bound for the capacity of a particular structural element, which has been loaded beyond its elastic limit, rather than for defining levels of damage (TM 5-1300, 1990). Alternatively, other physical parameters that are much easier to obtain, may be used to indicate damage levels. For example, support rotations, θ, or mid-span

deflection ratio, δ/L, are frequently used. Table 3.1 provides damage criteria for various structural elements expressed in terms of different measures (Drake *et al.*, 1989 and ASCE, 1980). These damage expressions are illustrated in Figure 3.4, which defines damage levels as a function of support rotation and mid-span deflection for reinforced concrete slabs. It is of importance to mention that shear deformations are different from flexural deformations due to their more localized nature. In flexure, formation of a plastic hinge requires that the hinge size be about equal to the member's depth. In shear, however, one may obtain a failure mechanism that is considerably more localized. Strain rate also plays a role in determining the failure criteria because of its influence on rupture strain and material strength (Crawford and Karagozian, 1995).

3.3.2 Localized damage criteria

Localized responses are typically related to main structural elements such as walls and roof slabs. The damage associated with such elements is mainly dominated by localized shear failure, which typically causes spalling and breaching. Such parameters can be obtained through 3-D non-linear finite element (FE) calculations. Bogosian (1994) modeled the effect of close-in explosions on a reinforced concrete panel using brick elements for concrete along with truss elements for steel. This type of modeling uses a continuum FE analysis, and needs knowledge of strain rate effects on modeled materials. A primary advantage of such a technique is that both the size of breach and the velocity of fragments can be accurately determined. Similar studies can be found in Crawford *et al.*, (1997). Alternatively, analytical expressions, based on experimental data, in the form of damage diagrams can be used as discussed in Section 3.4.

Table 3.1: Allowable ductilities and support rotations for various structural elements (Drake *et al.*, 1989 and ASCE, 1980)

Structural Element	Ductility Ratio (μ)
Beams	
Failing in shear (diagonal tension)	1.9
Failing in shear (shear-compression)	1.5
Failing in flexure with at least 1/4 as much compressive as tensile reinforcement	6.0
Beam-columns: failing in compression or by buckling	1.5
Two-way and flat slabs	
Failing in shear	2.0
Failing in flexure	10
Structural Element	**Support Rotation (θ) in degrees**
Ultimate flexural resistance is maintained. Additional rotation results in crushing of concrete.	0-2
Symmetrically reinforced with shear reinforcement or lateral restraint.	2-4
Symmetrically reinforced with shear reinforcement and lateral restraint.	4-12

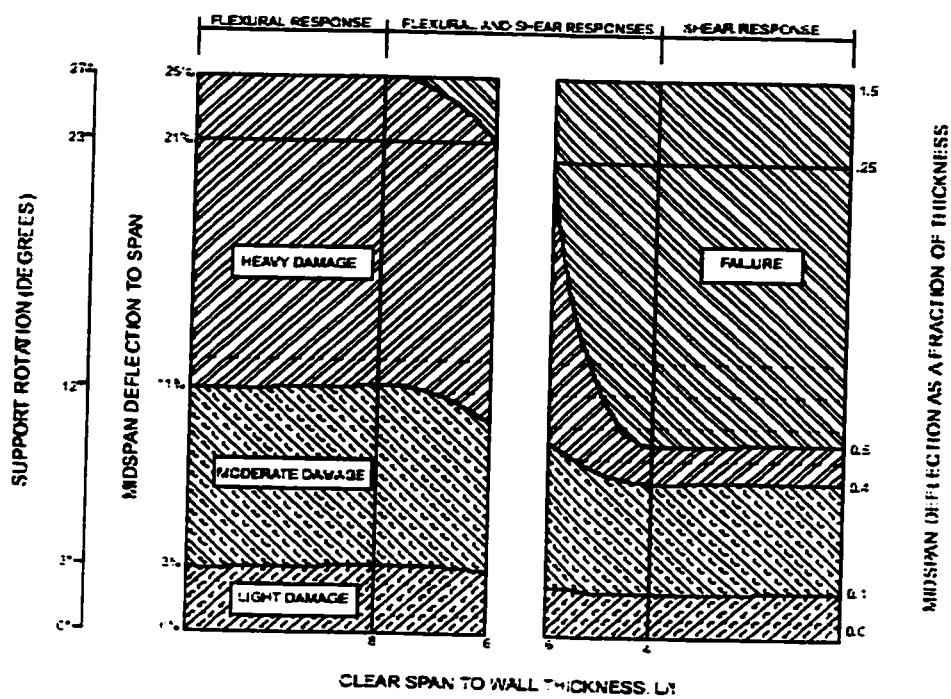

Figure 3.4: Damage criteria for reinforced concrete slabs (Crawford and Karagozian, 1995)

3.3.3 Blast-related studies

This section highlights the previous studies found in the open literature regarding the dynamic response of concrete structures subjected to actual or simulated blast loading, and the techniques proposed to increase the blast resistance capacity of existing structures with special attention to the use of externally bonded FRP composites.

Dynamic response to blast loading

An extensive experimental test program was conducted in the *Laboratoire Central des Ponts et Chaussees*, France (LCPC) during the period of 1990~1992 to investigate the high-speed dynamic behaviour and failure modes of concrete structures. Test specimens included plain and reinforced concrete circular slabs subjected to loads applied by a compressed-air version of shock tube. The 35-m shock tube can be filled with compressed air up to pressure of 6000 kPa (Toutlemonde and Boulay, 1993-b). Applying quasi-static loading (load duration being much greater than the natural period of structure) on plain slabs resulted in a bending failure mode and was characterized by radial cracks, as shown in Figure 3.5. Successive shocks with very short duration were applied to similar slabs until failure. Failure took place simultaneously by major radial crossing cracks accompanied by circular shear cracks along the support (see Figure 3.6). Tests were also performed on reinforced concrete slabs using different loading schemes. The bending mode was found to dominate slabs failure due to the bond failure between steel reinforcement and concrete. After a pattern of rather thin cracks was created as a result of small intensity shocks at the tension side, this network remained stable but the cracks were much wider during higher loads. It was observed that cracks in the middle

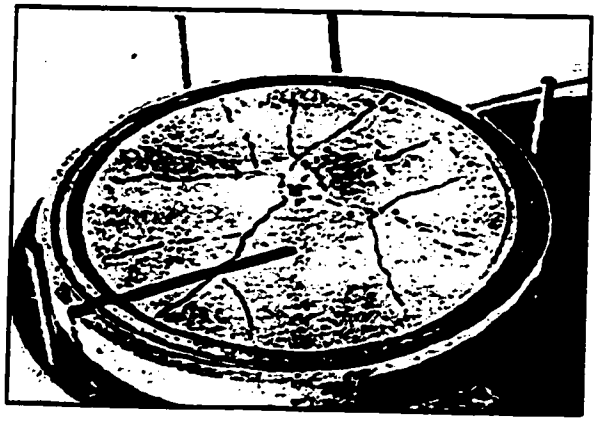

Figure 3.5: Bending failure of plain concrete slab under quasi-static load (Toutlemonde and Boulay, 1993-b)

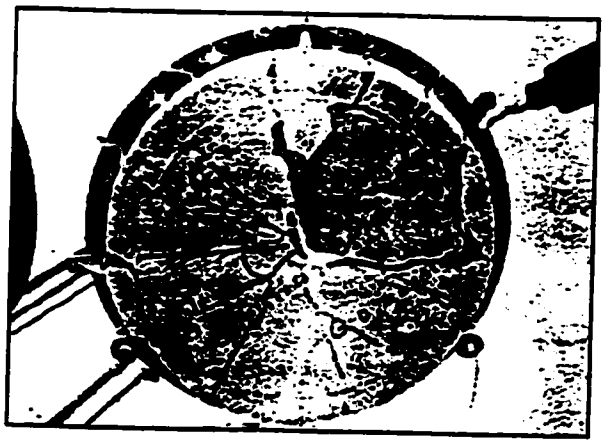

Figure 3.6: Bending-shear failure of plain concrete slab under successive shocks (Toutlemonde and Boulay, 1993-b)

Figure 3.7: Bending failure of reinforced concrete slab under successive shocks (Toutlemonde and Boulay, 1993-b)

were mostly parallel to the direction of the reinforcing mesh. Increasing load intensity resulted in total bending failure, and the reinforcing mesh ruptured through major cracks. Failure of slabs after successive blast shocks is shown in Figure 3.7. It can be concluded that for both quasi-static and multi shock loading, final rupture was controlled by the steel failure. Also, failure modes can be changed according to loading rate, concrete quality, and concrete-steel bond strength.

The Belgium Infrastructure Dep. sponsored an experimental program during the period of 1988~1992 to evaluate the effect of concrete strength on the blast-resistance capacity of reinforced concrete conventional and high strength steel-fibred concrete slabs of dimensions 1200 × 1200 × 160 mm (Naeyaert, 1993). Test slabs were subjected to close-in effects of blast pressures produced by detonation of high explosive 3.75 kg charges at standoff distance of 0.75 meter. Full test results were not released for publication. Naeyaert briefly described some results including the fact that steel-fibred concrete had better blast resistance than otherwise similar specimens without fibres. Also, the addition of steel fibres provides lower deflection, no breaching, and more blast resistance.

A more recent experimental program was conducted by *Wilfred Baker Eng.*, USA to test concrete masonry units (CMU) using the shock tube shown in Figure 3.8 (Personal communications, 2000). The CMU had dimensions of 2500 × 2500 mm with different orientations (with and without central openings). In order to assess the feasibility of using externally bonded FRP composites to enhance the out-of-plane blast resistance, some test specimens were retrofitted using unidirectional Kevlar fabric attached to both faces. Figure 3.9 shows a test wall before testing. Two brittle modes of failure were noticed as

Figure 3.8: Shock tube used for CMU testing

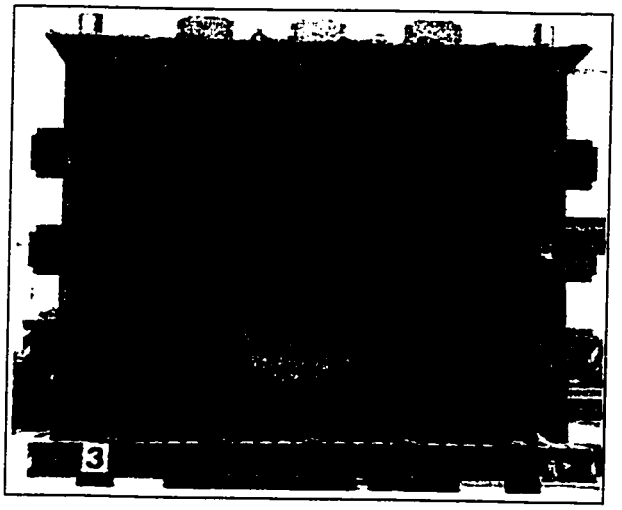

Figure 3.9: Kevlar-retrofitted CMU before testing

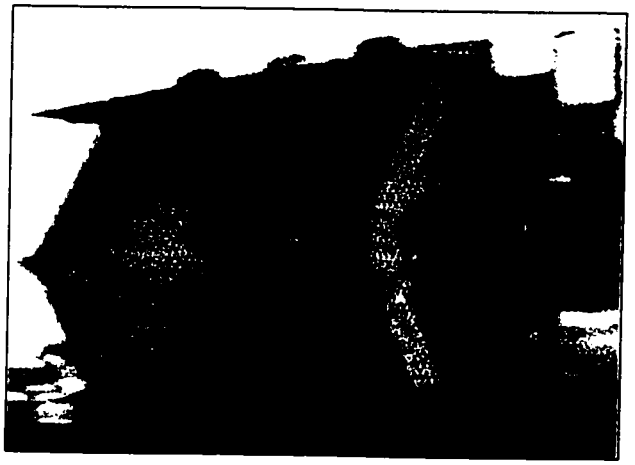

Figure 3.10: Bending failure of retrofitted CMU

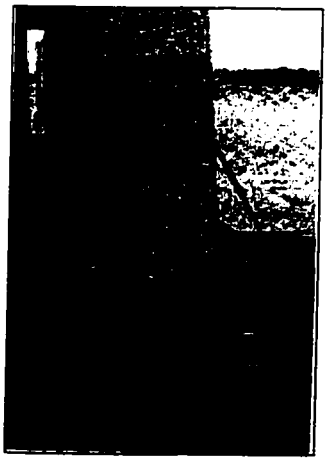

Figure 3.11: Shear failure

tensile/compressive failure in zones of high flexure, and shear failure near supports. It was noticed that the flexural behaviour of blast-loaded CMU can be improved by using Kavler fabrics. Flexural and shear failure of the CMU are shown in Figure 3.10 and 3.11.

Retrofitting of blast-loaded structures

The ability of using FRP composites to increase the flexural resistance of reinforced concrete members under static loads has been demonstrated through extensive experimental research during the past decades, and can be found in many references, see ACI (1995), ACI (1993) and JSCE (1993). Experimental and theoretical studies concerning the effect of FRP composites on improving the blast loading resistance of existing structures are very few. Target structures may be subjected to such hazardous loads resulting from accident or ill-intention. Yet, most civil structures are not designed against such extreme loads. On the other hand, although most military structures are designed according to blast-resistance guidelines, they may still face the same overloading problems due to the increased destructive effects of weapons.

This has encouraged some official agencies, such as the U. S. Department of Defence and the Israeli Home Front Command (HFC) to support research and development programs to test, develop and establish modern strengthening measures for existing buildings in order to increase their blast-resistance capacities. The following is an overview of the published research work in this field. After the Iraqi Scud missile attacks in 1991, the Israeli HFC started a five-year research program to test 151 structural and non-structural elements within four blast-loaded full-scale structures. The main goal was to establish effective measures to strengthen different elements, including windows, doors, walls and ceilings. Full results of the study are not available, but some of the recommendations

related to reinforced concrete walls (as structural members) and windows (non-structural elements) were revealed by Eytan (1994). They included application of additional inner ballistic covers and/or concrete layers to the inner and outer walls. The damage threshold for the retrofitted walls was enhanced by 52 % and 100 % for the two techniques. For windows, the use of additional 100-micron security film on the inner side of the glazing enhanced the damage threshold by 60 %. It was also found that the existing window frames should be replaced by special blast-resistant aluminium or steel frames.

Continuing the above research, in 1994 the Israeli HFC and the Israeli Civil Defence Force started a research program to study the effects of air blast explosions on reinforced concrete structures and masonry walls retrofitted with externally applied FRP composites (Muszynski, 1995). Two reinforced concrete cubic structures, similar to the in-service Israeli bomb shelters, were constructed and retrofitted using carbon fibres and kevlar/glass composites. Some walls and roofs were intentionally left bare for reference purposes. Three masonry walls of 2800 × 2600 mm dimensions were retrofitted with the same materials used for the reinforced concrete walls. Test specimens were subjected to an air blast originated from the detonation of 830-kg TNT at a 14.5 m standoff. Test walls were heavily instrumented to measure incident and reflected pressures, displacement and accelerations. Results related to the maximum displacement were published by Muszynski, (1995 & 1996). Displacement reduction of 40 and 25 % for the reinforced concrete walls retrofitted with Kevlar and carbon composites, respectively, were obtained. Kevlar retrofitted masonry walls displayed more ductile failure and energy absorption, and displacement reduction of about 30 %.

The dynamic behaviour of reinforced concrete structures under the effect of blast loads has been the focus of a few published studies. Beshara (1991) developed a numerical research that was mainly concerned with the development of strain rate dependent constitutive models for concrete under the effect of blast loading. He developed computational algorithms and modified solution procedures for various structural elements. The proposed models were implemented in a finite element computer program, which can be used for non-linear dynamic analysis of two-dimensional reinforced concrete structures subjected to blast loads. For more details, see Beshara (1994-a & b).

Using DYNA 3D Code, Crawford *et al.,* (1997) demonstrated the effectiveness of FRP composite jacketing to increase the blast-resistant capacity of reinforced concrete columns. DYNA3D is a finite element program that has capabilities to model blast waves resulting from different types of explosions. Two reinforced concrete structures were deigned according to the seismic loading zones 1 and 4, respectively. Selected columns of different cross sections (circular and rectangular) were retrofitted using steel and FRP composite jackets. Blast pressure was assumed to originate from the detonation of high explosive charges ranging from 682 to 1364 kg TNT equivalent at standoff distances ranging from 3.05 to 12.2 m. From the analytical results, it was concluded that

- Using FRP composite jacketing reduced the maximum displacement by 50~60 % and prevented the failure of both rectangular and circular columns under the maximum applied charge. However, jacketing did not prevent the propagation of high-pressure waves or fragments through the building.
- A simple and effective solution to reduce the damage effect on target structures is to increase, whenever possible, the standoff distance.

3.4 Damage Diagrams

In the literature, damage or response diagrams for structural elements exposed to blast loads are frequently presented in the form of plots that show three levels of damage referred to as *No damage*, *Spall*, and *Breach*. The damage definition is then expressed in terms of pressure-impulse diagrams that determine the degree of structure's susceptibility to blast loading. The following is a description of the damage curves and the possibility of using them to predict the damage condition of a structure at a certain loading level.

3.4.1 Spalling Diagrams

According to Kinney and Graham (1985), blast pressures produced by the detonation of high explosive charges may cause damage to target structures in three different manners

- Concrete spalling from the back face of the exposed panels, caused by stress propagation and wave reflection in the panel
- Deformation of the exposed panel
- Global deformation of the entire structure

The spalling phenomenon has been the concern of many studies, and has been treated in many design manuals to assess its effects. The US Army (1990) TM 5-1300 manual, introduced a response diagram in terms of the scaled thickness ($t/W^{1/3}$) of reinforced concrete panels versus scaled standoff distance ($R/W^{1/3}$), where W is the charge weight, t is the panel thickness, and R is the standoff distance. Spalling diagrams were developed using a considerable amount of experimental data collected from both the US Army tests and from the literature. The damage is defined in three different categories namely: no damage, spalling and breaching (Helge Langberg, 1993).

A similar diagram was independently introduced in the Norwegian Fortification Manual based on test data from the Second World War. It gives a larger spall region than in the US manual (see Figure 3.12). Damage diagrams raise a number of issues regarding the information needed for their use and the interpretation of their results. For instance, they do not account either for the dimensions of the structure or for its reinforcement details. This indicates that either damage is caused by the stress wave propagation, or that structural response is so local that it is independent of target dimensions. These issues have motivated researchers to introduce other forms of damage curves.

3.4.2 Pressure-impulse diagrams

The pressure-impulse (P-I) diagram is an easy way to mathematically relate a specific damage level to a combination of blast pressures and the corresponding impulses for a particular structural element. Jerrett (1968) introduced one of the most extensive databases for P-I diagrams. He used data obtained from bomb damage in the UK during World War II. An example of the P-I diagrams is shown in Figure 3.13 to obtain levels of damage of brick houses, in which region *A* corresponds to complete demolition and *B* means damage severe enough to necessitate demolition. Region *C* impulse causes partial collapse of the roof and one or two exterior walls that would render the house temporarily uninhabitable. Finally, region *D* refers to damage calling for urgent repair but is not severe enough to make building uninhabitable with at least 10 % of glazing being broken. There are, however other P-I diagrams that concern with human response to blast where three categories of blast-induced injury are identified as: primary, secondary, and tertiary injury. For more details on this subject, refer to Baker *et al.*, (1983).

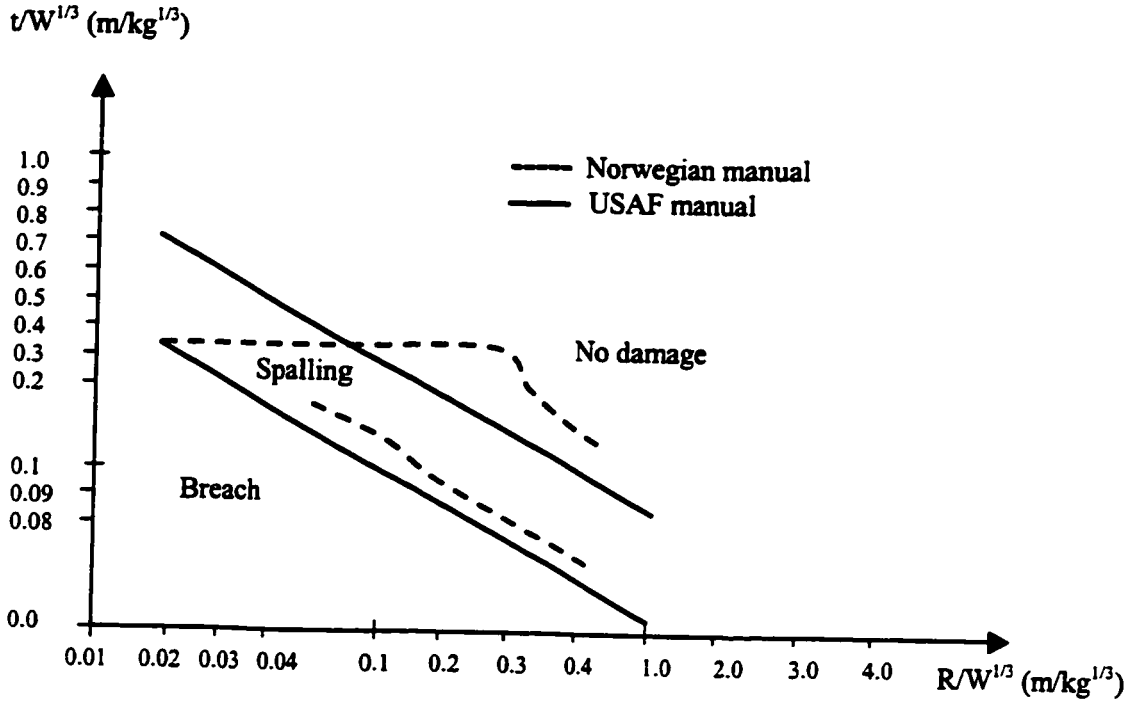

Figure 3.12: The US and Norwegian damage diagrams for reinforced concrete panels (Helge Langberg, 1993)

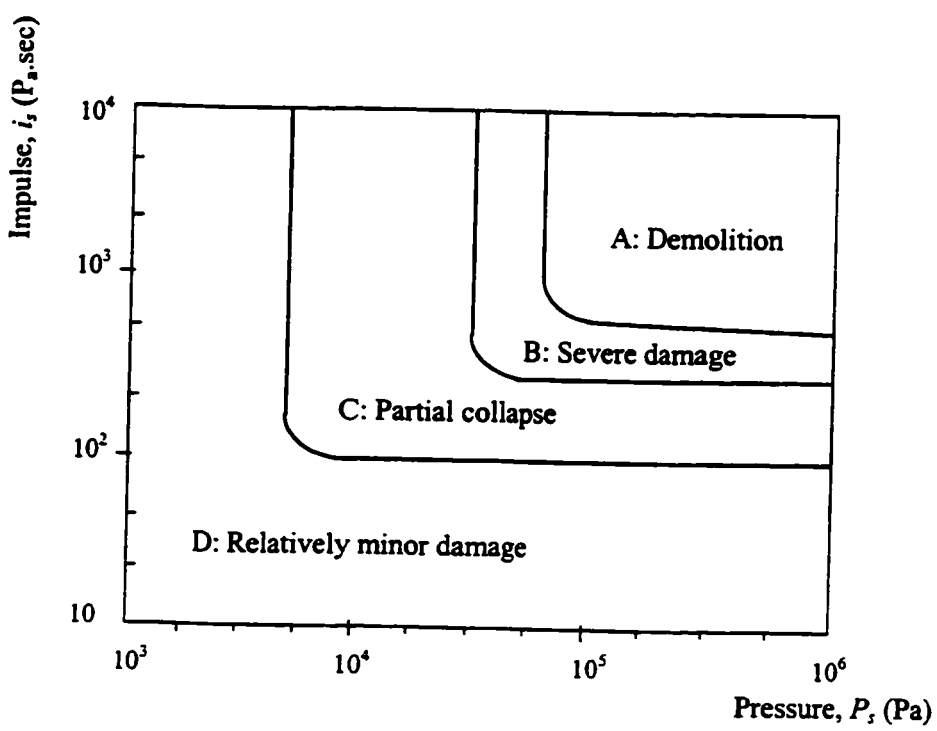

Figure 3.13: Pressure-Impulse diagram for building damage (Baker *et al.*, 1983)

3.5 Strain Rate Effects

The mechanical properties of concrete under dynamic loading conditions can be quite different from that under static loads. Since dynamic properties of almost all materials are strain-rate dependent, behaviour of structural elements under various dynamic loads can be predicted by considering the time-dependant properties of the materials. Bischoff and Perry (1991) introduced approximate ranges of the expected strain rates for different loading conditions as illustrated in Figure 3.14. It can be seen that ordinary static strain rate is located in the range of 10^{-6}~10^{-5} s^{-1}, while blast pressures normally yield loads associated with strain rates in the range of 10^{2}~10^{4} s^{-1}. These ranges agree with values given in the US Defence Special Weapons Agency (DSWA) report (Malvar and Ross, 1998).

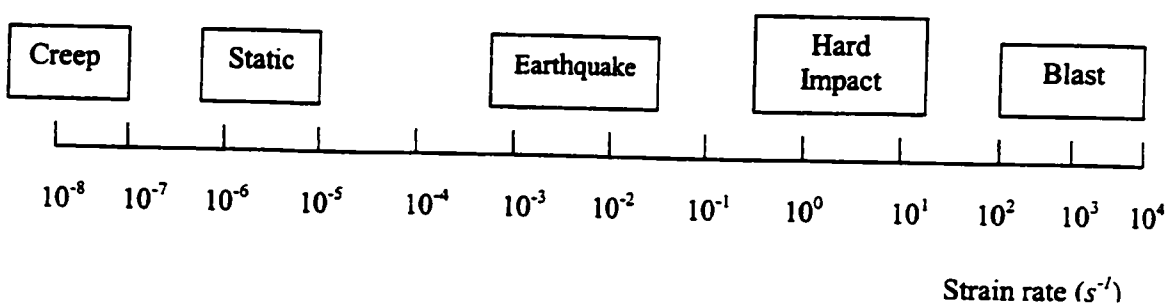

Figure 3.14: Strain rates associated with different loading conditions (Bischoff and Perry, 1991)

3.5.1 Testing at high strain rate

The importance of exploring effects of high-strain (loading) rates on both concrete and reinforcing steel is reflected in the extensive research work over the past eight decades. Strain rate, $\dot{\varepsilon}$, is defined as the rate of change of strain, ε, with time, t. It has been observed that at high strain rates the material microstructure is remarkably affected by the sudden change in the deformation mode. This arise to considerable mechanical property changes due to the so-called metallurgical effects (Murr, 1987). Consequently, increasing the strain rate results in higher dynamic material strength.

One commonly accepted way of presenting the dynamic increase in material strength is the dynamic increase factor (DIF), i.e. the ratio between dynamic strength and static strength of the material under consideration (Full details of this subject can be found in Biggs, 1964). Figures 3.15 and 3.16 show the effect of strain rate on concrete strength in compression and tension, respectively. The two plots summarize experimental data related to the effect of stain rate on material strength obtained over a period of more than 60 years. The large scatter in these data clearly indicates the considerable difficulties in establishing the influence of the strain rate on concrete strength. According to Bischoff and Perry (1991), the kind of dynamic testing necessary is much more complicated to carry out than similar static tests. Therefore, it is more important to consider what influence test parameters may have on the obtained results. Hence, the large scatter shown in Figures 3.15 and 3.16 can at least partially be explained by a mixed usage of important parameters such as: the concrete strength, specimen dimension, moisture content, test method, and loading (straining) rates.

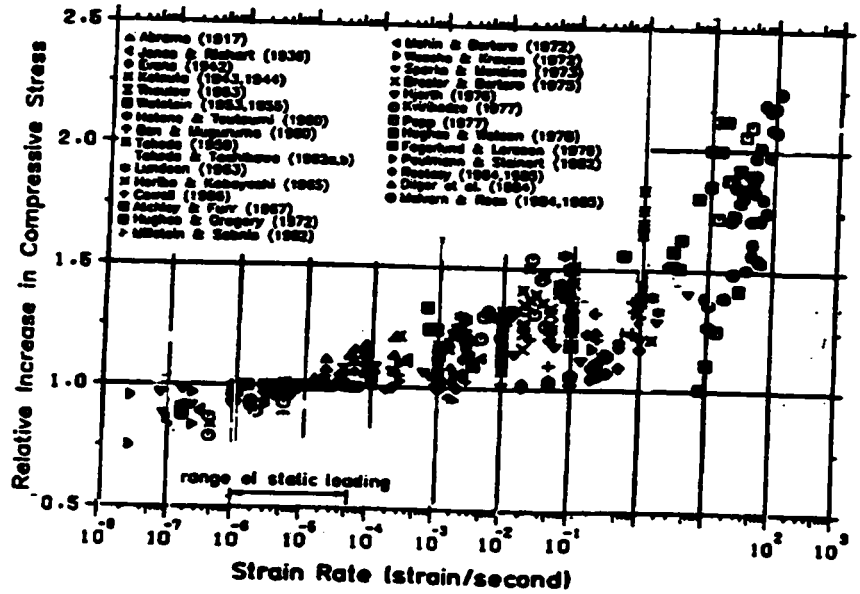

Figure 3.15: Strain rate effect on compressive strength of concrete (Bischoff and Perry, 1991)

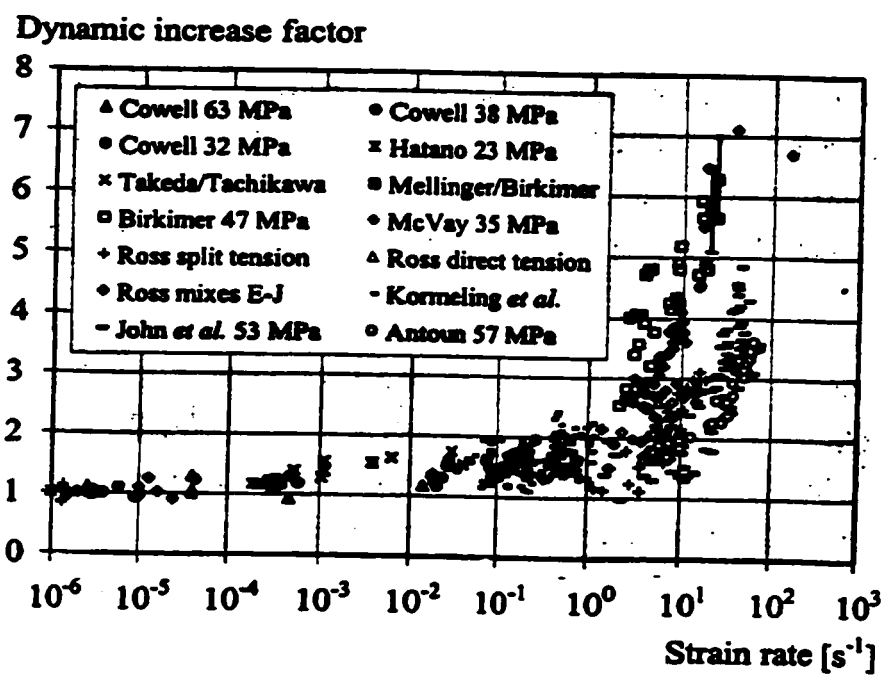

Figure 3.16: Strain rate effect on tensile strength of concrete (Malvar and Ross, 1998)

A number of theories have been put forth to explain the increase in concrete strength, yet none gives a precise proof to the observed phenomenon. According to Johansson (2000), the strain rate effect in concrete can be ascribed to two phenomena: viscous and structural effects. The former, which leads to relatively moderate strength enhancements at increased strain rate, can be said to occur at strain rates up to the so-called transition zone (30 s^{-1}), see Figure 3.17. A commonly accepted theory is that this increase is largely due to the presence of the free water in the concrete micropores. At strain rates above that of the transition zone, the dynamic strength increase is more dramatic (may reach up to four times the static one) because structural effects, i.e. inertia and confinement, dominate the dynamic strength contribution. This is further discussed in Zielinski *et al.*, (1981), Reinhardt *et al.*, (1990), and Rossi *et al.*, (1994, 1996).

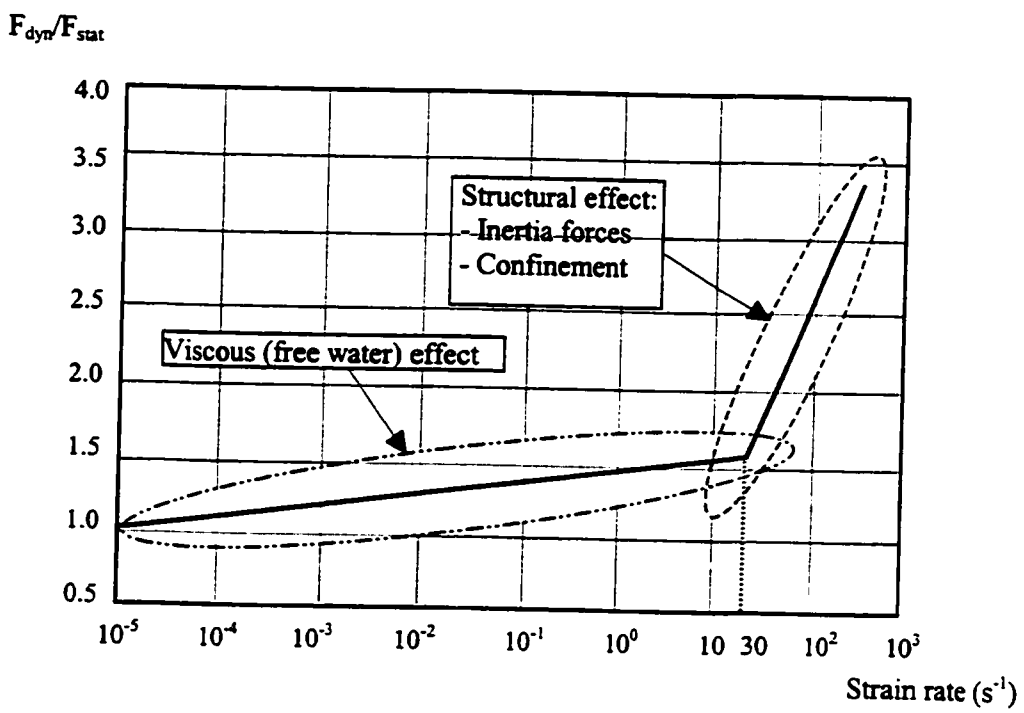

Figure 3.17: Strain rates at which the viscous and structural effects take place (Johansson, 2000)

3.5.2 Dynamic properties of concrete under high-stain rate

According to Fu *et al.*, (1991), the earliest dynamic tests on concrete in compression were conducted by Abrams (1917) to investigate the effect of straining (loading) rate on compressive strength of plain concrete. Following this, more dynamic tests were carried out during the 30s and 40s to explore the relation between the rate of loading and the compressive strength of plain and reinforced concrete, and the factors that govern this relation. The main conclusion of these pioneer works was that the higher the rate of straining (loading), the higher the compressive strength of concrete as well as the yield strength of steel.

Watstein (1953) conducted a series of experiments on plain concrete cylinders of dimensions 76 × 152 mm. Cylinders were prepared using two different concrete batches of 17.4 and 45.1 MPa compressive strength. Test specimens were subjected to uniaxial compression at a static strain rate in the range of 10^{-6} to 10^{-5} s^{-1}. High strain rate of 10 s^{-1} was also applied by means of a drop hammer machine. Test results indicated increase of 84 % and 85 % in compressive strength for the two batches, respectively.

To study the effect of concrete properties on strength gain, Atchley and Furr (1967) tested 60 plain concrete cylinders of dimensions 152 × 305 mm made of concrete strengths of 17.4, 25.7, and 34.7 MPa. Strain rates ranged from 5×10^{-6} to a high rate of 5 s^{-1}. One of the main findings was that strong concrete appears to be less sensitive to the rate of loading than weak concrete. Also two expressions were suggested to predict the dynamic strength of concrete. For loading rates up to 6944 MPa/s, the concrete strength increased by 25 %. An increase of about 38 % is expected for higher strain rates.

Spooner (1971) studied the effect of curing conditions on strain rate sensitivity of plain concrete. Specimens cured in water (wet concrete) showed an increase of 12 % in dynamic strength upon testing at strain rates ranging between 5×10^{-6} and 0.037 s^{-1}. He concluded that dry concrete (cured in air) showed less sensitivity to strain rate increase.

To investigate the effect of aggregate type on strain-rate sensitivity, Sparks and Menzies (1973) tested 48 rectangular plain concrete prisms of dimensions 102 × 102 × 203 mm. Three types of aggregate (gravel, limestone, and lytag) were used in sample preparation with corresponding static strengths of 30, 30 and 20 MPa, respectively. Samples were subjected to high loading rates of 0.001~10 MPa/sec. Limestone prisms showed an increase of 4 % in compressive strength under high loading rates, while lytag prisms had a 16 % strength increase under the same loading rates. It was concluded that weak concrete appears to be more sensitive to high loading rates than strong concrete.

Wakabayshi (1980) tested 45 plain concrete cylinders of dimensions 50 × 100 mm under uniaxial compression at strain rates of 2×10^{-5}~ 0.1 s^{-1}. Compared to compressive strength of concrete at static strain rate, an increase of about 24 % was observed upon testing at high strain rate of 0.05 s^{-1}. Also, it was found that peak stress; initial tangent modulus and therefore the stress-strain curve of concrete vary with increasing strain rates.

Figure 3.18 illustrates the strain rate effect on the stress-strain curve of concrete in compression, in which it can be shown that up to about 50 % of the load, the stress-strain curves in both loading conditions are almost the same. The dynamic strength of concrete, f'_{cd}, seems to have about 25 % increases over the static concrete strength, f'_c (TM 5-1300, 1990).

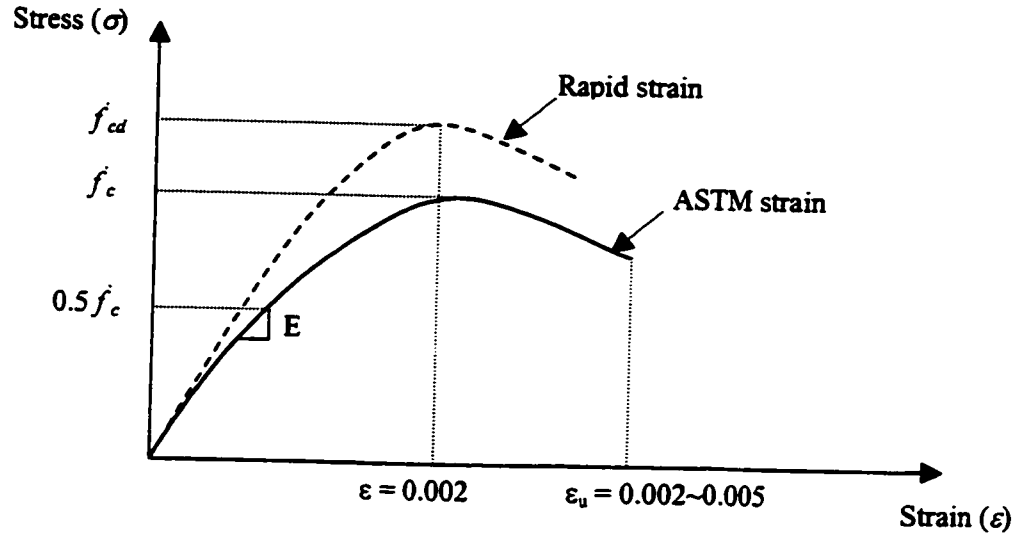

Figure 3.18: Strain rate effect on stress-strain curve of concrete (TM 5-1300, 1990)

Having established the direct relation between the rate of loading and compressive strength of concrete, researchers over the past two decades have studied the effect of increasing rate of loading on modulus of elasticity of concrete, strain values at both maximum stress and failure, and the stress-strain relationship. Scott *et al.*, (1982) conducted an extensive series of tests to confirm the effect of strain rates on the stress-strain relationship of both plain and reinforced concrete. Twenty-five reinforced concrete rectangular specimens of dimensions 450 × 450 × 1200 mm were subjected to concentric and eccentric loads at strain rates varying from 3.3×10^{-6} to 0.0167 s^{-1}. Test results indicated an increase of about 25 % in both stress and strain at failure by increasing the rate of straining. Also, the shape of the stress-strain curve of confined concrete was found to be strongly affected by change in loading rate, for a given stress level, the corresponding strain decreasing. As a result, both the secant and the rupture moduli significantly increased with increasing loading rate. Many researchers confirmed these findings, such as Dilger *et al.*, (1984), Malkar *et al.*, (1985), Soroushian *et al.*, (1986).

The U. S. Defence Special Weapons Agency (DSWA) sponsored a recent numerical research to study the response of reinforced concrete structures under the effect of high strain rates in the order of $10 \sim 10^3\ s^{-1}$ resulting from internal explosions. Complete results of the study were not released for publication. Some of these results are introduced by Malvar and Ross (1998), in which the apparent strength was remarkably increased, by more than 50 % for reinforcing steel and by more than 100 % and 600 % for concrete in compression and tension, respectively. They also proposed an enhanced expression that accounts for the effect of high strain rates on tensile strength of concrete, viz.

$$DIF = \frac{f_{td}}{f_{ts}} = \left(\frac{\dot{\varepsilon}}{\dot{\varepsilon}_s}\right)^{\delta} \qquad \dot{\varepsilon} \leq 1\ s^{-1} \qquad (3.2)$$

$$DIF = \frac{f_{td}}{f_{ts}} = \beta\left(\frac{\dot{\varepsilon}}{\dot{\varepsilon}_s}\right)^{\frac{1}{3}} \qquad \dot{\varepsilon} > 1\ s^{-1} \qquad (3.3)$$

where

- f_{td} and f_{ts} = the dynamic and static tensile strengths of concrete, respectively
- f_{td}/f_{ts} = tensile strength dynamic increase factor (*DIF*)
- $\dot{\varepsilon}$ and $\dot{\varepsilon}_s$ = high strain rate (up to $10^4\ s^{-1}$), and static strain rate ($10^{-6} \sim 10^{-5}\ s^{-1}$)
- $\log \beta = (6\delta) - 2$, $\delta = \dfrac{1}{1 + 8\left(f_c^{'}/f_{co}^{'}\right)}$ and
- $f_{co}^{'}$ = fraction of the compressive strength of concrete (can be assumed 10 MPa)

It was concluded that under high strain rate, greater than 200 s^{-1}, the dynamic increase factor could reach values up to 6. The magnitude of dynamic increase is dependent upon several factors including static strength of material under consideration and strain rate of applied load. In general, the higher the static strength of a material, the lower the increase in dynamic strength (lower strain rate sensitivity). The faster the martial is strained, the higher dynamic strength gain is expected. Figure 3.19 illustrates the relationship between strain rate of applied load and the *DIF* for structural steel, concrete and reinforcing steel.

3.5.3 Dynamic properties of reinforcing steel under high-stain rates

Due to the isotropic properties of metallic materials, their elastic and inelastic response to dynamic loading can easily be monitored and assessed (Fu *et al.*, 1991). Norris *et al.*, (1959) tested steel with two different static yield strength of 330 and 278 MPa under tension at strain rates ranging from 10^{-5}~0.1 s^{-1}. Strength increase of 9~21 % and 10~23 % were observed for the two steel types, respectively.

Dowling and Harding (1967) conducted tensile experiments using the tensile version of Split Hopkinton's Pressure Bar (SHPB) on mild steel using strain rates varying between 10^{-3} s^{-1} and 2000 s^{-1}. It was concluded from this test series that materials of body-centred cubic (*BCC*) structure (such as mild steel) showed the greatest strain rate sensitivity, the lower yield tensile strength of mild steel is almost doubled, the ultimate tensile stress was increased by about 50 %, the upper yield tensile strength considerably increased, and the ultimate tensile strain decreased by different percentages depending on the strain rate. Figure 3.20 illustrates the stress-strain relationships of mild steel under the effect of different strain rates varying from 10^{-3} to 1750 s^{-1}.

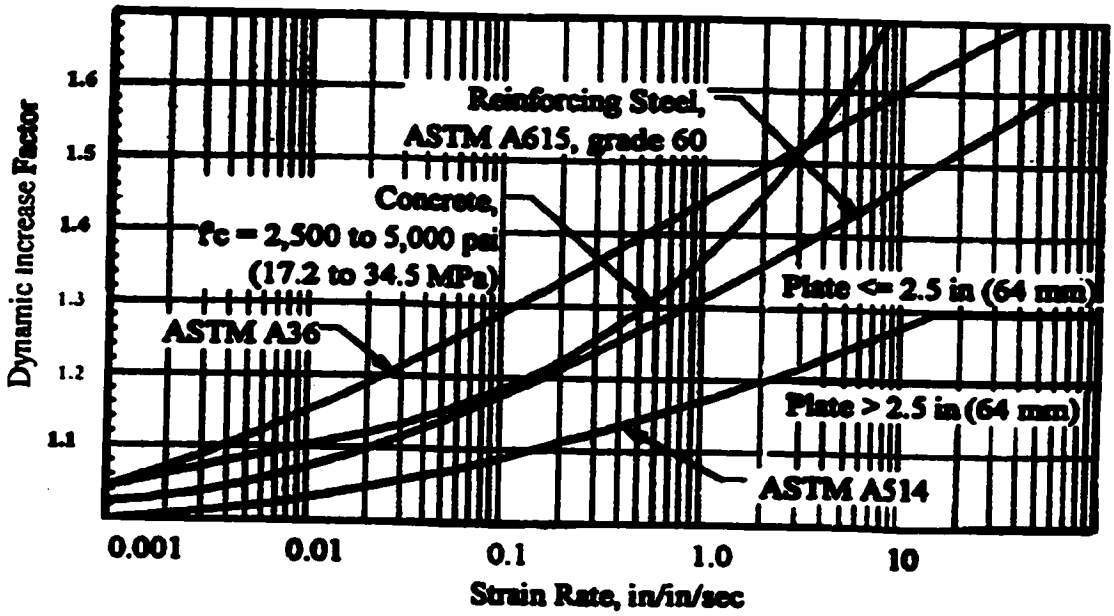

Figure 3.19: Strain rate effect on the dynamic strength of materials (TM 5-1300, 1990)

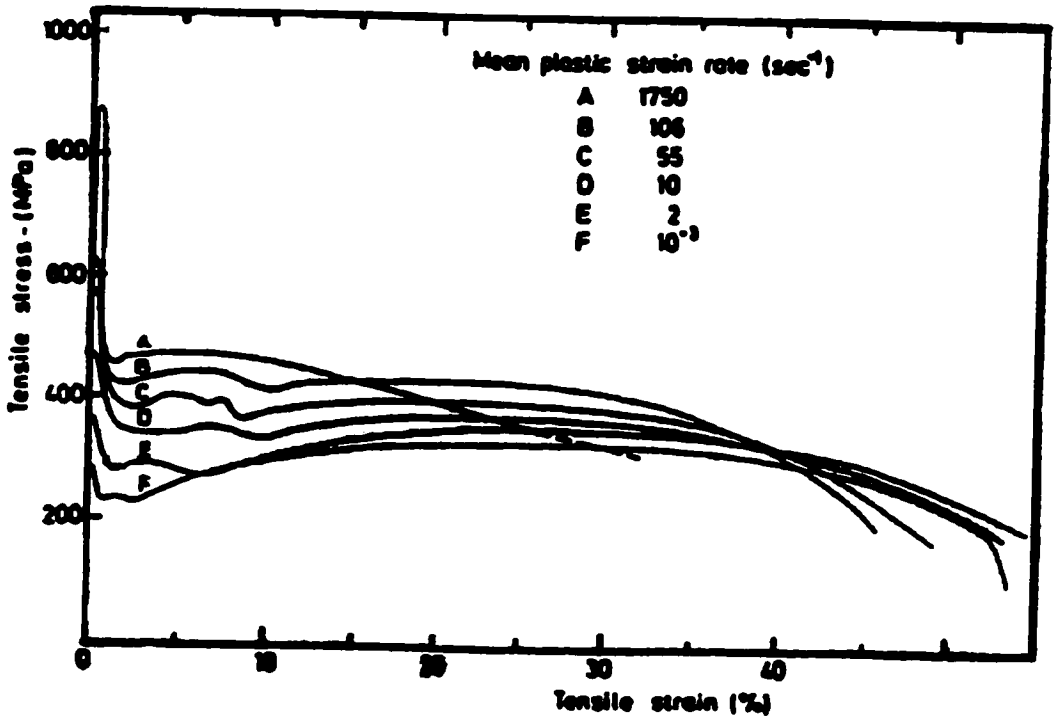

Figure 3.20: Strain rate effect on stress-strain of mild steel (Dowling and Harding, 1967)

Wakabayashi (1980) performed tension tests at strain rates of 5×10^{-6}~$0.1\ s^{-1}$ on 16 smooth and 16 deformed steel bars, all of 13 mm diameter. It was observed that both the upper and lower yield stresses of steel bars increased with increasing strain rate. The average increase ranged from 7~18 %. The strain rate apparently did not have effect on the modulus of elasticity, and little influence on the ultimate strength and the strain-hardening zone of the stress- strain relationship.

At the Naval Civil Eng. Laboratory (NCEL) USA, a series of dynamic tests were performed by Keenan *et al.*, (1983) to study the effect of high strain rates of order 10~100 s^{-1} on the mechanical properties of No. 6, 7 and 9 reinforcing steel bars with static yield strength between 276 and 338 MPa. Results for mild steel samples indicated an increase of about 60 % in the yield stress and this increase depended on the steel grade.

Malvar (1998) also studied strength enhancement of steel reinforcing bars under the effect of high strain rates. This was again described in terms of the *DIF*, which can be evaluated for different steel grades and for yield stresses, f_y, range from 290~710 MPa as:

$$\mathrm{DIF} = \left(\dot{\epsilon} / 10^{-4} \right)^{\alpha} \tag{3.4}$$

where for calculating yield stress $\alpha = \alpha_{fy}$, and

$$\alpha_{fy} = 0.074 - 0.04\,(f_y/414) \tag{3.5}$$

For ultimate stress calculations, $\alpha = \alpha_{fu}$, and

$$\alpha_{fu} = 0.019 - 0.009\,(f_y/414) \tag{3.6}$$

3.5.4 Dynamic properties of reinforced concrete in flexure

It is apparent that changing strain rate will alter the mechanical properties of both concrete and reinforcing steel. Of all high strain rate effects, the increase in concrete compressive strength and yield strength of steel are the most important. Consequently improving strength of the two main constituents (concrete and steel) is expected to increase the flexural capacity of reinforced concrete elements loaded at high strain rates.

Penzien and Hansen (1954) performed a series of tests on simple and continuous reinforced concrete beams. The main goal was to investigate the elastic behaviour of structural elements under the effect of impulse loads, which was provided by a high-pressure gas piston-cylinder arrangement. Two main conclusions were derived from this laboratory tests. First, the ultimate strains produced in the beams under the effect of the dynamic loads were found to be considerably larger than those produced in beams subjected to static loads of equal magnitude. The dynamic magnification factor, defined as the ratio between the maximum effective strains produced at a point under dynamic loading conditions to effective strains produced under equivalent static conditions, ranged from 1.5 to more than 3. Second, under the same dynamic loading conditions, the strength enhancement of steel was more predictable than that of concrete.

Aiming to study the effect of high strain rates on the dynamic behaviour of reinforced concrete elements, Bertero *et al.*, (1973) tested 4 simply supported, doubly reinforced beams having identical cross sections of 228 × 381 mm and span of 3657 mm. Test specimens were tested by two concentrated loads at the third points at high strain rates of 0.004 and 0.04 s^{-1}. It was pointed out that applying high strain rates increased both stiffness and the moment capacity at first yielding of steel reinforcement. This may

change the mode of failure in such a way that a brittle shear failure might occur in case of insufficient shear reinforcement.

The previous conclusions were confirmed by experimental tests conducted by Takeda *et al.*, (1971). They tested reinforced concrete beams of 150 × 200 mm cross section, and 2300 mm span at high loading rates ranging from 10^2 to 10^7 kN/s. Test results showed no apparent relation between strain rate and load-deflection characteristics of the tested beams. Also, it was demonstrated that reinforced concrete beams under high strain rates could fail in a brittle manner accompanied by some loss of shear strength of concrete, but in a ductile manner under the same loads applied statically.

More dynamic tests were conducted by Wakabayashi (1980), in which four (4) doubly reinforced concrete beams of 100 × 100 mm cross section and 900 mm span were tested under high strain rates of 0.01 s^{-1}. The main findings were that the load carrying capacity of reinforced concrete beams increased by about 30 % under such high strain rate, and that both the compressive strength of concrete and the tensile strength of steel were found to increase linearly with the logarithm of strain rate.

Price (1986) introduced in his study a new method for presenting the effect of dynamic loads by means of high displacement rates of 5~300 mm/s, corresponding to strain rates of 15~10^{-6} s^{-1}. Six reinforced concrete simply supported beams of 250 × 350 mm cross-section and 2700 mm span were divided into two groups of three each. Two different reinforcement ratios of 0.0038 and 0.0067 were used for the two groups, respectively. All test specimens were tested at the third points at high displacement rates. He concluded

that beams under faster rates of loading developed higher permanent deformations, and that high strains appear to have no effect on the flexural strength of the tested specimens.

The effect of high strain rates on bond in beam-column joints was the topic of experimental tests conducted by Chung and Shah (1989). They tested 12 small-scale reinforced concrete cantilever-type beams with different amount of shear reinforcements, and 3 identical exterior beam-column joint specimens at high strain rates in the order of 0.004~0.08 s^{-1}. A brittle mode of failure was observed for specimens tested under high strain rates. Since specimens subjected to high strain rates gain an increase in the tensile strength of concrete and enhancement in the bond strength, fewer cracks was observed. However, as indicated by Takeda *et al.*, the strength enhancement led to lower ductility at failure due to permanent fracture of reinforcing bars as a result of stress concentration.

3.5.5 Dynamic properties of FRP composites under high strain rates

The strain rate dependency of a given FRP martial is a function of the rate dependencies of its constituents, i.e. the resin matrix and the reinforcing fibres. Due to the complex interaction between the reinforcing fibres, which have a much higher strength and stiffness than the resin matrix, the dynamic properties of both materials at high strain rates are needed. Most of the available data in the literature related to effects of strain rates on polymeric matrix was obtained from compression tests.

Back and Campbell (1957) tested the effect of high strain rates on test specimens made of formaldehyde resin using the compression SHPB. Increasing the straining rates from 10^{-6}

to 500 s^{-1}, resulted in about double the initial slope of the stress-strain curve and the strength at a given strain. This was accompanied by a reduction in ductility.

The compression SHPB was also used by Lindholm (1968) to test epoxy resin specimens. He reported strength increase of threefold for a strain rate increase from 0.017 to 963 s^{-1}, and no brittle failure was observed. In more recent work, Welsh and Harding (1985) tested in tension epoxy resin specimens, and observed significant strength increase accompanied by a brittle failure at a tensile strain of about 3~4 % for all loading rates. A general conclusion can be drawn that polymeric matrix resins indicated a significant increase in strength under impact loading.

Unidirectional FRPs are mainly tested by tensile loads applied parallel to the direction of fibres. Welsh and Harding (1985) also tested specimens made of different unidirectional FRP composites having low fibre content of 17 % with an epoxy resin matrix. Tensile loads were applied in tension at strain rates between 10^{-4} to 900 s^{-1}. The unidirectional CFRP specimens showed almost no strain rate dependency (as indicated in Figure 3.21, a), while an increase of about 20 % in the fracture strength of the unidirectional GFRP sheets was observed under the high strain levels.

For woven-reinforced FRP composites there is likely more interaction between the fibres and the resin matrix. The increased interaction is believed to be the reason for the expected increase in the tensile modulus. Figure 3.21 (b) shows the effect of strain rate on the tensile stress-strain curves of fine-weave glass/epoxy specimens tested at strain rates from 10^{-4} to 900 s^{-1}. The tensile modulus increased from 20 GPa at a static strain rate of 10^{-4} s^{-1} to about 45 GPa when tested at a high stain rate of about 970 s^{-1}.

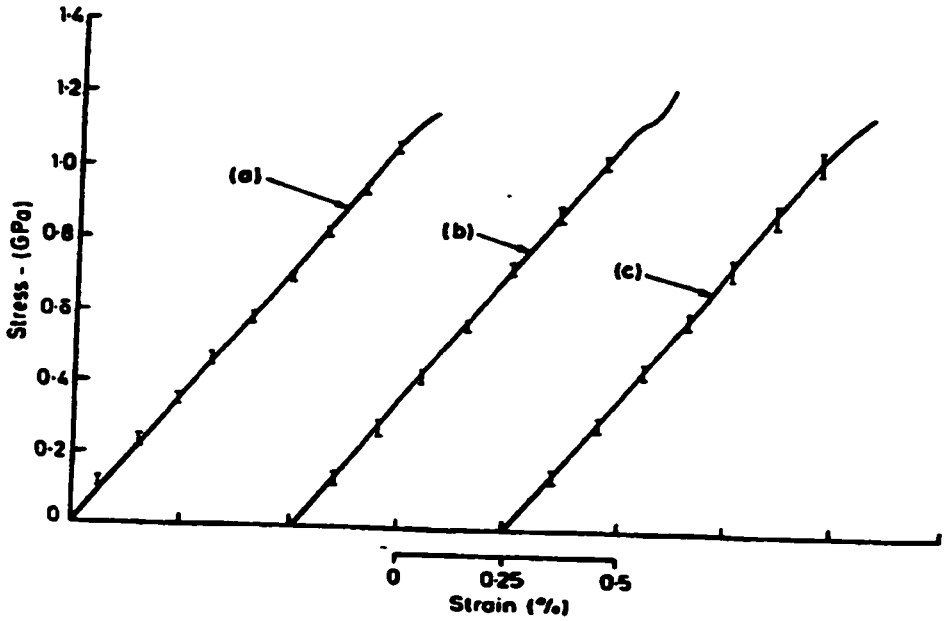

(a)

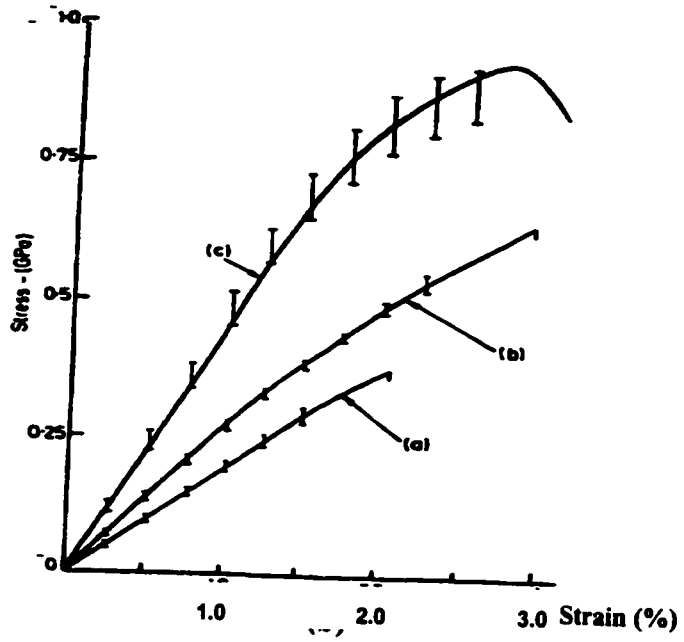

(b)

Figure 3.21: Effect of strain rate on tensile stress-strain curves for FRP materials. (a) Unidirectional carbon/epoxy specimen. (b) Fine-weave glass/epoxy specimen. Mean strain rates (s^{-1}): (a)_10^{-4}; (b)_10; (c)_450 to 900 (Welsh and Harding, 1985)

3.5.6 Summary

- In general, the higher the strain rate of applied loads, the greater the increase in material strength. In case of concrete, the compressive strength increase ranges over a wide range between 25~100 %.

- The tensile strength of concrete is more sensitive to high strain rates than its compressive strength. It can increase up to sixfold when the strain rate is increased from 10^{-6} to $10^{3}\ s^{-1}$.

- The strain rate sensitivity is inversely proportional to static strength of concrete, the lower the static concrete strength, the higher strength gains due to strain rate.

- As the strain rate increases, the nonlinearly of the stress-strain curve of concrete decreases. This results in a reduction in the ultimate strain at the maximum compressive stress. The effect of strain rate on the initial tangent modulus can be neglected, yet an increase in the secant modulus is observed.

- Increasing the strain rates will result in increases in strength and stiffness of reinforced concrete members.

- As a result of the strength improvement, the mode of failure may be shifted from the ductile flexural failure to a brittle shear failure with less energy absorption.

- The unidirectional CFRP appears to be strain rate independent, while increasing the straining rate increases the tensile modulus of GFRP fine weave by 4o %. However, the effect of strain rate on FRP composites needs more study.

Chapter 4

EXPERIMENTAL PROGRAM: SPECIMENS PREPARATION AND TESTING

4.1 General

This chapter deals with the experimental phase of the research where the scope and objectives behind the experimental program are introduced. Details of test panels, test set-ups, instrumentation for both blast and static testing, and test procedures are discussed. In addition, the mechanical and physical properties of the materials used in preparing the test specimens and a description of the test facilities are given.

4.2 Test Specimens

4.2.1 Geometry and test groups

A total of eighteen reinforced concrete flat panels of dimensions 1000 × 1000 × 70 mm were cast, cured for a period of 14 days and retrofitted using three different FRP materials. The ¼ scale test specimens represent dimensions of common reinforced concrete panels that are typically used as wall panels and/or roof slabs in both military fortificated structures and civil defence shelters. The test specimens were doubly reinforced with steel welded wire fabric sheets of designation MW 25.8 having bar

diameter of 5.74 mm, bar cross-sectional area of 25.8 mm^2, mass per unit area of 2.91 kg/m^2 and centre-to-centre steel bar spacing of 152 mm. Figure 4.1 illustrates the geometry and reinforcement details of the test specimens. All test specimens had an average concrete strength of 40.0 MPa, which was determined by testing twelve 150 × 300 mm concrete cylinders at the age of 70 days. The test specimens were divided into four main groups according to the type of FRP retrofitting layers (see Table 4.1) as follows:

- Group1 (***CS***): This control group consisted of five reinforced concrete panels: (CS_1, CS_2, CS_3, CS_4 and CS_5) without FRP retrofitting layers, and was considered as the reference group.
- Group 2 (***GSS***): Four reinforced concrete panels (GSS_1 through GSS_4) were retrofitted using two orthogonally oriented 500 mm wide SEH 51 E-Glass fabric bonded to each face. The glass fabric was not wrapped around the panels edges because it was too rigid to bend.
- Group 3 (***CSS***): Five reinforced concrete panels (CSS_1 through CSS_5) were retrofitted using 500 mm wide CF 150 carbon sheets bonded to each face. It was possible to wrap the carbon sheets around the panels edges.
- Group 4 (***CLS***): Four reinforced concrete panels (CLS_1 through CLS_4) were retrofitted with 80 mm wide *Sika CarboDur* carbon strips bonded diagonally across both faces, without wrapping them around panels edges.

A summary of the test specimens and schematic diagrams for the different orientations of retrofitting layers is given in Table 4.1.

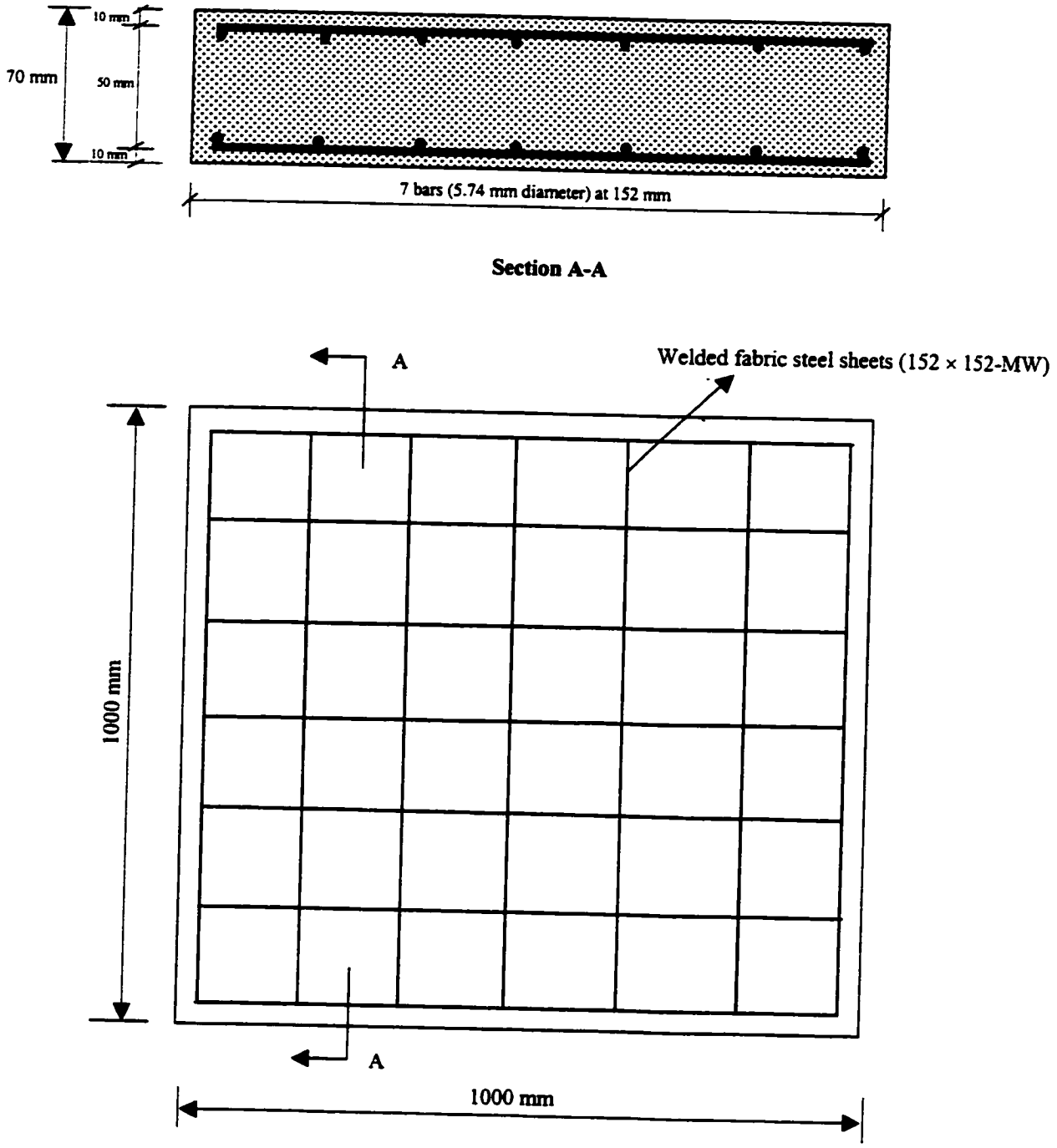

Figure 4.1: Test specimens: geometry and reinforcement details

Table 4.1: Details of test groups

Group No.	Group designation	No. of panels	Retrofitting FRP layers	Sheet anchorage	Orientation of retrofitting layers
1	CS	5	Control (as-built) specimens	Not applicable	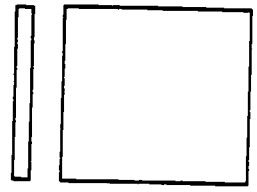
2	GSS	4	Two perpendicular layers of E-Glass SEH 51 attached to both concrete surfaces	No	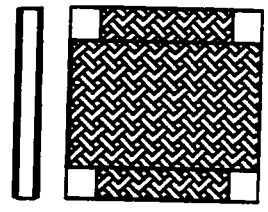
3	CSS	5	Two perpendicular layers of carbon fibre tow sheets attached to both concrete surfaces	Yes	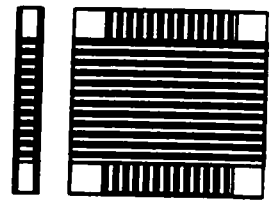
4	CLS	4	Two diagonal Sika *CarboDur* carbon strips attached to both concrete surfaces	No	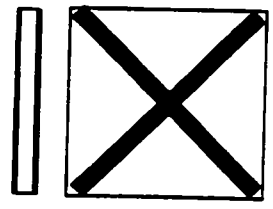

4.2.2 Specimens preparation

Due to laboratory space limitations, test specimens were prepared in two nominally identical concrete batches having the same compressive strength and mix proportions. The manufacturing process was started by preparing the forms with internal dimensions of 1000 × 1000 × 70 mm, using plywood reinforced with 50 × 100 mm wooden studs. Reinforcement meshes were cut into dimensions of 950 × 950 mm, leaving a 25 mm concrete cover on the form side faces. Reinforcement cages were shaped by welding the

top and bottom meshes together with a centre-to-centre distance of 50 mm. Strain gauges were attached to reinforcement at the desired locations, covered with a first coating layer. Following this, to reduce the risk of damage during placement and finishing, all strain gauges were covered with additional silicon coating layer. The instrumented steel cages were carefully positioned into the wooden moulds, and alignment was checked and corrected, as required. In order to provide a 10.0 mm concrete cover on the top and bottom faces of the panels, plastic chairs were wired to bottom reinforcement mesh.

Two ready-mixed concrete batches provided by a local supplier were used in preparing the test specimens. Both batches had a 10 mm maximum aggregate size, 100 mm slump and an average compressive strength of 35.0 MPa. The concrete was placed in a single layer and compacted using an electrical surface vibrator. Test specimens were finished, leveled and kept in moulds for about 28 days. During this period, test specimens were cured by watering and covering them with plastic sheets. After 28 days, the forms were removed, and the test specimens were ready for the application of the FRP layers.

4.2.3 Retrofitting procedure

The application process of the FRP layers was started by cleaning and lightly grinding the concrete surfaces. The first primer-coating layer was applied to the treated concrete surfaces and left to cure for 30 minutes. Thereafter, compounds of the epoxy resin were mixed and applied to the concrete surfaces by means of a roller within its recommended batch life (up to 15 minutes). FRP sheets were cut to the required lengths (1140 mm in case of CFRP sheets and 1000 mm in case of GFRP sheets) and placed on the surface on which the epoxy resin had been applied. The carbon sheets were cut using a pair of

scissors, while the carbon strips and glass sheets required a sharp utility knife to cut. The sheets were cut perpendicular to the fibre direction. In order to ensure full impregnation of the epoxy resin, using a roller, the sheets were squeezed in the direction of the longitudinal fibres. After a curing time of about 30 minutes, a second coat of epoxy was applied to the sheets and left to cure for a period of at least 24 hours. Using an overhead crane, the test specimens were flipped over, and similar steps were followed in applying two orthogonal FRP layers to the bottom surface. To ensure good anchorage, the carbon sheets were wrapped around specimen edges for a length of 70 mm from each edge.

The latter procedure was also followed when applying the carbon strips to the test specimens of group 4. The strips were cut into lengths of 1410 mm and then applied diagonally akin to X-bracing on both faces of the panels. A special type of epoxy resin, provided by the manufacture, was used to bond the carbon strips to the concrete surface. The epoxy resin was provided in two separate components (A and B), and was mixed before use at a ratio of 3 to 1, respectively.

In case of the glass sheets applied to test group 2, and due to the thickness of the sheets, it was difficult to attach the sheet ends to the panel sides. The two-component epoxy was mixed and the E-glass fabric was fully immersed in a bath of the epoxy resin. The cleaned panel surface was coated with an epoxy layer and the wet fabric was applied and squeezed in the main fabric direction to remove air bubbles. The same procedure was followed in applying the orthogonally oriented and the bottom surface FRP layers. A finish coat was applied to all panels as protection against the weather effects.

4.2.4 Specimen instrumentation

All test panels were equipped with similar instrumentation. Measurements of strains in the steel reinforcement, on concrete surface and in FRP layers were taken at nine locations using general-purpose strain gauges. Foil strain gauges measuring either 6 mm or 30 mm in length were used for strain measurements. Specifications for the strain gauges are shown in Table 4.2, while Figure 4.2 shows the location of the strain gauges.

In order to monitor the strain-time profile of test specimens, two strain gauges of 6 mm length were mounted on each reinforcement mesh at the mid-span and 1/3 of the panel diagonal (see Figure 4.2, a). Surface strains were captured using strain gauges of 30 mm length. Two strain gauges were glued to the mid-span and 1/3 diagonal points of the bottom surface, while three gauges were attached to the mid-span, 1/3 diagonal and 1/2-side length points of the top surface (Figures 4.2, b and c). The 60 mm length gauges were attached to the concrete surfaces in the case of the control panels, and to the FRP layers in the case of the retrofitted panels. Extreme care was taken in installing strain gauges, especially the 6-mm ones. A layer of silicon was applied on the gauges to protect them from both moisture and handling damage. Prior to testing and after each installation step, the gauge resistance was checked for proper resistance using a digital voltmeter.

Figures 4.3 through 4.6 show samples of the four test groups, including the control panel and three other panels after the application of the FRP layers and the mounting of the strain gauges. Wrapping carbon sheets around panel edges of test group 3 (as shown in Figure 4.5) is introduced as a simple anchorage technique where feasible. The effectiveness of such a technique will be highlighted when analyzing the test results.

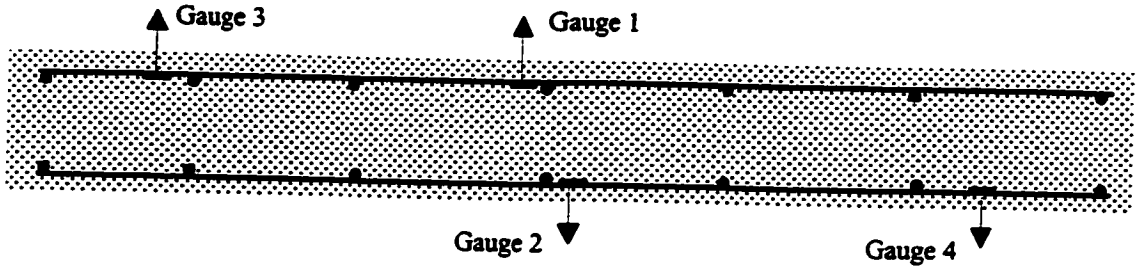

(a): Reinforcement strain gauges (6 mm length)

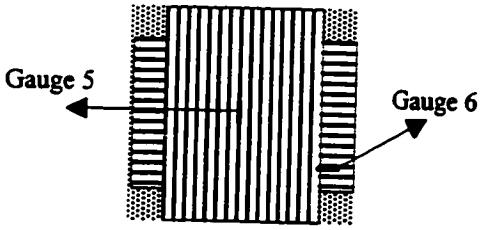

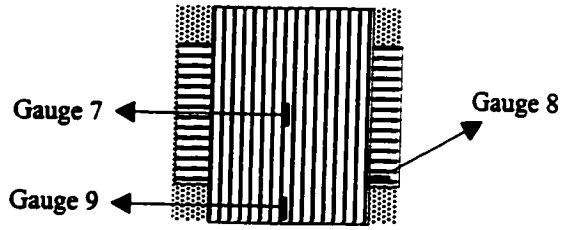

(b): Strain gauges on the bottom surface (30 mm)

(c): Strain gauges on the top surface (30 mm)

Figure 4.2: locations of the reinforcement and surface strain gauges

Table 4.2: Specifications of Foil strain gauges

Gauge location	Reinforcement	Concrete/FRP surfaces
Type	CEA-06-032UW-120	N11-FA-30-120-11
Gauge length, mm	6	30
Resistance, OHMS	120 ± 0.3%	120 ± 0.3%
Gauge Factor	2.08 ± 1.0%	2.12 ± 1.0%
Thermal Output,	2 μ/ °C	2μ / °C

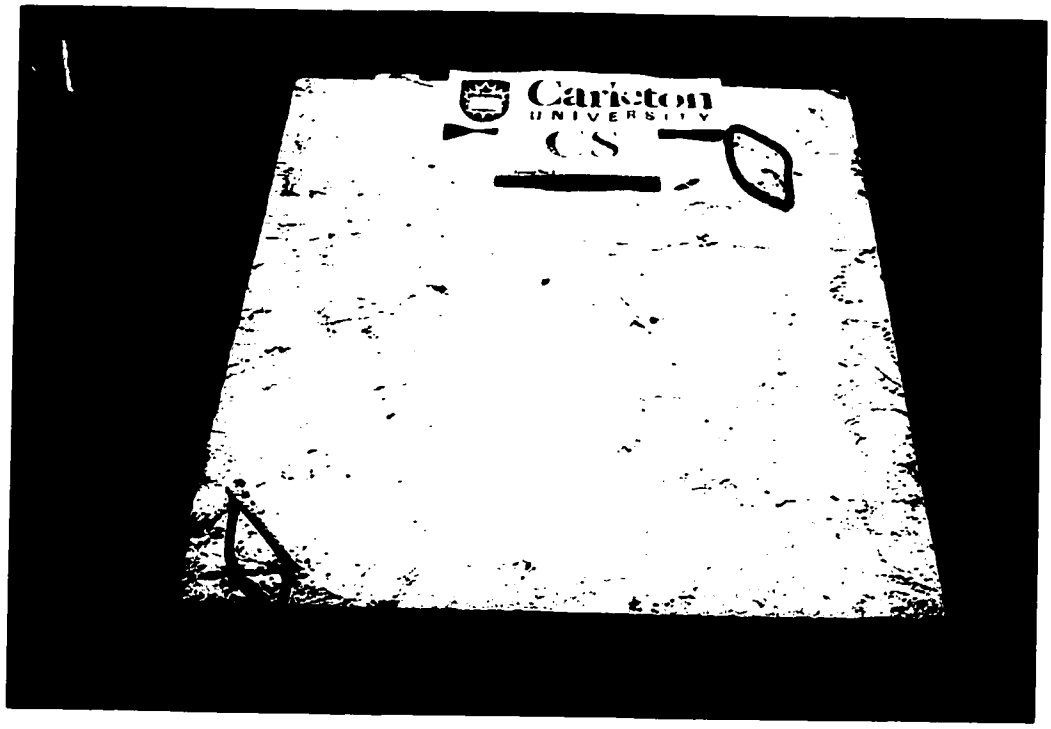

Figure 4.3: Typical control specimen (Group CS)

Figure 4.4: Typical glass-sheet retrofitted specimen (Group GSS)

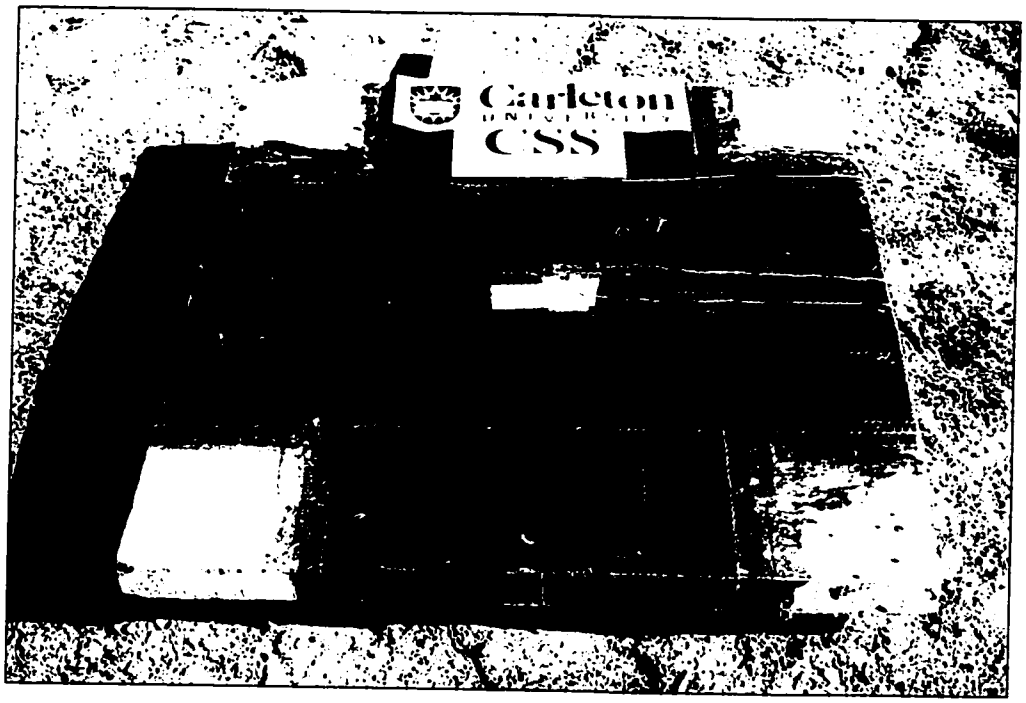

Figure 4.5: Typical carbon-sheet retrofitted specimen (Group CSS)

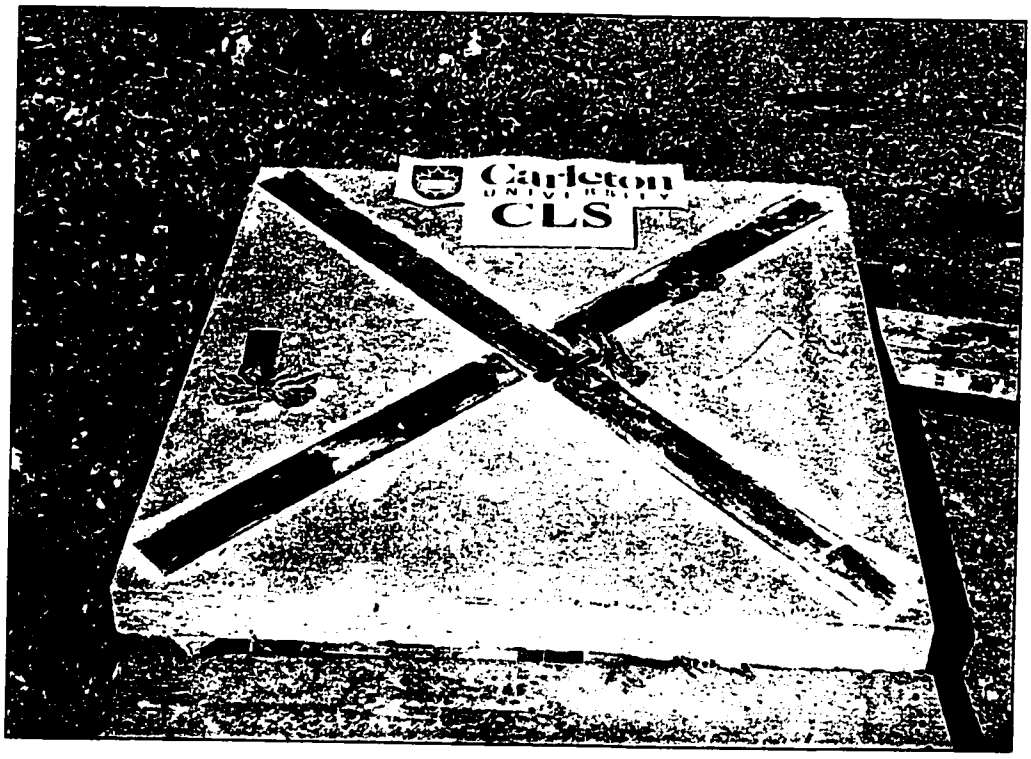

Figure 4.6: Typical carbon-strips retrofitted specimen (Group CLS)

4.3 Material Properties

This section presents the mechanical and physical characteristics of materials used in the manufacturing of test specimens. Some of these properties were provided by the manufacturers while others were obtained through laboratory tests in this investigation.

4.3.1 Concrete

Ready mixed concrete with a nominal compressive strength of 35 MPa, 100 mm slump and no air-entrainment was used to construct the test specimens. The maximum nominal aggregate size was chosen to be 10 mm in order to easily provide the 10 mm cover. However, due to space limitations in the laboratory, two concrete batches having nominally identical mix proportions and mechanical properties were used. Consistency of the fresh concrete was evaluated by measuring its slump. Slump values were found to be 90 mm and 95 mm for the two concrete batches, respectively, which was close to the desired slump of 100 mm.

At the beginning, the middle, and the end of each concrete casting operation, 6 cylinders (150 × 300 mm) were taken, which resulted in 36 concrete cylinders in total. This number was deemed to yield a representative sample of the concrete used in the construction of the test specimens. The standard specifications regarding the number of concrete layers and compaction were followed. Surfaces were leveled, finished, kept in moulds under plastic covers for 24 hours, and then removed from moulds to cure for 28 days.

At the age of 70 days, the cylinders were tested using the *Tinius Olsen 400,000 lb* universal testing machine at Carleton University. The cylinders labeled 1 through 4 for each concrete batch were tested under uniaxial compression. Table 4.3 summarizes

results of the compression tests, which reveal an average compressive strength, f_c', of 40 MPa. Figure 4.7 shows a typical stress-strain relation for one of the concrete cylinders tested in compression, with a maximum compressive stress of 40.8 MPa, corresponding to a strain of 0.0029, and an ultimate strain of 0.006.

The two cylinders labeled 5 and 6 in each batch were used to evaluate the tensile strength of concrete using the split cylinder method. Results are given in Table 4.4 with an average tensile strength, f_t, of 3.8 MPa. It is common to present the tensile strength of concrete in terms of the modulus of rupture, f_r. According to the CSA Standard A23.3 (1994), the modulus of rupture can be calculated in terms of the average compressive strength using the relation $f_r = 0.6\sqrt{f_c'}$, which yields a tensile strength of 3.8 MPa.

4.3.2 Reinforcing Steel

Test specimens were doubly reinforced with smooth welded wire fabric of standard designation 152 × 152-MW 25.8 × 25.8, where the 152 represents in the longitudinal (or transverse) direction bar spacing and the 25.8 gives the bar cross-sectional area in mm^2. The wire fabric was delivered in sheets having dimensions of 4400 × 1200 mm, 2.91 kg/m^2 mass per unit area and 170 mm^2 cross-sectional area per meter width. In the test panels, there were 7 bars per meter in both directions. The stress-strain characteristics of steel were determined by conducting four tension coupon tests. Tensile strain was measured using an extensometer (clip-on gauge) of 50.8 mm base length, which was connected to an X-Y plotter. An average yield strength of 540 MPa was obtained, corresponding to 0.0025 yield strain (see Figure 4.8).

Table 4.3: Concrete compressive strength at age of 70 days

Batch No.	Cylinder No.	Diameter, D mm	Length, L mm	Area, A mm^2	Load, P_u kN	Strength, f_c' MPa
1	1	150.0	302.5	17662.5	724.6	41.0
1	2	148.8	300.0	17381.0	713.0	41.0
1	3	148.6	302.0	17334.3	789.0	45.5
1	4	150.8	301.0	17851.4	721.0	40.4
2	1	149.4	303.0	17055.4	724.0	42.4
2	2	151.2	304.0	17946.2	803.0	44.7
2	3	150.0	302.0	17662.5	717.5	40.6
2	4	150.2	300.0	17709.6	722.0	40.8

- Note: The average compressive strengths of concrete for batches 1 and 2 are calculated as 41.9 and 42.1 MPa, respectively.

Table 4.4: Concrete tensile strength at age of 70 days

Batch No.	Cylinder No.	Diameter, D mm	Length, L mm	Contact Area, A_c mm^2	Load, P_u kN	Splitting strength Strength, f_t, MPa
1	5	150.0	300.0	141300.0	280.9	3.9
1	6	151.0	303.0	143664.4	261.0	3.6
2	5	149.0	304.0	142229.4	283.0	3.9
2	6	150.0	302.0	143655.0	277.0	3.8

- Note: The average splitting strengths of concrete for batches 1 and 2 are calculated as 3.8 and 3.9 MPa, respectively.

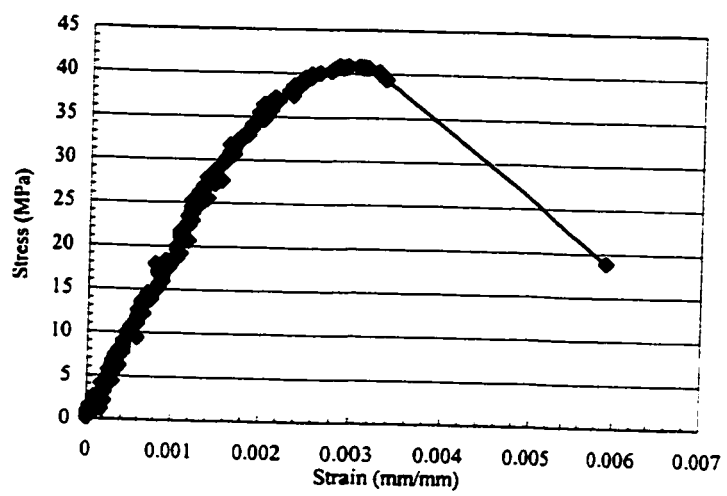

Figure 4.7: Typical stress-strain diagram for concrete in compression at age of 70 days

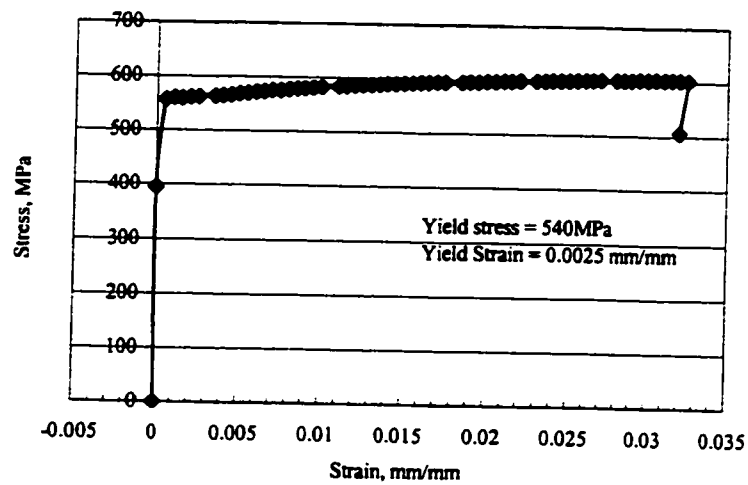

Figure 4.8: Tensile stress-strain diagram for steel mesh

4.3.3 FRP retrofitting materials

In the current experimental program, three different FRP composite materials were used to retrofit the panels: glass fibre sheets, carbon fibre sheets, and carbon fibre strips. The three FRP composites are commonly used for both laboratory and field retrofitting/repair purposes. The static properties of FRP composites have been the subject of extensive testing since the early 80s, and as a result, most of these properties are well defined. The following sections provide the mechanical and physical characteristics of these materials as well as those of the adhesive materials used in the current study.

Glass Fibre Reinforced Fabric and Epoxy Resin

Test group 2 was retrofitted using the Tyfo® SHE 51 Glass fabric provided by RJ Watson, Inc. The Fyfe Company TYFO Fibrwrap fabric has E-glass roving in the longitudinal direction and Kevlar 49/E-glass/thermoplastic adhesive roving in the lateral direction. Based on an average dry thickness of 1.2 mm, the E-glass fabric has a tensile strength of 560 MPa corresponding to a failure strain of 2.1 % and a tensile modulus of

27.5 GPa (Table 4.5). The resin system designated Tyfo® S is a two component epoxy. It requires from one week to one month to fully cure and reach ultimate material properties.

Carbon Fibre Reinforced Fabric and Epoxy Resin

The carbon sheets applied to test group 3 are unidirectional, high strength continuous fibers of thickness 0.11 mm. They are provided by Master Builders Inc. and are available under the commercial name CF 150 tow sheet. The fibre sheets have a tensile strength of 3480 MPa, and a tensile modulus of 230 GPa. The mechanical and physical properties of the carbon sheets are listed in Table 4.5 according to the manufacturer's specifications. Similarly, properties of the used epoxy resin are given in Tables 4.6 and 4.7, respectively.

Carbon Fibre Reinforced Strips and Epoxy Adhesive

Test group 4 was retrofitted using carbon fibre reinforced laminates (strips) commercially known as *Sika CarboDur* type *S*. The carbon strips have a thickness of 1.2 mm. They are available in continuous rolls of any length up to 250 m. Two 80 mm wide strips were applied diagonally to each surface using the structural high modulus, high strength epoxy paste *Sikadur 30*. The adhesive consists of two different compounds namely; component A and component B, which were mixed together with ratio 3:1 by weight. The mechanical and physical properties of carbon fibre laminates (*Sika CarboDur* type *S*) and the epoxy resin (*Sikadur 30)* are given in Tables 4.8 and 4.9, respectively, as provided by the manufacturer.

Table 4.5: Mechanical properties of Glass/ Carbon fibre sheets

Commercial Name	Density (kg/m^3)	Thickness (mm)	Tensile Strength (MPa)	Tensile Modulus (GPa)	Ultimate Elongation (%)
E-Glass fabric	2100	4.0	580	72.5	2.1
Carbon sheets	1820	0.6~1.0	3480	230	1.5

Table 4.6: Mechanical properties of Epoxy Resin components

Component	Tensile Strength (MPa)	Tensile Modulus (GPa)	Flexural Strength (MPa)	Flexural Modulus (MPa)	Compressive Strength (MPa)	Compressive Modulus (MPa)
Epoxy Putty	12	1.8	26	903	24	1076
Epoxy Primer	12	0.717	24	593	24	669
Saturant	54	3.034	124	3731	86	2621

Table 4.7: Physical properties of Epoxy Resin components

Component	Material Origin	Viscosity @ 24°C (cps)	Working Time @ 24°C (mins)	Density (kg/m^3)
Epoxy Putty	100 % solids Amine-cured epoxy	45000	40	1259
Epoxy Primer	100 % solids Amine-cured liquid epoxy	400	20	1103
Saturant	100 % solids Amine-cured epoxy	1350	45	984

Table 4.8: Physical and mechanical properties of Carbon Strips *Sika CarboDur S*

Density (g/cm^3)	Thickness (mm)	Width (mm)	Cross-Sec (mm^2)	Ultimate Elongation (%)	Volumetric Content (%)	Tensile Strength (GPa)	Tensile Modulus (GPa)
1.6	1.2	80	96	1.4	68	2.8	165

Table 4.9: Mechanical Properties of adhesive system *Sikadur 30*

Tensile Strength (MPa)	Tensile Modulus (GPa)	Bond Strength (MPa)	Density (kg/L)	Pot Life (mins)	Ultimate Elongation (%)
24.8	4.5	21.3	1.77	70	1

4.4 Preliminary Blast Tests

A series of preliminary shots was conducted to test the portable measuring devices, to evaluate the effect of boundary conditions on the obtained results and to reduce the uncertainties associated with the recorded measurements. In the following an overview of the phases of the preliminary blast shots, including objectives, description of blast facilities, measurement devices, test set-up and test specimens, is given.

4.4.1 Preliminary blast Phase (1)

It has been observed (Smith *et al.*, 1999) that when a blast wave impinges on a small-dimension target, reflected pressure is created on its front face. The reflected pressure does not persist, as the limited structure boundaries allow a part of the blast wave to propagate around the edges. This phenomenon is referred to as diffraction loading or blast wave clearing, which is typically associated with pressure drop. Two main sources of uncertainties are involved and are related to the time it takes the reflected pressure to drop (referred to as the clearing time), and the value of the new pressure. The average specific impulse on the front face of the structure is a function of these two factors, and some times it is hard predict it (Beshara, 1994-b). Accordingly, in assessing blast loads on small-dimension targets, the effect of blast wave clearing must be considered in order to correctly evaluate the blast-resistance capacity of such elements.

In order to evaluate the extent of the clearing effect on the blast-resistance capacity of small-dimension targets, a series of blast shots was conducted on 500 × 500 × 40 mm plain concrete patio slabs. The intention was to compare the ultimate static capacity of

the tested patio slabs to their blast resistance capacity. The latter was experimentally evaluated and analytically predicted using CONWEP software (Hyde, 1991), assuming infinite target dimensions.

To evaluate their static capacity, two identical patio slabs were simply supported on all four edges and tested statically at Carleton University's Materials and Structures Laboratory. The load was applied through a 300 mm diameter circular steel plate positioned at the centre of the slabs. The average ultimate static capacity of the slabs was determined as 9.2 kN.

The blast-resistance capacity of patio slabs was predicted using CONWEP software for a 2-meter standoff and 200 gm TNT equivalent weight. The breaching case (considerable damage), assuming infinite target dimensions was found to occur at a reflected overpressure of 182.5 kPa, which corresponds to an ultimate blast capacity of 45.6 kN.

To verify the blast resistance calculation results, four patio slabs were tested using a test set-up constructed at CERL, see Figure 4.9. The pressure-time history was captured using two piezoelectric gauges positioned at different distances from the explosion centre. The first shot was conducted using a charge of 176 gm located at 2.3-m standoff, which resulted in no apparent damage to the test sample. Using the same charge weight, the standoff was reduced to 1.53, 0.92 and 0.35 m, respectively, for the next three shots. Surprisingly, there was no damage during the first three shots. Failure occurred after the fourth shot at a recorded overpressure 1463 kPa, which corresponds to a blast capacity of 365 kN. The test results of Phase (1) demonstrate the need for appropriate test set-up and this will be discussed in detail in the following chapter.

4.4.2 Preliminary blast Phase (2)

The second series of the preliminary tests was conducted on concrete panels with dimensions of 1000 × 1000 × 70 mm. These dimensions were intentionally made equal to those of the main blast test specimens. The main objectives were to calibrate the portable measurement devices, to make a decision regarding the main blast test set-up and to determine the standoff distance and charge weight required to breach the test specimens.

Two multi pressure-gauge holders (370 mm long and 19 mm wide) with linear arrays of four pressure transducers were designed and manufactured using facilities of CERL. The transducer holders were intended to capture both the incident and the reflected pressures simultaneously. Each gauge holder could accommodate four pressure gauges of model PCB 111A with a 100-psi range, 50-mv/psi sensitivity, time constant of 1 sec and rise time of 1 μs. Data were recorded using 8-channel Yokagawa, DL 708 Digital Scope.

A reinforced concrete panel was mounted vertically and was held rigidly in a steel frame, with the panel centre being approximately 1.5 m above the ground surface. Gauge holder # 1, with pressure gauges 1, 2, 3 and 4 affixed to it, was mounted such that the centre of pressure gauge 1 was 25 mm from the panel centre, and lying in a plane parallel to the panel surface. Gauge holder # 2, with pressure gauges 5, 6, 7 and 8 affixed to it was positioned such that the centre of gauge 5 was 25 mm from panel edge and lying in a plane parallel to the panel edge (see Appendix *B* and Tolba *et al.*, 2000). The pressure transducers were connected to the conditioning amplifiers and the digital oscilloscope located in the instrumentation bunker 300 m away from the centre of explosion. Explosive charges were suspended at a distance of 2 m above the centre of the panel and

were remotely detonated. Six trials were performed using the same charge weight and standoff in order to limit the number of variables. Test set-up of Phase (2) is shown in Figure 4.10. Pressure was recorded and compared to CONWEP predictions. Results will be presented in the following chapter.

4.4.3 Supporting Frame

After observing the results of Phase 2 set-up, it was decided to place the panel specimen in a horizontal plane, fixed to a box-type frame buried in the ground. First, such a set-up eliminates the clearing effect of the blast waves because the ground surface acts as a target of infinite dimensions with test specimen constituting part of this unlimited surface. Second, it is possible to safely use the frame for more than one test without the need for maintenance after each blast shot. Third, wiring connections, a high-speed video camera, lighting and the deflection measurement device can be placed inside the buried box, which will reduce the risk of damage. Fourth, the ease of construction and the possibility of in-site assembly heavily reduce the labour and transportation cost. The only limitation is that frame dimensions are fixed, which permit only one specimen size.

The supporting frame was constructed using the facilities of CERL. Steel tubes, each with a cross-sectional area of 100 × 100 mm and length of 1000 mm were used to construct the frame of the box. Steel sheets of 7 mm thickness were welded to the tubes to form the box walls. To the top of the box a steel frame, comprising four angles, was welded. This frame was used to hold the specimen in a horizontal position. Figure 4.11 shows the internal components and complete shape of the box frame.

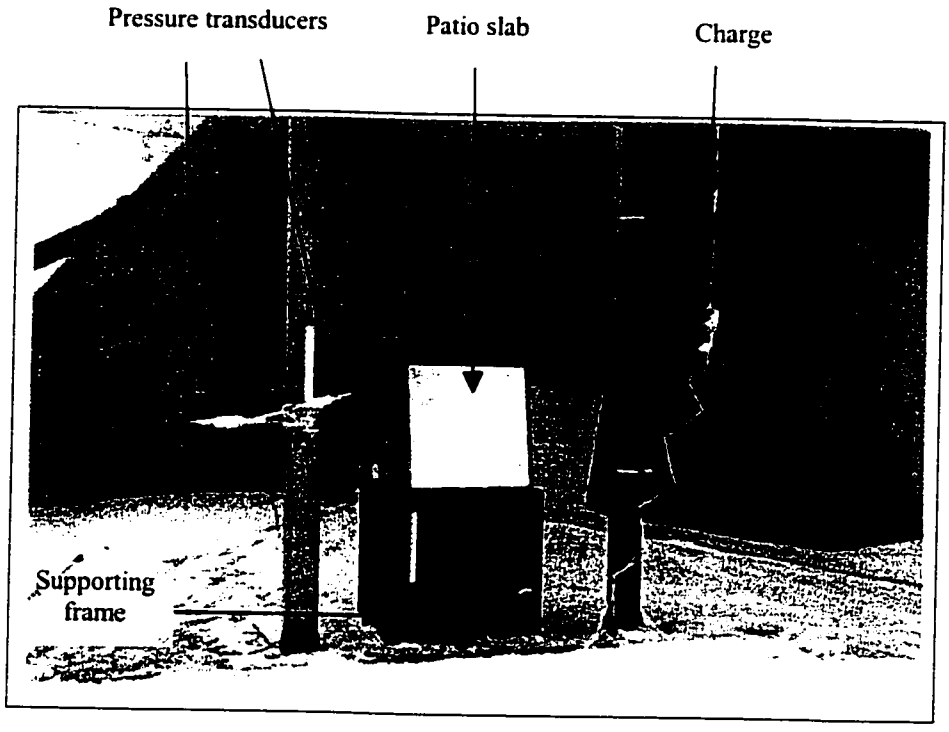

Figure 4.9: Test set-up of preliminary Phase (1)

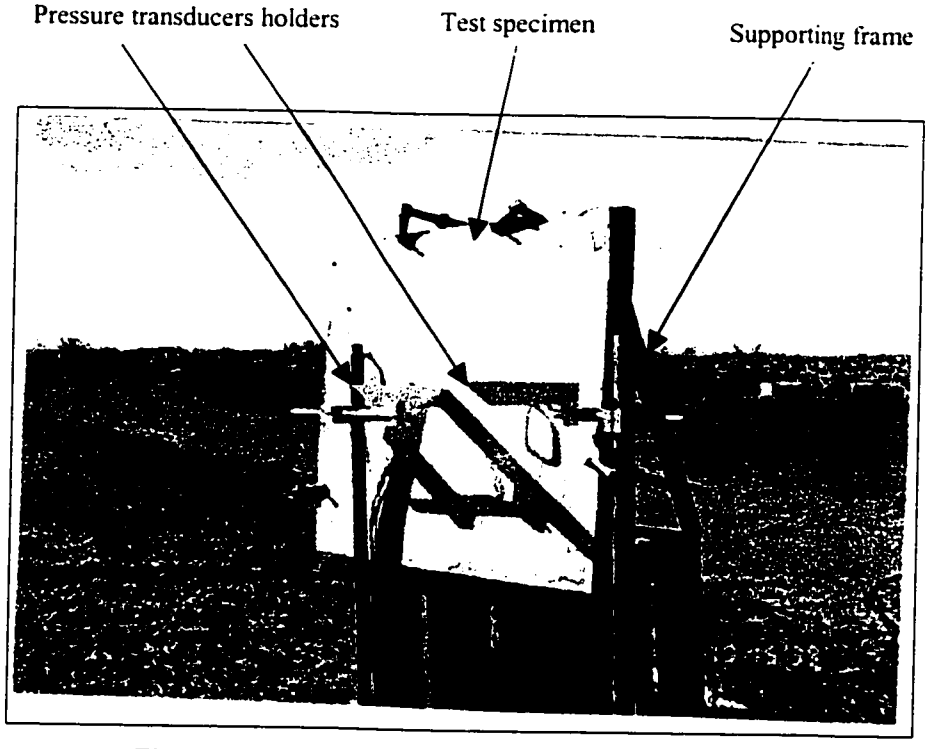

Figure 4.10: Test set-up of preliminary blast Phase (2)

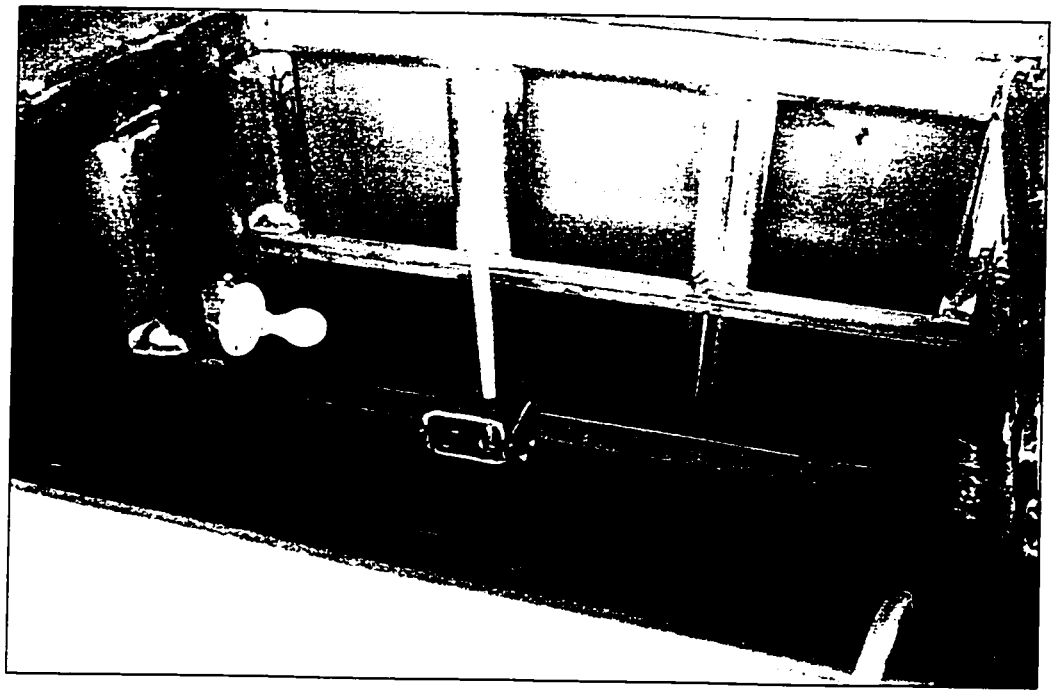

(a)

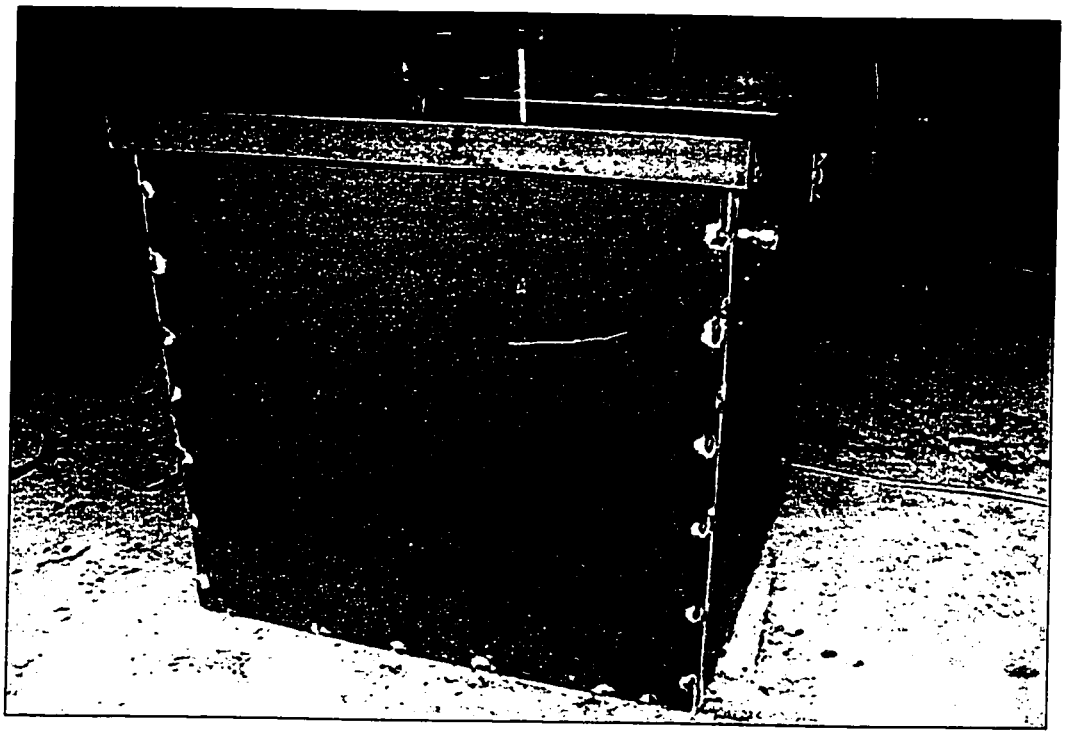

(b)

Figure 4.11: Supporting frame (a) Internal components and (b)Final shape

4.5 Main Blast Testing

In this section, the preparation of the main blast tests, including the procedure followed to construct the final blast test set-up, is presented. Since most published reports in this field ignore the description of the measuring and testing devices, blast test facilities and properties of all explosive-related materials are also highlighted.

4.5.1 Final test set-up

Preparation of final test set-up started by burying the steel frame, with its top being level with the ground surface. Three main cables were connected to the supporting frame. Two of them connected the explosion point to the instrumentation bunker (150 m away) namely; the pressure cable bundle, the strain cable bundle, and an AC power supply cable that was connected to a generator. For protection purposes, the cables were buried for a distance of 25 meters away from the explosion centre.

The next step involved placement of the test specimen in the test frame. This was done by using a 2.5-ton bobcat, which held the specimen above the frame while the strain wires were fixed to the connecting box inside the frame. Once the connections were completed, the specimen was lowered into position. Special care was taken to ensure that the deflection transducer was in contact with the bottom surface of the specimen in the final position. A rubber pad of the same width and length as the top-supporting angle was used to ensure uniform load distribution to the specimen edges. Figure 4.12 shows the various stages for the preparation of the final blast test set-up.

(a): Digging the ground for the box frame burial

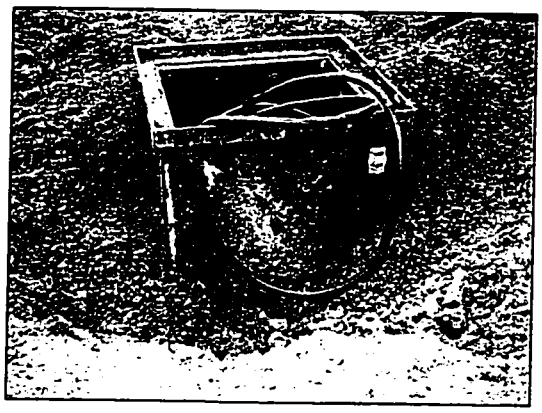

(b): Partially buried box frame

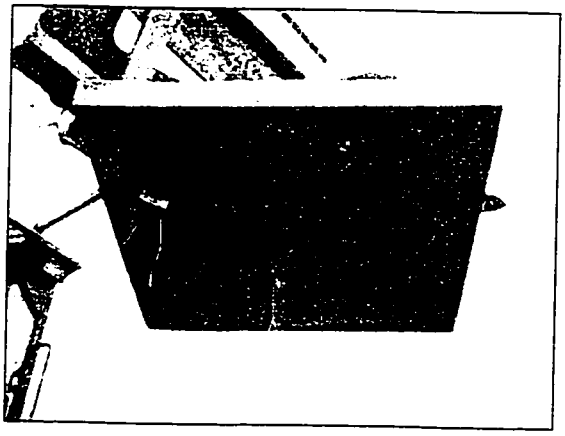

(c): Placement of test panel on top of the box

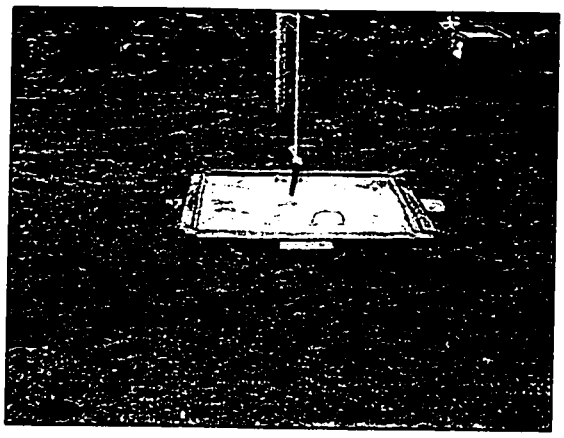

(d): The buried box frame and the test panel

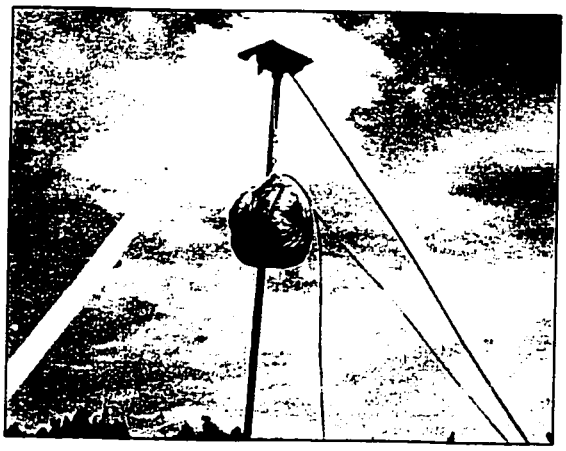

(e): Explosive charge placed above the test panel

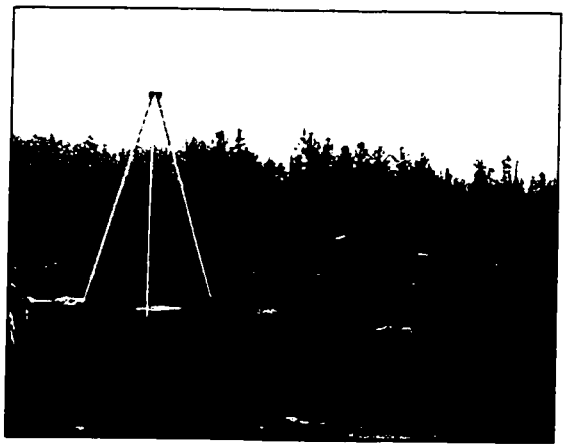

(f): Over-all view of the test set-up

Figure 4.12: Preparation steps of the final blast test set-up

4.5.2 Blast set-up instrumentation

The measurement devices in the final blast test set-up involved pressure transducers to capture incident and reflected pressures, Linear Variable Differential Transducer (LVDT) to record mid-span deflection and strain gauges to measure reinforcement and surface strains. In addition, a video camera was used to view the instantaneous displacements and to observe spalling or delamination. These devices are further described in the following.

Strain Gauge Conditioning Amplifier

The strain amplifier model 2310 manufactured by Measurements Group was used. The 10-channel portable Amplifier comprises a complete system that can display and record signals from both Foil and Piezoresistive strain gauge types on external equipment (such as a scope or multiplexer). It has a non-volatile digital storage, which can retain the data without line power for up to two years. Each 2310 Amplifier has its own AC power supply. The output signal is ± 10 V and should not exceed under any condition a peak voltage of ± 15 V. As the purpose was to measure dynamic data, it was important to use multiconductor shielded wires, and to minimize the wire extensions to reduce the electrical noise from the test environment. A quarter bridge with no filter was used for strain measurements. Through the 8-pin output plug located at the rear of the amplifier, the instrument could be connected to an oscilloscope, voltmeter, or any data recorder.

Dynamic pressure Transducers

Incident and reflected pressures were measured using the dynamic pressure transducers, series 111 A22. The PCB Quartz piezoelectric gauge measures dynamic and short-term pressures up to 1000 psi (6900 kPa) at a rise time of 2 microseconds. It works at a high

output level of 4 volts with sensitivity of 1 mV/psi. The internal structure of these pressure gauges contains rigid, multiplate quartz elements with an integral accelerometer to reduce motion sensitivity and to produce a high-level, low-impedance output, which fit most readout instruments. Figure 4.13 shows a PCB gauge, and Table 4.10 summarizes its specifications. A PCB 111 A22 reflected pressure transducer was mounted at the middle of each side of the supporting frame to measure the reflected pressure at the target surface. These gauges were at a fixed distance of 3.1m below the charge centre. To ensure a good reflecting surface, special care was given to the compaction and landscaping of the soil around these gauges. The free-field incident pressures were measured at two locations (some tests utilized three free field incident transducers). Prior to each test, gauge distances were checked and measurements were taken. The transducers were fitted in specific circular hosts that were designed to prevent any disruption of the incident pressure waves and to measure the free field pressure (see Figure 4.14). The circular hosts were fixed to stands of height 1.3 m, and were aligned with the explosive charge.

Data Acquisition System

Two YOKOGAWA digital oscilloscopes Model DL708E were used to store and display measurements of incident and reflected pressures, deflections, and strains. The 8-chanel portable scope has 10.4-inch colour monitor for data display, and a built-in printer for hard copy outputs with data capacity of 128 M words. It has the capability to capture up to 8 channels of data, with a maximum sampling rate of 10 MS/s. The data acquisition system was triggered using a fibre optic cable, which was placed inside the charge. As the charge initiates, the resulted light passes through the fibre optic cable and indicates

the zero time to the recording scope, which is referred to as the time zero. Following this, data collected was stored on the hard drive and transferred to another computer system for data reduction, plotting and reporting purposes. Table 4.11 summarizes the basic specifications of the digital scope, while Figure 4.15 shows a photo of the oscilloscope.

Deflection Measurement Device

Mid-span vertical deflection of test specimen was measured using a Linear Variable Differential Transducer (LVDT). The device was fixed to the supporting frame by means of a metal arm welded to the frame. To protect the device from direct contact with the bottom concrete surface, an extension rod was used between the LVDT and the panel. The LVDT was balanced to ensure an initial reading of zero (see Figure 4.16).

Table 4.10 Specifications of pressure transducers Model No. 111A24

Specifications	Measure
Range (5 volt output), psi	1000
Useful over range, psi	10000
Sensitivity, mV/psi	1
Rise time, microsecond	2
Resolution, psi	0.1
Dimensions, in	1.38 × 0.248
Weight, gm	6

Table 4.11 Specifications of digital scope Model DL 708E

Specification	Measure
External dimensions (W, H, D)	370 × 260 × 183 mm
Weight	5.3 kg
Max. sampling rate	10 MS/s
Bandwidth	4 MHz
No. of channels	8
Max. recording length	16 M
Display facility	10.4" colour Monitor
Data storage	Built-in HD

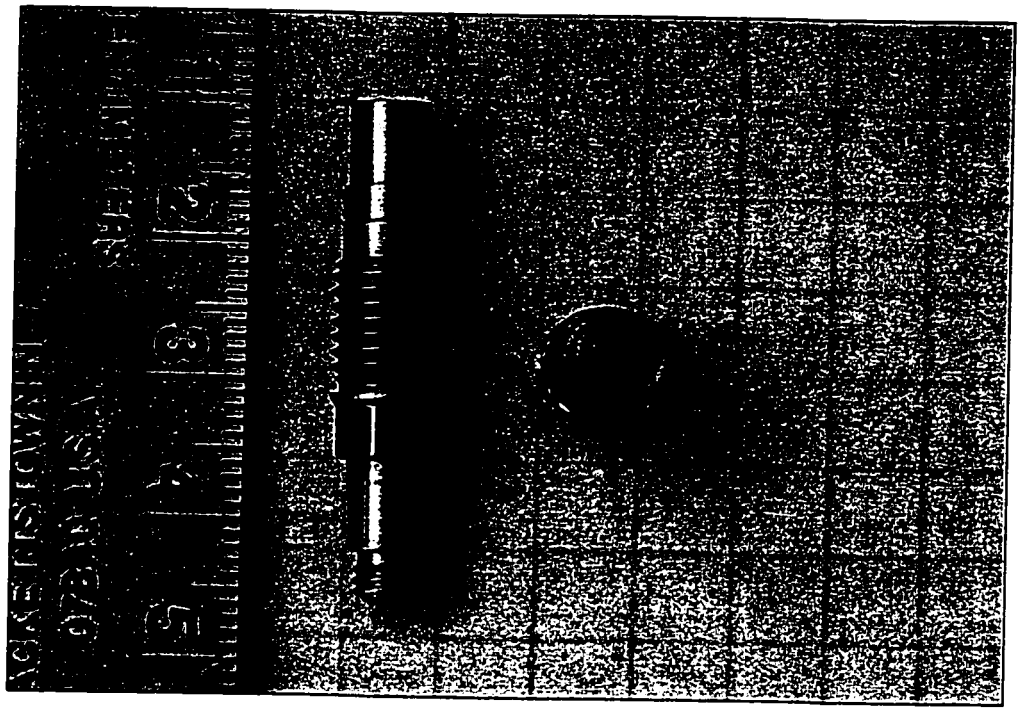

Figure 4.13: PCB 111 A24 reflected pressure transducer

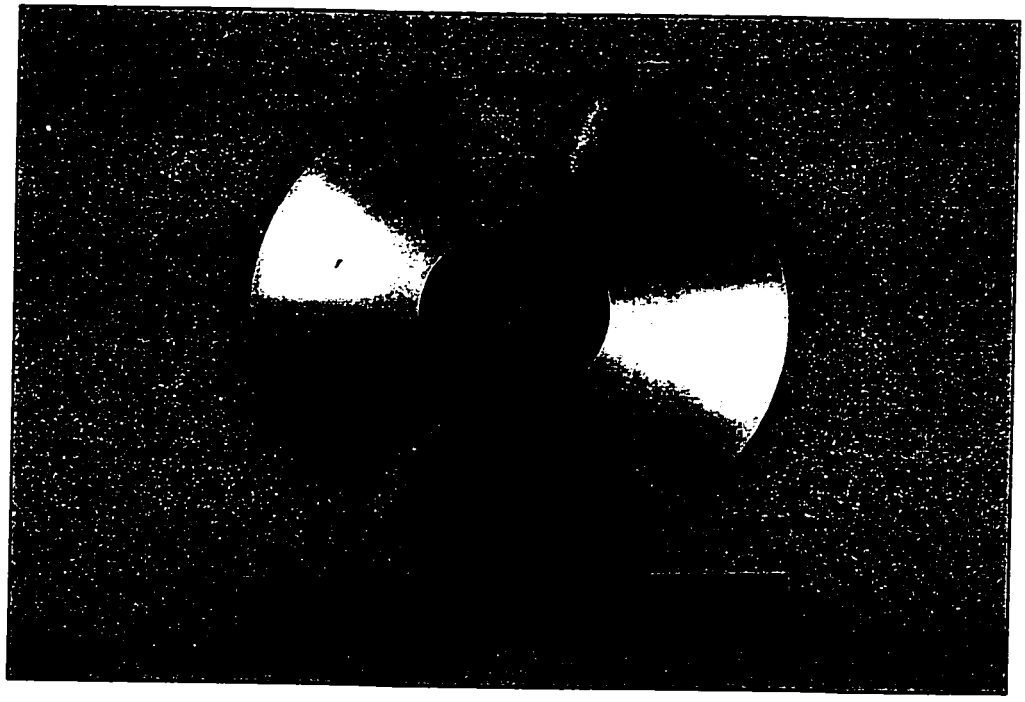

Figure 4.14: Circular metal disk used in measuring the incident pressure

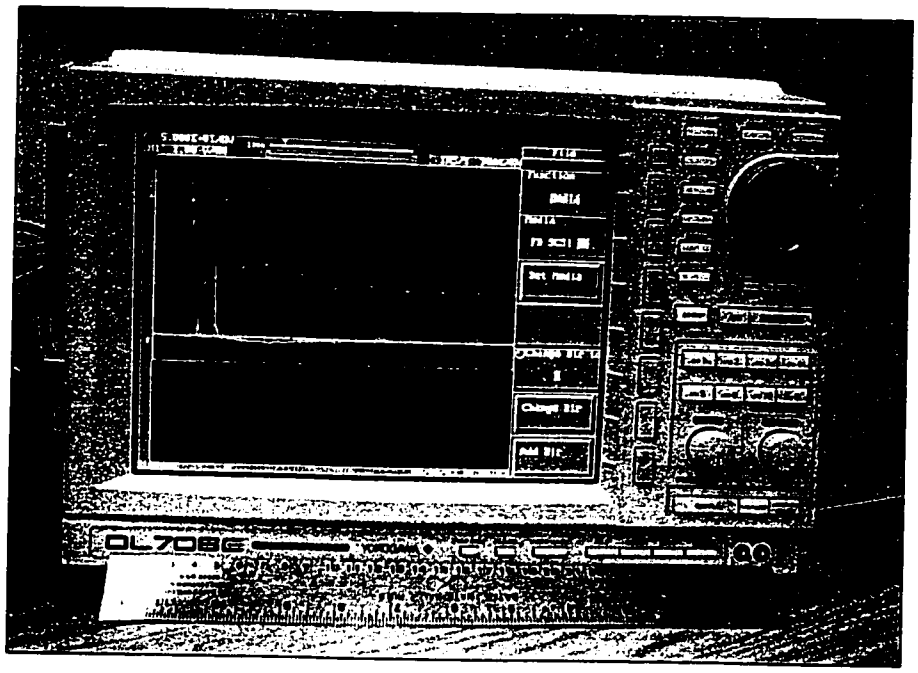

Figure 4.15: Digital oscilloscope Model DL708E

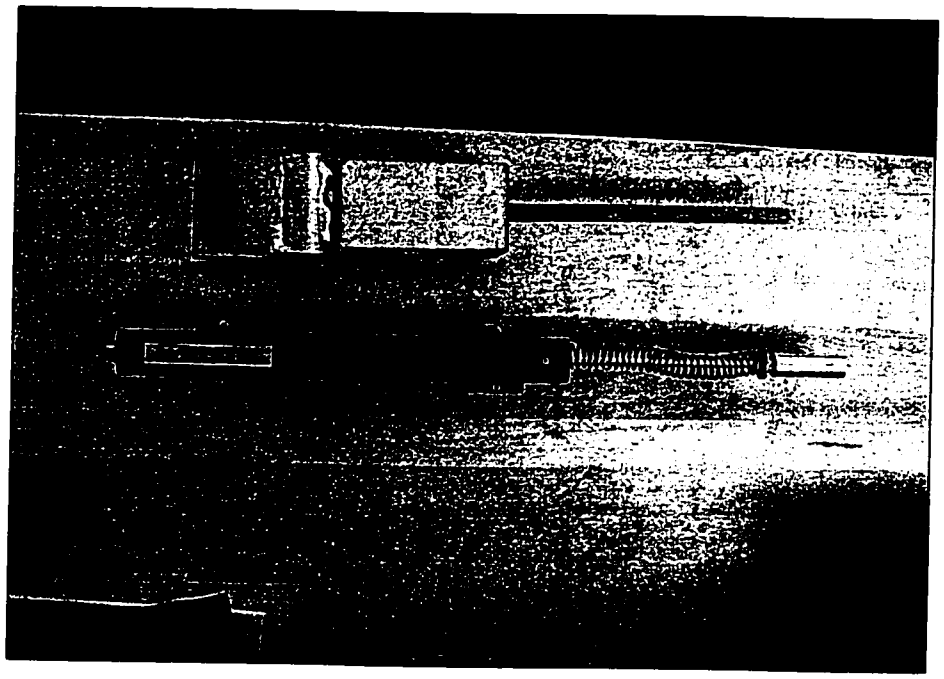

Figure 4.16: Displacement transducer and extension rod

4.5.3 Blast facilities

For safety considerations, all explosion facilities were provided and operated by the CERL personnel, specially when preparing and hanging the explosive charges. Due to the high cost of explosives, the relatively inexpensive agent ANFO (Ammonium Nitrate Fuel Oil) was used in the main test series. The following is a presentation of the characteristics and properties of the blast facilities and explosive materials

Blasting machine, cables and detonators

A blasting machine model CD 1500-10J was used to initiate the detonator. The machine uses 1500 Volts. Figure 4.17 shows the blasting machine. The blasting machine was connected to the explosive charge by means of a 2 km blasting cable. The blast cable is connected to a Static Master High Strength Electrical Detonator, which was fixed to a one lb booster. Upon the forming of the explosive charge, the booster and detonator along with a certain length of the blasting cable were imbedded into the middle of the charge. The function of the detonator is to initiate the booster, which in turn propagates the detonation wave to the main charge and triggers the chemical explosion.

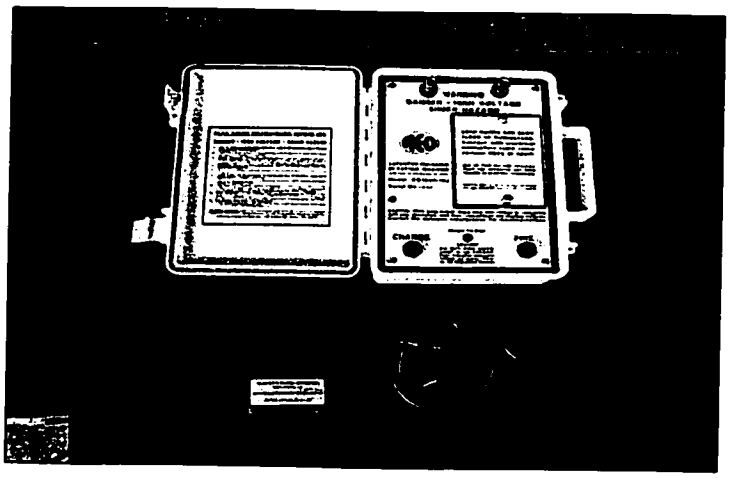

Figure 4.17: Blasting machine (model CD 1400-10J)

ANFO explosive

ANFO is a mixture of diesel fuel oil (FO) with ammonium nitrate (AN). ANFO is non-ideal explosive; its performance or release of energy is affected by many factors such as the mixing ratio of (AN) and (FO), the particle size, the moisture content and the degree of confinement. It has been found (Johansson and Persson, 1970) that a mixing ratio of 5.7 % FO and 94.3 % AN by weight gives the best explosive energy. The effect of fuel oil concentration on the explosive energy of ANFO is illustrated in Figure 4.18 and Table 4.12 lists the properties of bulk ANFO. In the current research, spherical charges were prepared using a factory-blended ANFO, each contained a one-lb Pentolite booster placed at the centre of the charge with an electrical detonator that was connected to the blasting machine using a 2-km blasting cable. A fibre optic cable was also fixed to the middle of the charge and extended to the bunker to trigger the instrumentation.

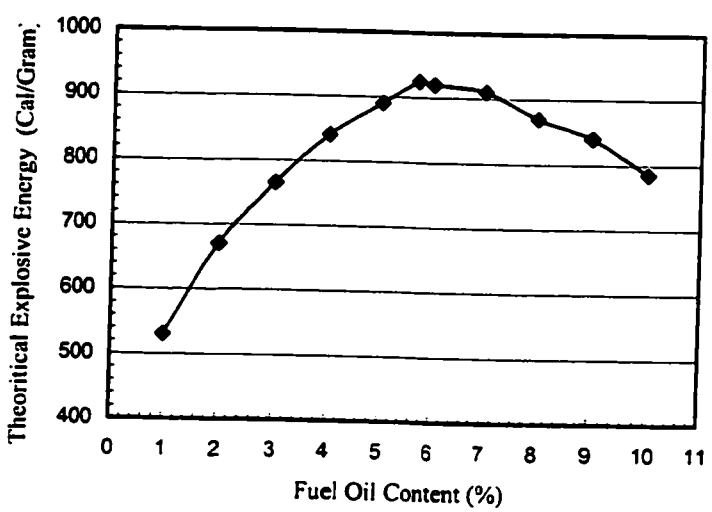

Figure 4.18: Effect of FO content on energy of ANFO explosive

Table 4.12 Properties of bulk ANFO (5.7% FO and 94.3% AN)

Specification	Measure
Bulk density, kg/m^3	850
Explosive energy, kJ/kg	3717
Detonation velocity, m/sec	3990
Volume of reaction products, L/kg	4757
Equivalent weight for pressure	0.82
Equivalent weight for impulse	0.82

4.5.4 Blast test procedure

The main blast test series was conducted on the Canadian Forces Base (CFB) in Petawawa that is located about 140 km west of Ottawa. The 1000 kg capacity explosion range is about 30 km away from the base. The blast testing was performed through two main periods; the first period extended from May 8 till 12, 2000, followed by the second period from May 29 till June 9, 2000.

Initial Testing

The first test period was aimed to establish more confidence in the estimated charge weight and standoff distance. The first two blast shots were successfully conducted on the control specimen CS_1 using 13.4 and 22.4 kg charges with 3 working reinforcement strain gauges and 4 surface strain gauges. Connections to incident and reflected gauges, video and deflection measurement device were checked. Incident and reflected pressures and mid-span deflection were successfully recorded, while neither strain measurements nor in frame videos were captured. Unexpectedly, due to a plane crash and the ensuing search within the surrounding area, further testing needed to be halted. Nevertheless,

based on test observations, to improve records during the following tests, some modifications to the supporting frame and the set-up were deemed necessary. The LVDT extension was replaced by a metallic one, which was expected to prevent the friction with the supporting base. In addition, a new clamping system, using four bolts per panel side was provided to the box frame in order to simplify the process of placing test panels.

Final Blast Testing

The test site on the range was chosen, and a ground pit was formed in the ground by means of two explosive charges. The frame was placed into the pit and the area around it was leveled. Surrounding objects were removed to keep the explosion area free of surfaces that could cause wave reflection to blast incident waves. The following procedure was typically followed for each test:

- The test specimen was carried close to the box frame. Rubber pads were placed on the top supporting angles. Strain wires were fixed to the cables through the assembly box and the power supply source was turned on. The in-box instrumentations including the LVDT, the video camera and the light bulbs were checked. The specimen was then put in position and held by means of the clamping system
- The area around the specimen was landscaped and partially compacted to give a consistent ground surface
- The wooden tripod supporting the explosive charge was erected, ensuring a standoff distance of 3 m
- The fibre optic cable, the blasting cable and all other connections were checked for proper functioning

- The exact locations of the incident pressure gauges from the centre of charge were measured and recorded
- Prior to leaving the explosion spot, photos were taken, and all the recording scopes and acquisition systems located in the bunker were checked
- All personnel were evacuated from the test area to a safe location, while only one person initiated the explosive charge at 1.5 km away from ground zero
- After the blast event, the operator called the area clear, and a procedure of saving the recorded data, turning the power source off, taking photos and comments, and replacing the test specimen was followed
- To save as much information about the failure mode of the test specimens as possible, crack patterns, concrete spalling, shape of FRP layers, and all related comments were recorded right after the explosion.

During the main blast test, seventeen blast shots were conducted. Panel CS_1 was tested using 13.4 and 22.4 kg charges. It was decided to observe the effect of repeated shots on test panels. The rest of specimens were tested only once. Four specimens were tested using 22.4 kg (50 lb) charges. The remaining tests were performed using 33.4 kg (75 lb) charges. Although most of the top surface strain signals were lost when the shock wave pulled the signal wires from the gauges, incident and reflected pressures, strains at bottom surfaces and reinforcement bars, mid-span deflections as well as videos from almost all blast experiments were obtained. The blast test schedule is shown in Table 4.13, where test date, charge mass and test specimens are specified for both blast-testing periods. The blast testing results will be discussed in the following chapter.

Table 4.13: Blast test schedule

Testing period	Test No.	Charge weight (kg)	Standoff distance (m)	Test groups and panels			
				CS	GSS	CSS	CLS
First period	1	13.4	3				
	2	22.4	3				
	3	22.4	3				
Second period	4	22.4	3				
	5	22.4	3				
	6	33.4	3				
	7	33.4	3				
	8	33.4	3				
	9	33.4	3				
	10	33.4	3				
	11	33.4	3				
	12	33.4	3				
	13	33.4	3				
	14	33.4	3				
	15	33.4	3				
	16	33.4	3				
	17	22.4	3				

4.8 Static Test

Static tests were conducted to evaluate the post-blast residual strength of the test panels. A comparison of the residual strength of unretrofitted test specimens with those of the FRP retrofitted samples may be used as a measure of the additional structural integrity provided by the FRP. Static tests were performed in the Civil Engineering Materials and Structures Laboratories at Carleton University. Each panel was simply supported along its four edges and subjected to a control load distributed over a 300 × 300 mm area through a steel plate (Figure 4.19). It consisted of a four sided supporting frame to fit the test specimen on and a hydraulic actuator. Deflections were recorded using dial gauges

located at 1/6 and 1/3 points of the span. Readings were manually recorded at the end of each 5 kN load increment up to failure.

Fifteen static tests were carried out, including thirteen post-blast panels and two intact samples (***CS₅*** and ***CCS₅***). The latter two samples were used to evaluate the failure load of test specimens before the application of blast load. During the first static test, carried out on panel ***CLS₁***, a loud bang was heard at a load of 60 kN, the test was stopped and the sample was inspected. The careful inspections showed no obvious failure and the test should have continued. This was too late because the gauges were moved. Therefore, the recorded 60 kN is not the real failure load of sample *c*. Results of the static tests will be presented in the following chapter.

Figure 4.19: Static test set-up

Chapter 5

EXPERIMENTAL RESULTS: ANALYSIS AND DISCUSSION

5.1 General

The test specimens described in the previous chapter were subjected to blast pressure resulting from the free-air detonation of high explosive charges. Following this, the samples were statically tested in order to evaluate their post-blast residual strength. This chapter is concerned with the presentation, analysis and discussion of the results of the blast and the static tests. Results of the blast test include incident and reflected pressures, strain in the reinforcement and on the FRP and concrete surfaces, and mid-span deflections. Deflection and failure load of each panel were recorded in the static tests. For the sake of clarity, the results are presented for each test group, including their structural behaviour, mode of failure, cracking patterns, reinforcement and surface strains, blast pressures and impulses, mid-span deflection, and residual static strength. Observations are made with respect to the various failure modes and relevant conclusions are drawn.

5.2 Preliminary Blast Tests

To ensure that the test equipment and instrumentation function properly, and to check the adequacy of the test set-up, a number of preliminary tests were conducted on unretrofitted panels. The following sections present the experimental results from the two preliminary phases of the test program.

5.2.1 Preliminary blast Phase (1)

Phase (1) was performed to evaluate the effect of wrap-around of shock waves on the ultimate carrying capacity of small-dimension targets. Test specimens were tested under static and blast loads. The charge size, standoff distance and results of the four blast tests in this phase are given in Table 5.1, which shows the recorded maximum incident and reflected pressures. Figure 5.1 shows three loads. The value of 9.2 kN is the maximum static capacity of the slab obtained in the laboratory. The load was applied through a circular steel plate. The value of 45.6 kN predicted by CONWEP is based on the resultant of the uniform reflected pressure acting on the slab. The reflected pressure was predicted by CONWEP based on the charge size and standoff distance given for blast shot # 4 in Table 5.1. Finally, the load of 365 kN was calculated using the measured value of the maximum reflected pressure for blast shot # 4 as given in the latter table.

The results in Figure 5.1 reveal that the maximum blast load of 365 kN, evaluated experimentally, is 8 times larger than that predicted by CONWEP (45.8 kN), and more than 40 times the measured static load capacity of 9.2 kN. The large difference between the CONWEP predictions and the blast test results are ascribed to the so-called wrap-around effect. Due to the limited dimensions of the test slab, the blast waves wrap around

its back side, creating a pressure opposite to the reflected pressure. The consequence is reduction in the net pressure to which the test slabs is subjected. CONWEP, on the other hand, assumes infinite target dimensions and consequently does not consider this effect. The difference between the static and the dynamic tests results may be attributed to the rate of loading and to the difference between the static and dynamic response of materials. As stated earlier, depending on the duration ratio, the structural response may be governed by impulse rather than pressure.

In order to obtain realistic test results, it is imperative to eliminate the wrap-around effect. One way of avoiding this effect is to mount the test specimens in a vertical frame with expanded sides made of steel. This would partially reduce the wrap-around effect on the test panels. Another option is to place the test specimens horizontally in a box frame, with the box being buried in the ground and the specimen being flush with the ground surface. This would practically eliminate the wrap-around effect.

Table 5.1: Results of the preliminary blast Phase (1)

Blast shot No.	Charge weight (gm)	Charge distance (m)	Incident pressure (kPa)	Reflected pressure (kPa)	Observed damage
1	175	2.25	55.93	135.22	None
2	185.9	1.53	120.75	349.3	None
3	180	0.92	-	-	None
4	185	0.35	355.8	1463	Failure

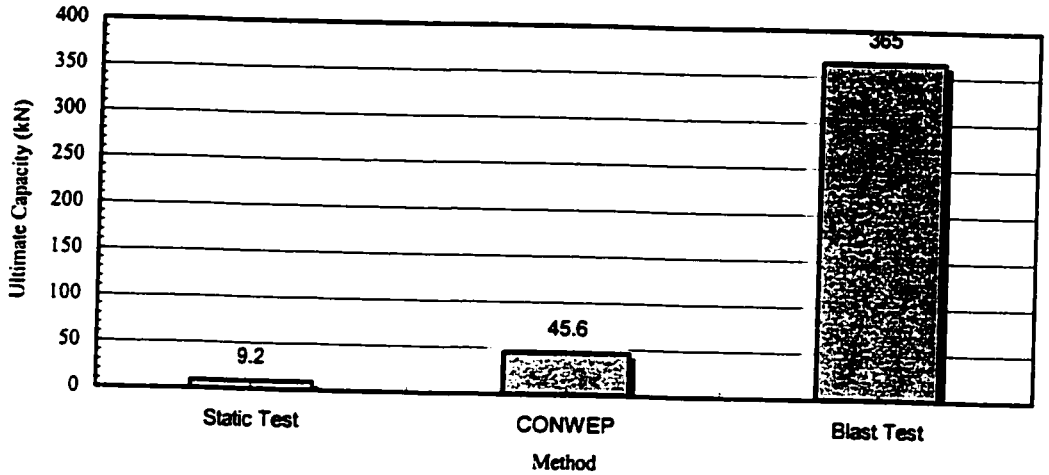

Figure 5.1: Comparison between ultimate load capacities of patio slabs

5.2.2 Preliminary blast Phase (2)

This preliminary phase was conducted to answer a number of questions regarding the final set-up: how to fix the test specimen (horizontally or vertically) such that the wrap-around effect could be eliminated? Where and how to put the explosive charge? What is the required standoff distance and charge weight? Fortunately, most of these questions had been answered after conducting this phase. The results are summarized in Table 5.2, which include values of incident and reflected pressures, impulses and positive durations.

Table 5.2: Results of the preliminary blast Phase (2)

Holder No.	Gauge No.	Gauge distance from the panel surface (mm)	Gauge distance to the charge centre (mm)	Pressure (kPa)		Reflected impulse (kPa.msec)	Positive duration (msec)
				P_i	P_r	I_r	t_o
Holder No. 1	1	25	1975	82.5	150.2	58.5	0.915
	2	55	1935	77.3	119.9	45.7	1.175
	3	140	1850	85.5	75.5	30.5	1.583
	4	255	1735	115.1	79.9	23.8	1.725
Holder No. 2	5	25	2075	73.9	132.3	52.5	0.751
	6	55	2035	58.1	94.4	33.7	0.830
	7	140	1950	87.8	55.5	24.2	1.247
	8	255	1835	95.5	47.5	19.7	1.751

From the test results obtained, the following conclusions could be drawn:

- First, the difference in reflected pressures and impulses recorded by gauges # 1 and 5 (located at the same distance from the panel surface) is of the order of 13 %. Based on this, and for the purpose of blast load calculations, it is reasonable to assume that the current blast waves resulting from an airburst are essentially planar.

- Second, the incident and reflected pressures at the same location were experimentally captured and the latter was found to be two times the former. Figure 5.2 shows the pressure-time profiles recorded by gauges 1 and 5, which were located at the same distance from the panel surface, but at distances of 1975 and 2075 mm from the charge centre, respectively. Two peaks can be recognized for each pressure profile, the first two peaks indicate incident pressures of 11.98 and 10.72 psi (82.5 and 73.9 kPa), and the second two peaks represent reflected pressures of 21.8 and 19.2 psi (150.2 and 132.3 kPa). Time shift between the two pressure peaks is the time required for blast wave to travel from the gauge to target surface and to return to the gauge after reflection. The slight difference in pressure readings between the two gauges is due to change in distance from the gauge to charge centre.

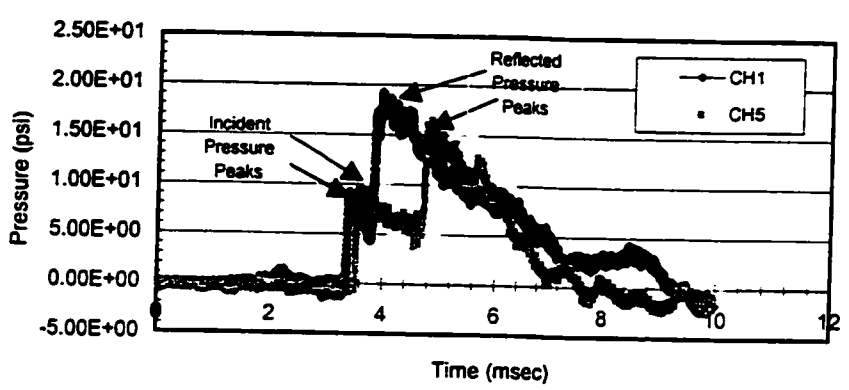

Figure 5.2: Pressure-time histories captured by Gauges # 1 and 5

- Third, after conducting six tests with the 185 gm charge, no noticeable damage was observed in the test specimen. This meant that due to limitations of the CERL range, the main blast tests had to be moved to the demolition range at the CFB Petawawa.

- Assuming a 3 m standoff distance, CONWEP was used to find the charge weight needed to breach the control specimen. The program CONWEP can predict the charge weight corresponding to a given standoff distance to breach a structure of known geometry and boundary conditions. The result of this analysis was that 22.4 kg of ANFO would be needed to breach the control panel. It was then decided to start with a charge mass of 13.4 kg as a starting point and to increase the charge mass to 33.4 kg to account for the expected strength increase due to the application of the FRP retrofitting layers.

- Finally, the portable measurement devices were calibrated and prepared for the main blast test. However, using the multi-gauge holders in the field was found to be time consuming, and did not fit in with the time restrictions for the use of the blast range. Therefore, separate incident and reflected pressure transducers were used in the main blast testing. Also, more work was still needed to calibrate the strain amplifiers, the deflection measurement device, and the design and manufacture of the main blast test frame.

5.3 Main Blast Tests

Results of main blast test will be presented including recorded measurements of reinforcement and surface strains, incident and reflected pressures and mid-span deflections. The presentation of results is arranged such that the structural behaviour of each test group may be separately discussed. Failure modes of concrete, i.e. spalling or crushing, and crack propagation were observed and recorded. Damage effects on the FRP layers, including debonding and anchorage failure are highlighted. A summary of the test results is tabulated at the end of each test group with their analysis and discussion.

5.3.1 Test Group (1)

Results of test Group (1) are used as a reference for comparison with the remaining results. Control specimen CS_1 was tested twice in blast shots 1 and 2, while specimens CS_2, CS_3 and CS_4 were tested using single charges in blast shots 8, 15, and 17. Blast wave parameters including pressure, impulse and positive duration are introduced as they measured during the blast tests using the oscilloscope. The following is a presentation of the structural behaviour, followed by full tabulation and illustration of the test results.

Structural Damage

Control panel CS_1 was tested twice, using 13.4 and 22.4 kg of ANFO. It was decided to start with a reduced blast pressure to ensure elastic behaviour. The 13.4 kg charge resulted in an average reflected impulse at the panel surface equal to 995 kPa.msec with an average reflected pressure of 2150 kPa. Any damage to the bottom surface of the panel could not be observed because it would have required taking the panel out which was not practical. Thus, observations for the 13.4-kg shot are related to the top surface, which did

not exhibit any cracks or concrete spalling. There were also no recorded strain signals. The maximum mid-span deflection was measured as 2.7 mm. Although, incident and reflected pressures were recorded, scatter in the results was noticed. It was concluded that energy released from such a charge was not enough to produce noticeable damage to the test specimen, but the maximum deflection of 2.7 mm indicates some cracking.

Using a 22.4-kg charge, a second shot was performed on the same test specimen, and this resulted in an average reflected impulse of 1344 kPa.msec with an average reflected pressure of 2538 kPa. The test specimen was cleaned and photos of the top surface were taken while still in position. On the top surface, a system of cracks (0.2 mm wide) and concrete scabbing of about 300 mm length and 10 mm depth were observed (Figure 5.3, a). The sample was taken out of the supporting frame and further observations about its mode of failure and crack pattern were made. Tensile cracks at the bottom surface had an interesting pattern as it followed the shape and spacing of the reinforcing bars. They formed a square of 500 × 500 mm in the middle then extended to the corners with a system of 45° cracks (Figure 5.3, b). Crack width varied between 0.5 and 1.5 mm. Shear cracks on all four sides of the panel were observed, two per side with inclination of 45°. Concrete spalling at the north edge was also noticed. The spalled region was 400 mm long and an average of 20 mm deep. Figure 5.3, (c) shows the damaged control specimen CS_1 after the two blast shots.

Incident and reflected pressures were recorded, but were scattered over a wide range. This can be due to insufficient soil compaction around the reflected gauges. Neither mid-span defection nor internal videos were captured. The reason for not recording deflection traces was thought to be due to the poor installation of the extension rod of the LVDT,

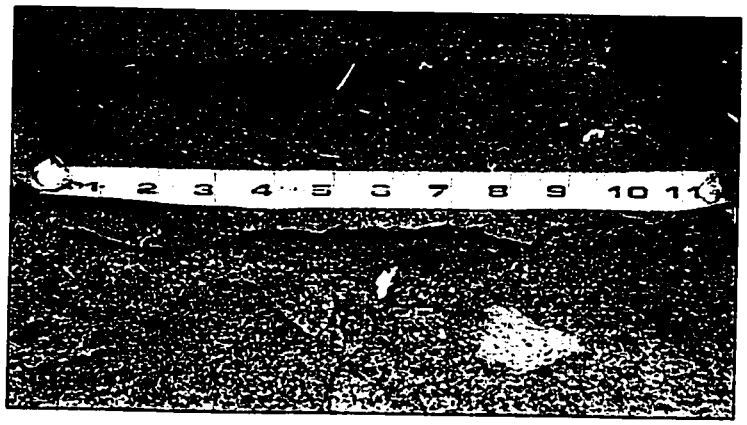

(a)

(b)

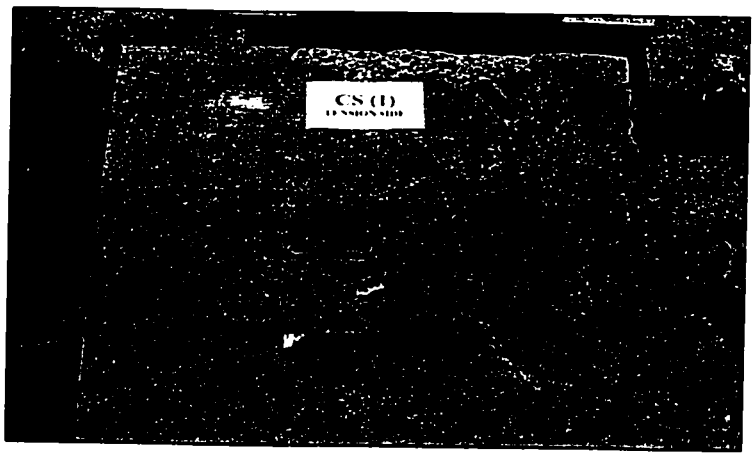

(c)

Figure 5.3: Panel *CS*$_I$ after the 22.4 and 33.4 kg shots (a) Concrete scabbing on the top surface (b) Diagonal cracks on the bottom surface (c) Bottom surface cracks

hence it was decided to replace it starting with test 3. As panel CS_1 was tested twice, it was felt that its observed modes of failure could not be used as reference. Accordingly, it was decided to test another as-built control specimen, CS_4, using one 22.4 Kg. (50-lb) charge.

Test specimen CS_4 was subjected to a 22.4 kg charge, a blast which yielded an average reflected impulse of 571 kPa.msec with an average reflected pressure of 3842 kPa. The value of the reflected impulse is very low and is not considered. The observed damage of panel CS_4 was less than that observed in panel CS_1 caused by the two successive shots. The top surface showed neither concrete spalling nor crushing. Only minor cracks of 0.15 mm width were observed. Shear cracks (up to 0.1 mm wide) were also noticed on the four sides at 45° with the horizontal. Tensile cracks of 0.5~1.0 mm wide had the same pattern as in panel CS_1 with a 300 × 300 mm middle square and diagonal cracks joining the square corners to the panel corners. No permanent deflection was recorded. It was concluded from visual inspection and measurement of crack width that the 22.4 kg charge resulted in a moderate level of damage to this control specimen. Panel CS_4 was used as a reference for the strengthened panels tested under the same charge. Figure 5.4 shows both the top and bottom concrete surfaces of control specimen CS_4 after exposure to 22.4 kg blast shot.

Control panels CS_2 and CS_3 were subjected to 33.4 kg charges that resulted in average reflected impulses of 1954 and 2412 kPa.msec, with average reflected pressures of 5059 and 5507 kPa for the two tests, respectively. Almost total failure of both specimens was observed. At the top surface, a local circular cavity of 500 mm diameter was formed and a permanent deflection of 10 mm was measured. Forty-five degree shear cracks of about

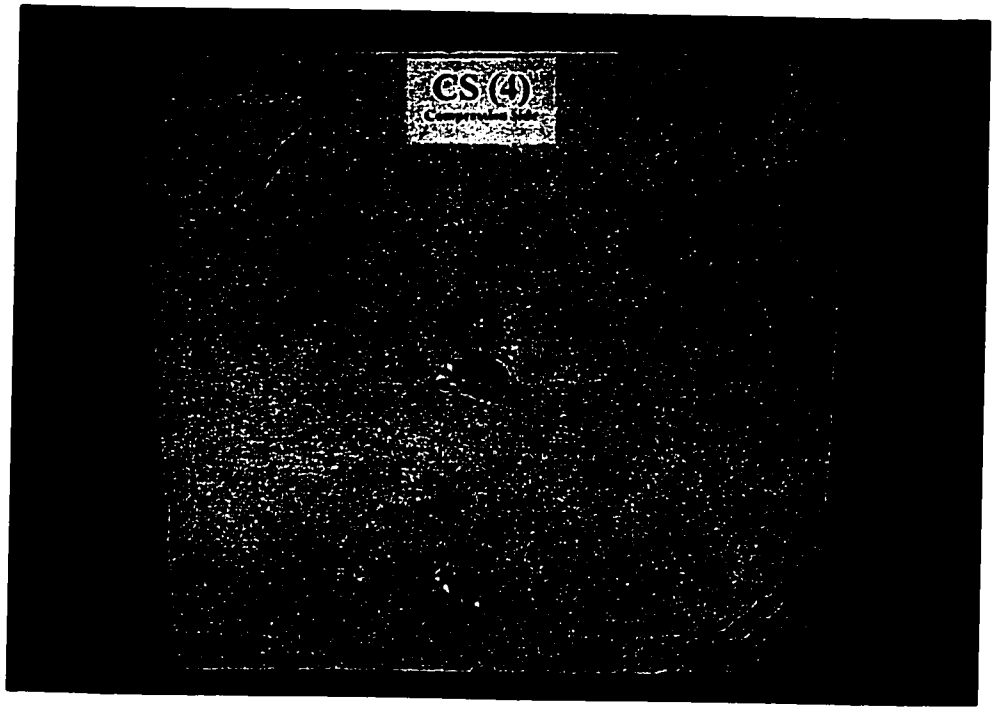

(a)

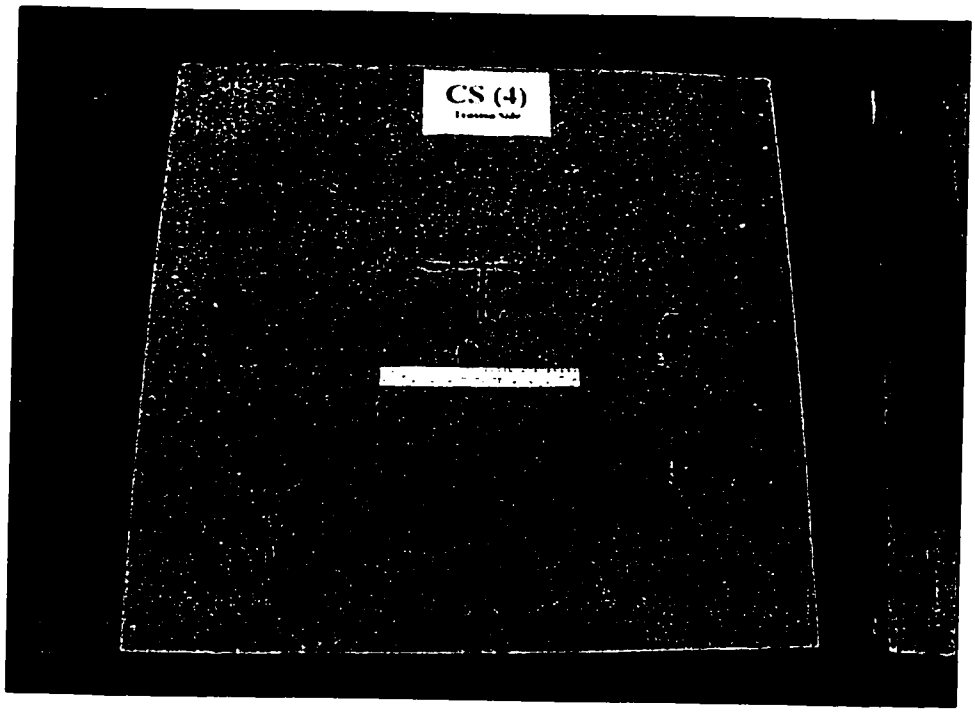

(b)

Figure 5.4: Panel CS_4 after a 22.4 kg blast shot
(a) Top surface, and (b) Bottom surface

1 to 3 mm width were observed on the four sides. At the bottom surfaces, approximately 4-mm wide cracks having the same pattern as in panels CS_1 and CS_4 were observed. The bottom concrete cover spalled off with wide visible cracks on the surface. The failure modes of these two specimens will be the reference for the strengthened specimens tested under the same charge size. Figures 5.5 and 5.6 show the failure modes of both the top and the bottom surfaces of specimens CS_2 and CS_3 after exposure to 33.4-kg shots. In the light of the preceding observation of Group (1), it can be stated that:

- The 13.4 kg charge produced an elastic response, causing only slight damage. Using a 22.4 kg charge resulted in moderate damage while using 33.4 kg charge completely breached the control specimens.
- Most of the strain gauges attached to the top surface (facing the direction of shock wave propagation) were lost due to the peel-off of the wiring connections before strain signals could be recorded. On the other hand, fortunately all other measurements, including reinforcement and bottom surface strains, mid-span deflections, and incident and reflected pressures were measured and recorded.
- Forty-five degree shear cracks were formed in all the test specimens and on all sides of each specimen. The direction of shear crack indicated that these cracks were formed by the suction effect of the pressure wave. The shear cracks pattern is most likely caused by the pressure wave propagating and subsequently being reflected by the frame bottom. The strengthened reflected pressure wave acted on the bottom surface of the test specimen and produced the observed crack pattern. The test specimen was subjected to the drag (suction) effect, which caused tensile stresses on the top surface and compressive stresses on the bottom surface, thus producing the

observed inclination of shear cracks. Examples of inverted shear cracks observed in test Group (1) are illustrated in Figure 5.7. It was initially thought that such cracks might be due to stress concentration at the edge clamp locations, but further deliberation revealed they were due to the suction as explained earlier.

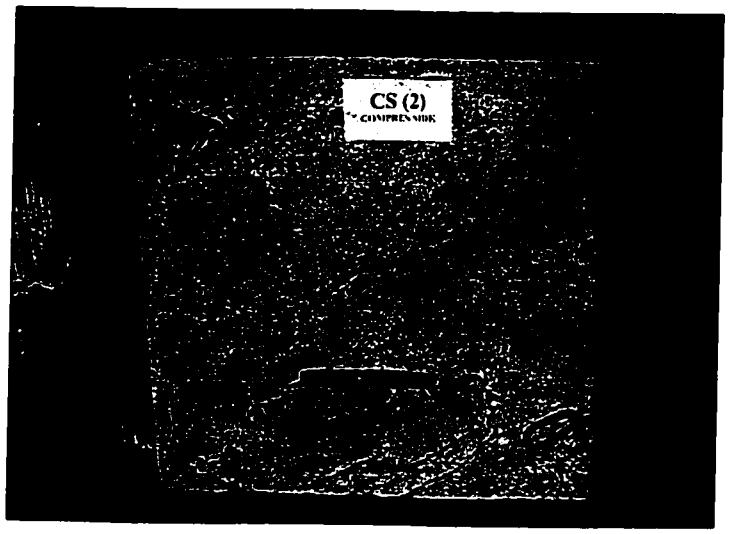

(a)

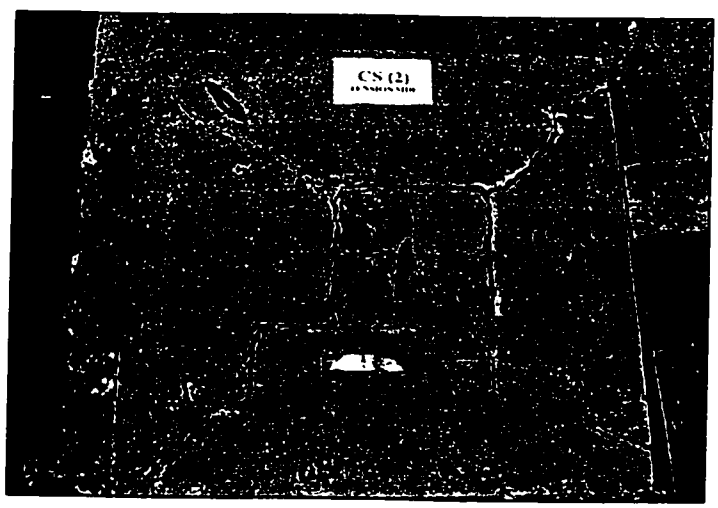

(b)

Figure 5.5: Panel CS_2 after a 33.4-kg blast shot (a): Top surface, and (b): Bottom surface

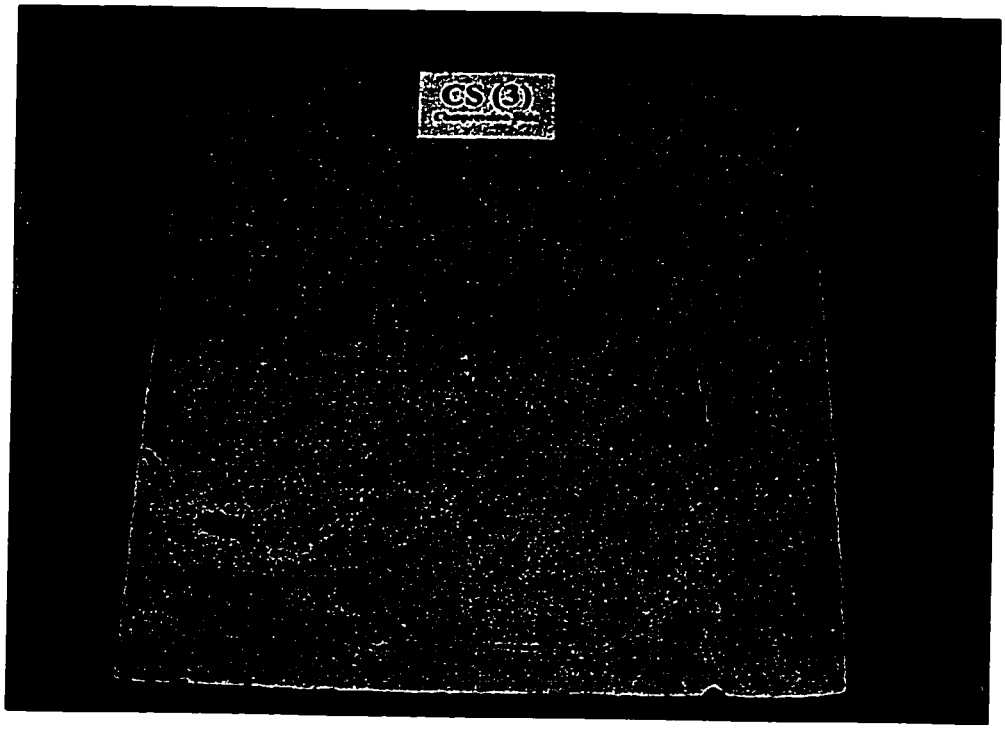

(a)

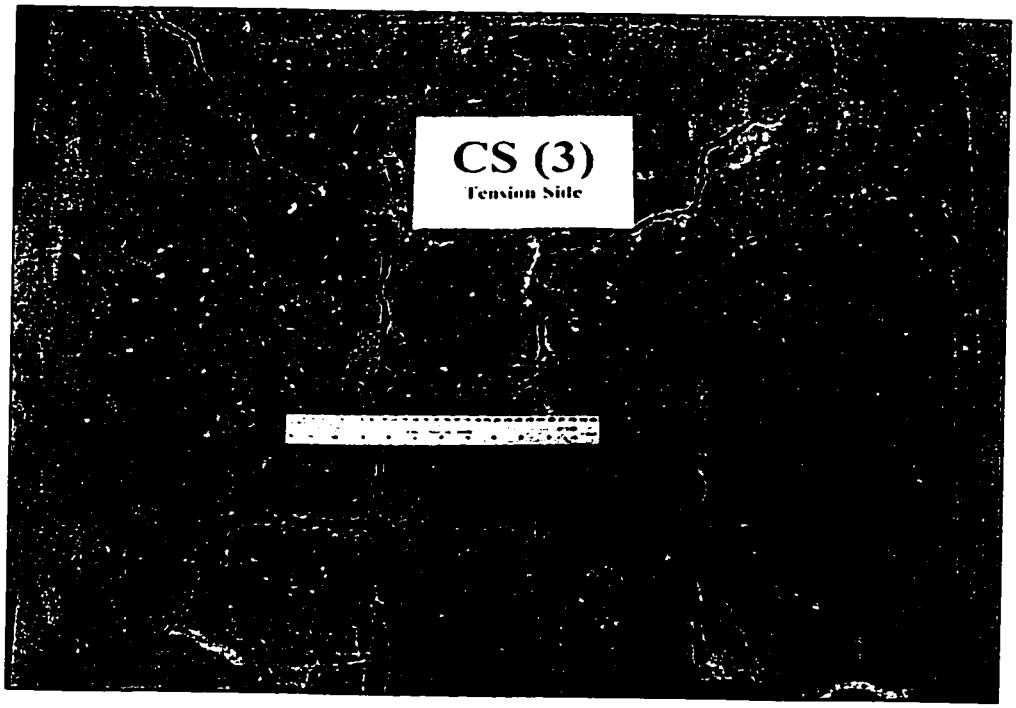

(b)

Figure 5.6: Panel *CS₃* after a 33.4-kg shot
(a): Top surface, and (b):Bottom surface

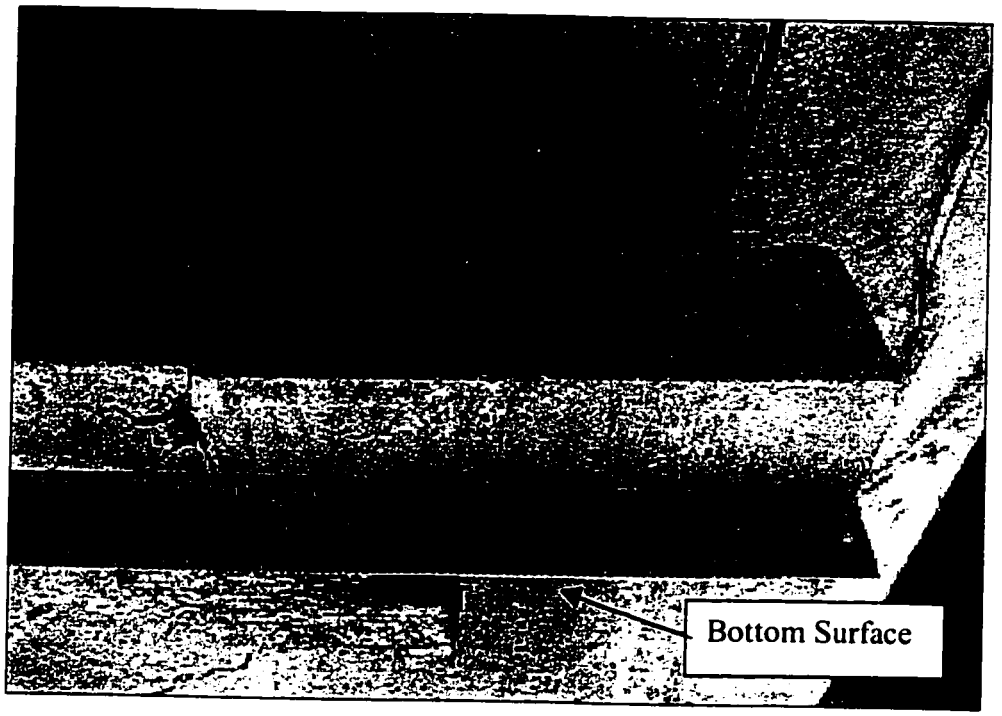

(a)

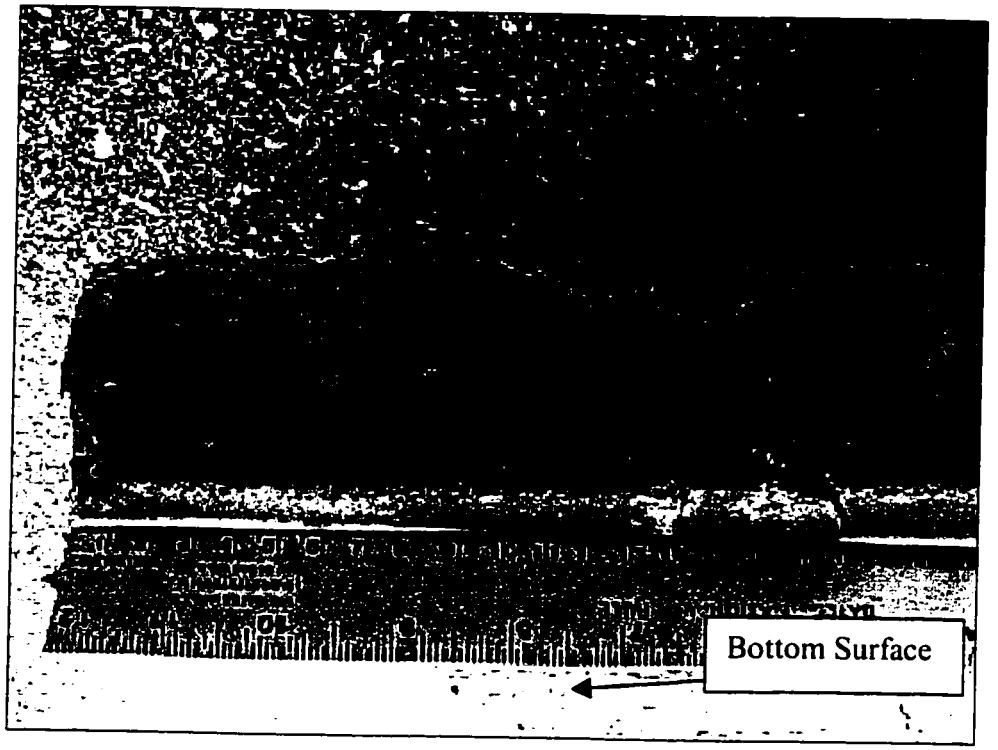

(b)

Figure 5.7: Inverted shear cracks of (a): Panel CS_2 and (b) Panel CS_3

Results of Group (1)

Experimental data recorded from testing of Group (1) included measurements of strain by means of 8 strain gauges, 2 incident and 4 reflected pressure transducers, and 1 LVDT for measuring deflection. Tables 5.3 through 5.5 show the complete set of results for this group. The recording scopes had a maximum sampling rate of one million sample/sec (MS/s). In other words, they could capture up to a million data points each sec. Based on this a time base was created that had a time step equal to 1/sampling rate (or one μsec).

Strain measurements are shown in Table 5.3 where the 8 channels denote the locations of the strain gauges (refer to Figure 4.2 in the previous chapter). No strain signals were recorded during blast test 1 due to gauge failure. In blast tests 2 and 17 (22.4 kg), strains of 3500~4375 μstrain were recorded that are in the inelastic range. Higher strains, up to 6350 μstrain in tests 8 and 15, were captured for the 33.4 kg tests.

In Table 5.4, pressure and impulse are given. Very low impulse was recorded in blast test 17, while the impulses for the two 33.4-kg charge tests differ by 23 %. Finally, mid-span deflections are given in Table 5.5. No deflection was recorded in test 2, and the deflections for the two 33.4-kg charge tests differed almost 37 %.

Sample of data for each test group are graphically illustrated, while the rest of the data are given in the appendices. Results of test 15 (Panel CS_3 under 33.4 kg of ANFO are presented as an example of test Group (1). Measured strains have been plotted in two separate figures, labelled (a) and (b). In each case, Figure (a) depicts the strain at the mid span point and at a 1/3 point of the slab diagonal for the top steel mesh or concrete surface, while Figure (b) shows the strain at similar locations on the bottom surface.

Table 5.3: Table 5.3: Strain measurements of test Group (1)

Test No.	Sample	Charge Weight (kg)	Strain x 10^{-6} Channel 1	Channel 2	Channel 3	Channel 4	Channel 5	Channel 6	Channel 7	Channel 8
1	CS_1	13.4	NC	NC	NC	NC	NC	NC	NC	NC
2	CS_1	22.4	3400	P	3500	3500	P	P	P	P
8	CS_2	33.4	1875	2730	1660	P	1650	P	5000	NC
15	CS_3	33.4	2000	2900	6350	1680	3800	600	1700	P
17	CS_4	22.4	NC	4375	NC	NC	NC	NC	NC	NC

Table 5.4: Pressure and impulse of test Group (1)

Test No. & (Sample)	Incident Pressure (kPa) FF_1	FF_2	Reflected Pressure (kPa) P_{r1}	P_{r2}	P_{r3}	P_{r4}	Average Reflected Pressure	Reflected Impulse (kPa.msec) I_{r1}	I_{r2}	I_{r3}	I_{r4}	Average Reflected Impulse
1 (CS_1)	537	100	1978	NC	2019	2453	2150	915	NC	996	1075	995
2 (CS_1)	P	97	1058	1950	NC	4595	2538	813	NC	572	1874	1344
8 (CS_2)	442	207	5249	5528	5298	NC	5059	2025	2050	1778	NC	1954
15 (CS_3)	P	123	5712	5540	5271	NC	5507	1950	2722	2553	NC	2412
17 (CS_4)	158	P	4823	4485	2219	NC	3842	955	520	427	NC	571

Table 5.5: Mid-span deflection of test Group (1)

Test No.	Sample	Charge Weight (kg)	Mid-Span Deflection (mm)
1	CS_1	13.4	2.7
2	CS_1	22.4	NC
8	CS_2	33.4	13.12
15	CS_3	33.4	9.53
17	CS_4	22.4	8.33

- Notes: NC = Not Captured, P = Poor Trace, and NU = Not in Use

Figures 5.8 and 5.9 show strain recorded in blast test 15. In Figure 5.8 (b), CH2 illustrates an example of signal loss after the first strain peak as indicated by the sudden increase to a value of 20000 μstrain, followed by a plateau to the end of the trace. In such cases only the first peak should be considered and the rest of the trace needs to be ignored. For full strain results, see Table 5.3. Real strain signals can be recognized in Figures 5.8 (a), where strain in steel ranged from 1680 to 6350 μstrain. A value of 3800 μstrain was obtained at the bottom concrete surface (Figure 5.9, b: CH5). Strains of this blast test will be considered as reference when comparison is made with the FRP retrofitted panels.

Pressure-time histories recorded for panel CS_3 are plotted as incident and reflected pressure and are referred to as (a) and (b) in each plot. In these diagrams, the effect of distance on the recorded pressures can be easily observed. For example, in Figure 5.10 (a), gauge FF1 located 5.48 m (18.04 ft) from the charge centre indicated a 248 kPa (36 psi) incident pressure, while gauge FF2, located at a distance of 9.47 m (31.17 ft) from charge centre, recorded a value of 123 kPa (18 psi). In addition, with reference to the horizontal axis of the graphs, a time difference of about 10 msec can be observed, which is the time required for the pressure wave to cover the 3.99 m distance between the two gauges. On the other hand, since the distance of all the reflected pressure gauges to the charge centre was the same, their recorded pressures were close without time lag between traces. The reflected impulses associated with the reflected pressures were calculated by the aid of the digital oscilloscope and are shown in Table 5.4. Mid-span deflections are plotted for panels CS_3 in Figure 5.11 with a peak of 9.53 mm. The deflection starts to increase (at a time equals to the time of arrival) from a value of zero to a maximum and then it decreases to minimum during the time of exposure (positive duration).

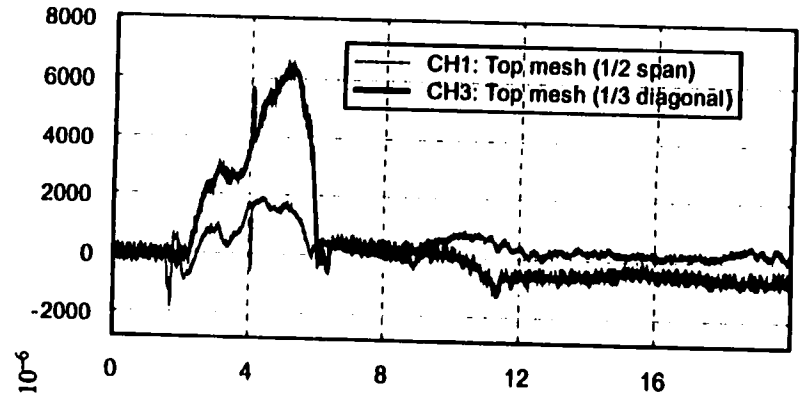

(a): Strains in the top steel mesh

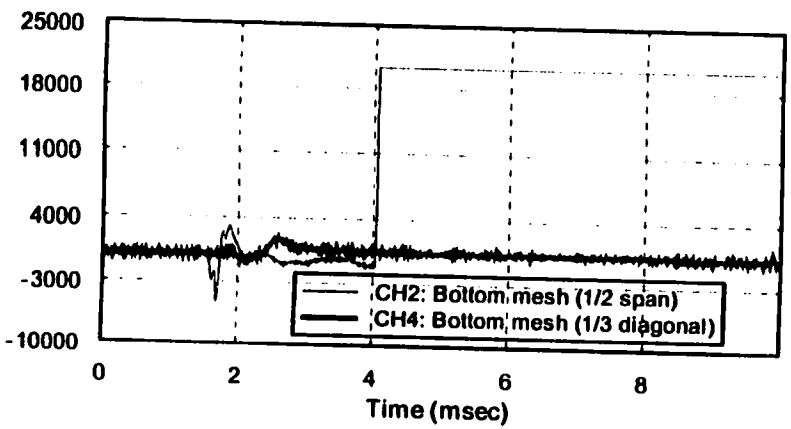

(b): Strains in the bottom steel mesh

Figure 5.8: Strain-time profiles in steel meshes (Blast test # 15: Panel CS3)

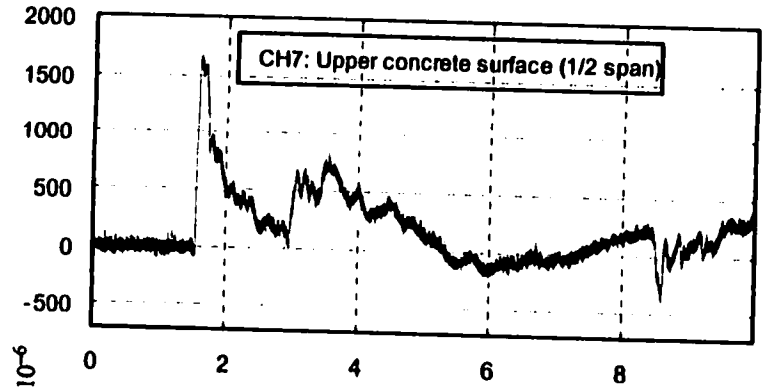

(a): Strains in the top concrete surface

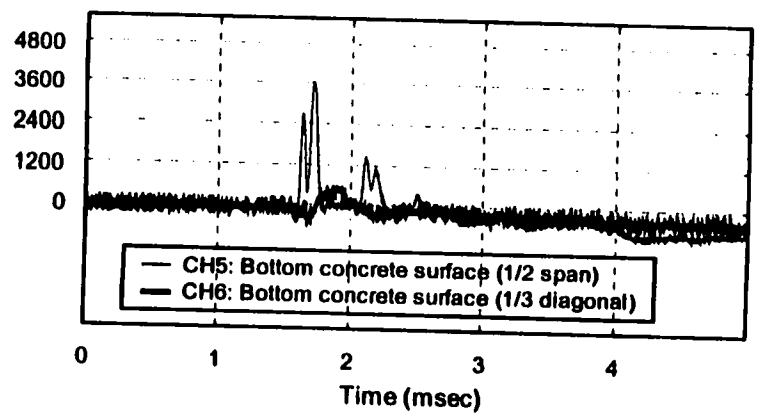

(b): Strains in the bottom concrete surface

Figure 5.9: Strain-time profiles on concrete surfaces (Blast test # 15: Panel CS3)

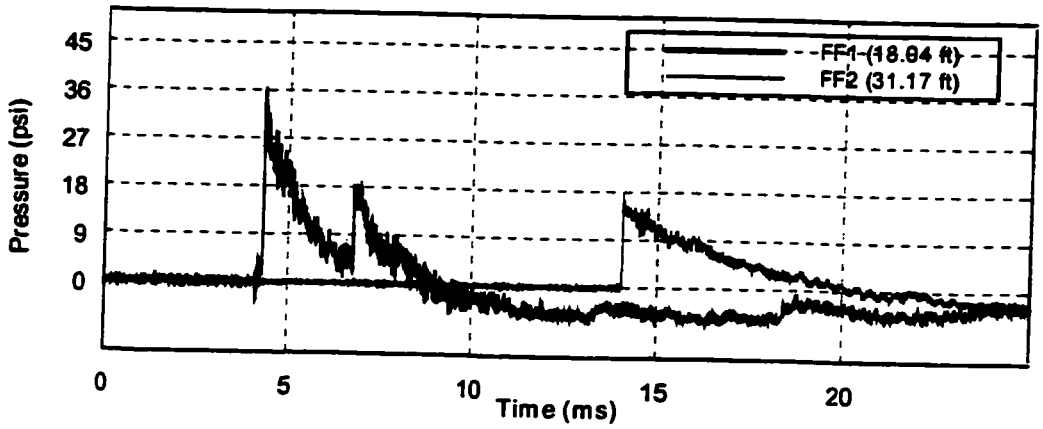

(a): Incident (free field) pressure-time profiles

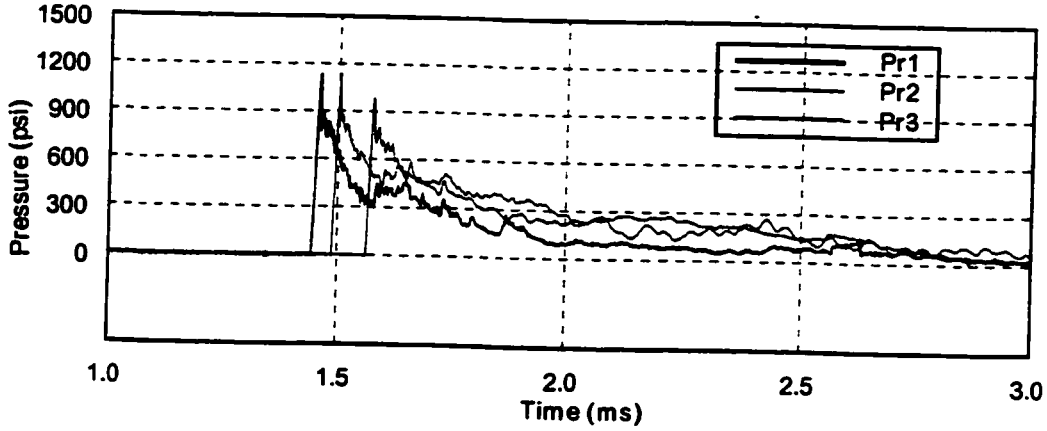

(b): Reflected pressure-time profiles

- 1 psi = 6.89 kPa.

Figure 5.10: Pressure-time profiles of blast test # 15 (Panel CS3)

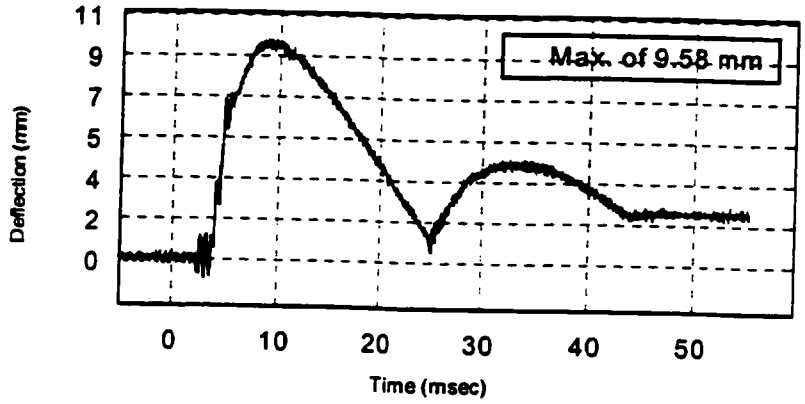

Figure 5.11: Mid-span deflection history for blast test # 15 (Panel CS3)

5.3.2 Test Group (2)

In test Group (2), four reinforced concrete panels were strengthened using 500 mm wide E-Glass fibre sheets applied in two orthogonal directions parallel to the slab edge. This sheet configuration left the four corner regions of the panels, each region being 250 × 250 mm un-strengthened. The GFRP retrofitted panels GSS_1 through GSS_4 were tested in blast tests 4, 7,12, and 14, respectively.

Structural Damage

The GFRP retrofitted panel GSS_1 was tested using 22.4 kg charge in blast test 4, and showed almost no damage. Good bond between the sheets and the concrete surfaces was observed. On both panel surfaces, inclined hairline cracks at 45° were observed in the four corners (Figure 5.12), and because of the presence of the sheets it was difficult to observe whether these cracks continued under the FRP layers. As sheets were not wrapped around panel edges, shear cracks were noticed on the four sides. Figure 5.13 shows the bottom (tension) surface of test specimen GSS_1 after the 22.4-kg blast shot.

Test panels GSS_3 and GSS_4 were tested using 33.4-kg charges in blast shots # 12 and 14 and reflected impulses of 1492 and 2239 kPa.msec were recorded, respectively. Moderate and moderate to heavy damage was observed for the two panels. Glass sheets in both panels showed good bond with the concrete surfaces, and no permanent deflection was recorded. Here 0.5 mm wide inverted shear cracks were observed in panel GSS_3 (Figure 5.14). Also, separation of the sheets along the edges was observed (Figure 5.15). The damage induced by the 50 % increase in charge weight manifested as bottom cracks of width 3 mm and concrete crushing at the northeast corner of panel GSS_4. Cracking and local damage of panel GSS_4 are shown in Figures 5.16 and 5.17.

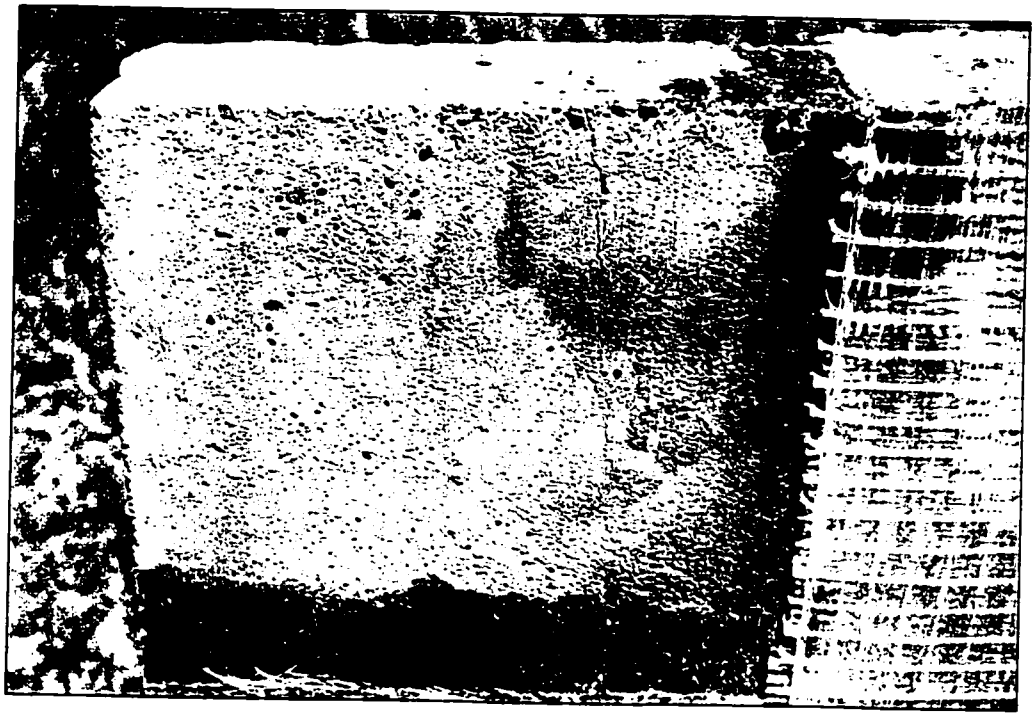

Figure 5.12: Hairline tensile cracks at uncovered square of Panel *GSS*$_1$ after a 22.4-kg blast test

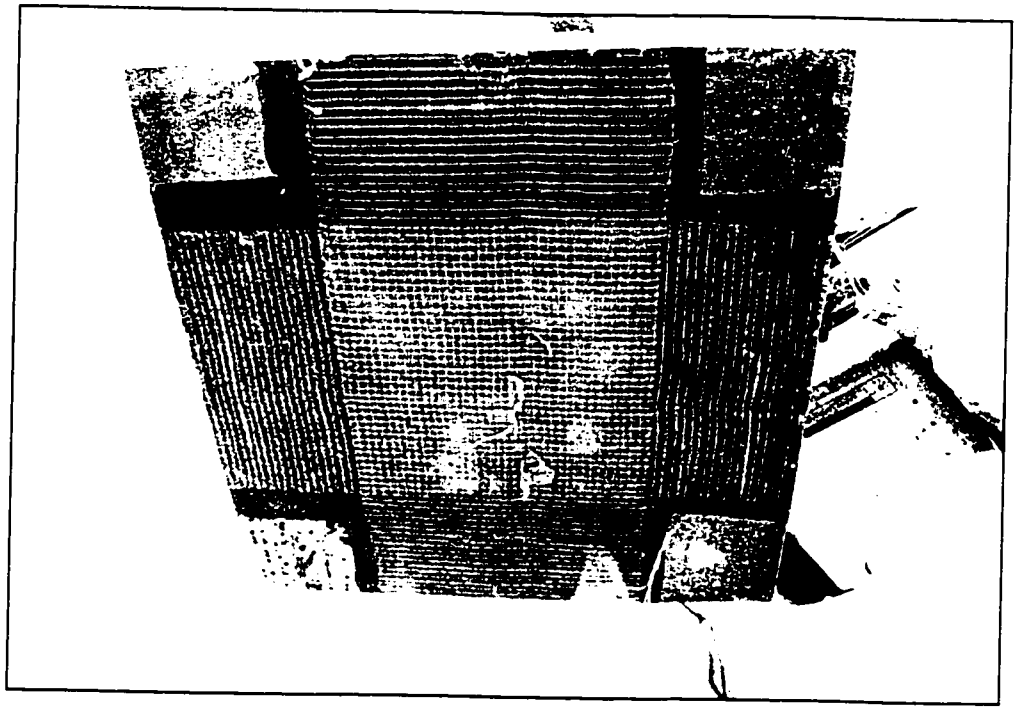

Figure 5.13: Bottom surface of Panel *GSS*$_1$ after a 22.4-kg shot

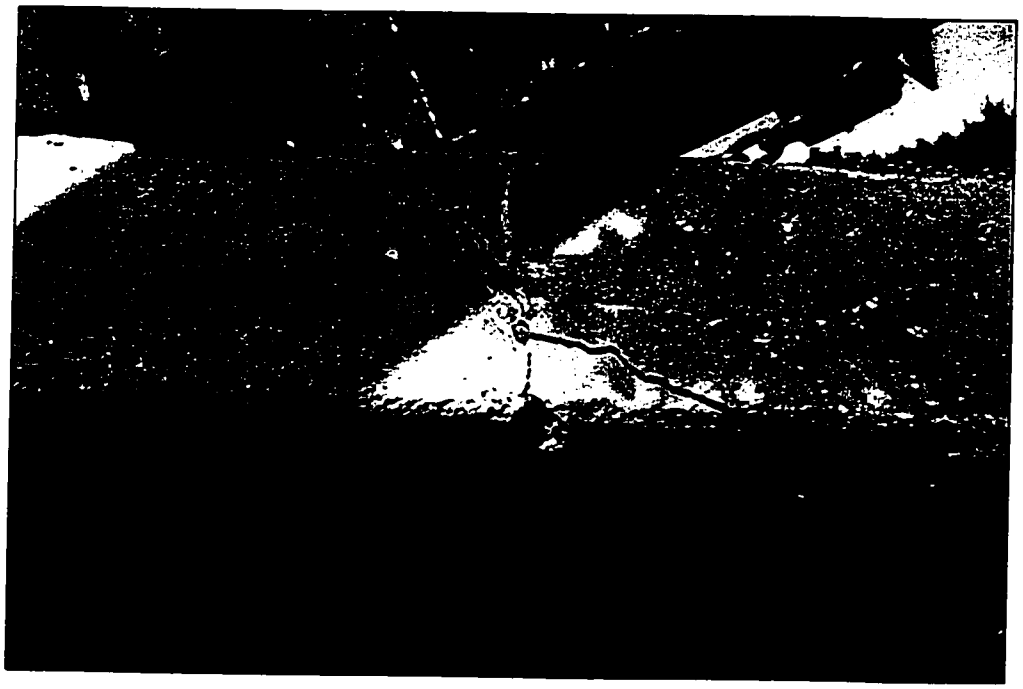

Figure 5.14: Side inverted shear cracks of Panel *GSS₃* after a 33.4-kg shot

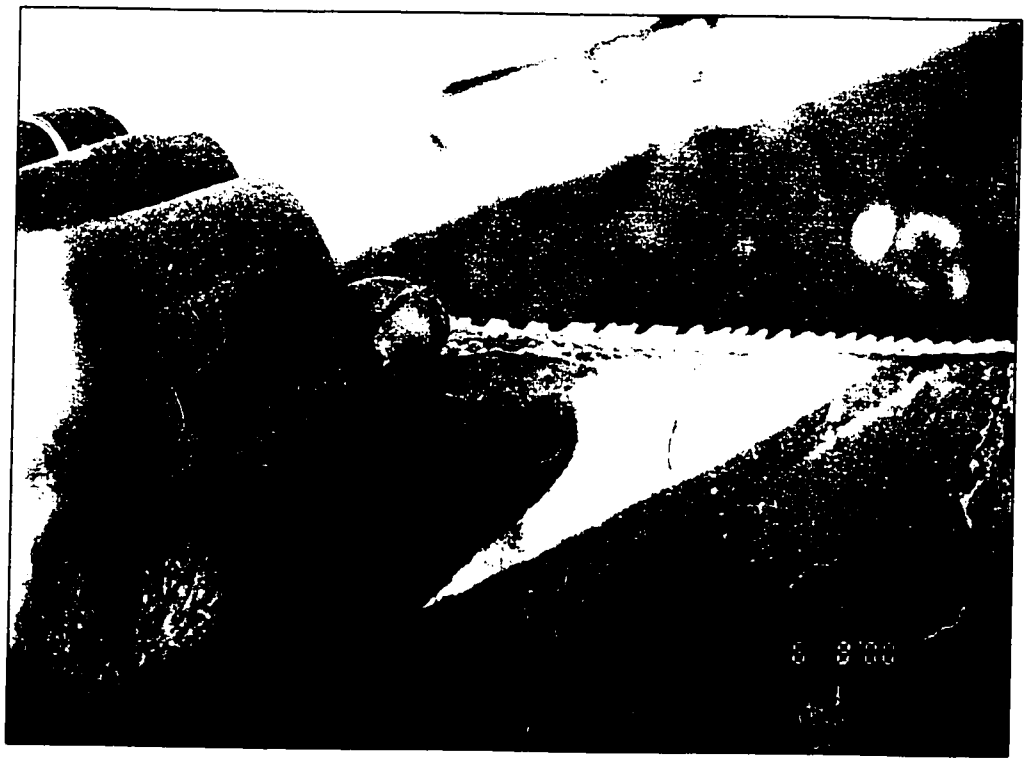

Figure 5.15: Delamination of glass Sheets along edges of Panel *GSS₃* after a 33.4-kg shot

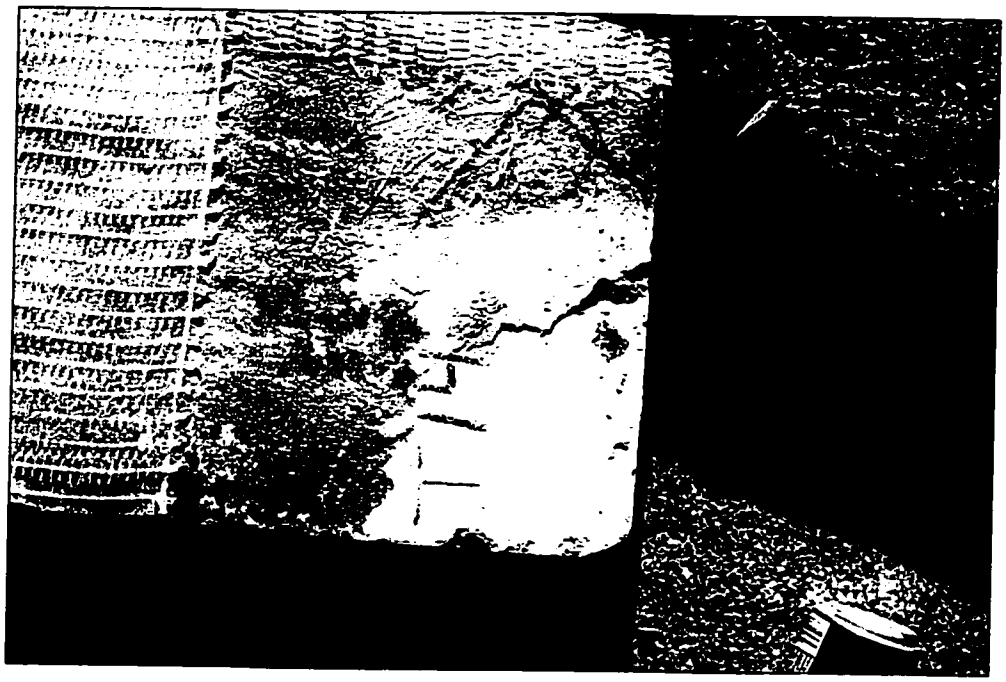

Figure 5.16: Tensile cracks of un-retrofitted corner region in Panel *GSS₄* after a 33.4-kg shot

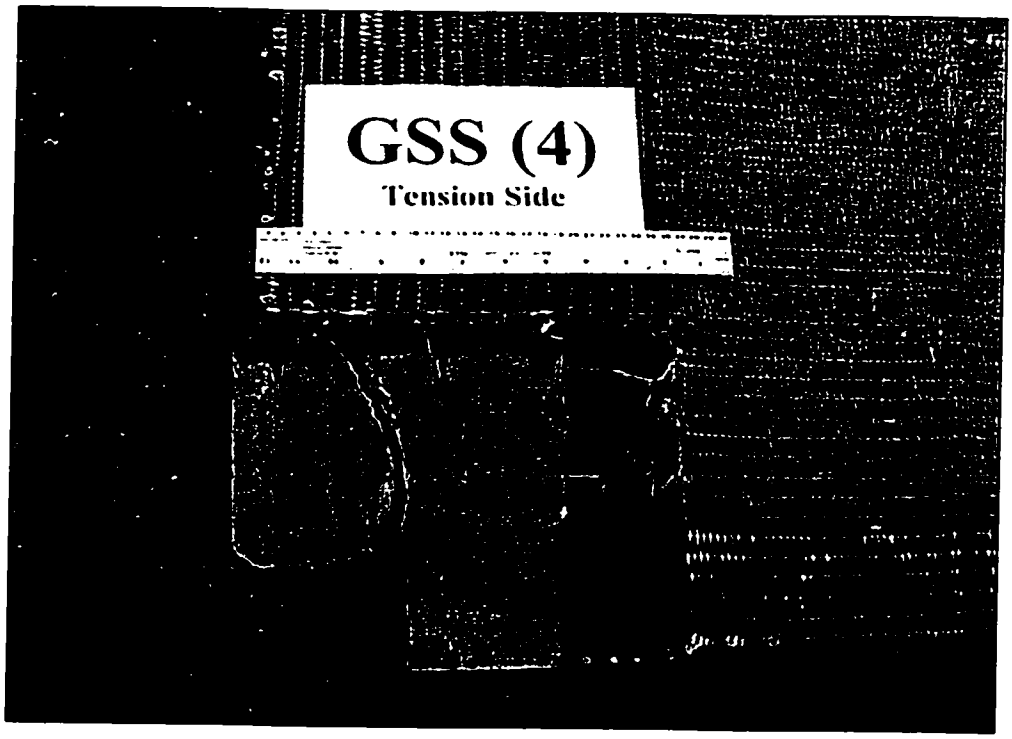

Figure 5.17: Local failure of un-retrofitted corner region in Panel *GSS₄* after a 33.4-kg shot

Unexpectedly complete crushing of specimen GSS_2 was observed when tested using 33.4-kg charge, which resulted in a reflected impulse of 1820 kPa.msec. Total failure accompanied by full delamination of the top glass sheet layers was observed. It was clearly noticed that the bond between the two glass layers was still effective, while bond failure occurred between the concrete surface and the glass sheets. This delamination likely occurred due to improper installation and/or poor epoxy resin properties. As the bond between the two glass sheet layers was still effective after the blast shot, the delamination could not be attributed to the poor quality of epoxy resin, thus it may be due to deficiencies in installation. This would explain the reason for the sheets delamination. It could be argued that due to the ineffectiveness of the sheets after their delamination, the substrate concrete failed.

Figures 5.18 through 5.20 show panel GSS_2 after exposure to 33.4-kg charge in blast test # 7. Figure 5.18 shows the test specimen in position after testing, where it can be noticed that delamination has occurred between the top glass sheets and the concrete that is held together by the bottom sheet layers and the steel reinforcement. In Figure 5.19, the test specimen is hoisted off the test frame to better demonstrate the extent of damage in this panel. Figure 5.20 shows the top surface, where concrete cover scabbing and crushing could be noticed.

Figure 5.18: Panel GSS_2 after a 33.4-kg shot (still in position)

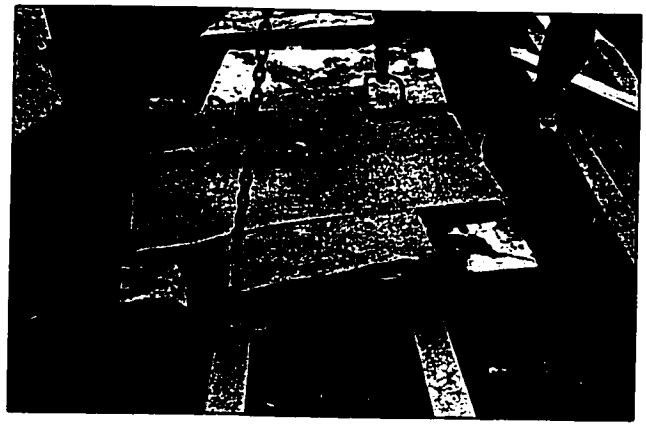

Figure 5.19: Panel GSS_2 after a 33.4-kg shot (Removing process)

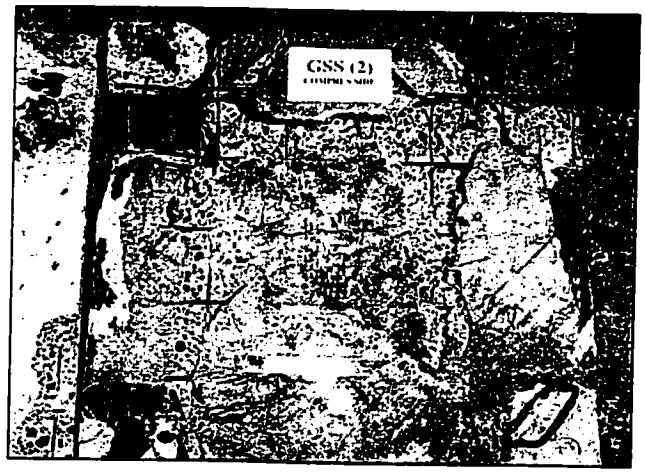

Figure: 5.20: Severe failure mode of Panel GSS_2 after a 33.4-kg shot

Results of Group (2)

Test results of Group (2) are shown in Tables 5.6 through 5.8. Table 5.6 shows the maximum measured strains, Table 5.7 shows the maximum recorded incident and reflected pressures as well as the impulse, and Table 5.8 shows the maximum measured mid-span deflections. If we compare the average reflected pressures in Table 5.7 with the same charge size average reflected pressures in Table 5.4, they are generally in good agreement. On the other hand, the relatively large difference between the average pressure values for specimen GSS_2 and GSS_3 signify the difficulty of achieving equal pressure under nominally similar test conditions. The same observation can be made with respect to the impulse values. Results of panel GSS_3 tested in blast shot 12 are graphically illustrated as being typical for this group.

Time-histories of strain in steel and GFRP layers are plotted in Figures 5.21 and 5.22, respectively. Noise traces and/or signal clip are recorded in some strain traces such as Figures 5.21 (b) and 5.22 (a), in which only the initial peak strain should be considered. From the strain results, it can be noticed that high strains, in the range of 11000~20000, in both the steel reinforcement and the GRP layers were captured in most tests. Most of the strain gauges again failed on the top surface, only gauge # 7 survived.

Pressure readings of panel GSS_3 in Table 5.7 are illustrated in Figure 5.23. The reflected gauge marked (P_{r4}) was removed, as it lost signal in most of the previous shots, and an incident pressure gauge was added and marked (FF_3) in order to study the effect of long distance on the incident pressure measurements. Pressure noise is shown in trace (P_{r3}) in Figure 5.23 (b), which showed trace clips after first or second clear pressure peak. The

incident pressures were recorded as 305 and 131 kPa, respectively. Reflected impulses were evaluated for the two reflected pressure readings as 1488 and 1495 kPa.msec, respectively. Mid-span deflection-time results are given in Table 5.8. A poor trace was obtained in test 12, while a maximum of 14.58 mm deflection was recorded in test # 7. Figure 5.24 shows the deflection history for Panel GSS_1. The results for other specimens are illustrated in Appendix C.

Table 5.6: Strain measurements of test Group (2)

Test No.	Sample	Charge Weight (kg)	Strain x 10^{-6} Channel 1	Channel 2	Channel 3	Channel 4	Channel 5	Channel 6	Channel 7	Channel 8
4	GSS_1	22.4	P	2375	1480	6500	10000	NC	P	P
7	GSS_2	33.4	1560	P	2000	P	10000	1875	P	NC
12	GSS_3	33.4	P	17000	20000	NC	750	P	14000	P
14	GSS_4	33.4	P	NC	11000	16000	9000	16000	8750	P

Table 5.7: Pressure and impulse of test Group (2)

Test No. & (Sample)	Incident Pressure (kPa) FF_1	FF_2	FF_3	Reflected Pressure (kPa) P_{r1}	P_{r2}	P_{r3}	P_{r4}	Average Reflected Pressure	Reflected Impulse (kPa.msec) I_{r1}	I_{r2}	I_{r3}	I_{r4}	Average Reflected Impulse
4 (GSS_1)	318	P	NU	4203	3858	3159	P	3741	1909	813	1309	NC	1344
7 (GSS_2)	418	170	NU	NC	3838	2281	P	3050	NC	2157	1488	P	1820
12 (GSS_3)	305	131	P	5215	NC	4489	NC	4995	1488	NC	1495	NC	1492
14 (GSS_4)	320	110	77	5030	4823	4951	NC	4933	2353	2050	2122	NC	2239

Table 5.8: Mid-span deflection of test Group (2)

Test No.	Sample	Charge Weight (kg)	Mid-Span Deflection (mm)
4	GSS_1	22.4	10.83
7	GSS_2	33.4	14.58
12	GSS_3	33.4	P
14	GSS_4	33.4	9.10

- Notes: C = Not Captured, P = Poor Trace, and NU = Not in Use

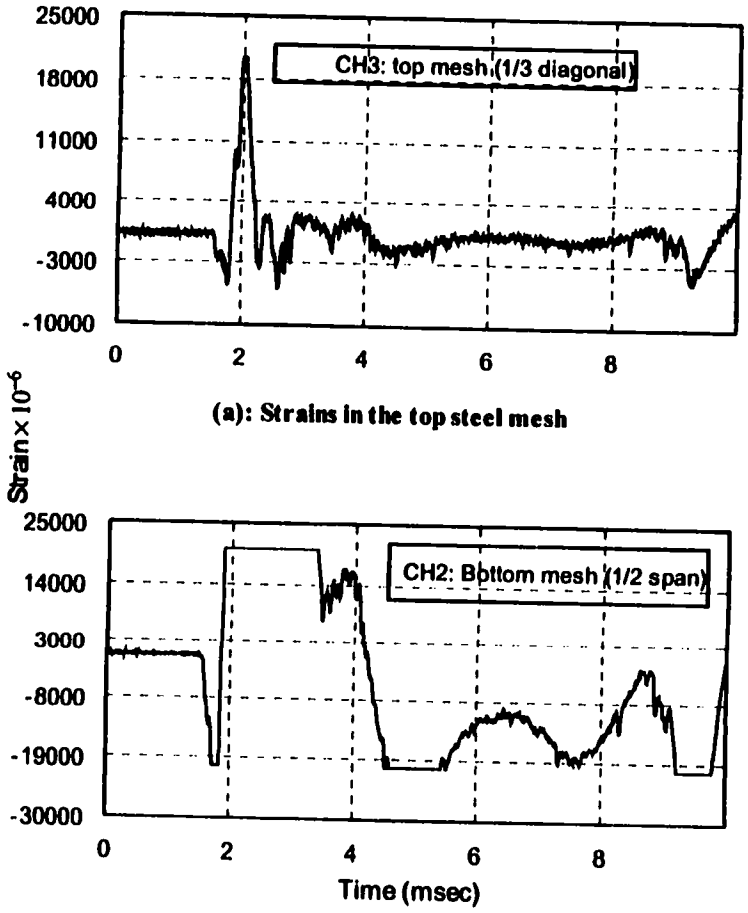

(a): Strains in the top steel mesh

(b): Strains in the bottom steel mesh

Figure 5.21: Strain-time profiles in steel meshes (Blast test # 12: Panel GSS3)

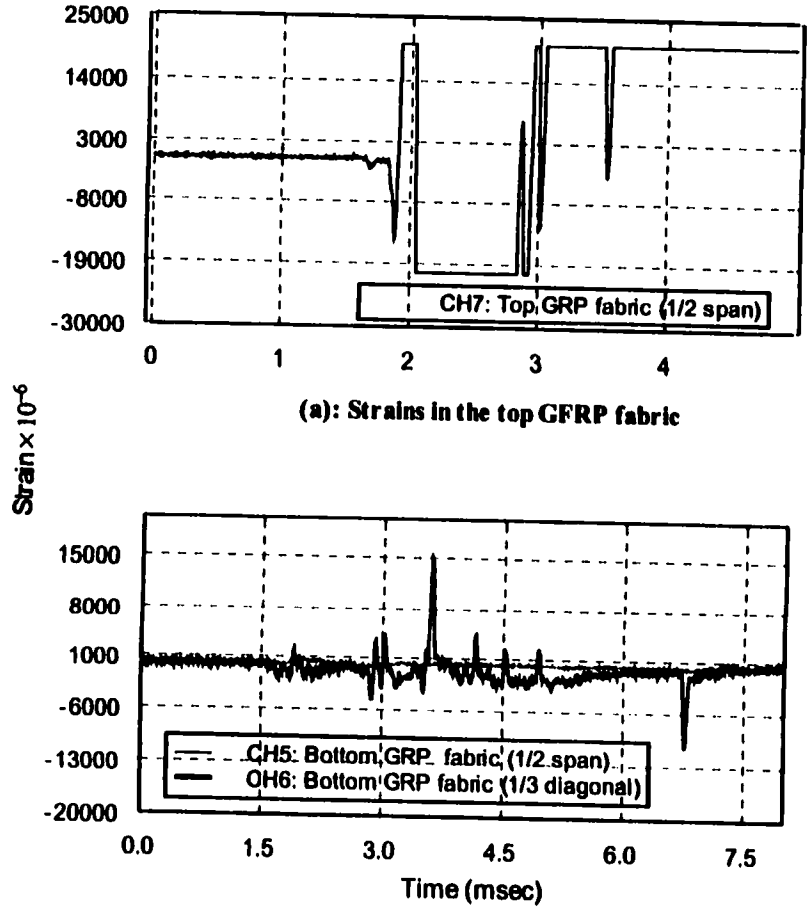

(a): Strains in the top GFRP fabric

(b): Strains in the bottom GFRP fabric

Figure 5.22: Strain-time profiles in the GFRP fabric (Blast test # 12: Panel GSS3)

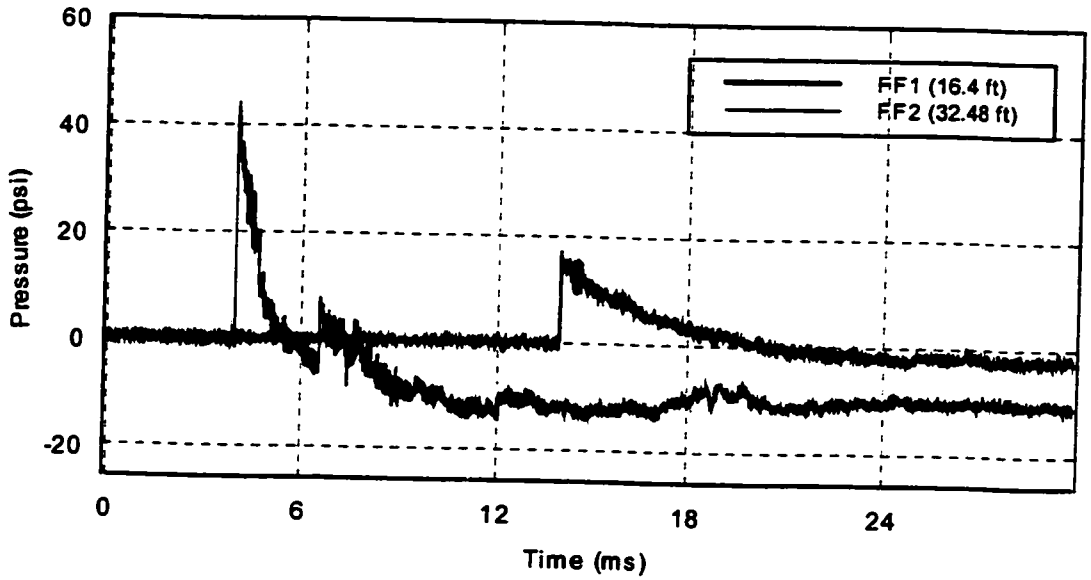

(a): Incident (free field) pressure-time profiles

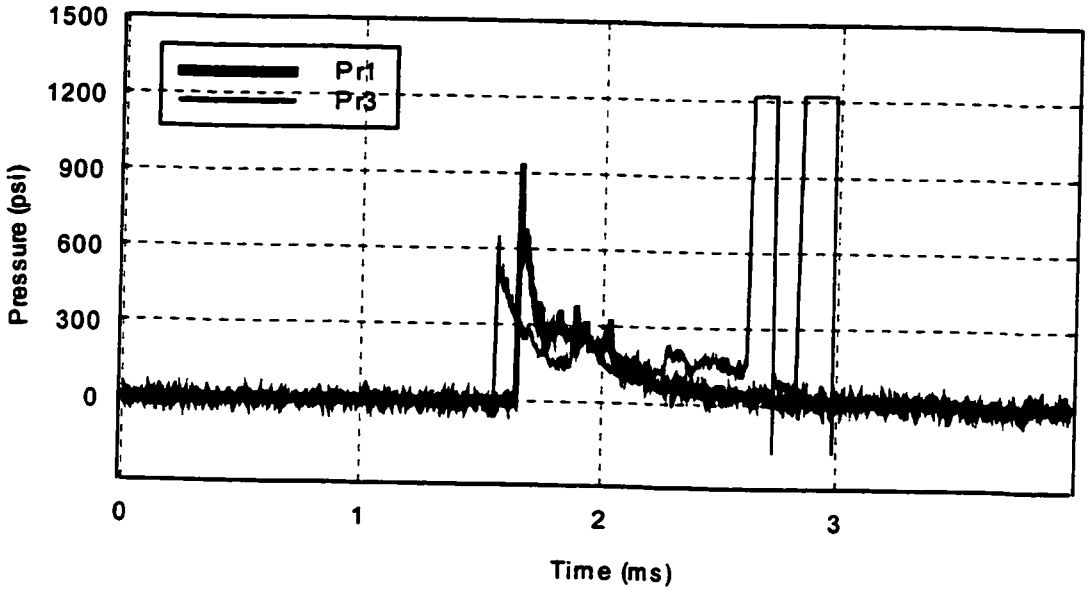

(b): Reflected pressure-time profiles

- 1 psi = 6.89 kPa.

Figure 5.23: Pressure-time profiles of blast test # 12 (Panel GSS3)

5.3.3 Test Group (3)

Four CFRP-retrofitted panels, ***CSS₁*** to ***CSS₄***, were tested in blast shots 5, 9, 11, and 13. The results are discussed below.

Structural Damage

Panel ***CSS₁***, subjected to 22.4 kg charge in test # 5 showed no light under a reflected impulse of 1581 kPa.msec. Only some surface cracks of width up to 0.2 mm were observed on the top and bottom un-retrofitted corners. Again, very fine inverted shear cracks were noticed on all four sides. There was no sign of sheet delamination or permanent deflection. This would reflect the expected structural behaviour, as the control specimen tested under the same charge weight (***CS₄***) exhibited moderate damage. Figures 5.24 and 5.25 show the effect of the 22.4 kg ANFO charge on the bottom surface of panel ***CSS₁***.

Test specimen ***CSS₂*** subjected to the effect of a reflected impulse of 1451 kPa.msec, produced by a 33.4-kg charge in blast test # 9 was moderately damaged, and did not show concrete failure or permanent deflection. Its top surface retained a sound bond with the carbon sheet layers, while sheet rupture of 200 mm was noticed on the bottom surface. Some inclined hairline cracks were observed in the four unretrofitted corners. Some peel-off of the sheets wrapped around concrete sides was also noticed. Figure 5.26 shows the damage to Panel ***CSS₂***. Inverted shear cracks appeared on the four sides, while minor concrete scabbing (50 mm length) was observed on the top surface. Also, sheet rupture at the bottom was noticed.

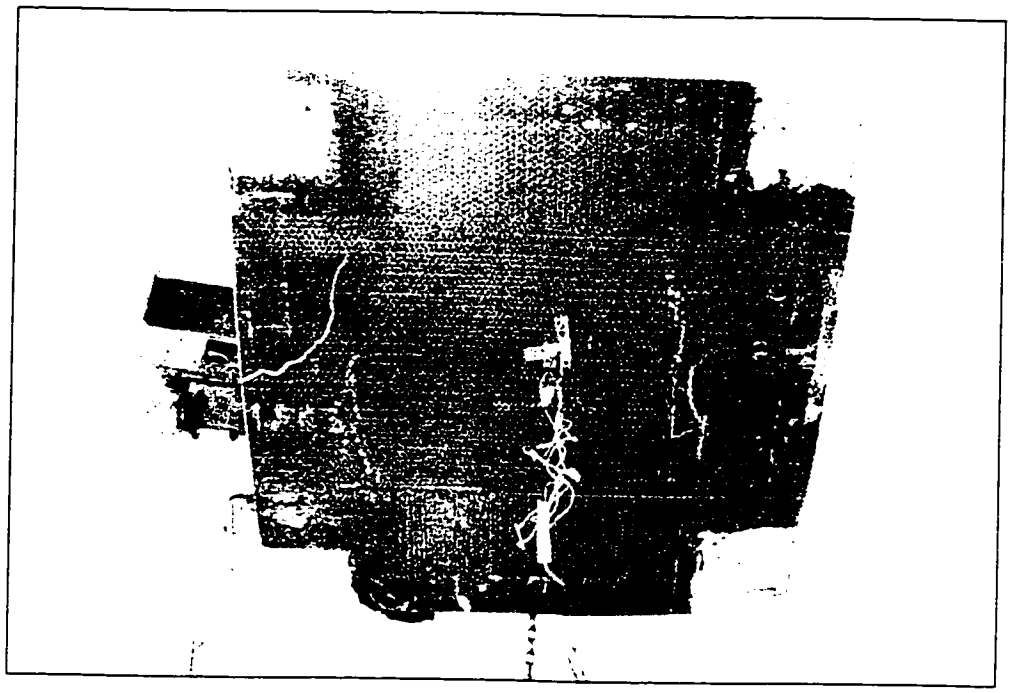

Figure 5.24: Bottom surface of Panel CSS_1 after a 22.4 kg shot

Figure 5.25: Tensile hairline cracks at the uncovered squares of Panel CSS_1 after a 22.4 kg shot

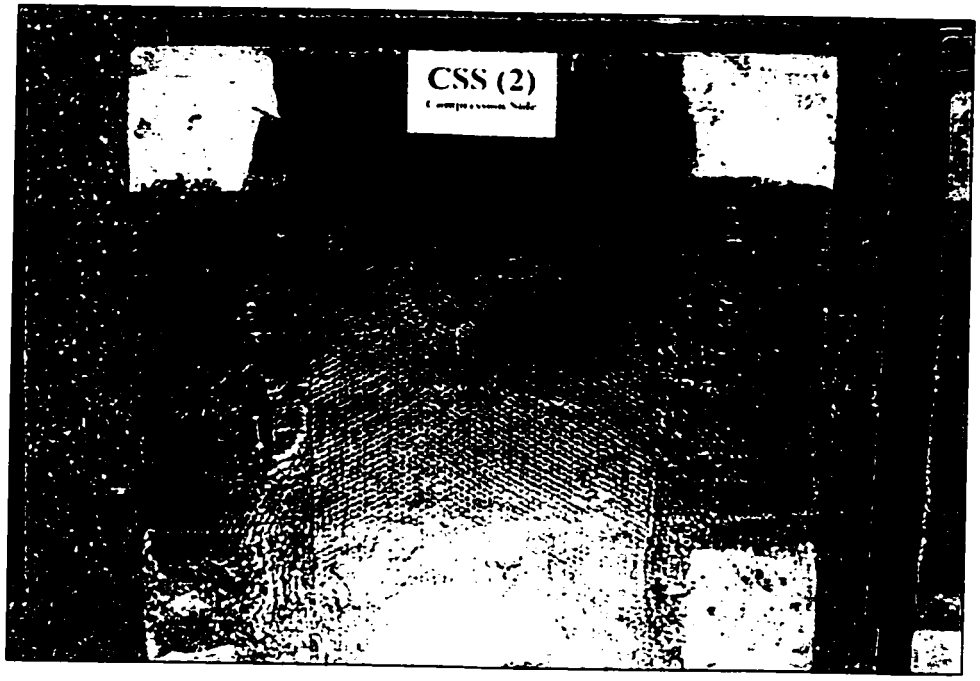

(a)

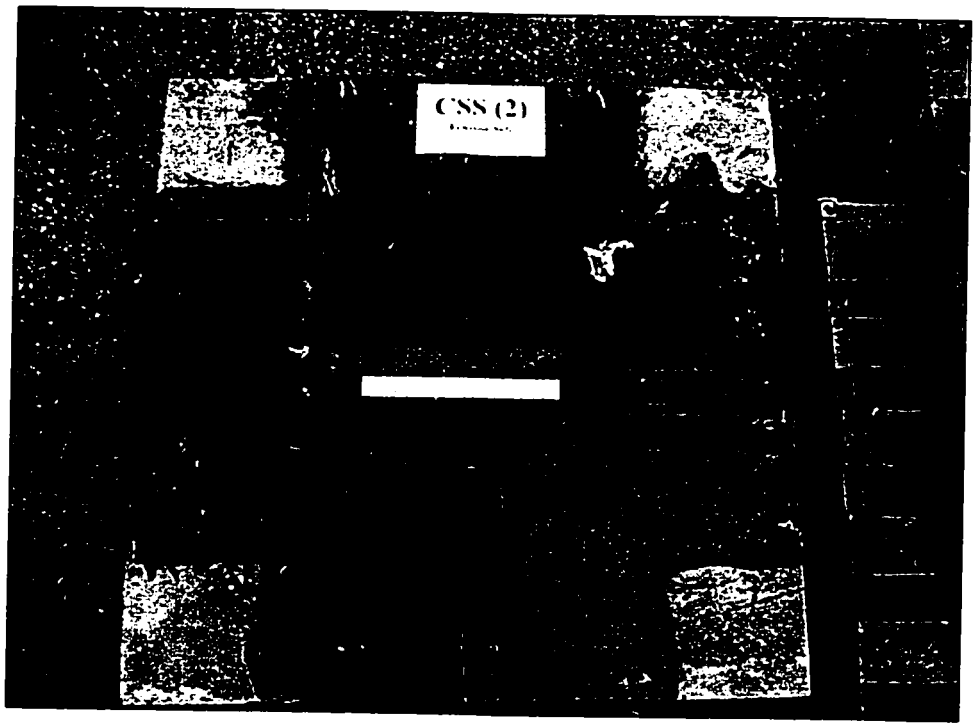

(b)

Figure 5.26: Panel *CSS*$_2$ after a 33.4 kg shot
(a): Top surface, and (b):Bottom surface

A similar structural behaviour was observed upon testing panel CSS_3 using a 33.4-kg charge, which produced a reflected impulse of 1723 kPa.msec. Carbon sheets showed good bond with the concrete surfaces, and no permanent deflection was recorded. The same inverted shear crack pattern, as described earlier, was formed on the four sides of the panel. On the bottom surface, wider cracks (1~2 mm) in the four uncovered corner regions were noticed. In addition, noticeable damage to the carbon sheets was observed. Compression and tension failure patterns of panel CSS_3 are shown in Figure 5.27.

Panel CSS_4 showed more structural damage than panels CSS_2 and CSS_3, even though it was subjected to the same charge weight (33.4 kg of ANFO) as the latter panels. The reflected impulse in this test was 1902 kPa.msec, compared to 1451 kPa.msec for panel CSS_2 and 1723 kPa.msec for panel CSS_3. At the top surface, concrete crushing in the four unretrofitted corners occurred, and a permanent deflection of 5 mm was recorded. Shear cracks of up to 2.0 mm wide were also noticed. At the bottom surface, carbon sheets were laterally (along the supporting edge) and longitudinally severed. However, the bottom carbon sheets remained bonded, holding the concrete pieces together and preventing concrete fragmentation. Although Panel CSS_4 showed more severe failure than the other two panels, its failure mode had the same basic pattern as the previous two panels. The difference in behaviour might be due to the higher impulse that this panel was subjected to. The failure patterns for the compression and tension surfaces of panel CSS_4 are shown in Figure 5.28.

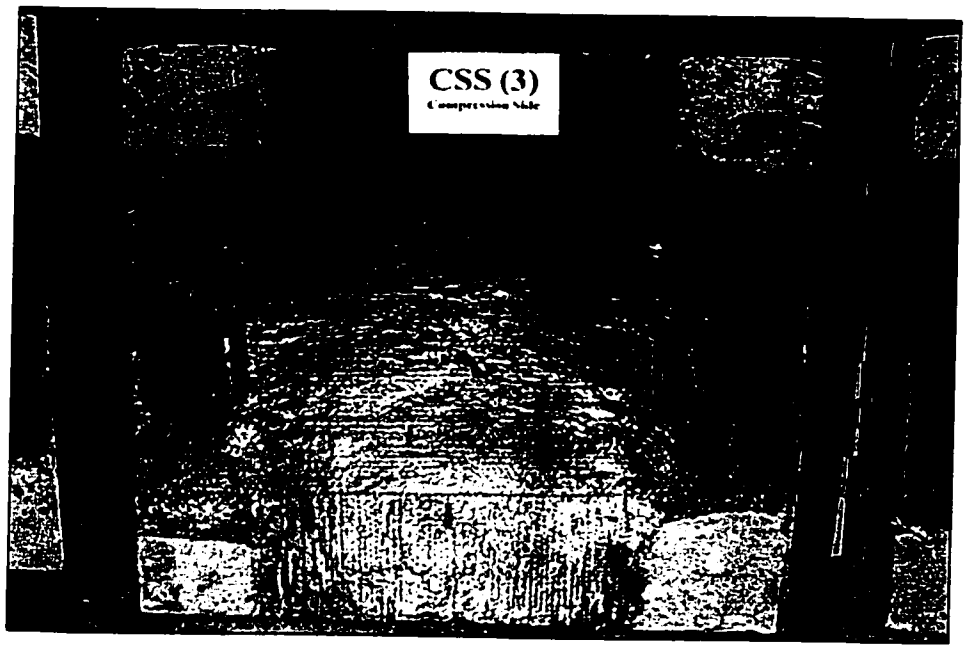

(a)

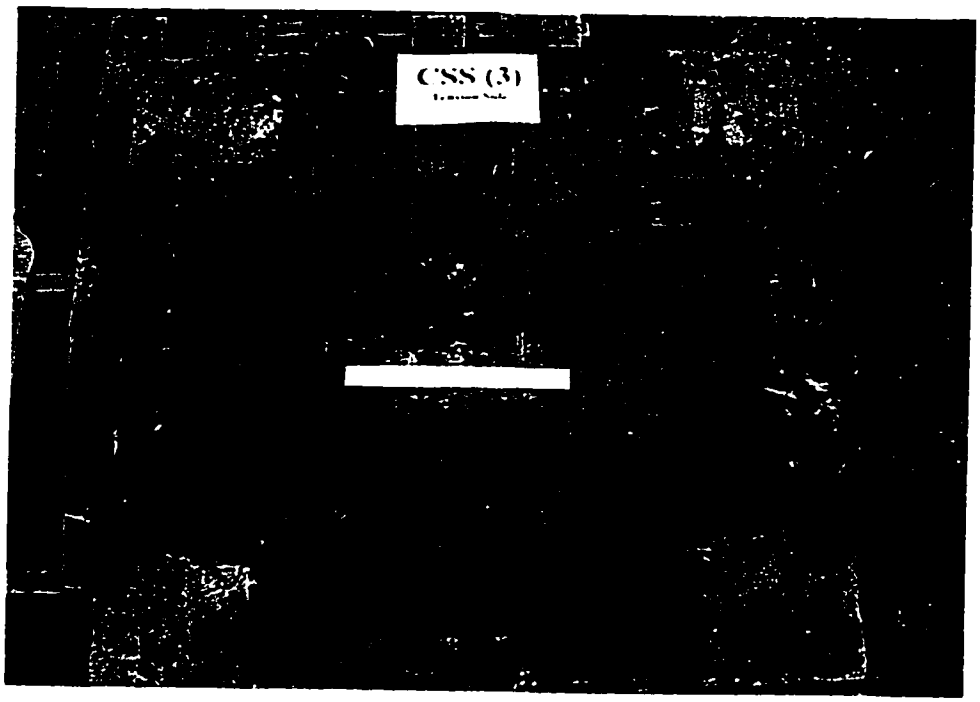

(b)

Figure 5.27: Panel *CSS*$_3$ after a 33.4 kg shot
(a): Top surface, and (b):Bottom surface

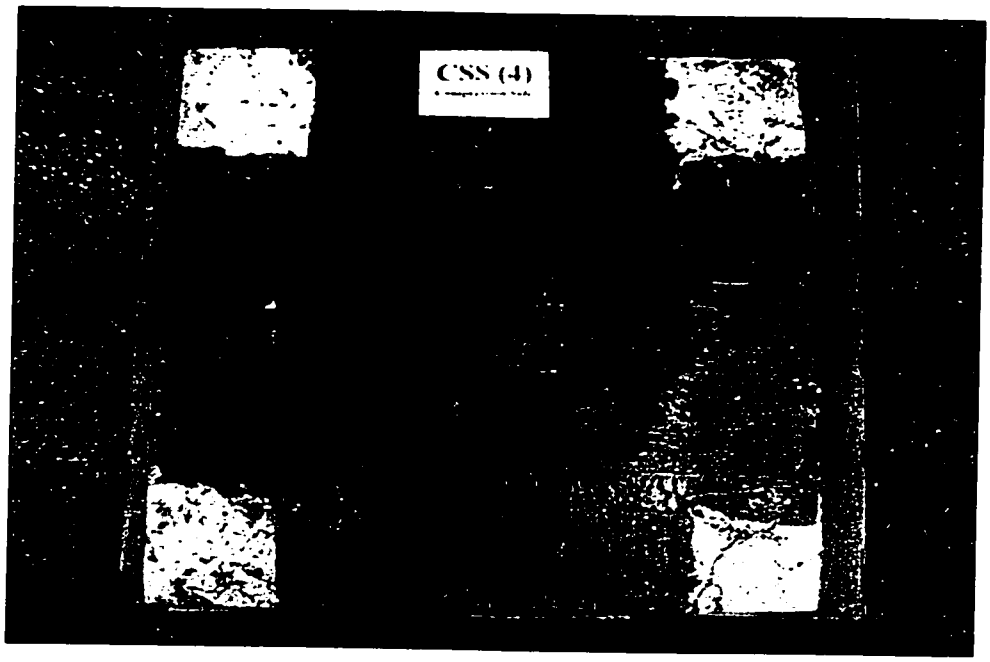

(a)

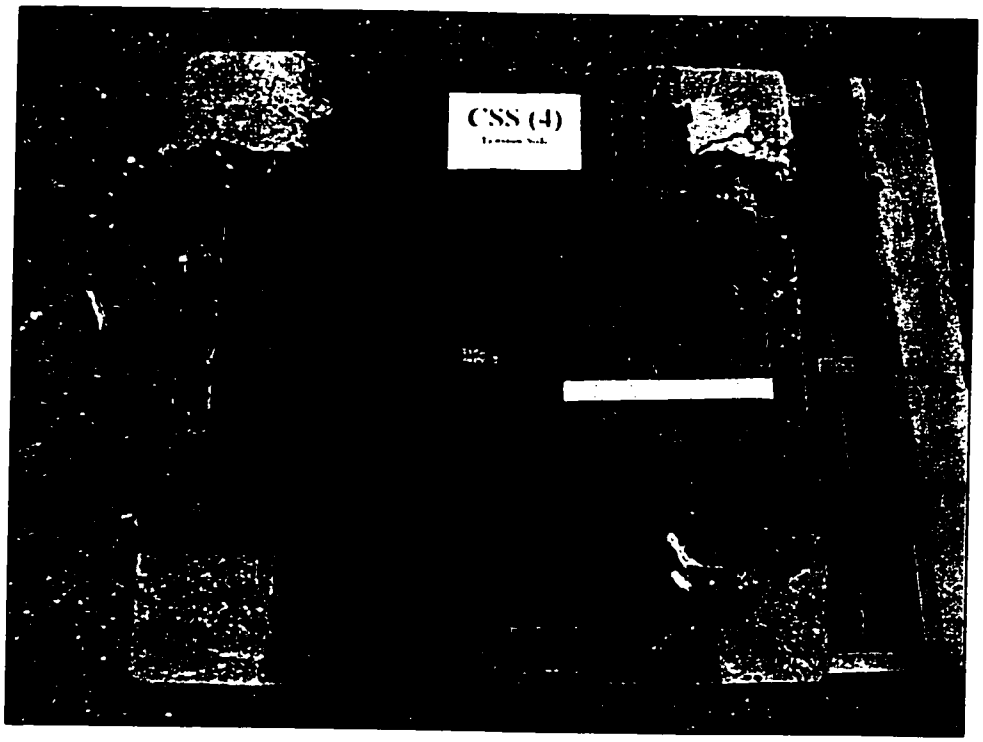

(b)

Figure 5.28: Panel *CSS*, after a 33.4 kg shot
(a): Top surface, and (b):Bottom surface

Results of Group (3)

Tables 5.9 to 5.11 show the measured experimental data for Group (3) as recorded in the field, including strains, pressures, impulses and mi-span deflections. Detailed recorded time histories are given in Appendix C.

Strain measurements are given in Table 5.9, where we observe that data was collected at most gauge locations. Nevertheless, because of the reasons previously mentioned, some noise and poor traces were still recorded. High strain values were recorded in both the reinforcement and in the CFRP layers (as high as 20000 μstrain). Low strains are measured in some tests, such as in test 11 (Gauge # 6 read 750 μstrain). These low values may be ignored. The high strain values in CSS_3 and CSS_4 are particularly noteworthy, for these specimens experienced extensive damage.

Pressures were recorded throughout the four blast shots of Group (3). Again, incident pressure showed more reliable records than reflected pressures. The reason is that the reflected pressure transducers were fixed to relatively small steel plates, and the soil around them was not adequately compacted. This was rectified starting with blast shot 10 by compacting the soil around the transducers. As a result, acceptable pressure differences between the four reflected pressure readings were recorded. This will be discussed and compared with CONWEP predictions in the following chapter. Reflected impulses are recorded as 1581, 1451, 1723, and 1902 kPa.msec. The first reading was for a 22.4-kg charge, while the rest were for 33.4-kg charge. Reflected impulses for the last two tests (11 and 13) showed good agreement. Table 5.10 shows pressure and impulse for Group (3) tests.

Deflections at mid-span are shown in Table 5.11. A maximum deflection of 13.85 mm was recorded in test 11, while a poor trace for blast test # 13 was obtained. The maximum deflection value in all the tests appear to be in basically the same range. This indicates that the displacement transducer was functioning properly.

Table 5.9: Strain measurements of test Group (3)

Test No.	Sample	Charge Weight (kg)	Strain x 10^{-6} Channel 1	Channel 2	Channel 3	Channel 4	Channel 5	Channel 6	Channel 7	Channel 8
5	CSS_1	22.4	2215	P	2280	P	8300	NC	P	NC
9	CSS_2	33.4	NC	NC	1875	6400	NC	20000	NC	NC
11	CSS_3	33.4	2550	2930	1000	10000	4280	600	NC	NC
13	CSS_4	33.4	NC	5900	2800	800	8650	20000	NC	NC

Table 5.10: Pressure and impulse of test Group (3)

Test No. & (Sample)	Incident Pressure (kPa) FF_1	FF_2	Reflected Pressure (kPa) P_{r1}	P_{r2}	P_{r3}	P_{r4}	Average Reflected Pressure	Reflected Impulse (kPa.msec) I_{r1}	I_{r2}	I_{r3}	I_{r4}	Average Reflected Impulse
5 (CSS_1)	344	P	4492	3552	2708	NC	3517	1089	1857	2102	NC	1681
9 (CSS_2)	373	P	5877	5591	3114	5201	4946	1578	1509	1554	1220	1451
11 (CSS_3)	550	138	5581	4754	5719	NC	5347	1847	1743	1585	NC	1723
13 (CSS_4)	320	138	4947	NC	5105	NC	5026	1488	NC	2322	NC	1902

Table 5.11: Mid-span deflection of test Group (3)

Test No.	Sample	Charge Weight (kg)	Mid-Span Deflection (mm)
5	CSS_1	22.4	10.83
9	CSS_2	33.4	11.58
11	CSS_3	33.4	13.85
13	CSS_4	33.4	9.58

- Notes: NC = Not Captured, P = Poor Trace, and NU = Not in Use

5.3.4 Test Group (4)

Diagonal carbon FRP strips were applied to both surfaces of test Group (4), akin to X-bracing. Test panels CLS_1 through CLS_4 were tested in blast shots 3, 6, 10, and 16, respectively. Presentation of test results is given below, and detailed graphical illustrations are shown in Appendix C.

Structural Damage

Panel CLS_1 was tested using 22.2 kg charge, which produced 1220 kPa.msec reflected impulse, and its inspection after the test showed neither delamination, nor permanent deflection, nor concrete spalling. Hairline cracks were noticed on both the top and bottom surfaces. Inverted fine shear cracks were also visible on all four panel sides. A wider system of surface cracks (up to 0.2 mm) was noticed on the bottom surface. Figure 5.29 shows both surfaces of panel CLS_1 after the 22.4-kg shot.

Panels CLS_3 and CLS_4 were tested using 33.4 kg charges in tests 10 and 16, and showed almost the same heavy damage. Reflected impulses were recorded as 1592 and 1743 kPa.msec for the two tests, respectively. On their top surfaces, local punching was observed in the form of a circular area, covering about 3/4 the panel surface, accompanied by a permanent deflection of about 5 mm. Surface cracks of up to 1.0 mm width were formed, along with inverted shear cracks on the four sides. On the top surface, cracks seemed to continue underneath the carbon strips, but the strips did not appear to have delaminated. On the bottom surface, in one case the carbon strips completely delaminated while in the other cases it partially delaminated (notice separation of the bottom strips in Panel CLS_3).

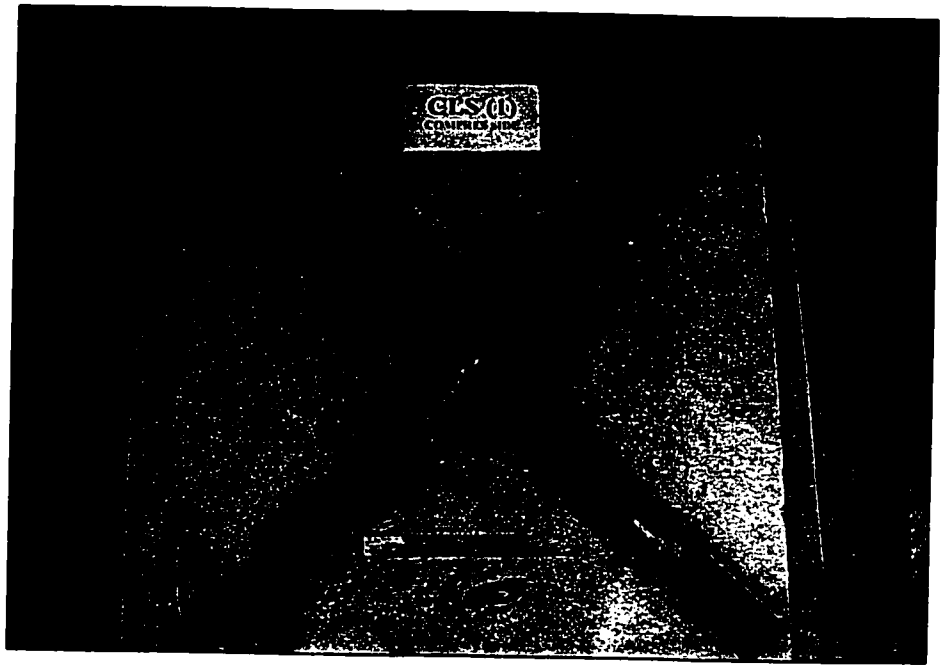

(a)

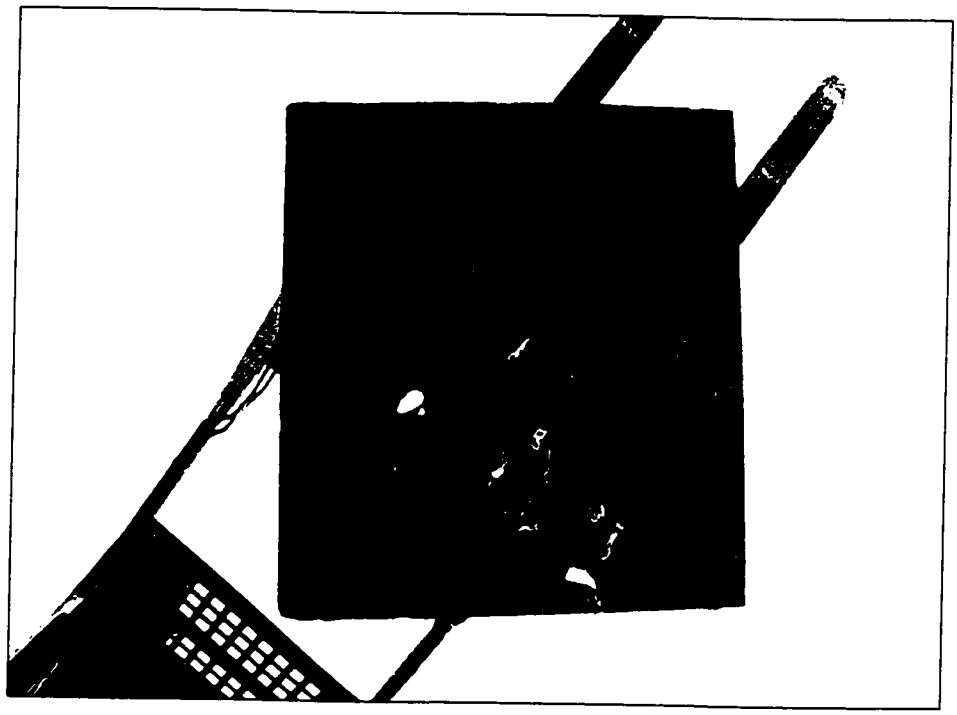

(b)

Figure 5.29: Panel *CLS*$_l$ after a 22.4 kg shot
(a): Top surface, and (b): Bottom surface

The delamination was accompanied by spalling of tension face concrete cover to a depth of about 5 mm, and wide tension cracks (2 mm). Figure 5.30 shows the process of taking panel CLS_3 out of the supporting frame, notice the separation of the bottom strips and the concrete cover spallation after testing. Also, Figure 5.31 shows the failure modes of both the top and the bottom surfaces of panel CLS_4, where a close similarity between the failure modes of the two panels is observed.

Panel CLS_2 was severely damaged by the detonation of 33.4-kg charge in test 6. A high reflected impulse of 2245 kPa.msec was recorded, which indicates a 35 % load increase for this test compared to tests 10 and 15 where the same charge weight was used. On the top surface, carbon strips peeled-off for lengths of 500 mm in both directions. A wide system of surface cracks (up to 3.0 mm) was visible, and 1.8 mm permanent deflection was measured. On the bottom surface, carbon strips completely peeled-off, and even wider surface cracks (up to 5 mm) appeared. Shear cracks on the four sides were noticed with a maximum width of 2 mm. The damaged surfaces of panel CLS_2 are illustrated in Figure 5.32.

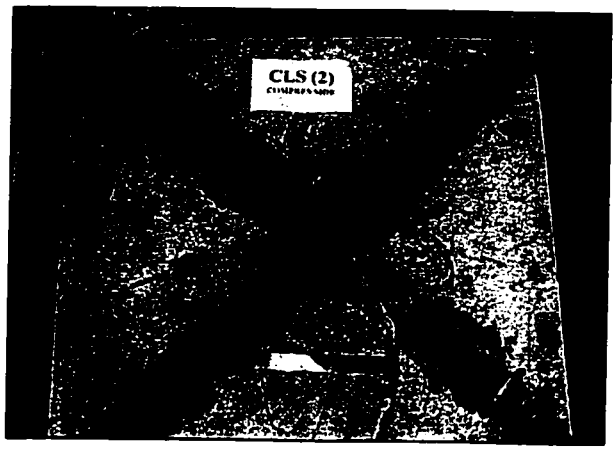

(a)

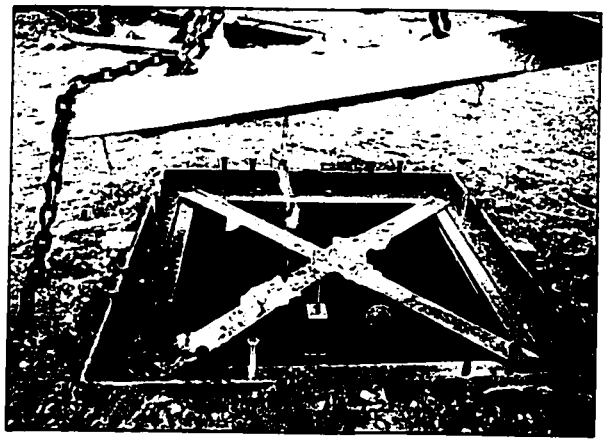

(b)

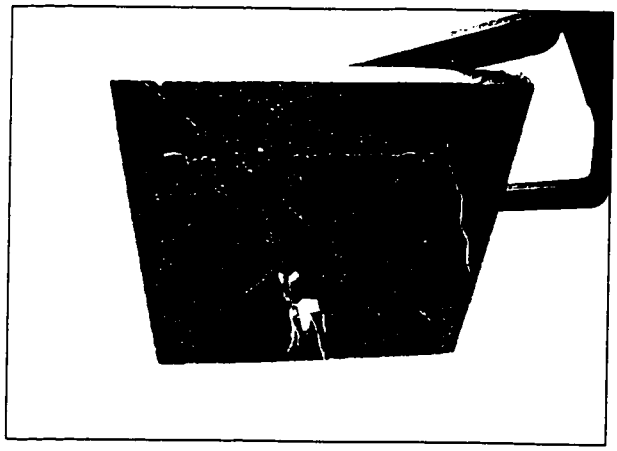

(c)

Figure 5.30: Panel *CLS₃* after a 33.4 kg shot
(a): Top surface, (b): Laminate separation, and (c): Bottom surface

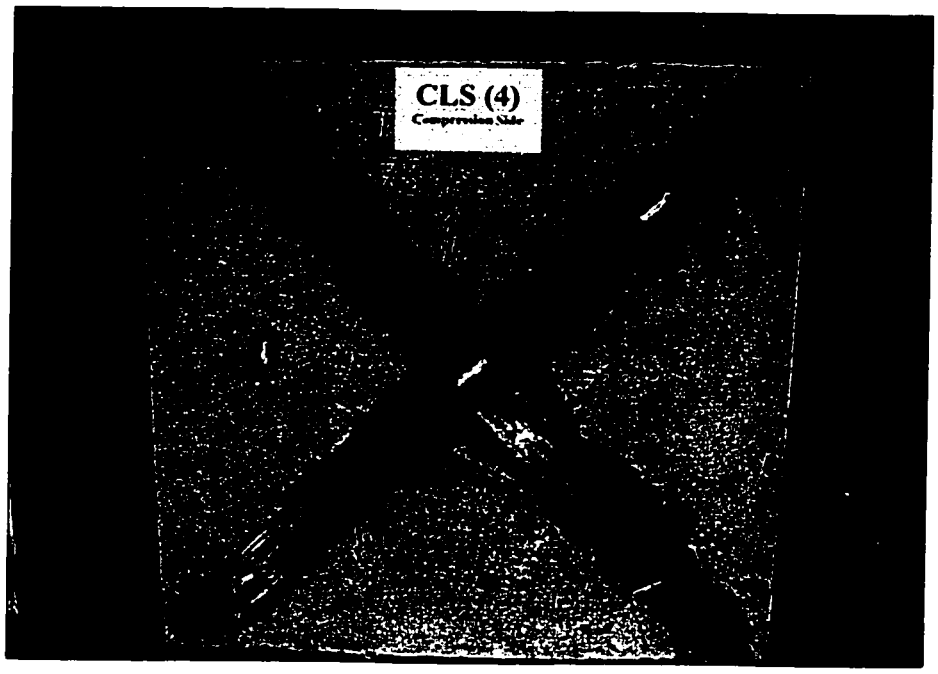

(a)

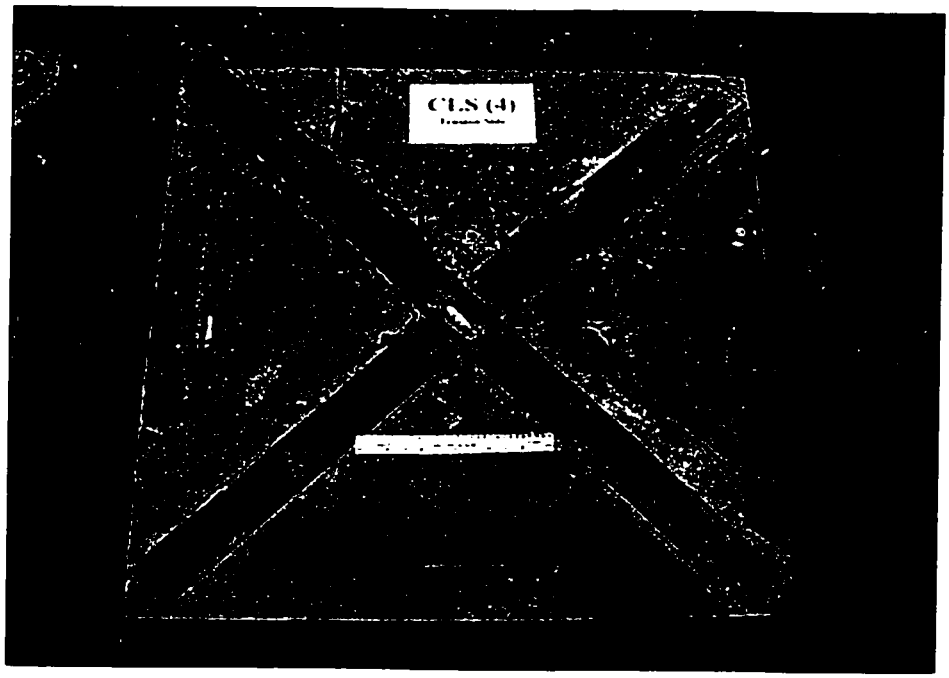

(b)

Figure 5.31: Panel *CLS₄* after a 33.4 kg shot
(a): Top surface, and (b): Bottom surface

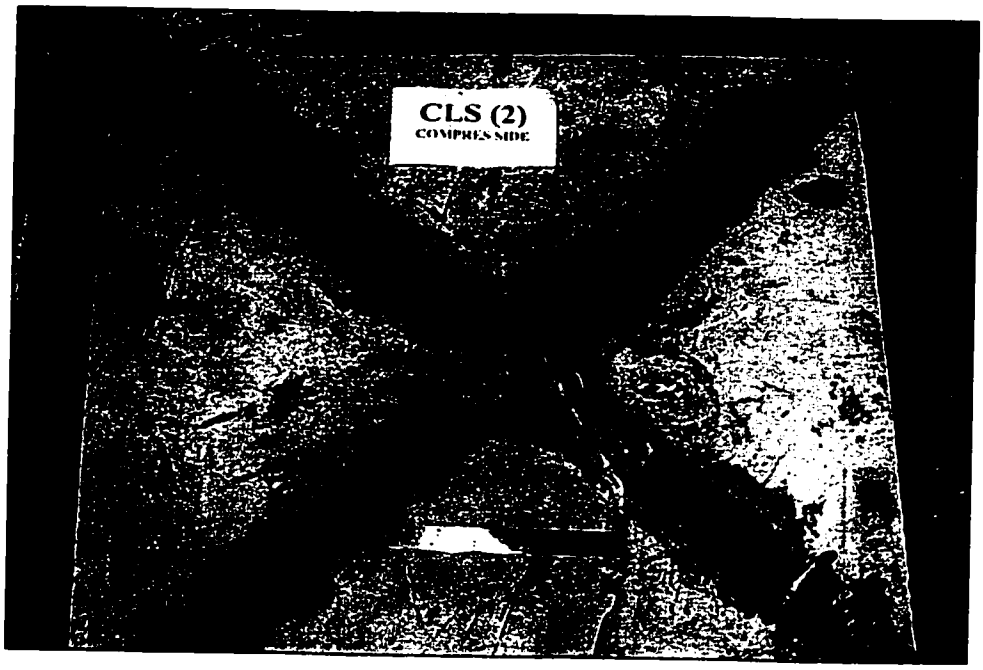

(a)

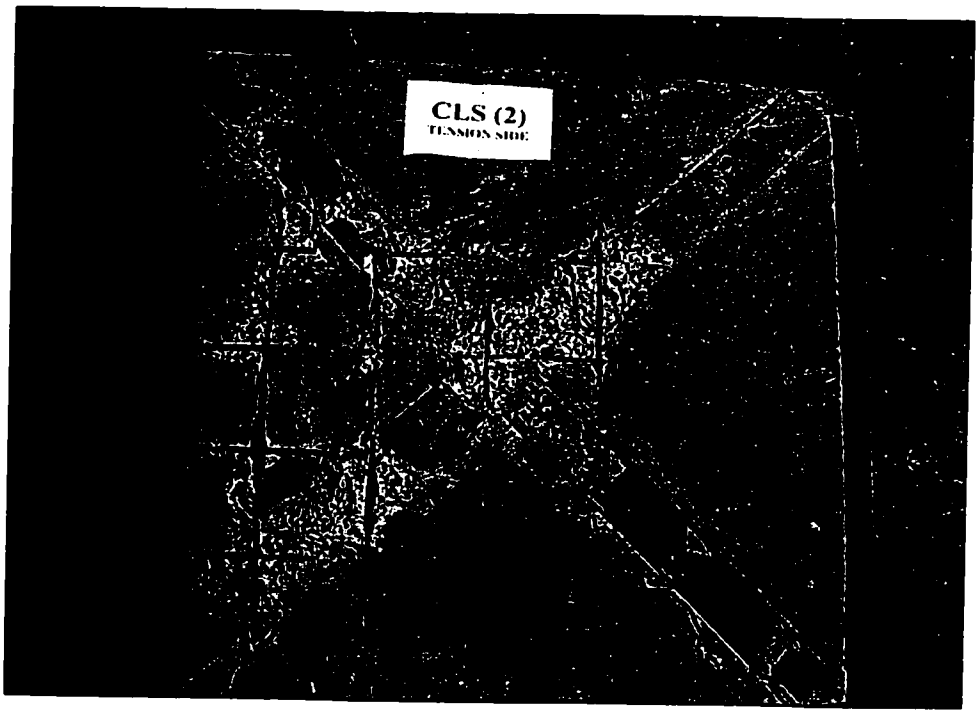

(b)

Figure 5.32: Panel CLS_2 after a 33.4 kg shot (a): Top surface, and (b): Bottom surface

Results of Group (4)

Tables 5.12, 5.13 and 5.14 show the measured parameters through out testing group 4 as recorded in the field including strains, pressures, impulses and mid-span deflections. Plots will be given in Appendix C. Reinforcement and strip surface strain measurements are given in Table 5.12, where high strains were recorded for both reinforcements (up to 20000 μstrain) and the carbon strip surfaces (as high as 10000 μstrain). In addition, it was possible to record strains from the top surface in test 10.

Complete pressure readings were recorded throughout the four blast shots. Secondary pressure peaks are recognized in some tests, followed by two successive similar peaks. The former pressure peak has occurred due to the ground reflection, while the latter peaks were due to reflection of the pressure waves upon hitting the side hills. Reflected impulses were recorded during the four tests as 1220, 2245, 1592, and 1743 kPa.msec, respectively (see Table 5.13). Although blast test # 6 was conducted using the same charge (33.4 kg) as tests 10 and 16, a much higher reflected impulse was obtained. This may be the reason for the total failure of panel CLS_2 tested in this blast shot.

The mid-span deflection-time profiles of Group (4) are shown in Table 5.14. A maximum value of 12.8 mm was recorded in blast test # 6 (panel CLS_2). In tests 5 and 16, after occurrence of the first deflection peak, traces were opened and did not return to zero (see Appendix C for full graph presentation).

Table 5.12: Strain measurements of test Group (4)

Test No.	Sample	Charge Weight (kg)	Strain x 10^{-6} Channel 1	Channel 2	Channel 3	Channel 4	Channel 5	Channel 6	Channel 7	Channel 8
3	CLS_1	22.4	3440	3440	3850	2500	P	P	1500	2200
6	CLS_2	33.4	1150	5100	1220	P	5350	7200	P	P
10	CLS_3	33.4	P	4700	10000	P	10000	P	2350	9300
16	CLS_4	33.4	P	15000	20000	2700	800	P	P	P

Table 5.13: Pressure and impulse of test Group (4)

Test No. & (Sample)	Incident Pressure (kPa) FF_1	FF_2	Reflected Pressure (kPa) P_{r1}	P_{r2}	P_{r3}	P_{r4}	Average Reflected Pressure	Reflected Impulse (kPa.msec) I_{r1}	I_{r2}	I_{r3}	I_{r4}	Average Reflected Impulse
3 (CLS_1)	511	P	2855	NC	3238	NC	3052	1350	NC	1047	NC	1220
6 (CLS_2)	389	P	NC	5554	5953	NC	5753	NC	2425	2057	NC	2245
10 (CLS_3)	295	135	5340	5158	3995	NC	4830	1840	1730	1220	NC	1592
16 (CLS_4)	255	113	5525	5455	5808	NC	5502	1550	1915	1557	NC	1743

Table 5.14: Mid-span deflection of test Group (4)

Test No.	Sample	Charge Weight (kg)	Mid-Span Deflection (mm)
3	CLS_1	22.4	9.15
6	CLS_2	33.4	12.8
10	CLS_3	33.4	11.87
16	CLS_4	33.4	P

- Notes: NC = Not Captured, P = Poor Trace, and NU = Not in Use

5.4 Failure Criterion and Overall Behaviour

Failure of the test panels is assumed to be governed by the level of strain in the reinforcing steel. This was found to be a reasonable means of determining failure when crack propagation could not be traced or in the case of insufficient energy produced by small-charge blast tests (Long, 1968 and Olson, 1991). Test specimens are said to have failed if their reinforcement strain exceeds yield strain by a factor of 4~5. One challenging task was to save reinforcement strain gauges from damage during concrete casting, and to keep the top surface gauges in position following the arrival of incident shock waves. In spite of these difficulties, strain signals were recorded from 65 % of the reinforcement gauges and from 51 % of surface strain gauges. Most of the lost surface gauges were on the top surface, where they faced the incident pressure waves, and their connecting wires peeled-off before capturing strain signals. The failure criterion will be based on two parameters, the maximum strain captured and the panel state after blast. If a retrofitted panel reached high reinforcement and/or surface strain, and at the same time did not fail, i.e. possessed residual strength, this will be used as proof of the effectiveness of the particular retrofitting technique.

For the same charge weight, the test results revealed that the FRP-retrofitted panels had more integrity and better capability to withstand blast pressure than the control panels. The following sections present comparison between the structural behaviour of the different test groups subjected to the same charge weight, which in general is expected to produce theoretically the same pressure and impulse. Comparisons include damage threshold, crack width and pattern on concrete surfaces, permanent deflection, and the general physical appearance of the FRP layers. Special attention will be given to damage

threshold as an important factor in assessing the vulnerability of blast-loaded target structures under a certain blast pressure. Damage threshold can be simply defined as the maximum blast pressure that a specific target can survive, and above which it will fail (Hinman and Hammound, 1997).

5.4.1 Panels tested using 22.4-kg charge

The control unretrofitted panel CS_4 and the FRP-retrofitted panels GSS_1, CSS_1, and CLS_1 were tested using 22.4-kg charges. The average reflected impulses in the four tests were evaluated as 571, 1344, 1681, and 1220 kPa.msec, respectively. The reflected impulse 571 kPa.msec is very low and most likely unreliable, and therefore will not be considered. The low impulse indicates improper gauge records, for the other three tests, an acceptable difference of about 15 % in reflected impulse values exists.

Control Panel CS_4, despite the apparently low reflected impulse, partially failed with a permanent deflection of 2.0 mm and minor concrete spalling on the bottom surface. On the other hand, under even higher reflected impulse levels, the three retrofitted panels displayed no failure, no concrete spalling, and no permanent deflection.

Surface cracks of average width varying between 0.2 and 1.0 mm formed on the top and bottom surfaces of panel CS_4, respectively. A system of inter-connected cracks was noticed on the bottom surface, having a pattern basically following the reinforcement mesh. This pattern results, as explained by Toutlemonde and Boulay (1993) in Section 3.3.3, from the close-in transient shock wave effect. On the bottom face of the FRP panels, surface cracks of 0.5 mm width were observed on the uncovered regions. This indicates crack width reduction of about 30~50 % for the retrofitted panels, but shear

cracks of almost the same width were noticed in all the panels. Since the FRP layers are not designed to assist in the shear strengthening of the panels, the observed shear response of the control and retrofitted panels is expected.

Under the 22.4-kg blast, the FRP layers maintained good bond with the concrete surfaces, no corner/edge delamination, and no fibre damage was observed. This was true for both panel CSS_1 (with wrapped ends) and Panels GSS_1, and CLS_1 (without wrapped ends).

The preceding observations with regard to the level of damage are confirmed by mid-span deflections measured under blast pressure. Notwithstanding the uncertainty of the deflection measurements, the FRP-retrofitted panels experienced maximum central deflections of 10.83, 10.83, and 9.15 mm, respectively. This indicates 30 %, 30 % and 10 % increase over the control panel maximum central deflection of 8.33 mm, respectively. The lower deflection of central panel CS_4 can be explained by the fact that its failure pressure was likely smaller than those of the similarly loaded retrofitted panel. The retrofitted panels were also able to undergo higher pressure without failure, thus they experienced greater maximum deflection. Figure 5.33 illustrates the deflection results of the 22.4-kg blast shots. Since it is well known that adding a layer of FRP does not significantly alter the effective moment of inertia of a reinforced concrete panel, the current deflection results tend to confirm this notion and its applicability to blast loaded structures. Another important point to mention is that local damage in a panel would not necessarily result in significantly higher deflection because deflection is governed by the stiffness of the panel as a whole while damage and high stress may be local phenomena.

Strain was recorded during the four 22.4-kg tests. Gauges 2 in control Panel CS_4 recorded 4375 μstrain in the bottom reinforcement. High strains were recorded on the FRP layers

for the retrofitted panels GSS_1 and CSS_1 (10000 and 8500 μstrain, respectively).

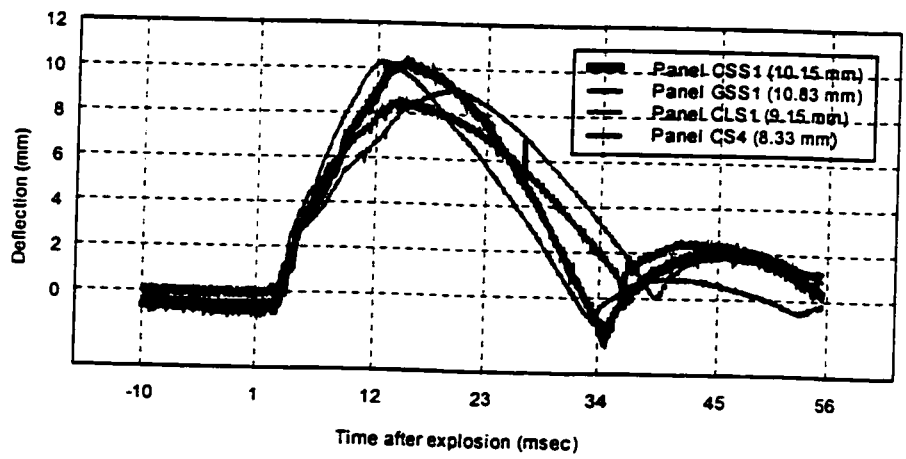

Figure 5.33: Mid-span deflection history of panels tested using 33.4-kg charges

The experimental data recorded in the 22.4-kg charge blast tests are summarized in Table 5.15. The table gives the basic information needed to analyze the structural behaviour of the panels tested under this charge, including the maximum values for reflected pressure and impulse, strain, and residual strength. Post-blast observations, including the extent of damage, crack width, concrete crushing/spalling, and FRP layers bonding/delamination. The observed damage is categorized as light, moderate, heavy, or severe. Light damage indicates that only hairline cracks are observed on the unretrofitted area with good bond between the FRP layers and the concrete surfaces. Moderate damage can be defined for the control panels by bottom surface cracks of width up to 1.5 mm and minor concrete spalling. For heavy damage, cracks are wider, and as high as 4 mm permanent deflections are large and concrete spalling is more heavy and extensive. The FRP panels experienced minor layer delamination in case of the moderate damage, while in case of heavy damage sheet rupture and concrete failure occurred in the unretrofitted areas. Finally, severe damage occurred in panels that totally crushed with total delamination of the FRP layers.

Table 5.15: Summary of experimental measurements and post-test observation for panels tested under 22.4-kg charge

Blast Test No.	Test Group	Panel	Reflected pressure (kPa)		Average reflected impulse (kPa.msec)	Maximum μstrain				Maximum central deflection (mm)	Post-blast residual static strength (kN)	Observed damage
						Reinforcing steel		Concrete surface/ FRP layer				
			Maximum	Average		Top	Bottom	Top	Bottom			
17	1	CS4	4823	3842	571	NA	4375	NA	NA	8.33	80.02	moderate
4	2	GSS1	4203	3741	1344	1480	6500	NA	10000	10.83	140.05	light
5	3	CSS1	4492	3517	1681	2280	NA	NA	8300	10.83	150.26	light
3	4	CLS1	3238	3052	1220	3850	3440	2200	NA	9.15	60.11*	light

- Note: NA = not available, P = poor trace
- * Test was stopped due to strip delamination

5.4.2 Panels tested using 33.4-kg charge

Based on the observations of the 22.4-kg tests, it was expected that the control panels would fail under the effect of the 33.4-kg charge while the FRP-retrofitted panels would suffer noticeable damage. For the eleven blast tests conducted using 33.4-kg charge, the average reflected impulse was found to be 1861 kPa.msec, and a difference in impulse records of about 20 % was recorded, which is remarkably good for blast tests.

Control panels CS_2 and CS_3 were severely damaged by the reflected impulses of 1954 and 2412 kPa.msec in tests # 8 and 15, respectively. Both panels displayed similar modes of failure, where a local circular punching area surrounded by a system of wide cracks appeared on the upper surface and a system of continuous and deep cracks, with an average width of 4 mm, formed on the bottom face. Maximum permanent deflection of 10 mm was recorded.

The FRP-retrofitted panels tested under 33.4-kg charges (three panels per each FRP group) displayed a more stable behaviour and moderate failure modes. This was evident by lack of permanent deflection, minor cracks in the unretrofitted corners, and minor concrete spalling/scabbing. The average tensile crack width for the FRP retrofitted specimens was found to be 2.5, 1.5, and 3 mm which indicates an average crack width reduction of 36 %, 62 % and 25 % for the panels ***GSS***, ***CSS***, and ***CLS***, respectively, compared to the unretrofitted panels. It is of importance to mention here that crack patterns could not be compared because of the existence of the FRP layers.

As some panels failed completely causing damage to the extension rod of the displacement LVDT, poor and/or no traces were recorded in some of the 33.4-kg blast

shots (tests12 and 16). Yet, recorded values gave an indication of mid-span deflection of the panels. This is shown in Figure 5.34, where examples of mid-span deflections for three FRP-retrofitted panels along with the control panel CS_2 are depicted. Mid-span deflections for panels GSS_4, CSS_2, and CLS_3 are 9.1, 11.58, and 11.87 mm, respectively, indicating average reduction of 30, 12 and 10 % in the central deflection compared to the control panel CS_2 that experienced 13.12 mm mid-span deflection. Similar relations could be noticed using different deflection records from the 33.4-kg shots. It can be concluded from Figures 5.33 and 5.34 that the maximum panel response occurred at time of 10~12 msec from the time of blast wave arrival. The average positive durations of these two charge categories (22.4 and 33.4 kg) were recoded as 1.66 and 1.96 msec, respectively, which confirmed the assumption that impulsive loading is dominating the structural behaviour of the test panels.

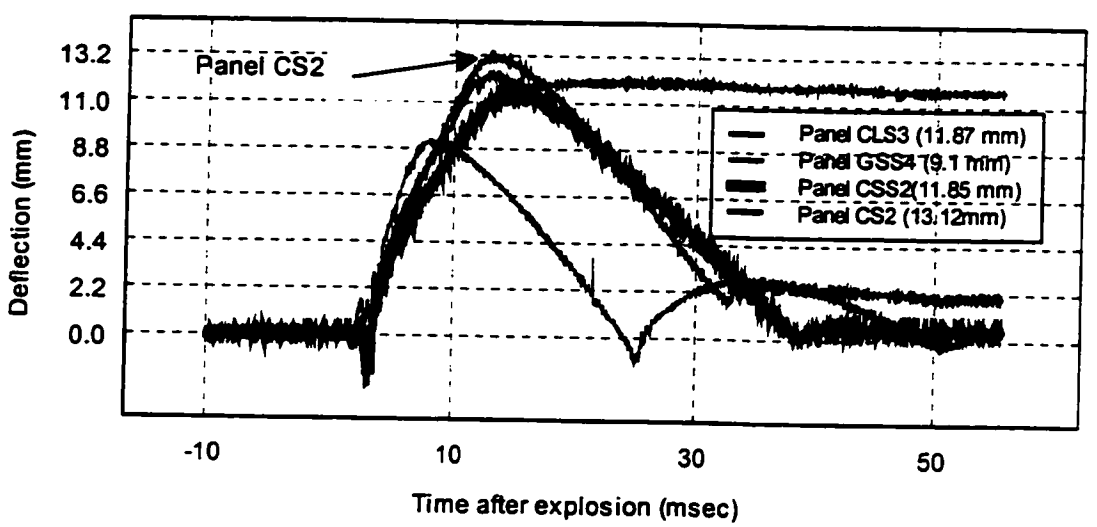

Figure 5.34: Mid-span deflection history of panels tested using 33.4-kg charges

Table 5.16: Summary of experimental measurements and post-test observation for panels tested under 33.4-kg charge

Blast Test No.	Test Group	Panel	Reflected pressure (kPa) Maximum	Reflected pressure (kPa) Average	Average reflected impulse (kPa.msec)	Maximum μstrain Reinforcing steel Top	Maximum μstrain Reinforcing steel Bottom	Maximum μstrain Concrete surface/ FRP layer Top	Maximum μstrain Concrete surface/ FRP layer Bottom	Maximum central deflection (mm)	Post-blast residual static strength (kN)	Post-blast Observed damage
8	1	CS2	5528	5059	1954	1875	2730	5000	1650	13.12	68.00	heavy
15	1	CS3	5712	5507	2412	6350	2900	1700	3800	9.53	93.00	heavy
7	2	GSS2	3838	3050	1819	2000	NA	NA	10000	14.58	NA	severe
12	2	GSS3	5215	4995	1492	20000	17000	14000	750	P	112.51	moderate
14	2	GSS4	5030	4933	2239	11000	16000	8750	16000	9.10	85.04	Heavy
9	3	CSS2	5877	4946	1451	1875	6400	NA	20000	11.58	135.00	moderate
11	3	CSS3	5719	5347	1723	2550	10000	NA	4280	13.85	72.00	heavy
13	3	CSS4	5105	5026	1902	2800	5900	NA	20000	9.58	NA	severe
6	4	CLS2	5953	5753	2245	1220	5100	NA	7200	12.80	NA	severe
10	4	CLS3	5340	4830	1592	10000	4700	9300	10000	11.87	58.07	heavy
16	4	CLS4	5808	5502	1743	20000	15000	NA	800	P	75.13	heavy

- Note: NA = not available, P = poor trace

Under the 33.4-kg charge, the FRP layers showed generally good bond to both concrete surfaces, but peel-off at panel edges in the case of glass retrofitted panels and at the corners of carbon strip retrofitted panels was observed. The delamination locations clearly reflect the importance of mechanical anchoring systems in using externally applied FRP composites. Also, at this high impulse (an average of 1860 kPa.msec), rupture of carbon sheets was observed at the bottom of panels CSS_2, and CSS_3. However, no fibre damage was noticed in the glass sheets and the carbon strips.

Unexpected failure was observed when testing panels GSS_2 and CLS_2 under reflected impulse of 1820 and 2245 kPa.msec, respectively. The panels suffered total delamination of the top glass sheets and the bottom carbon strips, and severe concrete crushing occurred in both panels. Concrete spalling at the bottom surface of both panels was also evident. Panel CLS_2 was subjected to an impulse that is 34 % higher than the average value for that charge size (1861 kPa.msec), and the carbon strips covered only 25 % of its area. This was the cause of the observed severe damage experienced by panel CLS_2. On the other hand, panel GSS_2 is severely damaged due to the effect of sheet delamination. The FRP layers peel-off might be due to improper installation or due to the tensile suction effect of the shock wave, a matter which needs further investigation. The delamination may be explained as follows

- The explosive charge is initiated, the shock wave travels to the target at supersonic speed, and then reflects upon hitting the target.
- The reflected pressure is much higher (at least two times) than the incident pressure as it is strengthened upon reflection by a target of density higher than air.

- Some of the shock energy is transmitted to the test specimen. The compression wave travels across the panel to the free surface. The rarefaction (tensile) wave travels back up through the panel, which causes the FRP layer delamination.
- In case of the bottom carbon strips, as the traveling shock wave passed through the test specimen, it directly caused separation. This reflects the importance of covering as much of the surface area as possible. In general, the more area is covered by FRP materials, the more gain in blast resistance capacity is expected.

Panel CSS_4, tested using 33.4-kg charge, experienced a high-reflected impulse of 1902 kPa.mesec and failed severely. This was manifested by the bottom sheet rupture. The upper sheets did not suffer as much damage as the bottom sheets. The difference with the glass sheet and carbon strips was that the carbon sheets maintained good bond to the concrete surfaces, held the crushed concrete in position, and prevented the projection of fragments. Accordingly, it was possible to take the panel out of the frame and test it statically for residual strength.

Strain comparisons were made in order to relate strains in the control panels to those in the FRP-retrofitted panels under the 33.4-kg charge. Strain values form the control panel CS_3 will be used as reference in the following comparisons. As an example, Figure 5.35 shows reinforcement strains at two different locations of control panel CS_3 and in the GFRP retrofitted panel GSS_3. Strain readings in the bottom steel mesh at 1/3 diagonal location were 6350 and 20000 μstrain for the two panels, respectively. This indicates about threefold increase in reinforcement strain in the retrofitted panel compared to the reference panel (see Figure 5.35, a). At the top mid-span of the same two panels,

reinforcement strains were found to be 2900 and 17000 μstrain, indicating more than 6 times strain increase in the GFRP retrofitted panel compared to the control panel CS_3, Figure 5.35 (b). Surface strain gauges, such as gauge #5 (bottom surface mid-span), of the two panels gave strains of 3800 and 11000 μstrain, respectively. This indicates 3 times more strain in the bottom glass sheets of panel GSS_3 compared to the concrete strain in the control panel. On the top surface at mid-span, for the GFRP layer and concrete surface, strains were found to be 1700 and 14000 μstrain, which indicates is more than 8 times strain in the top GFRP layer compared to concrete surface. This is illustrated in Figures 5.36 (a) and (b). It is of importance to mention here that the GFRP-retrofitted panel GSS_3 was not damaged after the 33.4-kg blast test, while the control panel CS_3 failed under the same charge weight. Finally the post-blast residual strength values in Table 5.16 also give an indication of the level of damage suffered by each specimen. In general, the ***GSS*** and ***CSS*** panels performed better and had higher residual strength. The residual strengths will be further discussed in the next chapter.

The high strains values, coupled with the observed damage in the panels, indicate that the GFRP and CFRP sheets increased the blast resistance of the panels. On the other hand, the CFRP strips did not significantly improve the panel's resistance. It is believed that the increase in resistance may be due to two sources. First, if the FRP layers cover a significant portion of the panel surface, then they may change the blast wave characteristics and blunt the shock front, resulting in less damage to the concrete. Secondly, the FRP increases the moment resistance of the panels. While the latter is easy to quantify, verification of the former needs further study and better measurement techniques.

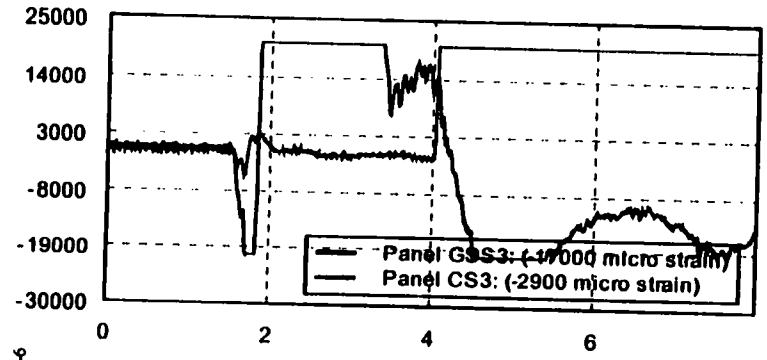

(a): Strains in the top steel mesh (CH3)

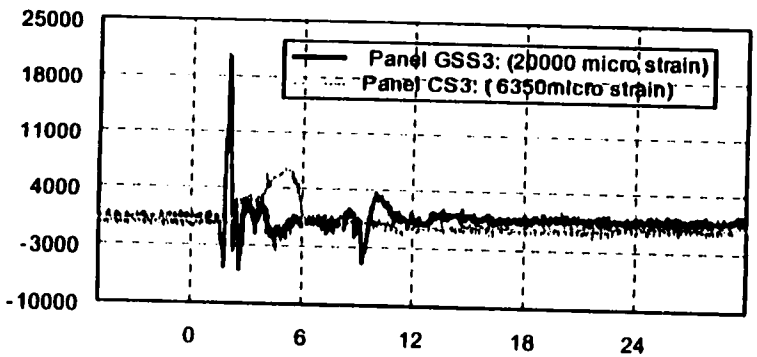

(b): Strains in the bottom steel mesh (CH2)

Strain × 10^{-6}

Time (msec)

Figure 5.35: Comparison between strains in the steel meshes of Panels GSS3 & CS3

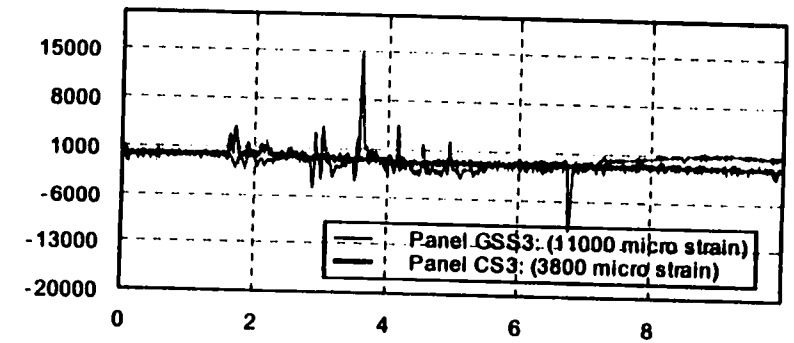

(a): Strains in the top GFRP fabric and concrete surface (CH7)

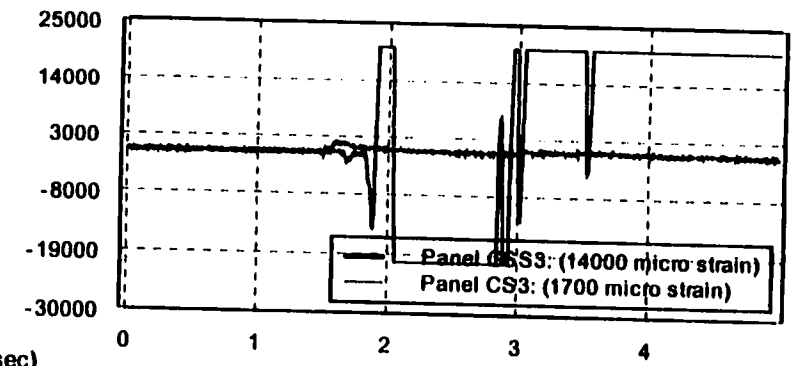

(b): Strains in the bottom GFRP fabric and concrete surface (CH5)

Strain × 10^{-6}

Figure 5.36: Comparison between strains in GFRP fabric and concrete surfaces of Panels GSS3 & CS3

5.5 Post-Blast Static Tests

In order to further quantify the extent and level of damage in the blast-tested panels, the damaged specimens were statically tested to find their post-blast residual strength. The panels derive their strength from the concrete, the steel and FRP reinforcement. It is recognized that as long as the concrete between the top and bottom steel layers is not completely destroyed, by virtue of the equal amounts of tension and compression reinforcement, the panels will be able to carry some residual load. Our objective is to compare this residual capacity with the capacity of the statically loaded control specimens described earlier in this chapter.

The panels were simply supported on all four edges and loaded with a central load applied through a 300 × 300 mm steel plate. The load was applied monotonically by a servo-controlled hydraulic actuator and central deflection was measured using dial gauges. In most cases the panels failed due to punching shear. The punching shear resistance of panels without shear reinforcement is primarily governed by the concrete strength and not by the presence of the flexural reinforcement.

Table 5.17 shows results of the static tests, where gauges G_1 and G_4 are located at the 1/6 span points and G_2 and G_3 are located at the 1/3 span points on either side of the central plate. It can be noticed that the failure loads for the panels tested using 22.4-kg charges are higher than those for the panels tested using 33.4-kg charges by a factor of 10 to 50 %. The average failure load of the two carbon sheet panels CSS_2 and CSS_3 that were tested using 33.4-kg charge is 102.75 kN. On the other hand, the failure load of panel CSS_5, the carbon sheet retrofitted panel that was only statically loaded, was 150 kN, which indicates almost 30 % loss in the panels strength due to exposure to blast loads.

Table 5.17: Results of the static tests

Test No.	Charge weight form the blast tests (kg)	Test Specimen	Failure Load (kN)	Deflection at failure (mm) Gauge Location G1	G2	G3	G4
1	22.4	CLS1	60.11	13.52	11.59	21.40	17.85
2	33.4	CS2	68.00	18.9	32.27	32.02	21.04
3	22.4	CSS1	150.25	20.48	31.04	31.28	23.49
4	22.4	GSS1	140.05	12.73	19.57	23.44	15.17
5	13.4 + 22.4	CS_1	55.00	14.50	15.29	20.34	13.17
6	33.4	CLS_3	58.07	15.70	15.14	19.72	13.44
7	33.4	CSS_2	135.00	7.45	15.52	21.90	19.10
8	0.0	*CS_5	120.00	19.55	31.1	31.40	17.75
9	22.4	CS_4	80.02	21.94	28.85	30.18	15.55
10	0.0	*CSS_5	150.01	22.91	25.44	25.41	14.33
11	33.4	CSS_3	72.00	15.05	27.90	29.20	15.75
12	33.4	CLS_4	75.13	15.43	25.75	25.90	15.95
13	33.4	CS_3	93.00	20.75	30.39	30.11	14.55
14	33.4	GSS_3	112.51	8.90	12.50	13.30	13.27
15	33.4	GSS_4	85.04	10.11	21.93	23.05	15.25

*Panels statically tested only

5.5.1 Panels tested using 22.4-kg charge

Panels CS_4, GSS_1, CSS_1, and CLS_1 were statically tested and their ultimate failure loads were recorded as 80.02, 140.05, 150.26, and 60.11 kN, respectively. This indicated increase of 65 %, 86 % and -24.9 % in the failure load of the retrofitted panels. The negative sign in the latter value indicates that failure load of panel CLS_1 was less than that of the control panel CS_4, and the reason for this was given in Section 5.2. A comparison among the residual failure loads of the four panels tested under 22.4-kg ANFO charge is shown in Figure 5.37.

Deflection data reported earlier are graphically illustrated in Figures 5.40 and 5.41, which indicate an enhancement in the load-deflection relationship of retrofitted panels.

For example in Fig. 5.40 (a), and at a load of 60 kN, deflections for the four panels were obtained as 16.5, 4.5, 10.1 and 13.5 mm, which indicates average deflection reduction of 62.5 %, 38.6 %, and 18.2 % for the three FRP retrofitted test groups, respectively. This gives an indication about the role of FRP composites. It is believed that the FRP does not significantly affect the stiffness of the panels. Therefore, the observed improvement is due to less damage in the concrete. The same behaviour was obtained at the 1/3 span location (Gauges # 2 and 3), as indicated in Figure 5.41. For the panels exposed to 22.4-kg charge, the GFRP-retrofitted panels showed the maximum deflection reduction among the three retrofitting materials, followed by the CFRP sheet retrofitted panels.

5.5.2 Panels tested under 33.4-kg charge

Panels tested using 33.4-kg charges maintained, as expected, less residual strength than those tested under 22.2-kg charges. A comparison among the failure loads of the four panels tested under 33.4-kg charge is shown in Figure 5.38. Failure loads were recorded as 68, 85, 135, and 75 kN for panel CS_2 and for the FRP panels GSS_4, CSS_2, and CLS_4, respectively. This indicates 25 %, 98 %, and 10 % increase in the residual strength for the retrofitted panels over the control panel. A comparison among the residual strength of test panels under different charges is given in Figure 5.39, which confirms that the higher the charge weight used in blast tests, the greater the loss in the post-blast residual strength.

Load-deflection relationships for the four gauge locations are shown in Figures 5.42 and 5.43. As an example of the deflection enhancement, in Figure 5.43 (a), at a load of 60 kN, deflection values were obtained as 25, 11.5, 6.5, and 17.5 mm for the four test specimens. Again, this indicated deflection reduction of 50 %, 74 %, and 30 % for the retrofitted panels. In this case, the panels retrofitted with CFRP sheets showed the least deflection.

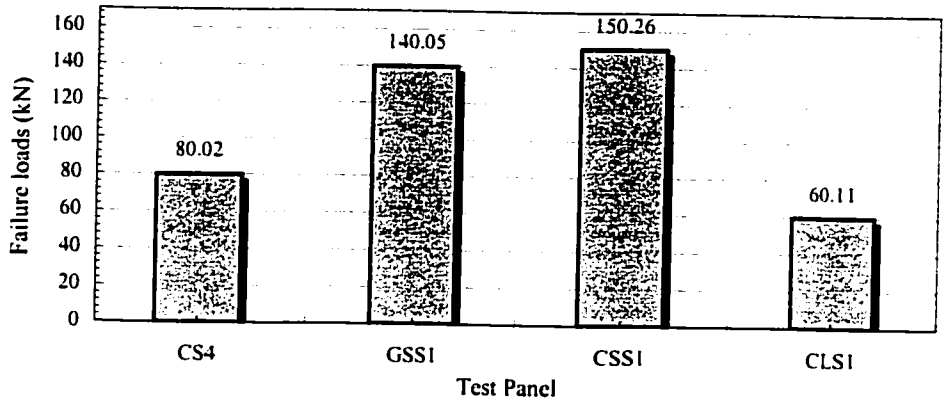

Figure 5.37: Comparison between failure loads of panels tested under 22.4-kg charge

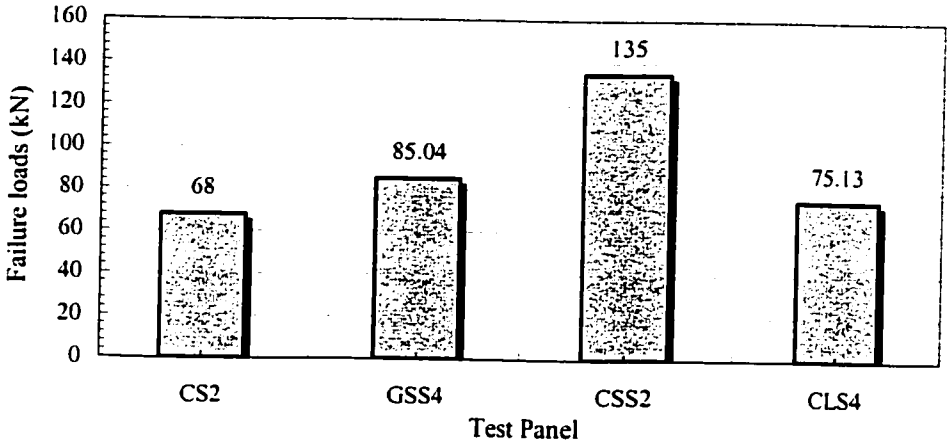

Figure 5.38: Comparison between failure loads of panels tested under 33.4-kg charge

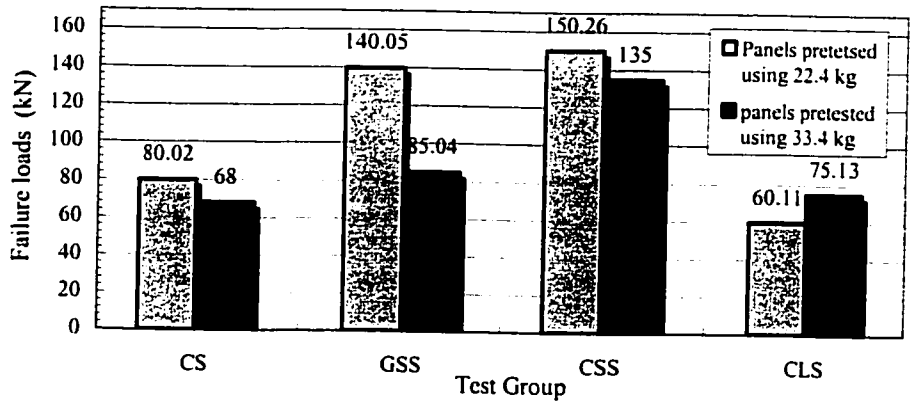

Figure 5.39: Comparison between failure loads of panels tested under various charges

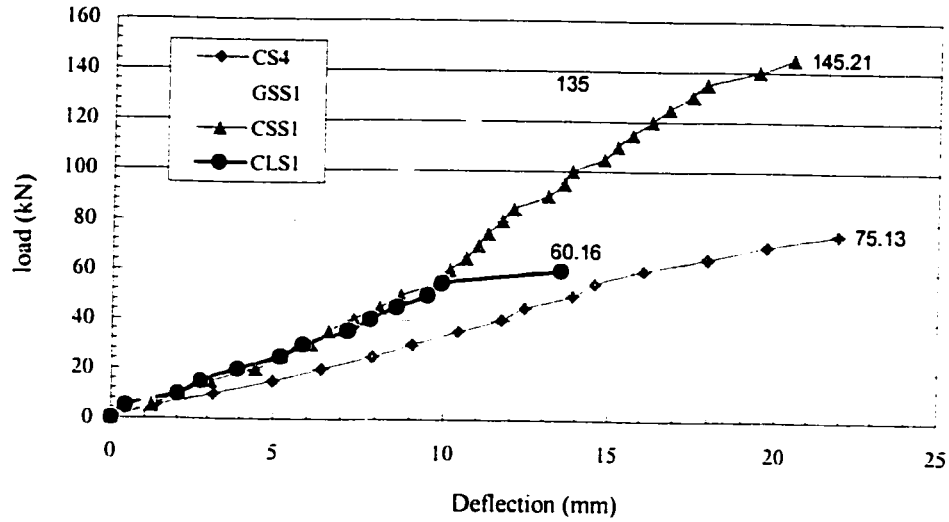

(a): Gauge # 1 (1/6 Span)

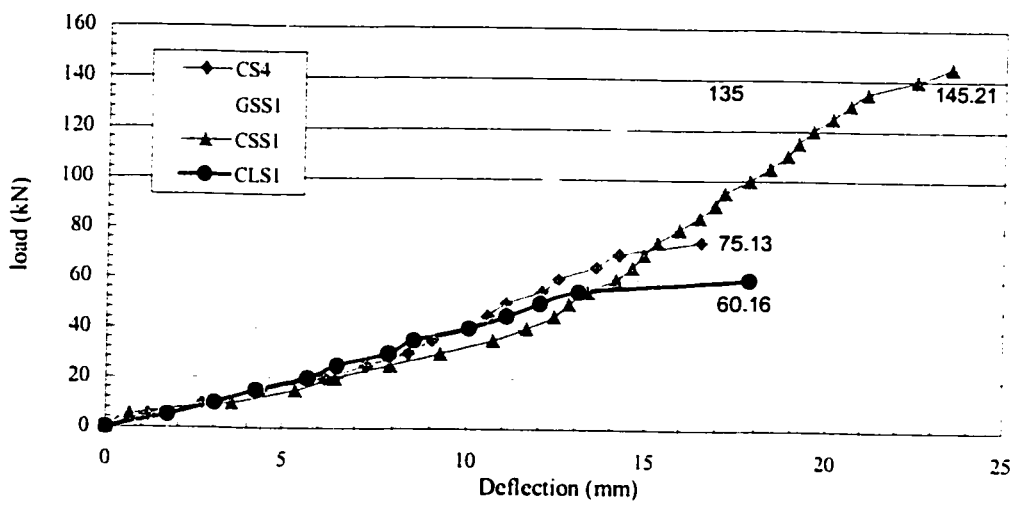

(b): Gauge # 4 (1/6 Span)

Figure 5.40: Load-deflection of panels pretested using 22.4 kg charges (1/6 span)

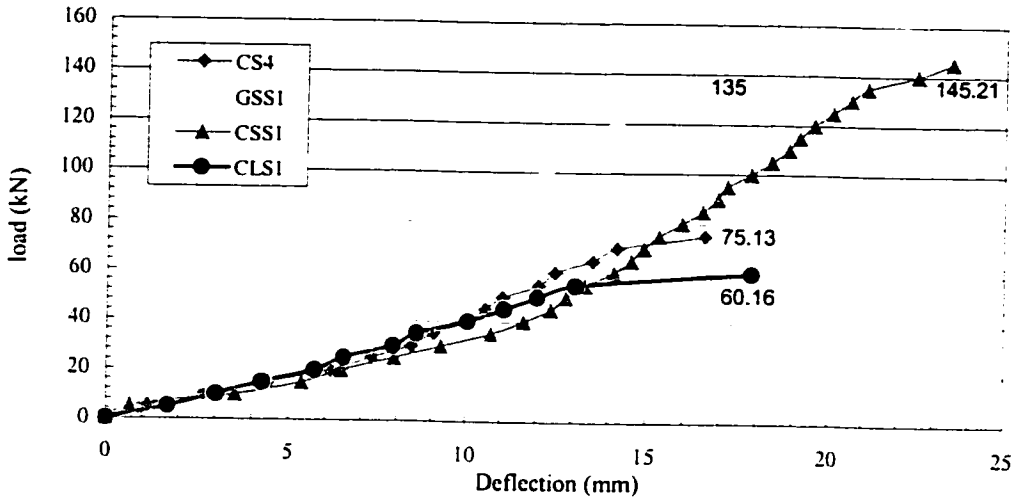

(b): Gauge # 2 (1/3 Span)

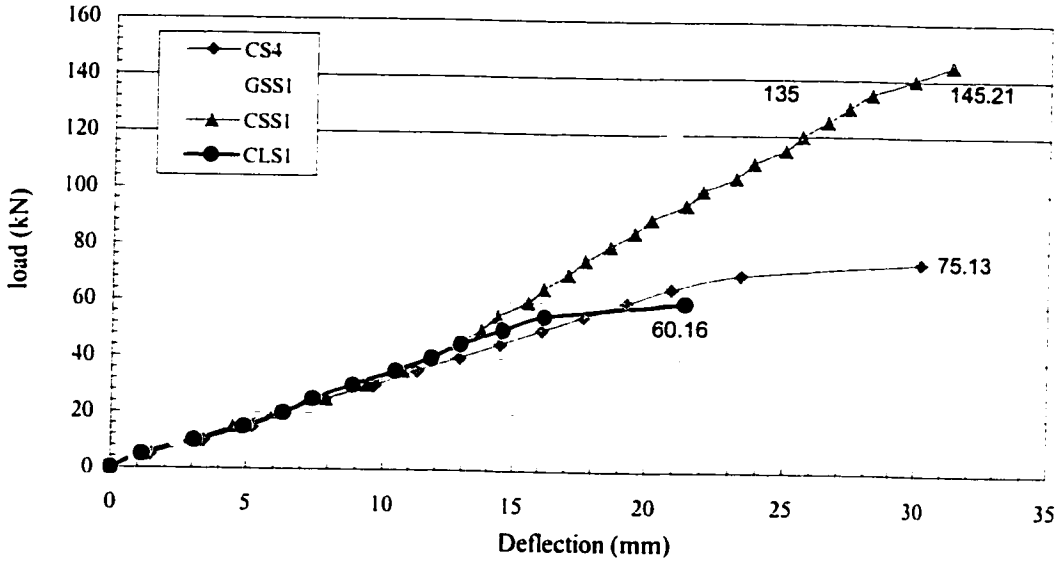

(b): Gauge # 3 (1/3 Span)

Figure 5.41: Load-deflection of panels pretested using 22.4 kg charges (1/3 span)

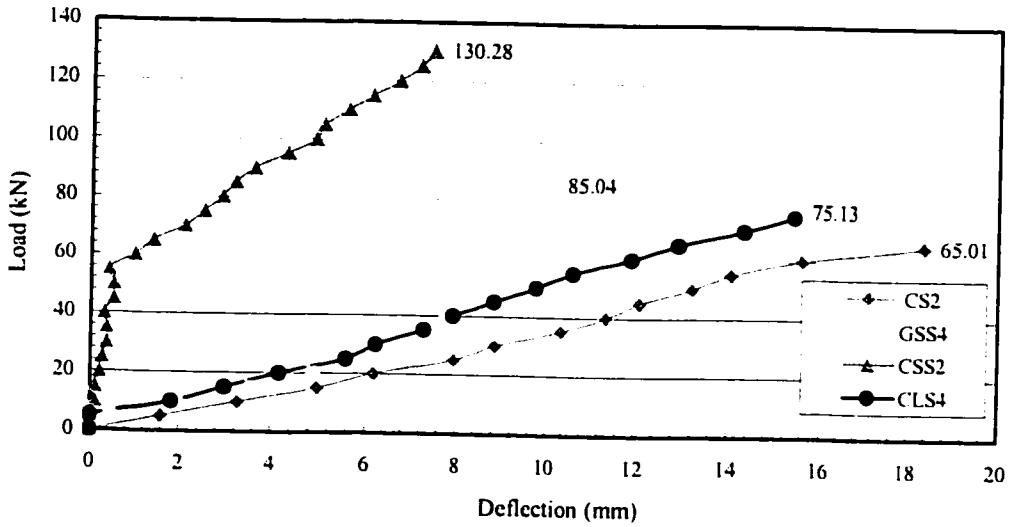

(a): Gauge # 1 (1/6 Span)

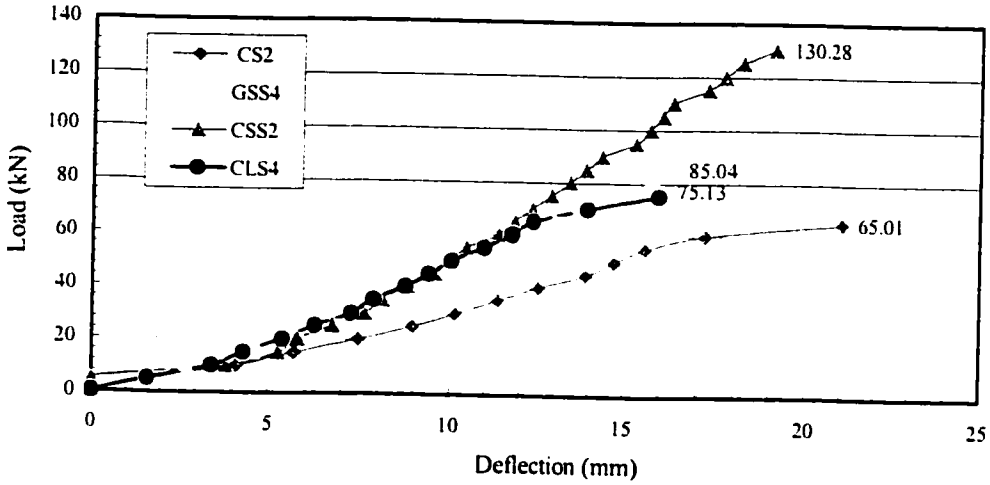

(b): Gauge # 4 (1/6 Span)

Figure 5.42: Load-deflection of panels pretested using 33.4 kg charges (1/6 span)

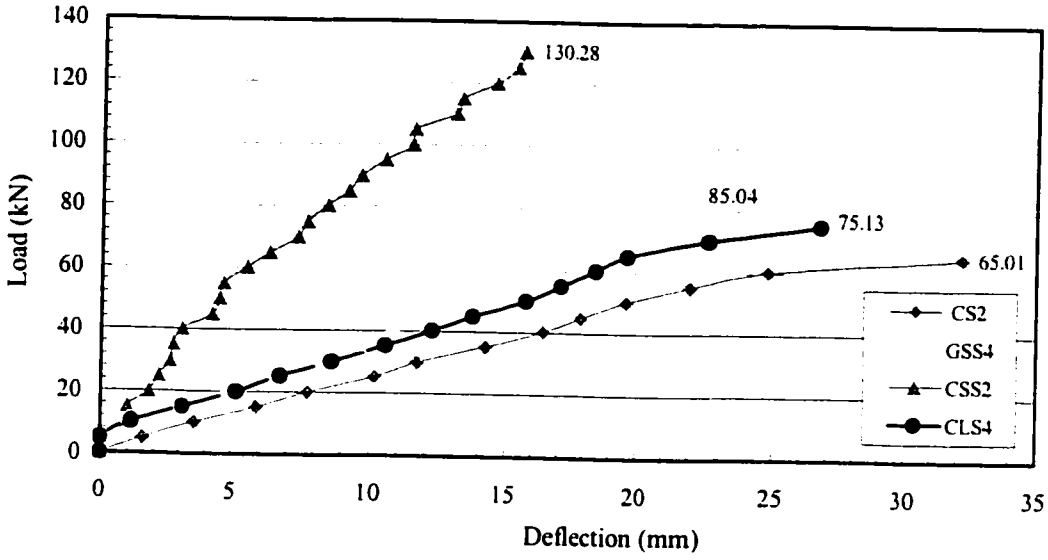

(a): Gauge # 2 (1/3 Span)

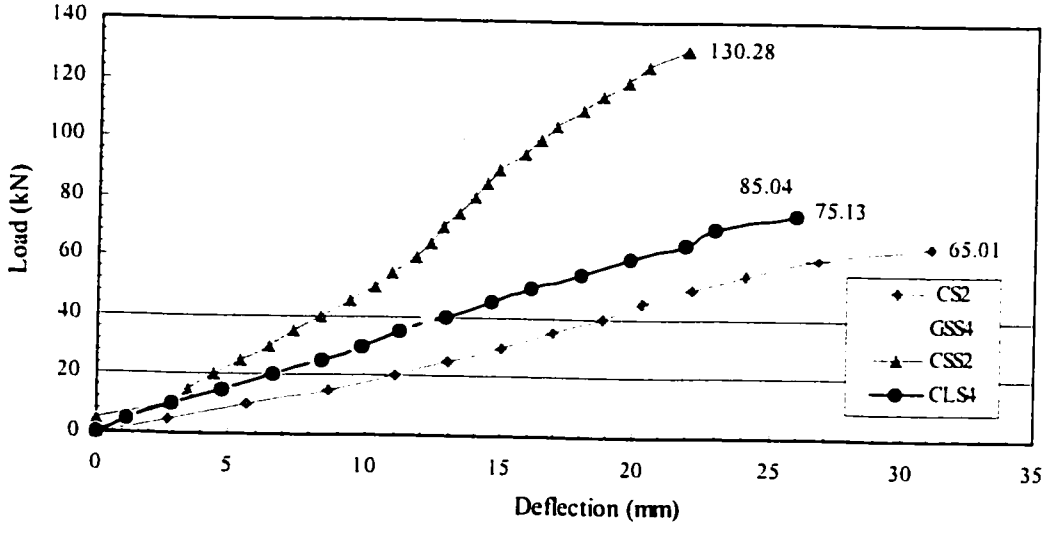

(b): Gauge # 3 (1/3 Span)

Chapter 6

ANALYTICAL STUDY

6.1 General

Although some commercial general-purpose finite element and finite difference software are capable of the non-linear dynamic analysis of structures (Crawford *et al.*, 1996), they do not completely meet the requirements of the current investigation. Full numerical simulation of the tested panels requires coupled computational fluid dynamic and nonlinear dynamic analysis of reinforced concrete structures. By coupling the two methods, the interaction between the blast waves and the structural response could be fully explored, but such a detailed analysis is beyond the scope of the present study. In this chapter an attempt is made to determine whether a simple closed-form solution can be applied to predict the dynamic response of the panels under the effect of blast loads.

A static analytical solution is also presented which is intended mainly to find the maximum elastic response of simply supported flat plates under the effect of blast loading. The solution could be applied to various blast loading effects and structural configurations. By means of such an analysis, one can compare the ultimate capacity of the panels with the maximum moment to which they are subjected. It is recognized that this is an approximate method, but given the paucity of detailed methods of design for blast loads, it is worth exploring.

The dynamic closed-form solution gives a quick prediction of the panels response, including their mid-span deflections, velocity, acceleration and stresses due to impulsive loading. The effect of high strain rate on panel materials behaviour is included in the current analysis. Results of the analytical method are compared with the corresponding experimental data to judge its accuracy.

6.2 Analytical Prediction of the Blast Wave Parameters

In order to assess the validity of analytical tools for predicting the blast wave parameters, instead of conducting blast experiments, the blast wave measurements will be compared with their corresponding values predicted by the CONWEP program. The CONWEP computer code, based on the U.S. technical manual TM5-1300 (1990), is commonly used to predict blast pressures and impulses. Its simplicity makes it a useful tool for calculation of blast wave parameters. The program uses a combination of analytical and empirical formulae to predict the parameters for various explosion sources, and then calculates the relevant blast loading on structures. The pressure-time profile exponentially decays according to the decay coefficient, θ, as

$$P(t) = P_{SO}\left(1 - \frac{t - t_A}{t_o}\right) e^{\frac{-(t-t_A)}{\theta}} \tag{6.1}$$

This expression limits the pressure profile to the positive phase only, and is similar to that given in Equation 2.1 in Chapter 2. The only difference is that in the CONWEP expression, the time of arrival, t_A, is subtracted from the total time, t, in order to start the positive duration at a time equal to the time of arrival.

CONWEP is used to predict the incident and reflected blast wave parameters for the 13.4, 22.4 and 33.4 kg ANFO charges located at a 3 m standoff distance. Results of the analysis, including reflected pressure, reflected impulse and positive duration are listed in Table 6.1, and are compared with the corresponding experimental data. The table shows that in general the predicted pressure and impulse are in good agreement with the experimental data. The average difference between the measured and predicted pressures and impulses for the 22.4-kg charges (5 tests) varies between 5 and 2 %, respectively. For the 33.4-kg charges (11 tests), the average difference varies from 6 to 2 %, respectively. The CONWEP prediction for the positive duration shows high values, up to three times the measured positive duration. This is because the program assumes that the explosive charge is spherical in shape and the target ideally reflects the shock waves. On the other hand, recorded positive durations are relatively low. Comparisons between measured and CONWEP predicted reflected pressures and impulses for all the test panels as shown in Figures 6.1 and 6.2, may be a better measure of the accuracy of the CONWEP program.

CONWEP predictions for the pressure-time profiles also agree well with the test measurements. Figures 6.3 to 6.5 show comparisons between the measured and the CONWEP predicted reflected pressure-time profiles for the three charge weights,

respectively. In these figures only the part of the measured pressure-time profile within the positive duration is illustrated because this is the portion of the blast pressure profile that is of practical interest in the current study.

It is concluded that the CONWEP program gives reasonable predictions for the blast wave parameters, and this makes it a useful tool in practice.

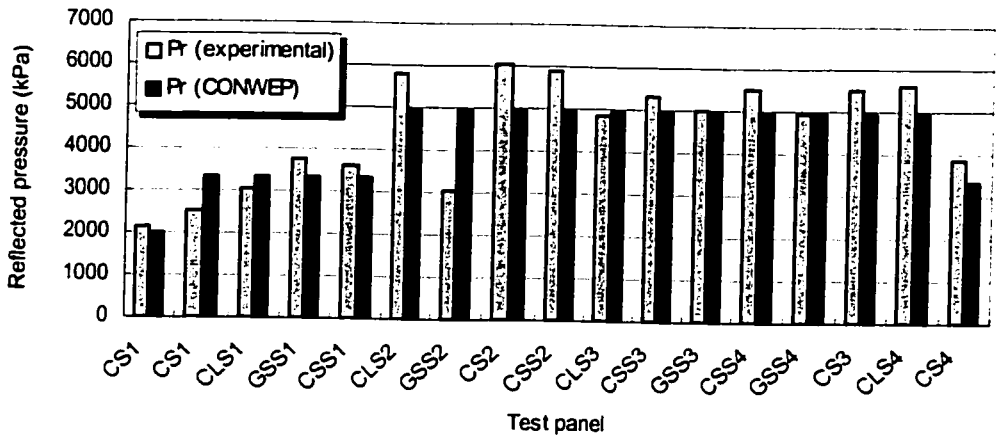

Figure 6.1: Comparison between measurements and CONWEP-predictions for reflected pressure (Average values)

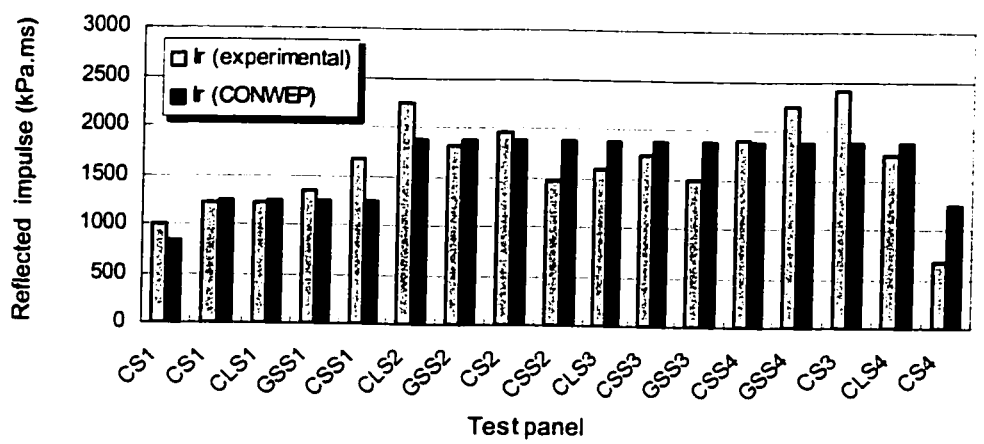

Figure 6.2: Comparison between measurements and CONWEP-predictions for reflected impulse (Average values)

Table 6.1: Comparison between experimental and CONWEP blast wave parameters

					Experimental Measurements			CONWEP Predictions			Ratio (Measured/Predicted)		
Test No.	Panel	ANFO Charge weight (kg)	TNT Equiv. weight (kg)	Scaled distance [m/(kg)$^{1/3}$]	Average reflected pressure (kPa)	Average reflected impulse (kPa.msec)	Average positive duration (msec)	Average reflected pressure (kPa)	Average reflected impulse (kPa.msec)	Average positive duration (msec)	Reflected pressure	Reflected impulse	Positive duration
1	CS1	13.4	10.99	1.349	2150	996	NC	2002.4	845	3.8	1.08	1.18	NA
2	CS1	22.4	18.37	1.137	2538	1344	NC	3323.7	1247	4.8	0.76	0.98	NA
3	CLS1	22.4	18.37	1.137	3052	1220	1.29	3323.7	1247	4.8	0.92	0.98	0.27
4	GSS1	22.4	18.37	1.137	3741	1344	1.62	3323.7	1247	4.8	1.13	1.08	0.34
5	CSS1	22.4	18.37	1.137	3517	1681	1.56	3323.7	1247	4.8	1.09	1.35	0.33
6	CLS2	33.4	27.39	0.995	5753	2245	1.77	4937.6	1686	5.5	1.18	1.20	0.32
7	GSS2	33.4	27.39	0.995	3050	1820	1.71	4937.6	1686	5.5	0.62	0.98	0.31
8	CS2	33.4	27.39	0.995	5059	1954	1.68	4937.6	1686	5.5	1.23	1.05	0.31
9	CSS2	33.4	27.39	0.995	4946	1451	1.53	4937.6	1686	5.5	1.20	0.78	0.29
10	CLS3	33.4	27.39	0.995	4830	1592	1.5	4937.6	1686	5.5	0.98	0.85	0.27
11	CSS3	33.4	27.39	0.995	5347	1723	1.35	4937.6	1686	5.5	1.08	0.92	0.25
12	GSS3	33.4	27.39	0.995	4995	1492	1.68	4937.6	1686	5.5	1.01	0.80	0.31
13	CSS4	33.4	27.39	0.995	5026	1902	1.41	4937.6	1686	5.5	1.12	1.02	0.26
14	GSS4	33.4	27.39	0.995	4933	2239	2.82	4937.6	1686	5.5	1.00	1.20	0.51
15	CS3	33.4	27.39	0.995	5507	2412	3.17	4937.6	1686	5.5	1.12	1.29	0.58
16	CLS4	33.4	27.39	0.995	5502	1743	2.92	4937.6	1686	5.5	1.14	0.995	0.53
17	CS4	22.4	18.37	1.137	3842	571	2.16	3323.7	1247	4.8	1.16	0.54	0.45

- The scaled distance is calculated based on the equivalent TNT charge weight (1 kg ANFO ≈ 0.82 kg TNT).
- The average ratios for reflected pressures are calculated as 1.01 and 1.06 for the two repeated charge weights, respectively.
- For the reflected impulse predictions, the ratios are found to be 0.98 and 1.
- The average experimental values are from several gauges described in Chapter 5.

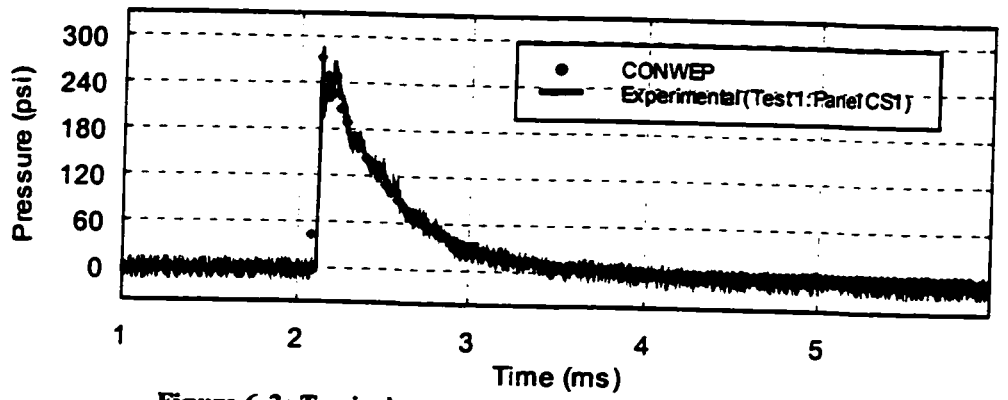

Figure 6.3: Typical comparison between experiemntal and CONWEP reflected pressure-time profiles under 13.4-kg charges

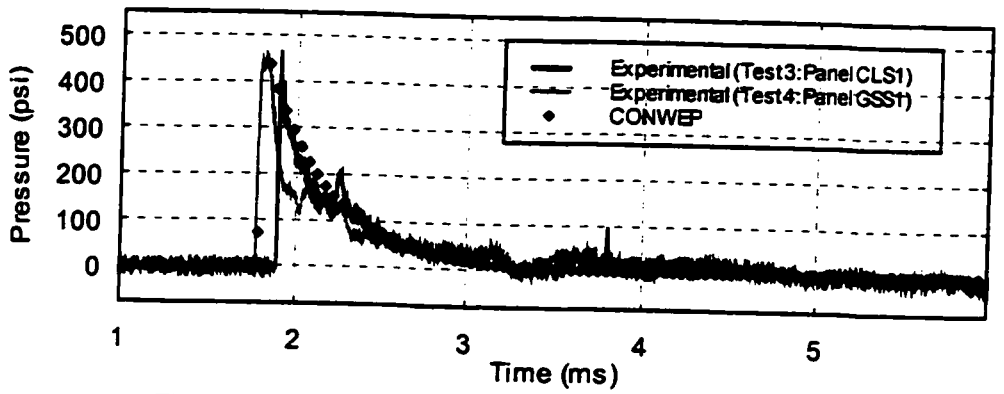

Figure 6.4: Typical comparison between experiemntal and CONWEP reflected pressure-time profiles under 22.4-kg charges

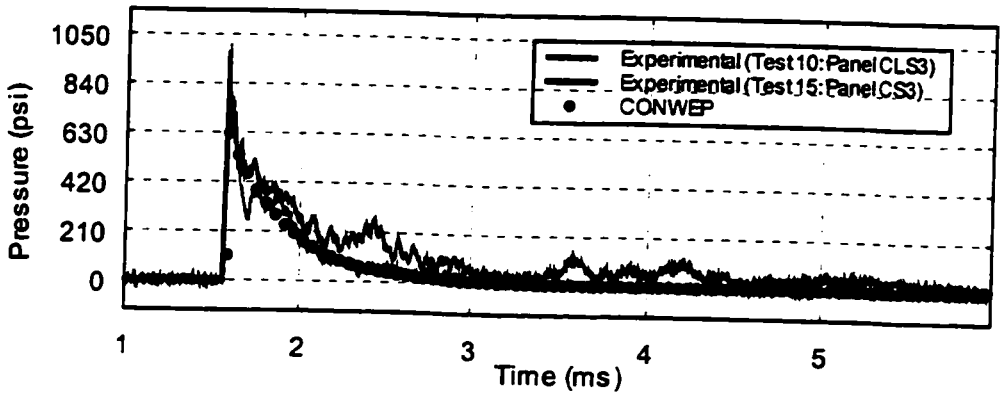

Figure 6.5: Typical comparison between experiemntal and CONWEP reflected pressure-time profiles under 33.4-kg charges

6.3 Static Response

The static analysis will be applied, using a closed-form solution and assuming linear elasticity, to determine the maximum mid-span deflection of the panels under the effect of uniformly distributed partial load. It may be recalled that such loading was applied to determine the static strength of some of the control panels, and to evaluate the residual strength of panels subjected to blast loads.

6.3.1 Elastic static analysis

The main objective is to verify the range of applicability of the concept of effective moment of inertia to the cracked panels. This concept is later used in the dynamic analysis of the blast-loaded panels. The test panels will be treated as simply supported linear elastic plates, subjected to a uniformly distributed load. The analysis is conducted according to the following procedure:

- According to Timoshenko and Krieger (1959) for a rectangular flat plate of side dimensions *a* and *b*, the deformed shape f (x, y) can be represented by

$$f(x, y) = \sum_{m=1}^{\infty} \sum_{n=1}^{\infty} a_{mn} \sin\left(\frac{m \pi x}{a}\right) \sin\left(\frac{n \pi y}{b}\right) \tag{6.2}$$

where *m* and *n* are integers, *x* and *y* are orthogonal coordinates parallel to sides *a* and *b*, respectively, and a_{mn} are coefficients.

In order to calculate any particular coefficient ($a_{m' n'}$) of this series, first we multiply both sides of Equation 6.2 by the term ($\sin\left(\frac{n' \pi y}{b}\right) dy$) and then integrate it from 0

to b. Since $\int_0^b sin\left(\frac{n\pi y}{b}\right) sin\left(\frac{n'\pi y}{b}\right) dy = 0$ for $n \neq n'$, and

$\int_0^b sin\left(\frac{n\pi y}{b}\right) sin\left(\frac{n'\pi y}{b}\right) dy = \frac{b}{2}$ for $n = n'$, we obtain

$$\int_0^b f(x, y)\ sin\left(\frac{n'\pi y}{b}\right) dy = \frac{b}{2}\sum_{m=1}^{\infty} a_{mn'}\ sin\left(\frac{m\pi x}{a}\right) \tag{6.3}$$

Next, we multiply both sides of Equation 6.2 by the term $(sin\left(\frac{m'\pi x}{a}\right) dx)$ and integrate it from 0 to a

$$\int_0^a \int_0^b f(x, y)\ sin\left(\frac{n'\pi y}{b}\right)\ sin\left(\frac{m'\pi x}{a}\right) dx\ dy = \frac{ab}{4} a_{m'n'} \tag{6.4}$$

from which

$$a_{m'n'} = \frac{4}{ab}\int_0^a \int_0^b f(x, y)\ sin\left(\frac{n'\pi y}{b}\right)\ sin\left(\frac{m'\pi x}{a}\right) dx\ dy \tag{6.5}$$

For a given load distribution q_o over the plate surface, the general coefficient a_{mn} can be obtained from the above integration as

$$a_{mn} = \frac{4q_o}{ab}\int_0^a \int_0^b sin\left(\frac{m\pi x}{a}\right)\ sin\left(\frac{n\pi y}{b}\right) dx\ dy = \frac{16\, q_o}{\pi^2\, m\, n} \tag{6.6}$$

where m and n are odd integers.

For a given function $f(x, y)$, terms of the series presented in Equation 6.2 are known per Equation 6.6, thus the total deflection, w, equals

$$w = \frac{1}{\pi^4 D}\sum_{m=1}^{\infty}\sum_{n=1}^{\infty} \frac{a_{mn}}{\left(\frac{m^2}{a^2} + \frac{n^2}{b^2}\right)}\ sin\left(\frac{m\pi x}{a}\right) sin\left(\frac{n\pi y}{b}\right) \tag{6.7}$$

In case of uniform load of intensity q_o, all even terms will vanish, and the maximum deflection at the plate centre, where $x = a/2$ and $y = b/2$, is

$$w_{max} = \frac{16\, q_o}{\pi^6 D} \sum_{m=1}^{\infty} \sum_{n=1}^{\infty} \frac{(-1)^{\frac{m+n}{2}-1}}{m\, n \left(\frac{m^2}{a^2} + \frac{n^2}{b^2} \right)^2} \tag{6.8, a}$$

Equation 6.8 (a) presents a rapidly converging series, where considering the first term only would yield an adequate approximation. In the case of square plate, the maximum deflection is expressed as

$$w_{max} = \frac{4\, q_o\, a^4}{\pi^6 D} \tag{6.8, b}$$

Now consider the case of a square plate of side dimension a, subjected to a single load P that is partially distributed over a central area of dimensions $u \times v$, as shown in Figure 6.6. In this case, the general term a_{mn} in Equation 6.6 can be written as (Timoshenko and Krieger 1959)

$$a_{mn} = \frac{16P}{\pi^2\, m\, n\, u\, v} \sin\frac{m\pi\xi}{a} \sin\frac{n\pi\eta}{b} \sin\frac{m\pi u}{2a} \sin\frac{n\pi v}{2b} \tag{6.9}$$

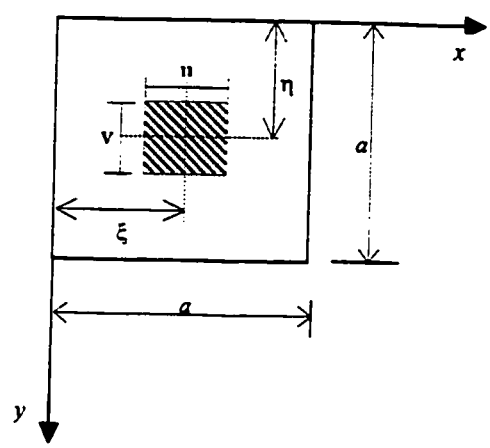

Figure 6.6: Square flat plate under partially distributed load

where ξ and η are the coordinates of the centre of the partially loaded area in Figure 6.6. In particular for $\xi = \eta = a/2$ and $u = v = a/3$, $a_{mn} = \dfrac{36\,P}{\pi^2\,a^2\,m\,n}$ which yields the maximum static deflection at the plate centre

$$w_{max} = \frac{0.01160\,P\,a^2}{D} \tag{6.10}$$

where the flexural rigidity, D, is defined in terms of the elastic modulus of concrete, E_c, the plate thickness, h, and the Poison's ratio, ν

$$D = \frac{E_c\,h^3}{12\left(1-\nu^2\right)} \tag{6.11}$$

Equation 6.10 is based on linear elasticity, therefore its inapplicability to reinforced concrete structures under loads greater than the cracking load is well-known. In practice, and according to the Canadian Concrete Design Code (CSA A 23.3, 1994), this equation may be applied to cracked reinforced concrete structure, provided the elastic rigidity D is replaced by an effective rigidity $E_c\,I_{eff}$, where E_c is the concrete Young's modulus and I_{eff} is an effective moment of inertia as given in the code (see Equation 6.46 in this chapter). The concept of an effective modulus is quite useful and is widely applied to statically loaded structures. Later in this thesis, the concept will be applied to blast- loaded panels to examine its applicability to dynamically loaded structures. However, in this section we will apply it to the statically loaded control panel CS_5. Agreement between measured load-central deflection curve of this panel and the predictions of Equation 6.10, using either D or $E_c\,I_{eff}$ will establish a benchmark with respect to the level of accuracy that can be expected in deflection

calculations even under static loads. Figure 6.7 shows the load- deflection curve of panel CS_5 when subjected to the partially distributed uniform load applied statically. The figure also shows the predictions of Equation 6.10 based on D and $E_c I_{eff}$.

In Figure 6.7 we observe that use of neither rigidity correctly predicts the actual deflection of the panel. Using the elastic rigidity underestimates the actual values while applying the effective rigidity overestimate them. The reason for the latter may be that large portions of the panel outside the loaded region were uncracked even when the load was relatively high.

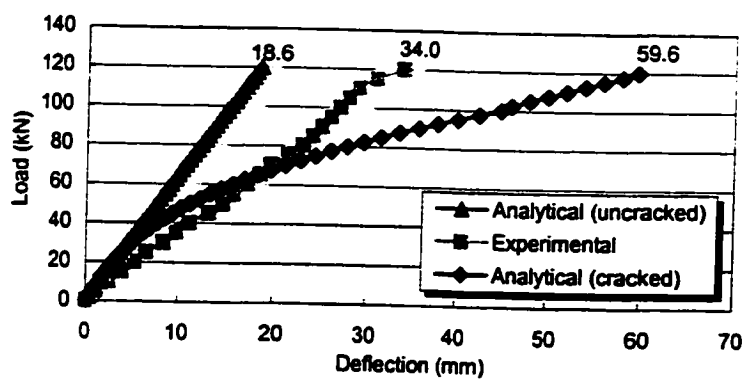

Figure 6.7: Comparison between experimental and analytical static central deflection of control panels

Let us examine the applicability of Equation 6.8 (b) to dynamically loaded panels. With reference to Table 6.1, CONWEP predictions for reflected pressures resulting from the detonation of 13.4, 22.4 and 33.4 kg ANFO charges located at 3-meter standoff distance are 2002.4, 3323.7, and 4937.6 kPa, respectively. We apply these pressures as uniformly distributed load over the surface of a control panel. The maximum elastic central deflections using D are 9.98, 16.6 and 24.6 mm for the three pressure values, respectively. Using $E_c I_{eff}$, the corresponding values are 32.1, 53.3

and 79.2 mm. This indicates nearly threefold increase in deflection values when using $E_c\ I_{eff}$ versus using D. Compared to the maximum deflections experienced by panels in the blast tests under those pressures, the use of $E_c\ I_{eff}$ results in remarkably unrealistic results. Even using D results in almost 2.5 to 3 times more deflection compared with the measured deflections (maximum of 14.6 mm).

It could be concluded from the preceding exercise that the analysis based on elastic theory is not a suitable method to predict the deflection of reinforced concrete panels under the effect of blast pressure, instead a full inelastic analysis must be performed, which is the topic of the following section.

6.3.2 Ultimate static capacity

The distributed load intensity required to fail the test panels is estimated below and the effect of applying different FRP retrofitting materials on their ultimate strength is examined. The ultimate moment capacity of the panels will be calculated using the strain compatibility method. The pressure required to fail the test panels is calculated by the yield line method. The experimental and the analytical results are compared in order to assess the adequacy of this static analysis approach.

Control panels

First, the ultimate static strength of these panels will be calculated neglecting the effect of strain rate, but the latter will be considered subsequently to assess its influence on the ultimate strength of the test panels. Using standard methods of flexural analysis, the

nominal ultimate moment capacity of the control panel is M_u = 5.2 kN.m/m. (see Appendix *A* for the detailed calculation).

Second, using the yield line theory (Ghali and Neville 1976), the ultimate moment per unit length in a square simply supported flat plate of side dimension, *a*, is related to the applied ultimate uniform load, q_u, as

$$q_u = \frac{24\,M_u}{a^2} \tag{6.12}$$

Substituting the value of M_u = 5.2 kN.m/m into Equation 6.12, the corresponding ultimate load intensity for the un-retrofitted panels is found to be 124.8 kPa. It is obvious from such an analysis that the control panels cannot sustain the rather high pressures predicted by CONWEP. Yet, in the test the control panel did not fail when it was subjected to the blast pressures generated by the 13.4 kg charge. The latter brings into question the validity of the elastic static method of analysis with respect to the current panels.

FRP-retrofitted panels

A CFRP-retrofitted panel is analyzed in detail in Appendix *B* to illustrate the strain compatibility method used to determine the ultimate moment capacity of the FRP-retrofitted panels. The effect of FRP layers bonded to the compressive face and to the tensile face transverse to the direction of analysis is neglected. Accordingly, only one layer of CFRP sheet, with an elastic modulus of 230 GPa, a tensile strength of 3480 MPa and a cross-sectional area of 55-mm^2 is considered in the analysis. The ultimate moment is calculated as M_u = 16.9 kN.m/m. Substituting M_u = 16.9 kN.m/m in Equation 6.12 gives a maximum distributed load of 405.6 kPa, which indicates more than 3 times

increase in the ultimate strength of the CFRP panel over the control panel. It is recognized that the FRP sheet is not applied over the entire surface of the panel and FRP does not yield, but the objective of this exercise is to obtain a rough estimate of the ultimate moment capacity of the retrofitted panels.

As explained earlier, panel CS_5 was statically tested under a partially distributed load. The failure load was found to be 120.1 kN. The corresponding value using the yield line theory is 124.8 kN, which agrees reasonably well with the experimental result, Figure 6.8. Note, however, that in the static tests the panels were not exactly subjected to uniform load over the entire surface, therefore the observed difference is not unexpected. On the other hand, using Equation 6.12, the load required to fail the CFRP retrofitted panel CSS_5 in flexure would be 405.6 kN. However this panel failed at a load of 150.1 kN in the test. But the panel failure mode was punching shear rather than flexure. Using CSA A23.3 (1994) provisions, the ideal punching shear resistance of all the panels prior to blast testing would be the same and would be equal to 182.15 kN (see Appendix B). It is clear that panel CSS_5 did not achieve its ideal strength, but we can use the actual punching capacity of this panel as reference when we determine the post-blast residual strength of the tested panels.

With reference to Table 5.17, we observe that panels CSS_1 and GSS_1 subjected to 22.4-kg charge reached 150 kN and 140 kN ultimate load while the corresponding unretrofitted panel CS_4 failed at 80 kN. Similar observations can be made about the panels subjected to the 33.4-kg charge. Thus the residual tests provide useful information about the extent of damage suffered by the concrete.

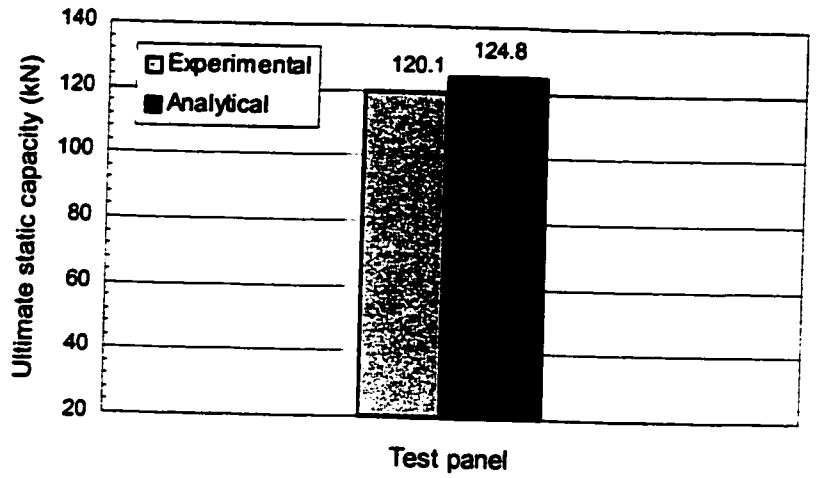

Figure 6.8: Experimental vs. analytical ultimate static capacity of control panel CS_5

6.4 Dynamic Response

The detailed dynamic response analysis of blast-loaded reinforced concrete panels should account for the nonlinearity of material, geometry and boundary conditions. One method that is sometime employed for dynamic analysis is the equivalent static method. The method uses static analysis with a load amplification factor that accounts for the dynamic effect of loads. Dynamic phenomena such as strain rate effects on material strength, time variation of loads, mass, stiffness, and plastic deformations are not included. Accordingly, the method yields rather crude results, and is not recommended for the dynamic analysis of blast-loaded structures (Biggs, 1964). For example, if we use the elastic deflection expression given in Equation 6.8 in conjunction with the uniform reflected pressures shown in Table 6.1, we would obtain excessively high moments, at least an order of magnitude larger than the ultimate moment capacity of the panels. Consequently, such an approach should not be used in practice.

Alternatively, depending on the degree of accuracy required, two possible approaches are available to analyze the interaction between blast loading and structures; namely, simple analytical blast models, which mainly use empirical formulae to determine the blast loading parameters, coupled with detailed dynamic analysis to predict the structural response, or hydrocodes, which use computational fluid dynamics to simulate the blast-structure interaction (Anderson, 1987). The later is complex and beyond the scope of the present work. This section presents a dynamic analysis method which is a compromise between complexity and possibly high accuracy on the one hand and relative simplicity and acceptable accuracy on the other.

6.4.1 Elastic dynamic analysis

A closed-form solution is derived based on a number of simplifying assumptions to determine the elastic dynamic and inelastic dynamic (see next section) response of reinforced concrete flat panels subjected to exponentially decaying blast loading. Gupta *et al.*, (1987) introduced a simplified dynamic analysis, which is based on the assumption of linear elasticity. This analysis was modified here and extended to account for the non-linear effect of concrete cracking and the FRP surface treatments on the dynamic behaviour of the test specimens. The target plate is idealized as a symmetric undamped single degree-of-freedom (SDOF) elastic system with simply supported edges as shown in Figure 6.9 (a). Although during the blast tests the plate was lightly clamped to the supporting frame, nevertheless the simply supported edge adequately represents the test condition.

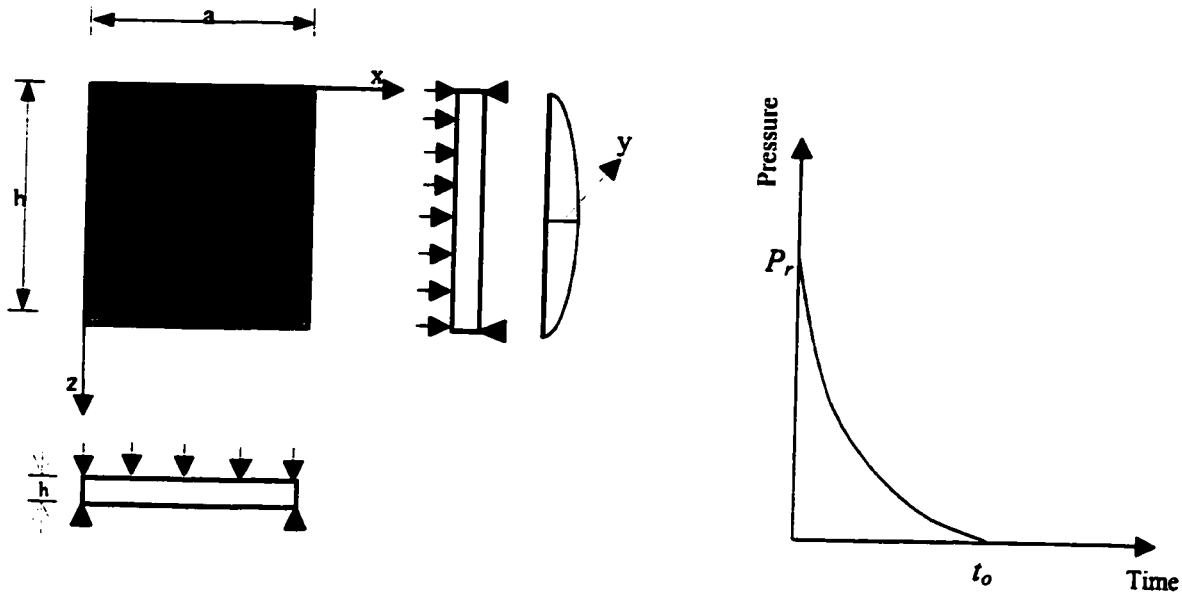

(a): Plate configurations

(b): Applied blast pressure

Figure 6.9: Geometry and loading conditions of simply supported flat plate

The plate is initially assumed to behave linear-elastically, taking a deformed shape according to a modified Navier form (Timoshenko and Krieger, 1959).

$$y = A_1 \sin\left(\frac{\pi x}{a}\right) \quad \sin\left(\frac{\pi z}{b}\right) \tag{6.13}$$

Blast loading is idealized as a decaying function with a maximum reflected pressure, P_r, and positive duration, t_o, Figure 6.9 (b). The dynamic response of the target plate is dominated by the impulsive loading regime, and the reflected impulse is calculated as the area under the pressure time profile as discussed in Section 2.8.3. The evaluation of blast loading starts by calculating the scaled distance, Z, and using the cube-root scaling law as follows:

$$Z = \frac{R}{W^{\frac{1}{3}}} \tag{6.14}$$

where W is the equivalent TNT weight and R is the distance between the plate surface and the charge centre. Knowing the scaled distance, the incident and reflected blast wave parameters, such as incident and reflected pressures, incident and reflected impulses, time of arrival and positive phase duration can be estimated using blast charts in (TM 5-1300, 1990) or using CONWEP.

To determine the pressure-time profile, the non-dimensional decay coefficient, $\alpha = t_o/\theta$, needs to be determined. This is achieved by assuming that the reflected pressure decays according to the modified Friedlander exponential function as (Baker, 1973)

$$P(t) = P_r\left(1 - \frac{t}{t_o}\right)e^{\frac{-\alpha t}{t_o}} \tag{6.15}$$

where t is the elapsed time since the arrival of the shock wave. The reflected impulse, I_r, acting on the plate surface is computed as the time integration of the pressure calculated from the time of arrival, t_A, to the end of the positive phase, $t_A + t_o$, and is given by:

$$I_r = \int_{t_A}^{t_A + t_o} P(t)\,dt \tag{6.16}$$

Substituting for $P(t)$ from Equation 6.15 into Equation 6.16 and performing the integration, the specific reflected impulse is obtained as (Baker, 1973)

$$I_r = P_r\, t_o\left[\frac{1}{\alpha} - \frac{1}{\alpha^2}\left(1 - e^{-\alpha}\right)\right] \tag{6.17}$$

This concludes the calculations of the blast wave parameters, which will be implemented into the following energy solution to evaluate the dynamic response of the panels.

The Lagrangian form of energy requires that for a system to be in equilibrium, the work done by the internal forces (kinetic energy, K, and strain energy, U) must equal to the work done by the external loads, W_e. Since A_1 is the time-dependant amplitude of the plate transverse displacement, y, this energy relation can be expressed as follows:

$$\frac{d}{dt}\left[\frac{\partial K}{\partial \dot{A}_1}\right]+\frac{\partial U}{\partial A_1}=\frac{\partial W_e}{\partial A_1} \tag{6.18}$$

The kinetic energy of a differential plate element with sides dx and dz is expressed in terms of the plate mass per unit area, m, and the plate velocity as

$$dK=\frac{1}{2}\,m\left(\dot{y}\right)^2\,dxdz \tag{6.19}$$

The total kinetic energy, K, is obtained by inserting the expression for y from Equation 6.13 into the above equation, and integrating dK over the plate surface

$$K=\frac{1}{2}m\left(\dot{A}_1\right)^2\int_0^a\int_0^b\,[\,sin\left(\frac{\pi x}{a}\right)sin\left(\frac{\pi z}{b}\right)]^2\,dx\,dz=\frac{1}{8}\,m\left(\dot{A}_1\right)^2 a\,b \tag{6.20}$$

Hence, the first term in Equation 6.18 can be obtained by differentiating K with respect to $\dot{A}_1$ as follows

$$\frac{d}{dt}\left(\frac{\partial K}{\partial \dot{A}_1}\right)=\frac{d}{dt}\left\{\frac{\partial}{\partial \dot{A}_1}\left[\frac{1}{8}\,m\,ab\left(\dot{A}_1\right)^2\right]\right\}\;=\frac{1}{4}\,m\,ab\,\ddot{A}_1 \tag{6.21}$$

The strain energy of the system can be written in terms of the modulus of elasticity, E, the plate thickness, h, and the Poisson's ratio, ν, as

$$U=\frac{Eh^3}{24(1-\nu^2)}\int_0^a\int_0^b[\left(\frac{\partial^2 y}{\partial x^2}\right)^2+\left(\frac{\partial^2 y}{\partial z^2}\right)^2+2\nu\left(\frac{\partial^2 y}{\partial x^2}\right)\left(\frac{\partial^2 y}{\partial z^2}\right)+2(1-\nu)\left(\frac{\partial^2 y}{\partial x\partial z}\right)^2]dxdz \quad (6.22)$$

Substituting for y from Equation 6.13, yields

$$\frac{\partial^2 y}{\partial x^2}=-A_1\left(\frac{\pi^2}{a^2}\right)\sin\left(\frac{\pi x}{a}\right)\sin\left(\frac{\pi z}{b}\right) \quad (6.23)$$

$$\frac{\partial^2 y}{\partial z^2}=-A_1\left(\frac{\pi^2}{b^2}\right)\sin\left(\frac{\pi x}{a}\right)\sin\left(\frac{\pi z}{b}\right) \quad (6.24)$$

$$\frac{\partial^2 y}{\partial x\,\partial z}=A_1\left(\frac{\pi^2}{ab}\right)\cos\left(\frac{\pi x}{a}\right)\cos\left(\frac{\pi z}{b}\right) \quad (6.25)$$

Substituting the latter relations in Equation 6.22 and performing the integration, the total strain energy can be written as:

$$U=\frac{Eh^3}{24(1-\nu^2)}\times\frac{ab\pi^4A_1^2}{4}\left[\left(\frac{1}{a}\right)^2+\left(\frac{1}{b}\right)^2\right]^2=\frac{Eh^3\,\pi^4\,abA_1^2}{96(1-\nu^2)}\left[\left(\frac{1}{a}\right)^2+\left(\frac{1}{b}\right)^2\right]^2 \quad (6.26)$$

Thus, the second term in Equation 6.18 can be obtained by differentiating U in the above Equation with respect to A_1

$$\frac{\partial U}{\partial A_1}=\frac{Eh^3\,\pi^4\,abA_1}{48(1-\nu^2)}\left[\left(\frac{1}{a}\right)^2+\left(\frac{1}{b}\right)^2\right]^2 \quad (6.27)$$

The external work, W_e, done by the uniformly distributed load $P(t)$ can be obtained as:

$$W_e=P(t)\int_0^a\int_0^b A_1\sin\left(\frac{\pi x}{a}\right)\sin\left(\frac{\pi z}{b}\right)dxdz=4P(t)abA_1/\pi^2 \quad (6.28)$$

Now the right hand side in Equation 6.18 can be obtained by differentiating W_e in the above equation with respect to A_1 as follows:

$$\frac{\partial W_e}{\partial A_1} = 4P(t)\frac{ab}{\pi^2} \tag{6.29}$$

Substituting Equations 6.21, 6.26 and 6.29 into Equation 6.18 yields

$$\frac{1}{4}\,\mathrm{mab}\,\ddot{A}_1 + \frac{E h^3\,\pi^4\,\mathrm{ab}\,A_1}{48\left(1-\nu^2\right)}\left[\left(\frac{1}{a}\right)^2 + \left(\frac{1}{b}\right)^2\right]^2 = 4P(t)\frac{ab}{\pi^2} \tag{6.30}$$

Multiplying all terms in Equation 6.29 by $(4/mab)$ results in

$$\ddot{A}_1 + \frac{E h^3}{12\left(1-\nu^2\right)}\frac{\pi^4}{m}\left[\left(\frac{1}{a}\right)^2 + \left(\frac{1}{b}\right)^2\right]^2 A_1 = P(t)\frac{16}{m\pi^2} \tag{6.31}$$

Introducing the notation, $\omega^2 = \{(D\pi^4/m)[(1/a^2)+(1/b^2)]^2\}$ and $k_1 = 16/m\pi^2$, where D is the out of plane rigidity and ω is the natural frequency of the panel, the above equation can be simplified as

$$\ddot{A}_1 + \omega^2 A_1 = k_1 P(t) \tag{6.32}$$

Now, the load function $P(t)$ in Equation 6.15 can be substituted in the equation above as

$$\ddot{A}_1 + \omega^2 A_1 = k_1 P_r\left(1 - t/t_o\right)e^{-\alpha\left(t/t_o\right)} \tag{6.33}$$

Choosing the coefficients $\phi = k_1 P_r$, $\beta = k_1 P_r/t_o$ and $\gamma = \alpha/t_o$, we obtain the final form of the equation of motion. For a simply supported flat plate subjected to an exponentially decaying blast wave resulting from the detonation of high explosive charge, the equation of motion is given in the following general form

$$\ddot{A}_1 + \omega^2 A_1 = (\phi - \beta t)\,e^{-\gamma t} \tag{6.34}$$

Equation 6.33 represents the equation of motion of the plate under the effect of the forcing function *P(t)*. In order to accurately predict the dynamic response, the solution to the plate equation of motion is divided into two phases; (1) the forced vibration phase within the period $t \leq t_o$, where t_o is the positive phase duration, (2) the free vibration phase when $t > t_o$, i.e. when the pressure load no longer acts on the plate.

Forced vibration phase

The general solution of Equation 6.34 within time $t \leq t_o$ is

$$A_1(t) = A \sin(\omega t) + B \cos(\omega t) + \left(\frac{1}{\rho}\right)\left(\phi - \frac{2\beta\gamma}{\rho} - \beta t\right) e^{-\gamma t} \tag{6.35}$$

where $\rho = \gamma^2 + \omega^2$, and A and B are constants of integration. Applying the two initial boundary conditions ($A_1 = \dot{A}_1 = 0$ @ $t = 0$) to the above equation, A and B are found as

$$A = \left(\frac{\gamma}{\rho\omega}\right)\left(\delta + \frac{\beta}{\gamma}\right) \text{ and } B = \left(\frac{1}{\rho}\right)\left(\phi - \frac{2\beta\gamma}{\rho}\right) \tag{6.36}$$

$$\text{where } \delta = \left(\phi - \frac{2\beta\gamma}{\rho}\right) \tag{6.37}$$

Knowing the constants of integration leads to the time-dependant displacement amplitude of a rectangular flat plate subjected to an air blast

$$A_1(t) = \left(\frac{1}{\rho}\right)\left[\left(\delta + \frac{\beta}{\gamma}\right)\left(\frac{\gamma}{\omega}\right) \sin(\omega t) - \delta \cos(\omega t) + (\delta - \beta t) e^{-\gamma t}\right] \tag{6.38}$$

The time-dependent amplitude of the plate velocity, $\dot{A}_1(t)$, can be determined by differentiating Equation 6.38 with respect to time, which yields

$$\dot{A}_1(t) = \left[\left(\frac{\delta\gamma + \beta}{\rho}\right)\cos(\omega t)\right] + \left(\frac{\delta\omega}{\rho}\right)\sin(\omega t) + \left(\frac{e^{-\gamma t}}{\rho}\right)(\gamma\beta t - \beta - \delta\gamma) \quad (6.39)$$

At time $t = 0$, the initial velocity of the plate according to Equation 6.39 equals zero, which agrees with the initial condition of the target plat at rest.

Similarly, the plate acceleration-time history can be directly evaluated by substituting the value of $A(t)$ obtained above into Equation 6.34, which results in

$$\ddot{A}_1 = k_1 P_r \left(1 - \frac{t}{t_o}\right) e^{-\alpha\left(\frac{t}{t_o}\right)} - \omega^2 A_1 \quad (6.40)$$

Substituting values of $\omega^2 = \{(D\pi^4/m)[(1/a^2)+(1/b^2)]^2\}$ and A_1 from Equation 6.38 into the above equation, the plate acceleration-time history is given by

$$\ddot{A}_1 = k_1 P_r \left(1 - \frac{t}{t_o}\right) e^{-\alpha\left(\frac{t}{t_o}\right)} - \left(\frac{\omega}{\rho}\right)\left(\delta + \frac{\beta}{\gamma}\right)[\gamma \sin(\omega t)] - \left(\frac{\omega^2}{\rho}\right)\left[(\delta\cos(\omega t)) - (\beta t - \delta)e^{-\gamma t}\right] \quad (6.41)$$

At rest, the plate initial acceleration, unlike the velocity, does not equal to zero, as substituting $t = 0$ in Equation 6.41 yields an initial acceleration

$$\ddot{A}_{1\,at\,t=0} = k_1 P_r = \frac{16 P_r}{m \pi^2} \quad (6.42)$$

The peak bending stress that occurs at the plate centre and attained at time equals to the positive duration, t_o, can be obtained based on elastic theory (Gupta *et al.*, 1987)

$$\sigma_{x\,max} = \frac{E h \pi^2}{2(1-\nu^2)} \left[\left(\frac{1}{b^2}\right)+\left(\frac{\nu}{a^2}\right)\right] \left[\frac{\delta\gamma+\beta}{\rho\omega}\sin(\omega t_o)-\left(\frac{\delta}{\rho}\right)\cos(\omega t_o)+\frac{\delta-\beta t_o}{\rho}e^{-\gamma t_o}\right] \quad (6.44)$$

Since the frequency is dependent on the elastic modulus of concrete, and since the elastic modulus is a function of the strain rate, it is required to take the latter into account. The effect of strain rate will be considered through the dynamic increase factor (DIF). The strain rate was experimentally determined as 200 s^{-1}. Substituting this value in Equation 3.7 given by Malvar (1998), the *DIF* for the reinforcing steel is calculated as 1.25. The *DIF* is multiplied by the static yield stress and the elastic modulus of the steel, resulting in new dynamic properties equal to 500 MPa and 250 GPa, respectively. A similar procedure was followed to evaluate the effect of strain rate on concrete properties using the suggestions of Malvar and Ross (1988). The dynamic elastic modulus, compressive strength and tensile strength are calculated as 33 GPa, 48 MPa and 4.8 MPa, respectively, for the concrete used in the current study. The dynamic properties of the reinforcing steel and concrete will be used throughout the analysis to calculate the dynamic response and strength of the test panels.

Before we can commence the calculation of the elastic dynamic response of the panels, we need to determine their natural frequency of vibration. Substituting values of D, m, a and b into the relation $\omega^2 = \{(D\pi^4/m)[(1/a^2)+(1/b^2)]^2\}$ results in a value of the natural frequency of the plate equal to 1390.5 rad/sec. The corresponding plate natural period of vibration, T, equals to $2\pi/\omega$ and is 4.5 msec. Given the small dimensions of the test panels, this value for the natural period is not unexpected. Now it is of importance to determine the duration ratio of test panels. For the very short positive durations recorded from the tests (1.29 to 3.17 msec, Table 6.1), the duration ratio, t_o/T, is calculated as 0.28

to 0.4. Although the duration ratio is higher than the limit of 0.1, the impulsive loading regime is still dominating the panel response. With the load and natural frequency of the panels known, one can proceed to calculate time histories of the panels central deflection, velocity, acceleration and bending stress using Equations 6.38, 6.39, 6.41 and 6.44, respectively. Such calculations can be conveniently performed using the computer program MATLAB [46] and results of one such analysis for the control panels are shown in Table 6.2. Notice that blast wave parameters, including reflected pressure, reflected impulse and positive duration, predicted by CONWEP for the three charge weights are used to find the responses in Table 6.2.

As stated earlier, the solution for the forced-vibration phase is valid till time equals to or less than the positive duration. Accordingly, the mid-span deflection of the panels is monitored over a time period t_o. Eleven time intervals are selected, starting with $t_1 = 0$ to $t_{12} = t_o$, where t_o equals to the positive duration as measured in the field. Table 6.2 shows results of the elastic dynamic analysis including central deflection, velocity, acceleration and stress under the effect of blast loads resulting from the three charge weights. The responses were calculated for a time equal to the positive duration corresponding to charge weights of 13.4, 22.4 and 33.4 kg, which are 3.8, 4.8 and 5.4 msec, respectively.

The main interest is in the central displacement and velocity of panels at the end of the time interval t_o, as they will be considered as initial conditions when analyzing the free vibration response. For the 13.4-kg charge in Table 6.2, the central deflection and velocity are 3.5 mm and -9.6 m/sec, respectively, while the corresponding values in the case of the 22.4-kg charge are 7.7 mm and –0.9 m/sec, and for the 33.4-kg are 8.2 mm

and 15.4 m/sec. The elastic dynamic results are further illustrated in Figures 6.10 to 6.12. In Figure 6.10, the calculated mid-span deflections of the control panel under the three impulse levels are shown, in which the maximum deflections for the three load charges are found to be 3.6, 7.9 and 9.4 mm, respectively, corresponding to 1.9, 2.0 and 2.1 msec.

The central velocity-time and acceleration-time histories under the three impulse levels are shown in Figures 6.11 and 6.12, respectively. It can be noticed that the increase in the applied reflected impulse resulted in an increase in the velocity and acceleration of the test panels.

Table 6.2: Elastic dynamic response under various reflected impulses (Forced-vibration)

845 kPa.msec reflected impulse (13.4-kg charge)					1247 kPa.msec reflected impulse (22.4-kg charge)					1686 kPa.msec reflected impulse (33.4- kg charge)				
Time (ms)	Def. (mm)	Vel. (m/s)	Acc. (m/s^2)	Stress (MPa)	Time (ms)	Def. (mm)	Vel. (m/s)	Acc. (m/s^2)	Stress (MPa)	Time (ms)	Def. (mm)	Vel. (m/s)	Acc. (m/s^2)	Stress (MPa)
0.0	0.0	0.0	19046	0.0	0.0	0.0	0.0	31497	0.0	0.0	0.0	0.0	46858	0.0
1.4	-3.2	8.7	-11767	0.0	1.3	-5.6	22.4	-11471	0.0	1.2	-5.6	38.1	-7466	0.0
1.6	-3.6	3.4	-15184	-39.3	1.7	-7.2	14.3	-21901	-47.0	1.7	-8.1	28.3	-27619	-54.8
1.9	-3.6	-2.7	-16646	-19.8	2.0	-7.9	2.1	-27999	-22.6	2.1	-9.4	9.3	-40802	-23.6
2.1	-3.3	-9.0	-16007	16.8	2.4	-7.4	-11.8	-28699	24.8	2.5	-9.3	-14.4	-44000	35.0
2.3	-2.6	-14.7	-13360	39.1	2.7	-6.0	-24.6	-23904	51.6	2.9	-7.4	-36.8	-36515	65.3
2.6	-1.6	-19.0	-9030	32.1	3.1	-3.5	-34.0	-14513	36.7	3.3	-4.2	-52.6	-20127	40.6
2.8	-0.4	-21.5	-3530	1.1	3.4	-0.5	-38.1	-2251	-10.4	3.7	-0.2	-57.8	1317	-24.8
3.1	0.8	-21.7	2487	-32.8	3.8	2.5	-36.2	10638	-58.1	4.2	3.7	-51.2	22799	-88.2
3.3	2.0	-19.6	8318	-47.1	4.1	5.2	-28.2	21801	-74.3	4.6	6.8	-33.9	39294	-106.9
3.6	3.0	-15.4	13277	-32.0	4.5	7.0	-15.7	29198	-47.0	5.0	8.4	-9.9	46938	-66.8
3.8	3.5	-9.6	16782	3.1	4.8	7.7	-0.9	31472	7.4	5.4	8.2	15.4	43928	8.7

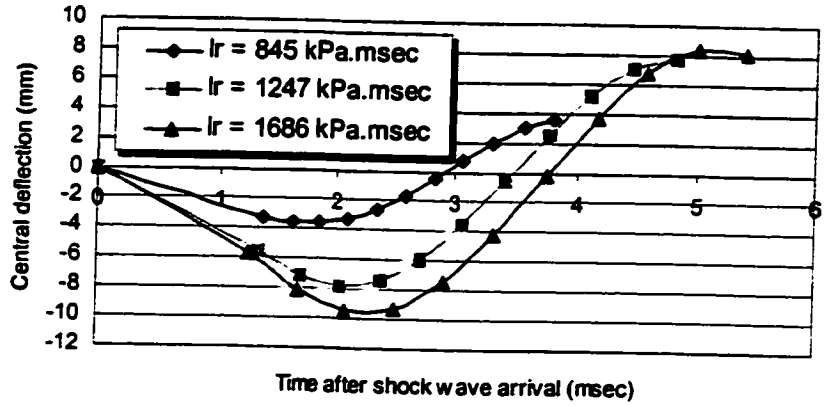

Figure 6.10: Elastic central displacement history of control panels under various reflected impulses (Forced-vibration phase)

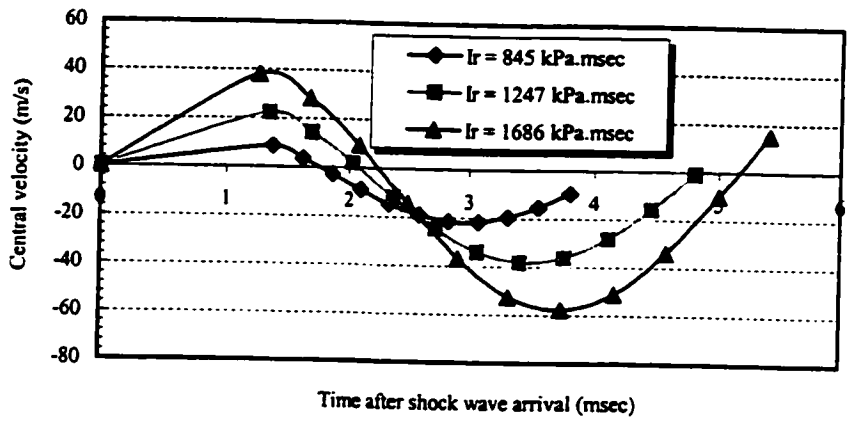

Figure 6.11: Elastic central velocity history of control panels under various reflected impulses (Forced-vibration phase)

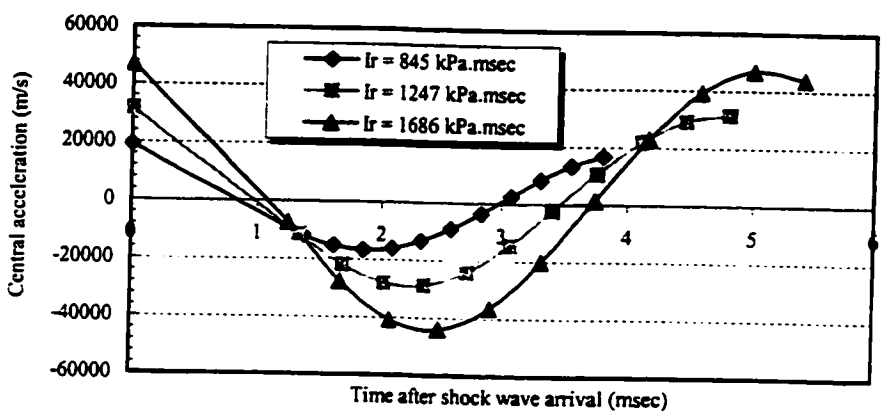

Figure 6.12: Elastic central acceleration history of control panels under various reflected impulses (Forced-vibration phase)

The stresses calculated by this method are extremely high, reaching maximum of 47, 74 and 106 MPa for the three impulse levels (Tables 6.2). Obviously, the concrete will not be able to sustain such high stresses. In fact, the concrete stresses would be distributed nonlinearly and in the following the effect of the concrete nonlinearity is explained.

The stress state of the concrete section during its loading history can be classified according to its maximum value as shown in Table 6.3. The classification in Table 6.3 assumes three possible states for any section, namely uncracked, cracked elastic and cracked inelastic. The appropriate moment of inertia corresponding to each state is indicated in the table. The criteria in Table 6.3 may be used to select the appropriate moment of inertia according to the maximum concrete stress acting on section. It is obvious that analyses for the first two states, where the concrete behaviour is still linear, can be easily conducted. In the third state, the concrete non-linearity dominates the behaviour of the section accompanied by high compressive stresses, and a detailed non-linear analysis should be considered to evaluate the moment-curvature relationship, which will follow. This type of analysis is of importance in order to realistically understand the concrete behaviour, and to use the proper moment of inertia.

Table 6.3: Stress state of a reinforced concrete section at different loading stages

Maximum concrete stress	$\sigma_{t\,max} < f_r$	$\sigma_{c\,max} < 0.5 f_c$	$\sigma_{c\,max} > 0.5 f_c$
Concrete behaviour	Uncracked	Cracked (linear)	Cracked (non-linear)
Stress block diagram	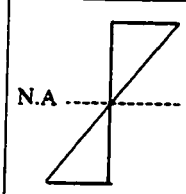	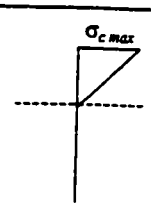	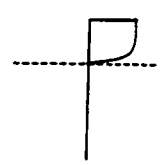
Moment of inertia to be considered in the analysis	I_{gross}	I_{eff}	I_{cr}

Free vibration phase

The effect of blast load lasts for a maximum time equals to the positive phase duration. Following this, at time $t > t_o$, the blast pressure is no longer applied and the plate response can be treated as a free vibration response initiated by the displacement and velocity reached at the end of the previous phase. The response amplitude of the free-vibration phase is denoted as $A_2(t)$, and is given by

$$A_2(t) = \left(\frac{\dot{A}(t_o)}{\omega}\right) \sin(\omega t') + A(t_o)\cos(\omega t') \tag{6.45}$$

where $t' = t - t_o$. This is similar to the forced vibration phase (see Equation 6.35), but the particular integral, containing the effect of the load, vanishes. The two coefficients $A(t_o)$ and $\dot{A}(t_o)$ are the central displacement and velocity experienced by the panel at the end of the forced vibration phase, as given in Table 6.2, and will be used as initial boundary conditions in the current phase. The superposition of the plate responses in the two vibration phases (Equations 6.38 and 6.45) represents the full dynamic response.

6.4.2 Inelastic dynamic analysis

The inelastic dynamic analysis was carried out assuming that the displacement shape function does not change with either the plate stiffness or with the time, and is governed only by the geometric and boundary conditions (Pan and Watson, 1996). Thus, the shape function introduced in Equation 6.13 can be applied to the inelastic dynamic analysis.

The maximum deflection of the plate is influenced by the change in its stiffness and/or the loading condition. Keeping the applied load constant, any reduction in the plate

stiffness increases its maximum deflection. Stiffness reduction is caused by concrete cracking and concrete nonlinearity. The effect of cracking can be taken into account by considering the effective moment of inertia of the plate section instead of its gross moment of inertia. Consequently, the flexural rigidity, D, that was used earlier in the elastic dynamic analysis will be replaced by the effective rigidity, $E_{cd}\, I_{cr}$, of the plate section. Here, E_{cd} is the dynamic modulus of concrete.

According to the CSA standard A23.3 (1994), the effective moment of inertia, I_{eff}, is

$$I_{eff} = I_{cr} + \left(I_{gross} - I_{cr}\right)\left(\frac{M_{cr}}{M_a}\right)^3 \qquad \leq I_{gross} \tag{6.46}$$

where I_{cr} and I_{gross} are the cracked and gross moments of inertia, respectively, M_{cr} is the cracking moment and M_a is the maximum moment acting on the section. The cracking moment is calculated using

$$M_{cr} = \left(\frac{f_{rd}\, I_{gross}}{y_t}\right) \tag{6.47}$$

where f_{rd} is the dynamic modulus of rupture of concrete and y_t is the distance from the neutral axis to the extreme tension fibre. In calculating the gross moment of inertia, the Poison's effect is taken into account as follows

$$I_{gross} = \frac{h^3}{12\,(1-\nu^2)} \tag{6.48}$$

where I_{gross} is expressed per unit width of the plate (Ghali and Favre, 1976).

The cracked moment of inertia is calculated using the transformed section concept as

$$I_{cracked} = \frac{b(y_c)^3}{3} + nA_s(d - y_c)^2 \tag{6.49}$$

where n is the modular ratio, i.e. the ratio of the elastic modulus of steel to elastic modulus of concrete, A_s is the reinforcement area, d is the effective depth and y_c is the distance between the neutral axis in the cracked transformed section and the extreme compression fibre. Section cracking is assumed to occur right at the beginning of the free vibration phase, and thus the cracked moment of inertia of the section is used in the calculation of the cracked natural frequency. Accordingly, the value $E_{cd}I_{cr}$ replaces the flexural rigidity, D, resulting in a new coefficient $\omega^2_{cracked}$ as follows

$$\omega^2_{cracked} = \frac{E_{cd} I_{cr}\, \pi^4}{m} \left[\left(\frac{1}{a^2}\right) + \left(\frac{1}{b^2}\right)\right]^2 \tag{6.50}$$

Using the effective rigidity $E_{cd}\, I_{cr}$, the natural frequency expressed in Equation 6.50 is calculated as 450.6 rad/sec. In order to calculate the dynamic response of the panels in the free-vibration phase, the effect of section cracking, by using the appropriate section rigidity in calculating the natural frequency, ω, should be taken into account. This leads to the definition of the natural period of vibration of the panels in the free vibration phase, and thus the time over which the response is monitored.

Table 6.4 gives a sample calculation of the natural frequency of the panels under the effect of 845 kPa.msec reflected impulse (13.4-kg charge), where the uncracked and cracked frequencies are calculated using the expression given earlier for the uncracked ω and that of the cracked ω in Equation 6.50. In Table 6.4, it can be noticed that in the forced vibration phase the test panel is not expected to vibrate for a full period, since the

time for this phase (3.8 msec) is les than the period T (4.5 msec). On the other hand, within a time interval of about 14 msec, the panel is expected to have one full period within the free vibration phase.

Table 6.4: Natural frequencies of control panels under I_r = 845 kPa.msec (t_o = 3.8 msec)

Time after shock arrival (msec)	Panel state	Vibration response	Natural frequency, ω, (rad/sec) Uncracked	Cracked	T=2π/ω (msec)
0	Elastic	Forced	1390.5		4.5
1.9	Elastic	Forced	1390.5		4.5
3.8	Elastic	Forced	1390.5		4.5
3.9	Inelastic	Free		450.6	13.95
8.45	Inelastic	Free		450.6	13.95
13.1	Inelastic	Free		450.6	13.95
17.75	Inelastic	Free		450.6	13.95

Results of the inelastic dynamic analysis for control panels, under the effect of the three impulse levels are given in Table 6.5. The maximum inelastic central deflections are 4.7, 11.3 and 15.9 mm, which are 30 % to 50 % higher than the corresponding elastic dynamic deflections calculated earlier. The velocity and the acceleration histories showed an increase by increasing the charge weight. As the main focus at this stage is on the dynamic central deflection, Figure 6.13 shows the dynamic deflection-time history of the control panels under the three impulse levels, where both the elastic and inelastic responses are super positioned to illustrate the full response of the panels within a time equals to the natural period of the free vibration phase. A deflection increase of twofold is noticed by increasing the charge weight by 67 % from 13.4 to 22.4 kg, while the 50 % increase in the charge weight from 22.4 to 33.4 kg is accompanied by a deflection increase of about 41 %. In all cases, the panels completed full vibration period within a time equal to its natural period based on the cracked section properties (14 msec).

Table 6.5: Inelastic dynamic response under various reflected impulses (Free-vibration)

845 kPa.msec reflected impulse (13.4-kg charge)				1247 kPa.msec reflected impulse (22.4-kg charge)				1686 kPa.msec reflected impulse (33.4- kg charge)			
Time (ms)	Def. (mm)	Vel. (m/s)	Acc. (m/s^2)	Time (ms)	Def. (mm)	Vel. (m/s)	Acc. (m/s^2)	Time (ms)	Def. (mm)	Vel. (m/s)	Acc. (m/s^2)
3.8	3.5	0.0	80071	4.8	7.7	0.0	118164	5.4	8.2	0.0	159764
4.5	4.7	0.0	80071	5.6	6.4	0.0	118164	5.9	-1.3	0.0	159764
5.9	-0.4	21.2	16506	6.2	-0.9	32.8	-10452	6.8	-10.4	43.3	-43726
6.8	-3.1	9.7	-69000	6.8	-7.5	-6.2	-117232	7.7	-15.9	-25.9	-141129
7.7	-4.7	-18.6	-58914	7.7	-11.3	-38.4	12093	9.0	-15.9	-40.7	101642
9.0	-4.7	-24.3	32848	9.0	-11.3	1.3	117913	9.8	-13.4	34.9	100970
10.2	-3.1	0.5	80061	10.2	-7.5	33.5	-12205	10.2	-10.4	19.7	-141574
11.5	-0.4	22.0	17761	11.5	-1.0	-6.0	-117143	11.5	-1.4	-49.3	-43008
12.9	2.4	10.9	-68421	12.9	5.8	-37.7	13680	12.9	8.2	-5.8	159696
14.0	4.5	-17.5	-60010	14.0	10.7	2.4	117655	14.0	15.0	46.0	-20758

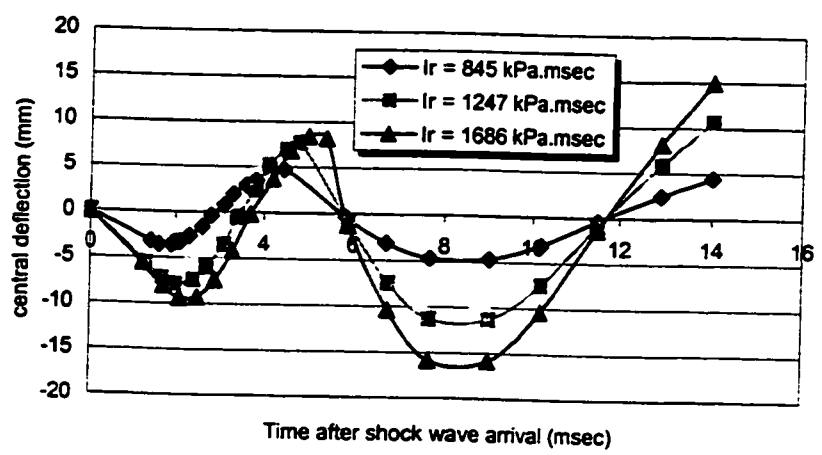

Figure 6.13: Dynamic mid-span deflection histories of control panels under various reflected impulses (Full response)

6.4.3 Effect of the FRP retrofitting layers

Experimental results from static tests have shown that retrofitting reinforced concrete members by moderate amounts of externally bonded FRP layers has negligible effect on their cracking moment (Saadatmanesh and Ehsani, 1991). Therefore, M_{cr} for both the retrofitted and as-built panels will be calculated according to Equation 6.50. The cracked moment of inertia of FRP-retrofitted panels, I_{FRPcr}, can be evaluated by analyzing the transformed section after concrete cracking, which gives

$$I_{FRP_{cr}} = \frac{b(y_c)^3}{3} + n A_s (d - y_c)^2 + n_{FRP} A_{FRP} (h - y_c)^2 \tag{6.51}$$

where, n_{FRP} and A_{FRP} are the modular ratio and the cross sectional area of the FRP layer under consideration, respectively. For the panels retrofitted with FRP, the cracked moment of inertia, I_{FRPcr}, is calculated (see Appendix B). Accordingly, the natural frequency ω_{FRP} for the FRP-retrofitted panels is evaluated as

$$\omega^2{}_{FRP} = \frac{E_{cd} I_{FRP_{cr}} \pi^4}{m} \left[\left(\frac{1}{a^2}\right) + \left(\frac{1}{b^2}\right)\right]^2 \tag{6.52}$$

Using a similar procedure to that described earlier, the dynamic response of the FRP-retrofitted panels was calculated for the forced-vibration and the free-vibration phases under the effect of the three impulse levels. The analytical central deflection of FRP-retrofitted and control panels are shown in Table 6.6 for the 1686 kPa.msec reflected impulse. The maximum deflections are obtained as 12.4, 8.7 and 13.8 mm for the glass sheet, carbon sheet and carbon strip panels, respectively, indicating 28 % to 55 % deflection reduction compared to the control panel (15.9 mm). Central deflection-time histories are further illustrated in Figure 6.14.

Table 6.6: Central dynamic deflections of FRP-retrofitted and control panels under 1686 kPa.ms reflected impulses (Full response)

Time after shock wave arrival (msec)	Central deflection (mm)			
	Control panel	GFRP sheet-panel	CFRP sheet-panel	CFRP strip-panel
0.0	0.0	0.0	0.0	0.0
1.2	-5.6	-3.1	-4.4	-4.9
1.7	-8.1	-4.5	-6.3	-7.0
2.1	-9.4	-5.2	-7.3	-8.2
2.5	-9.3	-5.1	-7.3	-8.1
2.9	-7.4	-4.1	-5.8	-6.4
3.3	-4.2	-2.3	-3.3	-3.7
3.7	-0.2	-0.1	-0.2	-0.2
4.2	3.7	2.0	2.9	3.2
4.6	6.8	3.7	5.3	5.9
5.0	8.4	4.6	6.6	7.3
5.4	8.2	4.5	6.4	7.1
5.9	-1.3	-0.7	-1.0	-1.1
6.8	-10.4	-5.7	-8.1	-9.1
7.7	-15.9	-8.7	-12.4	-13.8
9.0	-15.9	-8.7	-12.4	-13.8
10.2	-10.4	-5.7	-8.1	-9.1
11.5	-1.4	-0.7	-1.1	-1.2
12.9	8.2	4.5	6.4	7.1
14.0	15.0	8.2	11.7	13.0

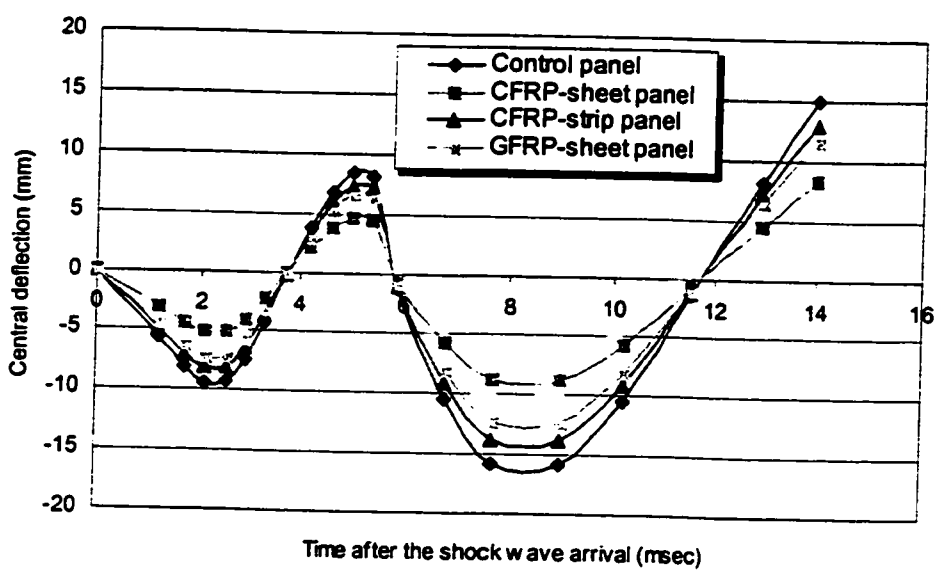

Figure 6.14: Central deflection-time history of control and FRP panels under 1686 kPa.ms reflected impulses (Full response)

In order to verify the results obtained from the inelastic dynamic analytical solution, comparison between the analytical results and the experimental measurements is made. The deflection comparison is considered for a reflected impulse of 1686 kPa.msec resulting from 33.4-kg charge. The reason of choosing such an impulse level was that eleven blast tests were conducted using such a charge weight and nine experimental central deflections were recorded. Figure 6.15 shows in a bar chart such a comparison. The closed-form showed, in general, reasonable agreement with the experimental measurements given the complexity of deflection field measurements and the assumptions made in the analytical solution.

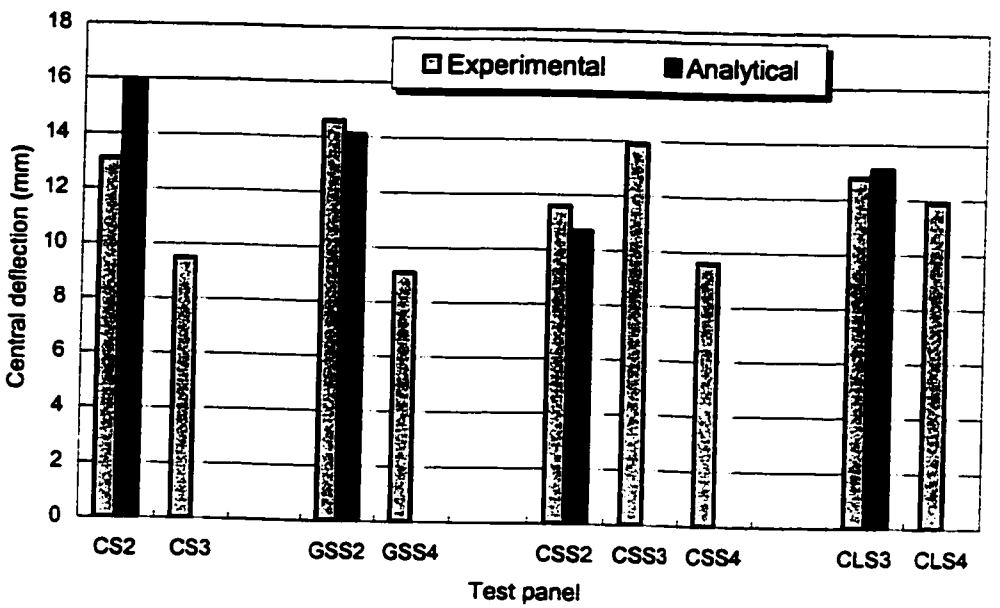

Figure 6.15: Comparison between experimental & analytical central deflection of test panels under 1686 kPa.ms reflected impulse

6.4.4 Panel moment

Since the stresses calculated previously using the elastic analysis were too high, we need to reconsider the method of stress calculation. However, instead of dealing with stresses directly, it is more convenient to determine the moment, which is in fact a stress resultant. The moment and curvature are related as follows

$$M_x = -D\left(\frac{\partial^2 y}{\partial x^2} + \nu\frac{\partial^2 y}{\partial z^2}\right) \tag{6.53}$$

Note that Equation 6.53 applies to both linear and nonlinear materials, provided the appropriate flexural rigidity is used. Since we are dealing with a symmetrical plate loaded with a uniform load, at the centre of the plate, $M_x = M_z$ is maximum, where

$$M_{x\,max} = -D\,(1+\nu)\left(\frac{\partial^2 y}{\partial x^2}\right) \tag{6.54}$$

The question of whether one should consider the Poisson's effect in the cracked plate arises. In conformity with Ghali and Favre's (1976) suggestion, we will include it. Thus

$$M_{x\,max} = -E_{cd}\,I_{eff}\,(1+\nu)\left(\frac{\partial^2 y}{\partial x^2}\right) \tag{6.55}$$

where we have replaced the elastic flexural rigidity by the effective flexural rigidity of the concrete panel, $E_{cd}\,I_{eff}$. The latter is necessary because the tested panels were all cracked under the applied reflected impulses.

Since $\frac{\partial^2 y}{\partial x^2} = -A_1\frac{\pi^2}{a^2}\sin\left(\frac{\pi x}{a}\right)\sin\left(\frac{\pi z}{b}\right)$, substituting for A_1 from Equation 6.38 yields

$$M_{x\,max} = E_{cd}\,I_{eff}\,\frac{\pi^2}{a^2}\,A_1(1+\nu)\sin\left(\frac{\pi x}{a}\right)\sin\left(\frac{\pi z}{b}\right) \tag{6.56}$$

Since at the plate centre $x = z = a/2$ and A_1 is given by Equation 6.38

$$M_{x\,max} = E_{cd}\, I_{eff}\, \frac{\pi^2}{a^2}\,(1+\nu)\left(\frac{1}{\rho}\right)\left[\left(\delta+\frac{\beta}{\gamma}\right)\left(\frac{\gamma}{\omega}\right)\sin(\omega t) - \delta\cos(\omega t) + (\delta - \beta t)e^{-\gamma t}\right] \quad (6.57)$$

Equation 6.57 presents the bending moment-time history of the control panel in terms of the displacement amplitude, A_1. We can calculate the maximum bending moment of test panels over a time interval equal to or less than the positive duration using Equation 6.57. For $t > t_o$, the plate is in a state of free vibration and the maximum moment is given by the dynamic moment of inertia times the plate angular acceleration. The moments in this phase will be self-equilibrating, but they will not be discussed further in this analysis.

In order to evaluate the effect of the section properties before and after cracking, the bending moment from Equation 6.57 will be calculated for the three impulse levels assuming four different values for the moment of inertia, viz. I_{gross}, I_{eff},, $I_{cracked+\nu}$ (including the Poisson's effect), and $I_{cracked}$ (excluding the Poisson's effect). Henceforth, we shall refer to these as the four states of the section. This leads to an idealization of the moment-curvature relationship of the panels as shown in Figure 6.16.

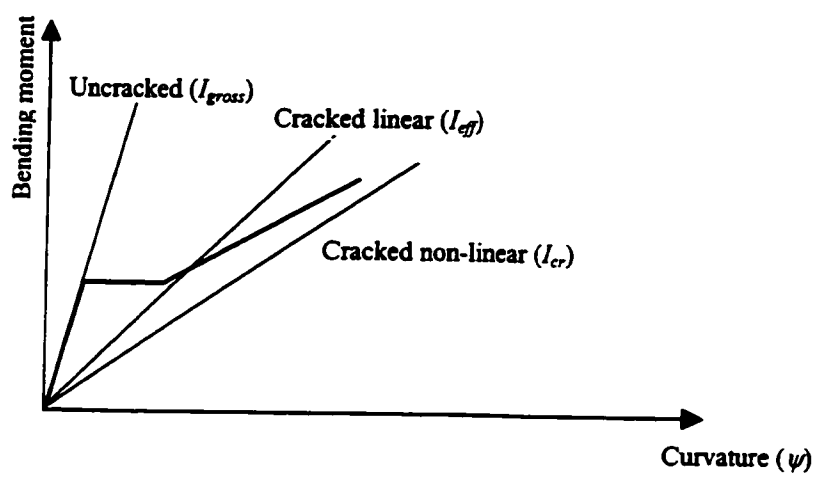

Figure 6.16: Moment-curvature relationship of concrete at various load stages

The intent is to choose the appropriate value of the moment of inertia that most reasonably can be used to predict the ultimate dynamic bending moment acting on each panel. Results for the four section states under the effect of various impulse levels are given in Tables 6.7 through 6.9. Figures 6.17 to 6.19 illustrate the dynamic bending moment results under the three impulse levels. For the 845 kPa.msec impulse, the maximum moments are found to be 44.9, 18.1, 8.7 and 8 kN.m, corresponding to the flexural rigidities in the four states, respectively. It is obvious that using I_{gross} gives a very high moment, which can not be sustained by any of the sections. Using $I_{cracked}$, on the other hand, resulted in a maximum moment of 8 kN.m, which is about 23 % higher than the ultimate dynamic moment capacity of the control panels (6.46 kN.m, see Appendix *A*). In calculating the dynamic properties of reinforcing steel, a *DIF* of 1.25 is used, which, according to Malvar (1998), could be as high as 2. The increase in the dynamic yield stress may account for the 23 % difference. Including the Poisson's effect, ν, increased the moment by 9 % compared to the moment without including ν, and the resultant 8.7 kN.m moment is 35 % higher than the ultimate dynamic moment capacity of the un-retrofitted panels. In all cases, the use of the first two parameters (I_{gross} or I_{eff}) results in unrealistic moment capacities, and should not be used. Similar conclusions could be drawn from the results of the 1246 and 1686 kPa.msec impulse, which further confirm that $E_{cd}\, I_{cr}$ gives the most reasonable prediction of the ultimate moment capacity of the panels.

Table 6.7: Dynamic bending moment under 845 kPa.msec impulse

Time (ms)	$M_{(left)}$	$M_{(lgross)}$	$M_{(lcracked + v\ effect)}$	$M_{(lcracked)}$
0.0	0.0	0.0	0.0	0.0
0.3	0.0	0.0	0.0	0.0
0.7	-1.4	-3.3	-0.6	-0.6
1.0	-4.9	-12.0	-2.3	-2.1
1.4	-9.4	-23.4	-4.5	-4.1
1.7	-13.9	-34.4	-6.7	-6.1
2.1	-17.1	-42.3	-8.2	-7.5
2.4	-18.1	-44.9	-8.7	-8.0
2.8	-16.6	-41.0	-7.9	-7.3
3.1	-12.5	-30.9	-6.0	-5.5
3.5	-6.4	-15.9	-3.1	-2.8
3.8	-2.6	-6.3	-1.2	-1.1

Table 6.8: Dynamic bending moment under 1247 kPa.msec impulse

Time (ms)	$M_{(left)}$	$M_{(lgross)}$	$M_{(lcracked + v\ effect)}$	$M_{(lcracked)}$
0	0.00	0.00	0.00	0.00
1.3	0.00	0.00	0.00	0.00
1.7	-3.13	-7.75	-1.50	-1.38
2	-10.95	-27.16	-5.26	-4.82
2.4	-20.28	-50.28	-9.73	-8.92
2.7	-27.75	-68.82	-13.32	-12.21
3.1	-30.05	-74.52	-14.42	-13.22
3.4	-26.30	-65.22	-12.62	-11.57
3.8	-16.78	-41.60	-8.05	-7.38
4.1	-3.70	-9.18	-1.78	-1.63
4.5	9.68	15.5	4.64	4.26
4.8	-7.85	-19.47	-3.77	-3.45

Table 6.9: Dynamic bending moment under 1686 kPa.msec impulse

Time (ms)	$M_{(left)}$	$M_{(lgross)}$	$M_{(lcracked + v\ effect)}$	$M_{(lcracked)}$
0	0.00	0.00	0.00	0.00
1.2	0.00	0.00	0.00	0.00
1.7	-5.45	-13.52	-2.62	-2.40
2.1	-18.60	-46.13	-8.93	-8.18
2.5	-33.08	-82.03	-15.88	-14.55
2.9	-42.13	-104.47	-20.22	-18.54
3.3	-41.13	-101.99	-19.74	-18.10
3.7	-29.30	-72.66	-14.06	-12.89
4.2	-9.90	-24.55	-4.75	-4.36
4.6	10.90	13.5	5.23	4.80
5	26.35	35.2	12.65	11.59
5.4	-1.48	-3.66	-0.71	-0.65

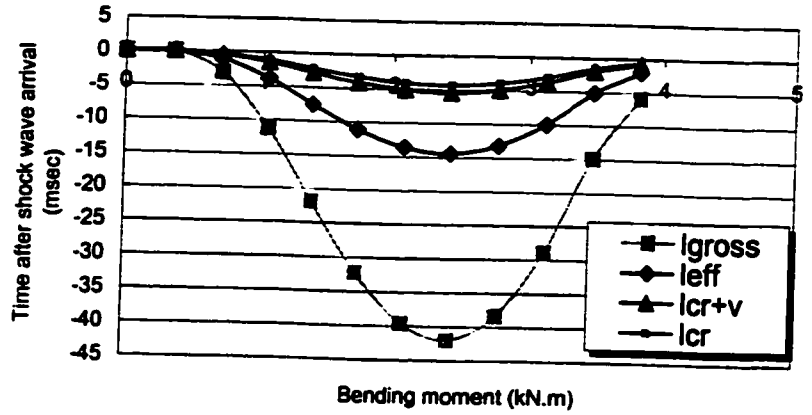

Figure 6.17: Effect of moment of inertia on bending moment under 845 kPa.msec reflected impulse

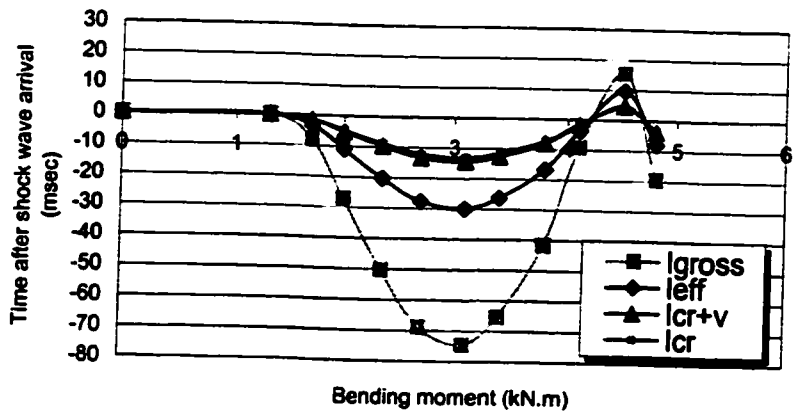

Figure 6.18: Effect of moment of inertia on bending moment under 1247 kPa.msec reflected impulse

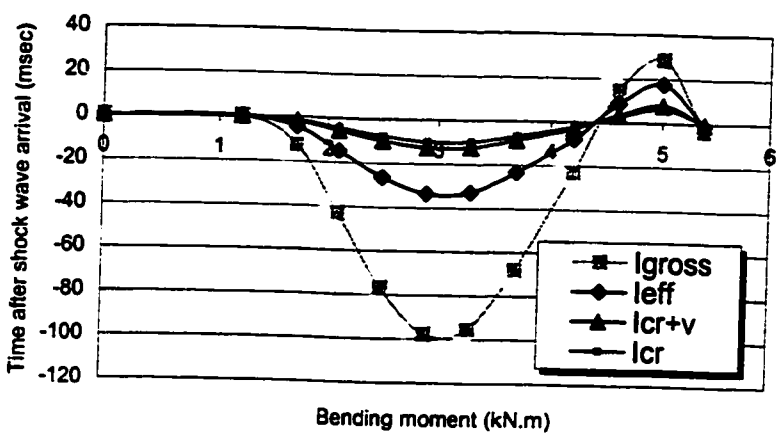

Figure 6.19: Effect of moment of inertia on bending moment under 1686 kPa.msec reflected impulse

The dynamic moment capacity of the GFRP sheet and CFRP sheet retrofitted panels are found to be 26.9 kN.m and 21.1 kN.m. We notice that no moment in Tables 6.7 to 6.9 based on I_{cr} is larger than the flexural capacity of these panels. Therefore, theoretically one should not expect heavy damage.

Accordingly, it is concluded that for higher impulse values, the moment exerted on a reinforced concrete slab or panel should be based on the cracked moment of inertia. On the contrary, deflections may be calculated using either the effective or the cracked moment of inertia. The latter is justified because the maximum moment in a simply supported slab or panel is not significantly affected by the magnitude of the moment at other locations in the panel. Hence failure may be initiated even if the moment in only one region exceeds the capacity of the panel.

On the contrary, maximum deflection is obtained by integrating the curvature of the panel over its entire surface. A peak in the curvature diagram that is limited to a small region of the panel, for instance the failure region, does not necessarily increase its maximum deflection dramatically.

The important observation that can be made based on the results of this chapter is that moment and stresses in concrete structures can not be accurately estimated using elastic methods of analysis in conjunction with blast pressures applied as static load. It is essential that proper dynamic analysis be performed and that the appropriate rigidity of the members is considered in the analysis.

Chapter 7

SUMMARY, CONCLUSIONS AND RECOMMENDATIONS

7.1 Summary

Sixteen 1000 × 1000 × 70 mm reinforced concrete panels were tested under blast loads resulting from 13.4, 22.4 or 33.4 kg of ANFO at a standoff distance of 3 m. The panels were divided into four groups. Each group consisted of nominally identical specimens. The panels in Group (1) were as-built and were used as control specimens. The panels in Group (2) were retrofitted with 500 mm wide GFRP sheets, those in Group (3) were retrofitted with similar CFRP sheets, while those in Group (4) were retrofitted with diagonally applied 80 mm wide CFRP strips. Two panels, one as-built and one retrofitted with CFRP sheet, were statically tested with a partially distributed central load.

The panels were mounted as the lid of a steel box and the box was buried in the ground, with the panels being flush with the ground surface. Using a tripod, the explosive charge was hung above the panels. During the test both blast wave parameters, i.e. pressure-time

history and impulse, as well as FRP and steel reinforcement strains were measured. In addition using an LVDT, the panels central deflection-time histories were also recorded.

The recorded blast wave parameters showed reasonable consistency in the values of the maximum incident pressure and positive phase duration in repeated tests using the same charge size. Furthermore, the reflected pressure was generally found to be nearly twice the incident pressure.

The blast parameters were relatively accurately predicted by the available software CONWEP, both maximum reflected pressure and positive phase duration were predicted reasonably well. Furthermore, the pressure-time histories followed a decay function similar to the Friedlander exponential relation.

Post-blast observations revealed extensive cracking in all the panels subjected to the impulse generated by the 33.4-kg charge. Under the 22.4-kg charge, the FRP retrofitted panels, in particular panels retrofitted with FRP sheets rather than strips, performed well in contrast with the control panels and the FRP laminate retrofitted panels. Both the CFRP and GFRP sheet retrofitted panels suffered minimal damage, while the other panels experienced extensive damage. These observations were confirmed by the post-blast residual strength tests of the panels. Whereas the GFRP and CFRP sheet retrofitted panels had residual strengths of 140 kN and 142 kN, respectively, the control panel had a residual strength of 80 kN and the CFRP laminate retrofitted panel had a residual strength of 60 kN. Overall, under the 33.4 kg charge similar observations were made, but it was not possible to achieve the same blast pressure and impulse for nominally similar charge size and standoff distance. It was observed that the GFRP sheet generally reduced the

maximum reflected pressure compared to the control panels while the CFRP had less effect on the maximum reflected pressure. On the other hand, the FRP sheets may have blunted the blast shock front and may have mitigated its effect on the concrete.

Of course, the FRP increases the flexural capacity of the panels and this in turn increases its blast resistance. The latter can be easily quantified using standard methods of concrete analysis, with due regard to the influence of strain rate on the strength of concrete and steel reinforcement.

A closed-form analytical solution was applied in this study to investigate the elasto-dynamic and plasto-dynamic response and strength of the panels. The solution was suitably modified to account for concrete cracking and nonlinearity. The modified solution, termed plasto-dynamic analysis, yielded results that are in reasonable agreement with the corresponding experimental data. On the other hand, the elasto-dynamic analysis, based on elastic properties of concrete and gross concrete section, failed to give correct results. Similarly, using the maximum reflected pressure as a uniformly distributed load would not give proper results because the stresses due to such load would be excessive and well beyond the dynamic resistance of the panels.

In the light of those observations, the following conclusions are drawn form the current investigation.

7.2 Conclusions

(1) In order to prevent the wrap-around effect of blast waves on small-dimension targets, one must devise a suitable test set-up

(2) In the final test set-up used here, where the specimen was mounted in a steel box, with the box being buried in the ground and its lid flush with the ground surface, the wrap-around effect was avoided.

(3) The reported pressure variations of different locations on the test panel surface verified the planarity of the shock wave for the chosen standoff distance of 3.0 m in the current testing program.

(4) The measured reflected pressures were found to be generally nearly double the incident pressure.

(5) For repeated charges of nominally the same size and standoff distance, the reflected and incident pressure sometimes varied substantially. This highlights the need for replicate test specimen in blast testing.

(6) The measured reflected impulses for tests with nominally the same charge size and standoff distance were quite close. This indicates that peak pressure is more sensitive to small changes in the surface conditions of a test specimen.

(7) Covering the concrete surface with bonded GFRP sheet would appear to reduce the peak reflected pressure. The observed reduction was of the order of 10 %, but no such reduction was observed for the CFRP sheets or laminates.

(8) The measured positive phase duration of the blast pressure time history in the current tests was in the order of 1.6 to 3.2 msec. This resulted in a duration ratio of 0.2 to 0.3, and panel response was governed by impulse rather than pressure.

(9) The computer program CONWEP predicted the blast wave parameters relatively accurately. Therefore, this program constitutes a useful tool for practical design.

(10) CONWEP predictions for impulse, positive phase duration and maximum reflected pressure were reasonably close to the average values of these quantities from nominally identical blasts.

(11) The application of the GFRP and CFRP sheets to the panels surfaces prevented damage due to blast waves emanating from 13.4 Kg of ANFO explosive at a 3 m standoff distance. When an otherwise similar unretrofilted control panel was subjected to the same blast, it suffered noticeable damage.

(12) Applying CFRP laminates in the form of X-brace to the two surfaces of some panels did not improve their blast resistance of the panel because the laminates in some cases completely debonded.

(13) The bond between the CFRP or GFRP sheet and the concrete surface was not significantly affected by the blast impulse.

(14) Light or moderate blast damage in the form of cracking was observed in all the panels. In particular, 45° through shear cracks were noticed on the four sides of all the panels. Thus, it was concluded that the FRP did not assist the panels in resisting

shear cracks, but post-blast static tests revealed that these cracks did not have any detrimental effect on the residual strength of the panels.

(15) When subjected to an average reflected impulse of 1686 KPa.msec generated by the 33.4-Kg ANFO charge, the control panels and the CFRP laminate retrofitted panels experienced heavy damage, in the form of concrete crushing and steel yielding.

(16) The response of the panels can be predicted using inelastic dynamic analysis, but the use of equivalent static analysis is not recommended because it predicts unrealistically high moments and stresses in the panels. Similarly, the yield line method coupled with the peak reflected pressure does not provide a reasonable estimate of the failure load of the panels.

(17) Modelling the panels as an undamped single degree of freedom system subjected to a decaying pressure profile provides a good estimate of the measured response of the panels.

(18) When the flexural rigidity of the panels is represented either by the effective rigidity of the cracked panels, per CSA A233-94 recommendation, or by the cracked rigidity ($E_c I_{cr}$), the predicted deflections of the panels are close to their measured values.

(19) When calculating the panels moments/stresses under high impulse, the assumption of cracked elastic concrete section does not give acceptable results. On the other hand, using the $E_c I_{cr}$ gives a much better estimate of the moment acting on the panels. The preferable approach for finding the moments acting on the panel would be to use the moment-curvature relation of the panels.

(20) The dynamic moment capacity of the panels, whether retrofitted or as-built, can be calculated using the strain compatibility method in conjunction with the strain rate dependent properties of concrete and reinforcement.

(21) Since the GFRP sheet provided almost the same level of blast resistance as the carbon sheet, due to the lower price of GRFP, it may be a more suitable material for practical applications.

7.4 Recommendations for future work

- Further blast experiments are required to enhance the proposed field test set-up in terms of better measuring techniques for deflection and surface strains.

- The application of externally bonded FRP composites to cubic full scale structures would give a better idea about the anchoring systems that may improve the bond between the retrofitting layers and concrete surfaces.

- Multi-target blast experiments would be more economical taking advantage of the fact that blast waves propagate in spherical paths. In other words, arranging different targets on the perimeter of a circle that has the explosive charge in its centre would equally distribute the blast pressure on targets according to their distance to the centre of explosion. In this case, studying the effect of applying different FRP materials configurations and/or amounts as well as factors affecting concrete properties can be economically studied.

- Other types of structural members such as columns and beams should be retrofitted and tested against blast.

- Ideally, nominally identical specimens should be subjected to increased blast loads to determine their blast resistance threshold, and to quantitatively determine the relationship between the FRP properties and their blast enhancement capacity.

- An attempt should be made to see whether the closed-form solution proposed here can be extended to other types of members and to full structures.

- A detailed numerical study using computational fluid dynamic can be conducted to model the effect of airbursts on hard target, and to predict the dynamic response of the system, accounting for structure-blast interaction.

References

[1] Abrams, D. A. (1917), "The effect of rate of application of load on the compressive strength of concrete," Proc. ASTM, 17, pp. 364-365.

[2] ACI (1993),"International Symposium on fibre reinforced plastic reinforcement for concrete structures," Eds. A. Nanni and C.W. Dolan, ACI SP 138.

[3] ACI (1995), "State-of-the-art report on fibre reinforced plastic (FRP) reinforcement for concrete structures".

[4] Agbabian, M. S. (1985), "Design of structures to resist nuclear weapon effects," ASCE manual on engineering practice, No. 42, N. Y.

[5] ASCE (1980), "Structural analysis and design of nuclear plant facilities, " Manual No. 58, Committee on nuclear structures and materials of the structural division of the American Society of Civil Engineering, New York, NY.

[6] Atchley, B. L. and Furr, H. L. (1967), "Strength and energy absorption capabilities of plain concrete under dynamic and static loadings," ACI journal, 64, pp. 745-756.

[7] Back, P. A. and Campbell, J. D. (1957), "Dynamic properties of materials at high rates of strain," Proc. Int. conference on material properties at high stain rates, Session 6, Paper 2, London.

[8] Baker, W. E. (1973)."Explosions in air," University of Texas Press, Austin, TX.

[9] Baker, W. E.; Cox, P. A.; Westine, P. S.; Kulesz, J. J. and Strehlow, R. A. (1983), " Explosion hazards and evaluation," Elsevier Scientific Publishing Company, New York.

[10] Baker, W. E.; Westine, P. S. and Dodge F. T. (1991), "Similarity methods in engineering dynamics, " Elsevier Scientific Publishing Company, 384 pp.

[11] Bertero, V. V.; Rea, D.; Mahin, S. and Atalay, M. B. (1973), "Rate of loading effects on uncracked and repaired reinforced concrete members, " Proc. 5th world conference on earthquake engineering, Rome, 1, pp. 1461-1470.

[12] Beshara, F. B. (1991), "Non-linear finite element analysis of reinforced concrete structures subjected to blast loading, "Ph. D. thesis, City University, U.K.

[13] Beshara, F. B. (1994-a), "Modeling of blast loading on aboveground structures-I. General phenomenology and external blast, " Computers & Structures, Vol. 51, No. 5, pp. 585-596.

[14] Beshara, F. B. (1994-b), "Modeling of blast loading on aboveground structures-II: internal blast and ground shock," Computers & Structures, Vol. 51, No. 5, pp 597-606.

[15] Bichoff P. H. and Perry S. H. (1991), "Compressive behaviour of concrete at high strain rates, "Materials and structures, **24**, pp. 425-450.

[16] Biggs, J. M. (1964), "Introduction to structural dynamics," McGraw-Hill Publishing Company, USA.

[17] Bogosian, D. (1994)," Parametric analysis of 12-Inch substantial dividing walls, TR-94-20, " Karagozian & Case, Glendale, CA, USA.

[18] Brode, H. L. (1955), " Numerical solution of spherical blast waves, " Journal of App. Phys., Vol. 26, No. 6, pp. 766-775.

[19] Crawford, J. E. and Karagozian, J (1995),"The behaviour and design of conventional structural components which are to resist blast loadings," Karagozian & Case, TR-95-52.1, Glendale, CA, USA.

[20] Crawford, J. E.; Malvar, L. I.; Wesevich, I. W.; Valancius, I. and Reynolds A. (1997),"Retrofit of reinforced concrete structures to resist blast effects, "ACI Structural Journal, V. 94, No.4, July-August.

[21] CSA Standard CAN-23.3-94 (1994)," Design of concrete structures."

[22] Dilger, W.; Kand, R.; and Kowalczyk, R. (1984),"Ductility of plain and confined concrete under different strain rates," ACI journal, Jan.-Feb., pp. 73-81.

[23] Dowling, A. R. and Harding, J. (1967), " Tensile properties of mild steel under high strain rates," Proc. 1st HERF conf., University of Denver, 2, 7.3.1.

[24] Drake, J. L., Twisdale, L. A., Frank, R. A. and Dass, W. C. (1989), "Protective constriction design manual," Final report, ESL-TR-87-57, November.

[25] Duranovic, N. and Watson, A. (1994), "Impulsive loading on reinforced concrete slabs-blast loading function, "3ed Int. conference on structures under shock end impact, Madrid, Span 1-3 June, pp. 63-70.

[26] Eytan, R. (1994), "Practical methods for increasing the blast resistance of existing buildings, "Proceeding of the third international conference, Structures under shock and impact, ed. P. S. Bulson, Madrid, Spain, 1-3 June.

[27] Fu, H. C.; Erki, M. A.; and Seckin, M. (1991), "Review of effects of loading rate on concrete in compression," Journal of structural engineering, Vol. 117, No. 12, pp. 3645-3659.

[28] Ghali, A. and Neville, A. M. (1977)," Structural analysis a unified classical and matrix approach, " Chapman and hall, London, New York, 773 pp.

[29] Glasstone, S. and Dolan, P. J. (1977), " The effects of nuclear weapons," The US Department of Defence, 3rd edition.

[30] Gupta, A. D.; Gregory, F. H.; Bitting, R. L. and Bhattacharya, S. (1977), "Dynamic analysis of an explosively loaded hinged rectangular plate," Computers & Structures, Vol. 26, No. 12, pp 339-344.

[31] Harding, J. and Welsh, L. M. (1987),"The effect of high strain rate on material properties," In materials at high strain rates, Ed. T. Z. Blazynski, Elsevier Applied Science, Essex, England, pp. 133-186.

[32] Hinman, E. E. and Hammound, D. J. (1997), "Lessons from the Oklahoma City bombing: Defensive design techniques, " ASCE Press, N Y 10017-2398.

[33] Hopkinson, B. (1915), " British ordnance minutes 13565".

[34] Hyde, D. W. (1990) CONWEP (Conventional Weapons Effects), Computer program, U. S. Army Waterways Experimental Station, Mississippi. USA.

[35] Jarrett, D. E. (1968), "Derivation of British explosive safety distance," Annals of the New York Academy of Science, 152, Article 1, pp. 18-35.

[36] Johansson, C. H. and Persson, P. A. (1970)," Detonics of high explosives, " Academic Press, London and New York.

[37] Johansson, M. (2000), " Structural behaviour of concrete frame corners of civil defence shelters," Ph. D. thesis, Dep. of structural engineering, Chalmers University of technology, Goteborg, Sweden.

[38] JSCE (1993), " State-of-the-art report on continuous fibre reinforcing materials, Research committee on continuous fibre reinforcing materials, Japan society of civil engineers, Tokyo.

[39] Keenan, W. and Feldman, A. (1983), "The yield strength of intermediate grade reinforcing bars under rapid loading," Naval Civil Eng. Lab., Calif., USA.

[40] Kinney, G. F. and Graham, K. J. (1985), "Explosive shocks in air," Springer-Verlag, New York, USA.

[41] Langberg, H. (1993), "Response of concrete structures subjected to close-in detonations," in Structural concrete slabs under impulsive loads, Ed. Krauthammer, T., Research Library, U. S. Army Engineer Waterways Experiment Station, Vicksburg, Mississippi, USA, pp. 5-14.

[42] Lindholm, U. S. (1968)," Mechanical behaviour of materials under dynamic loads," Springer, New York.

[43] Long, B. R. (1968), "Dynamic response of simply supported beams under blast loading (U), "Defence Research Establishment Suffield (DRES) project No. D53-16-01-12, Alberta, Canada.

[44] Malvar, L. J. (1998)," Review of static and dynamic properties of steel reinforcing bars, "ACI material Journal, Volume 95, No.5, pp. 609-616.

[45] Malvar, L. J. and Ross, C. A. (1998)," Review of strain rate effects for concrete in tension" ACI material Journal, Volume 95, No.6, pp. 735-739.

[46] MATLAB program (1999): User guide version 5.3, The Mathworks Inc., Natick, Ma, USA.

[47] Mays, G. C. and Smith, P. D. (1995), "Blast effects on building, "Thomas Telford Publications, London, 121 pp.

[48] Mills, C. A. (1987), "The design of concrete structures to resist explosions and weapon effects, " Proceedings of 1st Int. Conference on concrete for hazard protections, Edinburgh, pp. 61-73.

[49] Mlakar, P. F.; Vitaya-Udom, K. P.; and Cole, R. A. (1985), "Dynamic tensile-compressive behaviour of concrete," ACI Journal, 82(4), pp. 484-491.

[50] Murr, L. E. (1987)," Metallurgical effects of shock and high-strain rate loading," in materials at high strain rates, Ed. T. Z. Blazynski, Elsevier Applied Science, Essex, England, pp. 1-46.

[51] Muszynski, L. C. (1996)," Explosive field tests to evaluate composite reinforcement of concrete and masonry walls, " Second Int. Conference. On Composites in Infrastructures, Eds. Saadatmanesh, H.; and Ehsani, M. R.

[52] Muszynski, L. C.; Purcell, M. R. and Sierakowski, R. (1995)," Strengthening concrete structures by using by externally applied composite reinforced materials," Proceedings of 7th International symposium on Interaction of effects of munitions with structures, Mannheim, Germany, pp. 291-298, April 24-28.

[53] Naeyaert, CE. (1993)," A combination of steel fibres and conventional reinforced in protective concrete structures subjected to near miss explosions, contact explosions, direct hits and explosions after penetration," Infrastructure Dep. Belgium, Structural concrete slabs under impulsive loads, Ed. Krauthammer, T., Research Library, U. S. Army Engineer Waterways Experiment Station, Vicksburg, Mississippi, USA.

[54] Newmark, N. M. (1953), "An engineering approach to blast resistance design, " Proceedings of ASCE, Volume 79, Separate No. 309.

[55] Newmark, N. M. (1972), "External blast, " Proceedings of Int. Conf. On the planning and design of tall buildings, ASCE, Volume 79, Separate No. 309.

[56] Newmark, N. M. and Hansen, R. J. (1961), "Design of blast-resistant structures, "in Shock and Vibration Handbook, Volume 3, Eds. Harris and Crede, McGraw-Hill.

[57] Norris, G. H.; Hansen, R. J.; Holly, M. J.; Biggs, J. M.; Namyet, S. and Minami, J. K. (1959), "Structural design for dynamic loads," McGraw-Hill Book Co., Inc., New York, USA.

[58] Olson, M. D. (1991), "Development of methods for modeling structural response and predicting failure of structures subjected to blast loading-Phase V, "Department of Civil Engineering, University of British Columbia, Vancouver, B.C., Canada.

[59] Pan, Y. and Watson, A. (1998), "Effect of panel stiffness on resistance of cladding panels to blast loading, " Journal of engineering mechanics, April 1998, pp 414-421

[60] Personal connections (2000), Wilfred Baker Eng., San Antonio, TX.

[61] Reinhardt, H. W.; Rossi, P. and van Mier J. G. (1990), "Joint investigation of concrete at high strain rates of loading," Materials and Structures, Vol. 23, pp. 213-216.

[62] Rogers, G. L. (1959), "Dynamics of framed structures, "John Wiley & Sons, Inc. New York.

[63] Rossi, P. and Toutlemonde, F. (1996), "Effect of loading rate on the tensile behaviour of concrete: description of the physical mechanisms," Materials and Structures, Vol. 29, pp. 116-118.

[64] Rossi, P.; van Mier J. G.; Toutlemonde, F.; Le Maou, F. and Boulay, C. (1994), "Effect of loading rate on the strength of concrete subjected to uniaxial tension," Materials and Structures, Vol. 27, pp. 260-264.

[65] Saadatmanesh, H. and Ehsani, M. R. (1991), "Fibre Composite bar for reinforced concrete construction," Journal of Composite Materials, Vol. 25, February 1991, pp. 188-203.

[66] Scott, B. D.; Park, R. and Priestley, M. J. N. (1982), "Stress strain behaviour of concrete confined by overlapping hoops at low and high strain rates," ACI Journal, Volume 79, No.1, pp. 13-27.

[67] Smith, P. D. and Hetherington, J. G. (1994), "Blast and ballistic loading of structures," Butterworth-Heinemann Ltd, London, 313 pp.

[68] Smith, P. D.; Rose T. A. and Saotonglang, E. (1999), "Clearing of blast waves from building facades," Proc. of the Institution of Civil Engineers: Structures and Buildings, Paper 11858, May 1999, Thomas Telford Limited, London, pp.193-199.

[69] Soroushian P.; Choi K-B. and Alhamad, A. (1986)," Dynamic constitutive behaviour of concrete," ACI journal, Mar.-Apr., pp. 251-259.

[70] Sparks, P. R.; and Menzies, J. B. (1973), "The effect of rate of loading upon the static and fatigue strengths of plain concrete in compression, "Magazine of concrete research, 25 (83), pp.73-80.

[71] Spooner, D. C. (1971), "Stress-strain-time relationships for concrete, "Magazine of concrete research, Vol.23, No.75/76, pp.127-131.

[72] Takeda, J. and Tachikawa, H. (1971), "Deformation and fracture of concrete subjected to dynamic load, "Proc. of the International conference on mechanical behaviour of materials, Kyoto, Japan, 4, pp. 267-277.

[73] Task committee on blast resistance design (1997), "Design of blast resistant buildings in petrochemical facilities," ASCE publication, Reston, Virginia.

[74] Temoshinko, S. P. and Woinowski-krieger, S. (1959),"Theory of plates and shells," 2nd edition, McGraw-Hill, New York.

[75] TM 5-1300 (1990), "Design of structures to resist the effects of accidental explosions," US Department of the Army Technical Manual.

[76] Tolba, A. F.; Razaqpur, A. G.; Abd El Halim, A. O.; Contestabile, E. and Guilbeault, R. (2000), " Evaluation of blast loading distribution on the surface of a reinforced concrete slab," 29th DDESB seminar, New Orleans, Louisiana, USA, July 18-20.

[77] Toutlemonde and Boulay (1993-a), "Shock-tube tests of concrete slabs, " Materials and Structures, **26**, pp. 38-42.

[78] Toutlemonde and Boulay (1993-b), "Dynamic failure modes of concrete slabs: experimental evidence and questions," in Structural concrete slabs under impulsive loads, Ed. Krauthammer, T., Research Library, U. S. Army Engineer Waterways Experiment Station, Vicksburg, Mississippi, USA, pp. 69-78.

[79] Wakabayshi, M. (1980), "Dynamic loading effects on the structural performance of concrete and steel materials and beams, " Proc. 7th world conference on earthquake eng., Istanbul, Turkey, 6(3), pp. 271-744.

[80] Watson A. (1993), "Experimental analysis in the laboratory and in the field: approaches, observations, needs," in Structural concrete slabs under impulsive loads, Ed. Krauthammer, T., Research Library, U. S. Army Engineer Waterways Experiment Station, Vicksburg, Mississippi, USA, pp. 81-96.

[81] Watson, A. J. (1994), "The response of civil engineering structures to impulsive loads," 3rd International conference on structures under shock end impact, Madrid, Span. 1-3 June, pp. 3-10.

[82] Watstein, D. (1953), "Effect of straining rate on the compressive strength and elastic properties of concrete," ACI Journal, Volume 49, No.8, pp. 729-744.

[83] Woodson, S. C., (1993), "Response of slabs: in plane forces and shear effects," in Structural concrete slabs under impulsive loads," Ed. Krauthammer, T., Research Library, U. S. Army Engineer Waterways Experiment Station, Vicksburg, Mississippi, USA, pp. 51-68.

[84] Zielinski, A. J.; Reinhardt, H. W. and Kormeling, H. A. (1981), "Experiments on concrete under uniaxial impact tensile loading," Materials and Structures, Vol. 14, No. 80, pp. 103-112.

Appendices

Appendix A:

1. Ultimate static moment capacity of control panels

The maximum static capacity of control panels was calculated based on the analysis of 1000 × 70 mm cross-section using the strain compatibility method. The panel is doubly reinforced, i.e. $A_s = A'_s = 197.92$ mm^2, and the natural axis for the untracked section is at the mid-height ($c = h/2 = 35$ mm). At failure, the natural axis shifts upwards as shown in Figure A.1, and the distance between its new location and the extreme compression fibre, c, can be found as follows:

1. Assume a value for c equals to 8 mm, from the strain diagram, $\frac{\varepsilon'_s}{d'-c} = \frac{\varepsilon_{cu}}{c}$

   where ε_{cu} is the ultimate compression strain at failure, equals to 0.0035, and d' is the distance from the compression fibre to center of the upper steel reinforcement, i.e. 10 mm. This yields $\varepsilon'_s = \frac{0.0035 \times (10-8)}{8} = 0.000875$. Also, the stress block parameters are defined in terms of a 40 MPa concrete strength as

   $\alpha = 0.85 - 0.0015\, f'_c = 0.85\text{-}0.0015\ (40) = 0.79 \geq 0.67$ ok

   $\beta_1 = 0.97 - 0.0025 f'_c = 0.97\text{-}0.0025\ (40) = 0.87 \geq 0.67$ ok

2. The steel compression force, C'_s, is given as

   $C'_s = \varepsilon'_s E_s A_{s'} = 0.000875 \times 200000 \times 197.92 = 34636$ N. Observing here that the steel compression force has a positive sign, which means that it turned to a tensile force (opposite to the assumed direction).

3. The steel tensile force, T_s, is given as $T_s = f_y A_s$, = 400 × 197.92 = 79168 N

4. The concrete compression force, C_c, in defined by

   $C_c = \alpha f'_c b \beta_1 c = (0.79 \times 40) \times 1000 \times (0.87 \times 8) = 219936$ N

5. From the force equilibrium 79168 + 34636 ≠ 219936.

6. Try a new value of c as 6 mm, which results in $\varepsilon'_s = \dfrac{0.0035 \times (10-6)}{6} = 0.002333$

7. New value for C'_s and C_c are then obtained as 92363 N and 164952 N, respectively, while T_s remained the same.

8. From the new force equilibrium: $T_s + C'_s = C_c$, (79168 + 92363 ≅ 164952).

9. Using a value of $c = 6$ mm results in an equivalent depth of the stress block of $a = \beta_1 \times c = 0.87 \times 6 = 5.22$ mm (refer to Figure A.1). The ultimate moment of the section can be evaluated by taking moment about point 0 as follow

   M_u = 79168 × (60 − 6) + 92363 × (10 − 6) + 164952 (6 − 5.22/2) = 5203711 N.mm (5.2 kN.m).

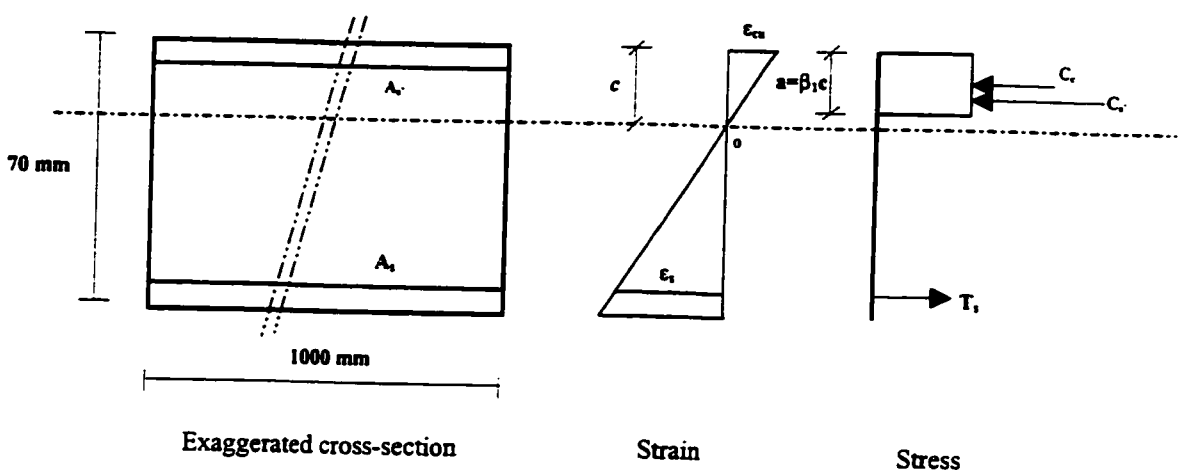

Figure A.1: Ultimate cross-sectional analysis of control panels at failure

2. Ultimate dynamic moment capacity of control panels

Considering a *DIF* of 1.25 for both steel and concrete, the dynamic properties of steel are 500 MPa and 250 GPa for its yield stress and elastic modulus, respectively. For concrete, the dynamic elastic modulus, compressive strength and tensile strength are found to be 33 GPa, 48 MPa and 4.8 MPa, respectively. Substituting the dynamic properties in the previous analysis results in new stress block parameters

- $\alpha = 0.85 - 0.0015\, f'_c = 0.85\text{-}0.0015\ (48) = 0.778 \geq 0.67$ ok
- $\beta_1 = 0.97 - 0.0025 f'_c = 0.97\text{-}0.0025\ (48) = 0.85 \geq 0.67$ ok

Assuming that the location of the neutral axis remains the same ($c = 6$ mm), the forces in the stress diagram are recalculated as

- $C'_s = \varepsilon'_s E_{sd} A_s = 0.002333 \times 250000 \times 197.92 = 115436.84$ N
- $T_s = f_{yd} A_s = 500 \times 197.92 = 98960$ N
- $C_c = \alpha f'_{cd}\, b\, \beta_1\, c = 0.778 \times 48 \times 1000 \times 0.85 \times 6 = 190454.4$ N

From which, $T_s + C'_s \cong C_c$. The ultimate dynamic moment of the section can be evaluated by taking the moment about point 0 as follow

- $M_u = 98960 \times (60 - 6) + 115436.8 \times (10 - 6) + 190454\ (6 - 5.1/2) = 6462655$ N.mm

The ultimate dynamic moment capacity of the control panels is 6.46 kN.m.

Appendix B:

1. Ultimate static moment capacity of FRP-retrofitted panels

One longitudinal layer of CFRP is assumed to be perfectly bonded to the lower surface of the panel having a tensile strain ε_f' and tensile force T_{fl}. The CFRP sheet properties are 230 GPa, 3480 MPa and 55 mm^2 for E_{CFRP}, f_{CFRP} and A_{layer}, respectively. The effect of the CFRP sheets bonded to the upper surface and to the orthogonal direction to the analyzed section is neglected (Figure B.1). In order to find the ultimate moment capacity of the CFRP-retrofitted section, the strain compatibility method is employed as follows:

1. Assume a value for c equals to 15 mm (in this case $c > d'$), and from the strain diagram, $\frac{\varepsilon_s'}{c-d'} = \frac{\varepsilon_{cu}}{c}$. Again, ε_{cu} = 0.0035 and d' = 10 mm. This yields $\varepsilon_s' = \frac{0.0035 \times (15-10)}{15} = 0.001167$. The tensile strain in the CFRP layer is also calculated from the strain diagram as $\frac{\varepsilon_{ft}}{h-c} = \frac{\varepsilon_{cu}}{c}$, from which ε_{ft} = 0.012833. The stress block parameters, α and β_l were calculated as 0.79 and 0.87, respectively, and $a = \beta_l \times c = 13.05$ mm.

2. The steel compression force, C_s', is given as

   $C_s' = \varepsilon_s' E_s A_s, = 0.001167 \times 200000 \times 197.92 = 46182.65$ N.

3. The steel tensile force, T_s, is the same as before = 79168 N

4. The tensile force of the CFRP layer, $T_{CFRP} = f_{CFRP} A_{layer} = (E_{CFRP} \times \varepsilon_{ft}) \times A_{layer}$

   $\therefore T_{CFRP} = 230000 \times 0.012833 \times 55 = 162337.45$ N

5. The concrete compression force, C_c, is

$$C_c = \alpha f'_c b \beta_1 c = (0.79 \times 40) \times 1000 \times (0.87 \times 15) = 412380 \text{ N}$$

6. From the force equilibrium: $T_{CFRP} + T_s \neq C_c + C'_s$

7. Try a new value of c as 10 mm, which results in $\varepsilon'_s = \frac{0.0035 \times (10 - 10)}{6} = 0.00$

8. New value for C_c is then obtained as 274920 N, while T_s remained the same.

9. For a maximum strain in the CFRP layer of 1.5 %, $T_{CFRP} = 189750$ N

10. From the new force equilibrium, $T_s + T_{CFRP} = C_c$, $(79168 + 189750 \cong 274920)$.

11. Using a value of $c = 10$ mm results in an equivalent depth of the stress block of

$a = \beta_1 \times c = 0.87 \times 10 = 8.7$ mm (refer to Figure B.1).

12. The ultimate moment of the section can be evaluated by taking moment about point 0 as follow

$M_u = 79168 \times (60 - 10) + 189750 \times (70 - 10) + 274920\ (10 - 8.7/2) = 16896698$ N.mm (16.9 kN.m).

13. For a GFRP panel of 600 mm^2 cross-sectional area, the ultimate moment is calculated as $M_u = 21.5$ kN.m.

2. Ultimate dynamic moment capacity of CFRP-retrofitted panels

A similar procedure to the explained earlier was followed to account for the dynamic effect on the properties of the reinforcing steel and concrete. The ultimate dynamic

moment capacity of the GFRP and CFRP retrofitted panels are calculated as 26.9 and 21.1 kN.m, respectively.

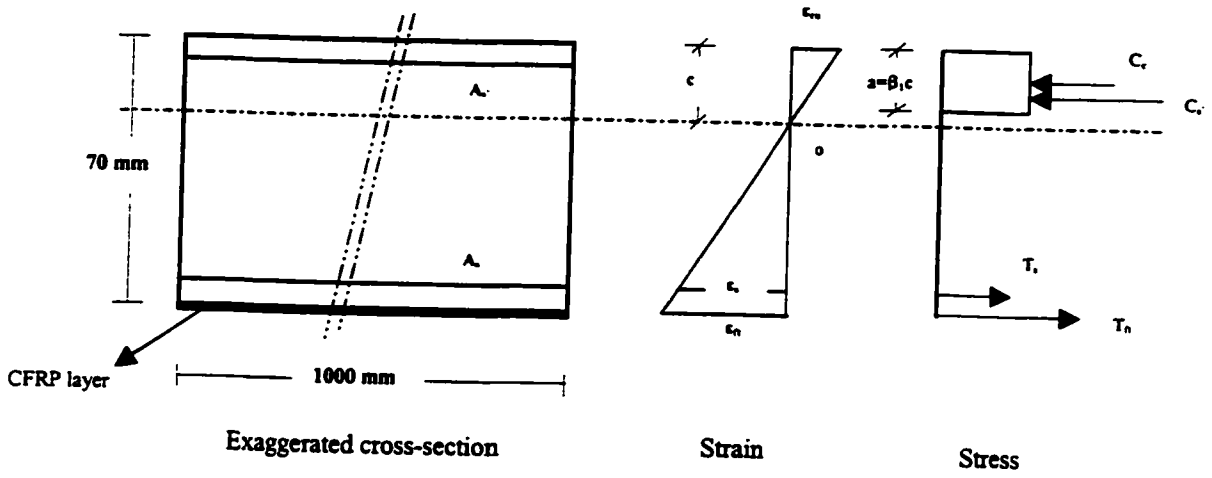

Figure B.1: Ultimate cross-sectional analysis of CFRP-retrofitted panels

3. Punching shear calculations

- According to CSA A23.3 –94, the ideal punching shear capacity of the slabs can be calculated assuming a 300 × 300 mm punching area, as $V_r = 0.4\sqrt{f'_c}\, b_o\, d$. Here, b_o is the punching area perimeter and d is the effective depth of the slab. For b_o = 1200 mm and d = 60 mm, V_r = 182.14 kN.

- The factored punching shear would be 0.6 V_r = 109 kN. This indicates the range of punching shear load that the slab under consideration may fail at to be 109 to 182 kN.

4. Calculations for the moment of inertia and natural frequency of test panels

- The gross moment of inertia of test panels is calculated using the relation $I_{gross} = \frac{b\,h^3}{12}$, and is 2.858×10^{-5} m^4.

- The cracked moment of inertia of the control panels is calculated according to the relation $I_{cracked} = \frac{b(y_c)^3}{3} + nA_s(d - y_c)^2$, and is 3.126×10^{-6} m^4.

- The flexural rigidity, D, is determined for $h = 0.07$ m and $E_c = 28000$ MPa as $D = \frac{E_c\,h^3}{12(1-\nu^2)}$, and is 833681.56 N.m

- Within the forced vibration phase, the uncracked frequency of the control panels is $\omega^2{}_{uncracked} = \frac{D\pi^4}{m}\left[\left(\frac{1}{a^2}\right)+\left(\frac{1}{b^2}\right)\right]^2$, for $m = 168$ kg, $a = b = 1$ m $\omega = 1390.5$ rad/sec.

  The natural period of vibration of the control panels in this phase is given by $T = 2\pi/\omega$ and is 4.5 msec.

- Within the free vibration phase, the cracked frequency of the control panels is $\omega^2{}_{cracked} = \frac{E_c I_{cr}\,\pi^4}{m}\left[\left(\frac{1}{a^2}\right)+\left(\frac{1}{b^2}\right)\right]^2$, for $m = 168$ kg, $a = b = 1$ m $\omega = 450.55$ rad/sec.

  The natural period of vibration of the control panels in this phase is given by $T = 2\pi/\omega$ And is 13.95 msec.

- Similarly, the cracked moment of inertia of the FRP panels is calculated according to the relation $I_{FRP_{cr}} = \frac{b(y_c)^3}{3} + n\,A_s(d - y_c)^2 + n_{FRP}\,A_{FRP}\,(h - y_c)^2$, and are 7.845×10^{-6} , 7.46×10^{-6} and 1.2×10^{-6} m^4.

- The natural frequencies are calculated in the forced vibration and the free vibration according to the relations $\omega^2{}_{uncracked} = \frac{D\pi^4}{m}\left[\left(\frac{1}{a^2}\right)+\left(\frac{1}{b^2}\right)\right]^2$ and $\omega^2{}_{FRP} = \frac{E_{cd} I_{FRP_{cr}}\,\pi^4}{m}\left[\left(\frac{1}{a^2}\right)+\left(\frac{1}{b^2}\right)\right]^2$, respectively.

5. Preliminary blast shots: Phase (2)

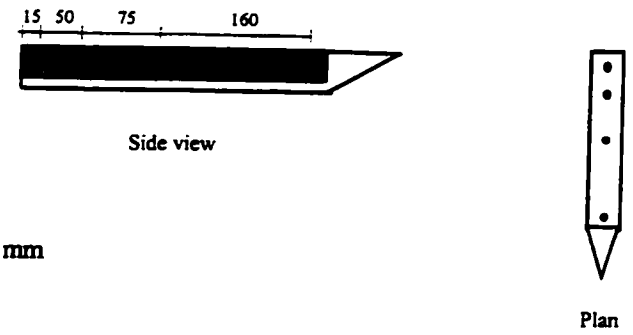

* Dimensions in mm

(a)

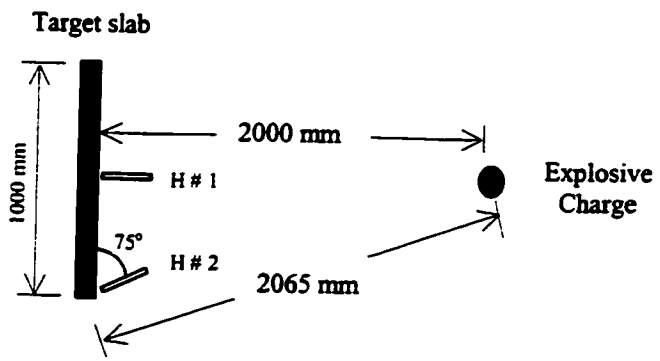

(b)

Figure B.2: (a) Schematic of the pressure-gauges holder (b) Schematic plan of the test set-up

Appendix C: Illustration of the experimental results

Group (1)

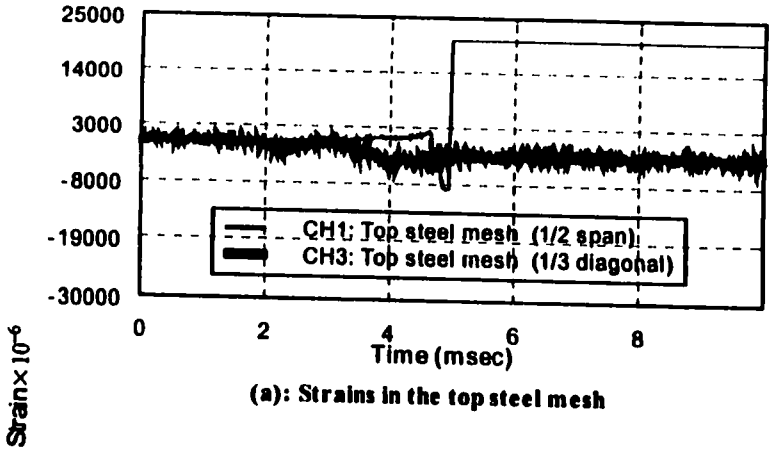

(a): Strains in the top steel mesh

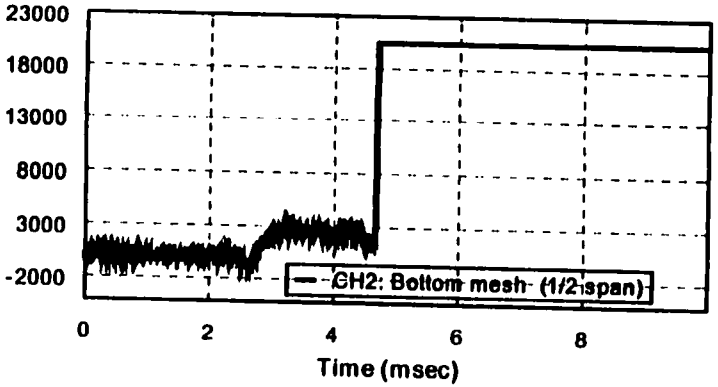

(b): Strains in the bottom steel mesh

Figure C.1: Strain-time profiles in steel (Blast test # 8: Panel CS2)

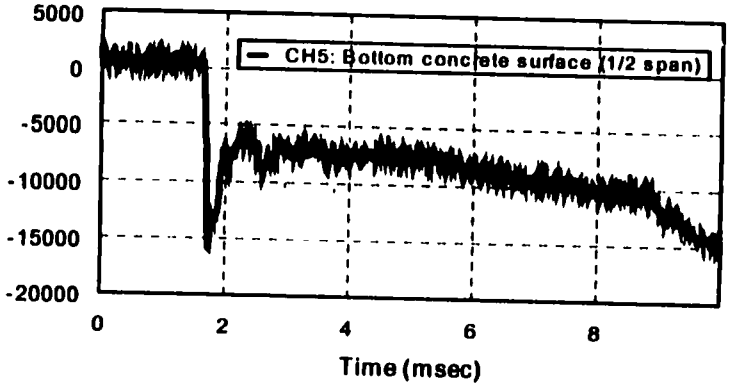

(b): Strains at the bottom concrete surface

Figure C.2: Strain-time profiles on concrete surfaces (Blast test # 8: Panel CS2)

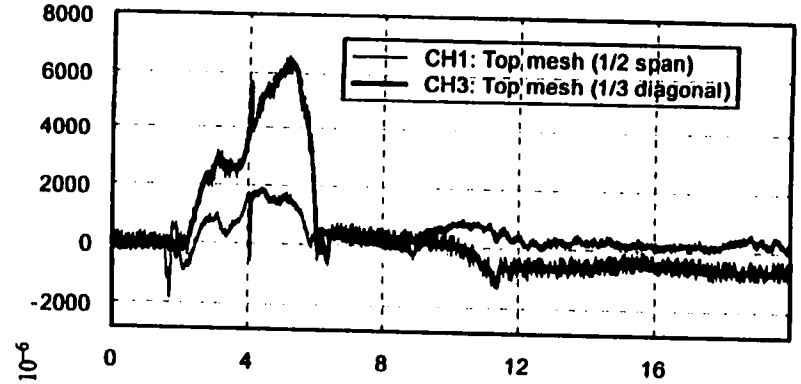

(a): Strains in the top steel mesh

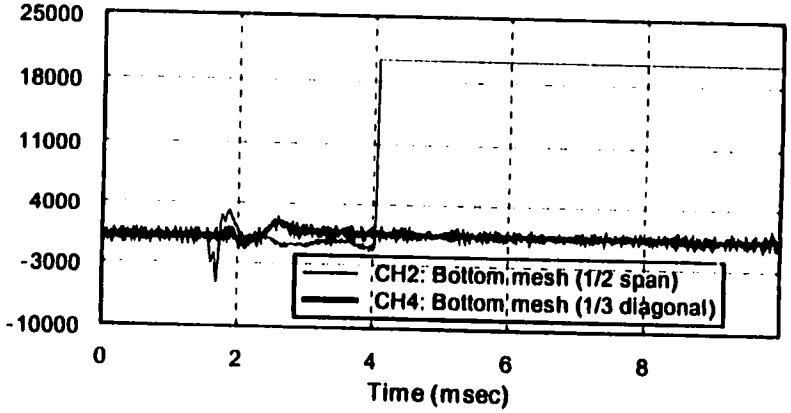

(b): Strains in the bottom steel mesh

Figure C.3: Strain-time profiles in steel (Blast test # 15: Panel CS2)

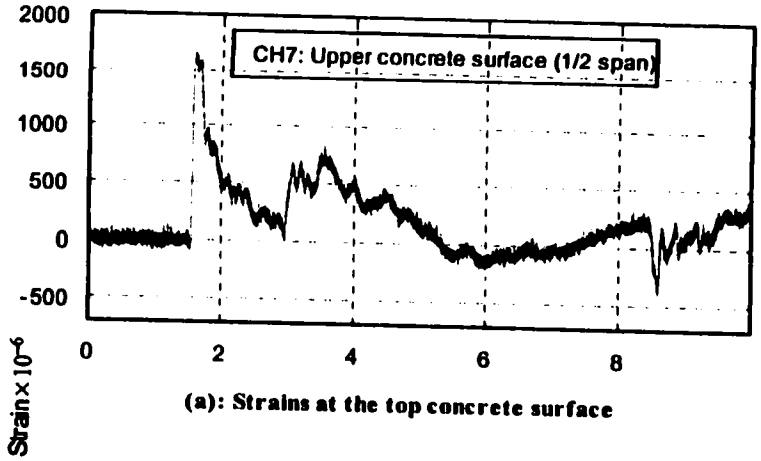

(a): Strains at the top concrete surface

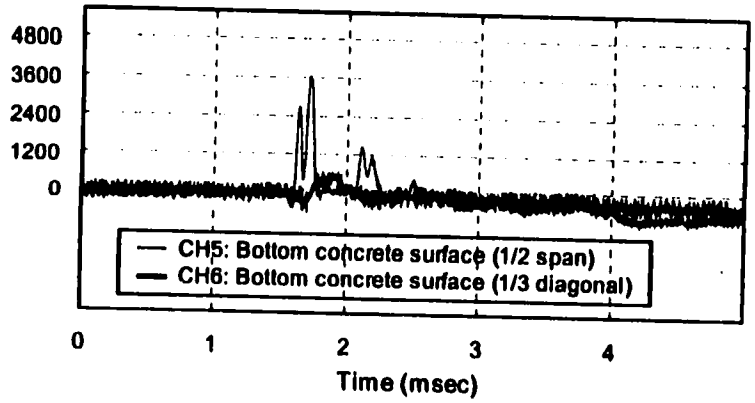

(b): Strains at the bottom concrete surface

Figure C.4: Strain-time profiles on concrete surfaces (Blast test # 15: Panel CS2)

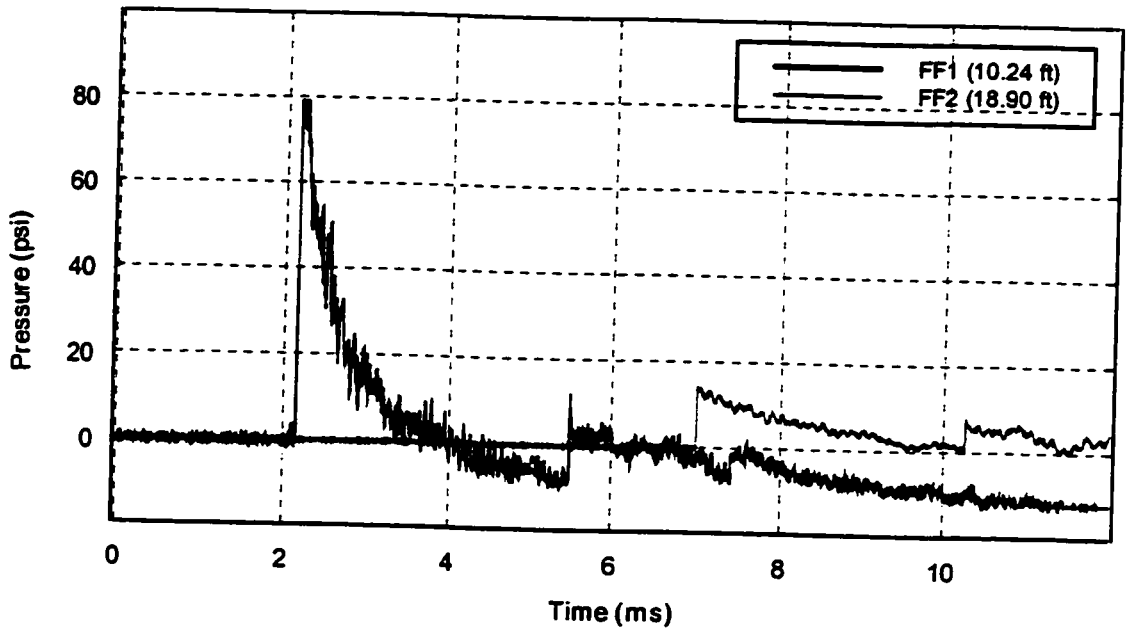

(a): Incident (free field) pressure-time profiles

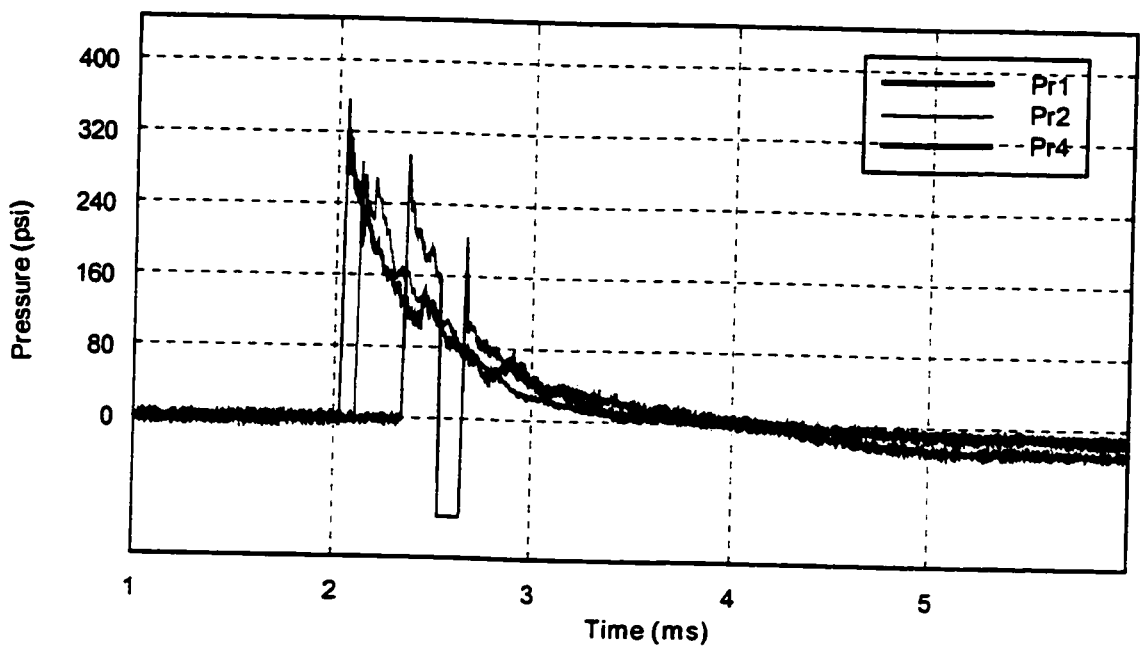

(b): Reflected pressure-time profiles

Figure C.5: Pressure-time profile for blast test # 1 (Panel CS1)

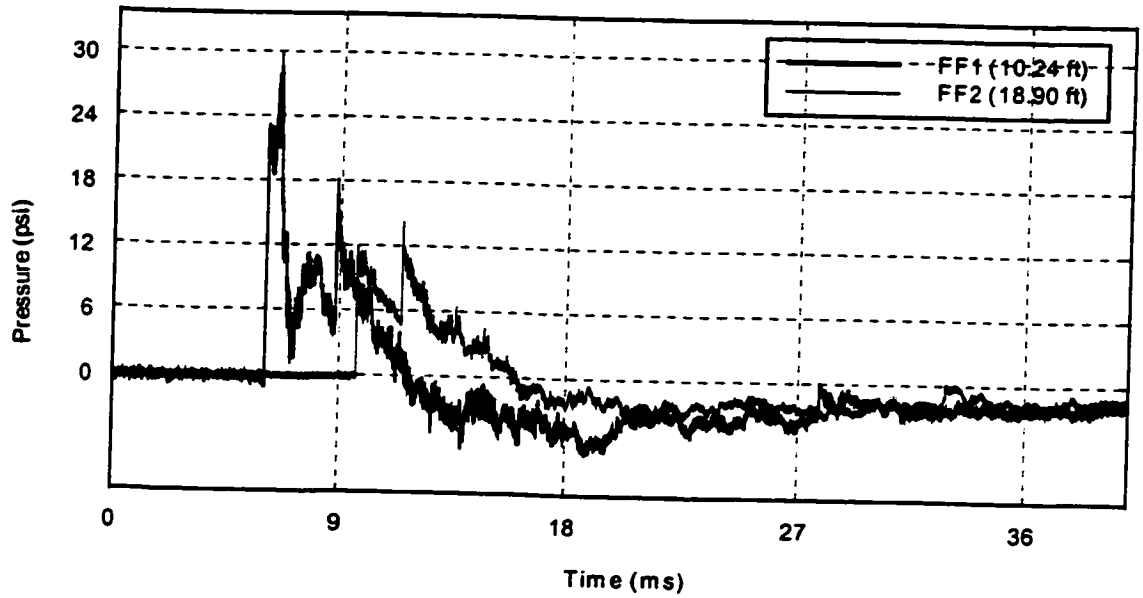

(a): Incident pressure-time profiles

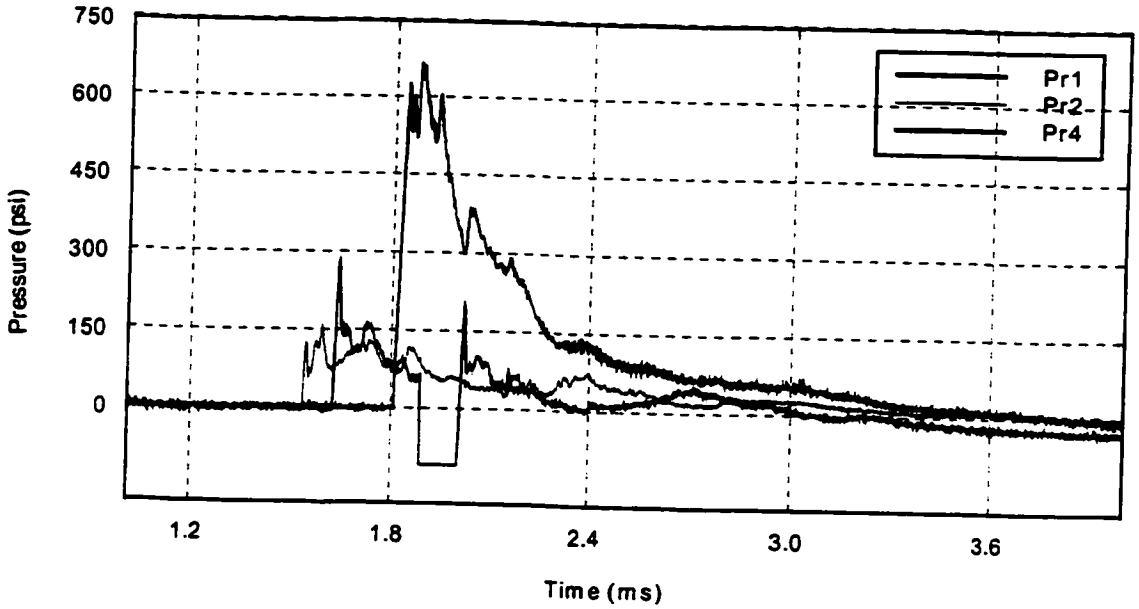

(b): Reflected pressure-time profiles

Figure C.6: Pressure-time profile for blast test # 2 (Panel CS1)

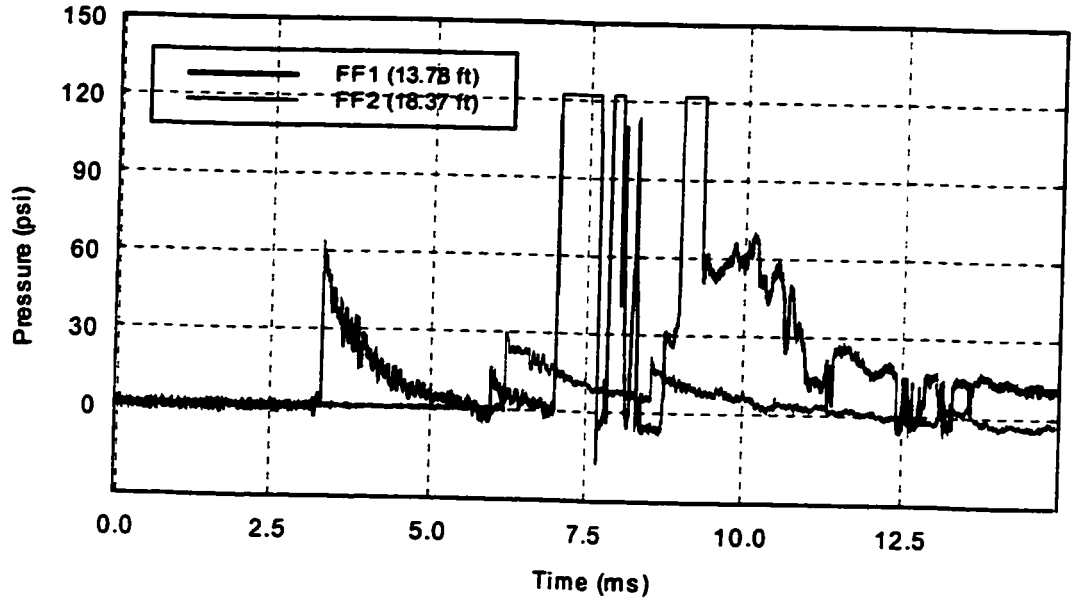

(a): Incident (free field) pressure-time profiles

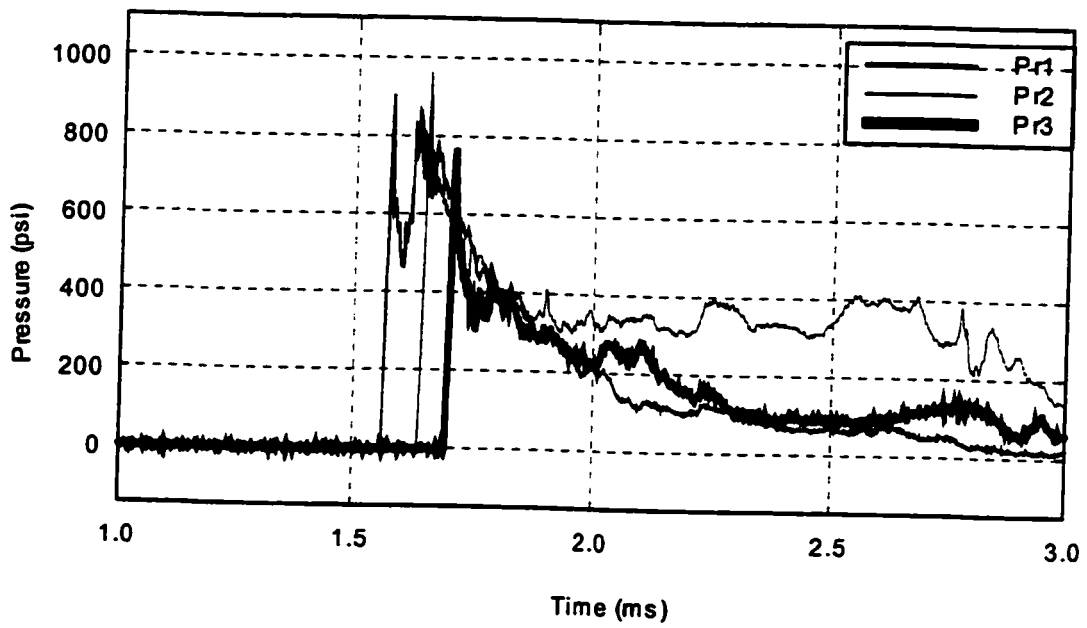

(b): Reflected pressure-time profiles

Figure C.7: Pressure-time profile for blast test # 8 (Panel CS2)

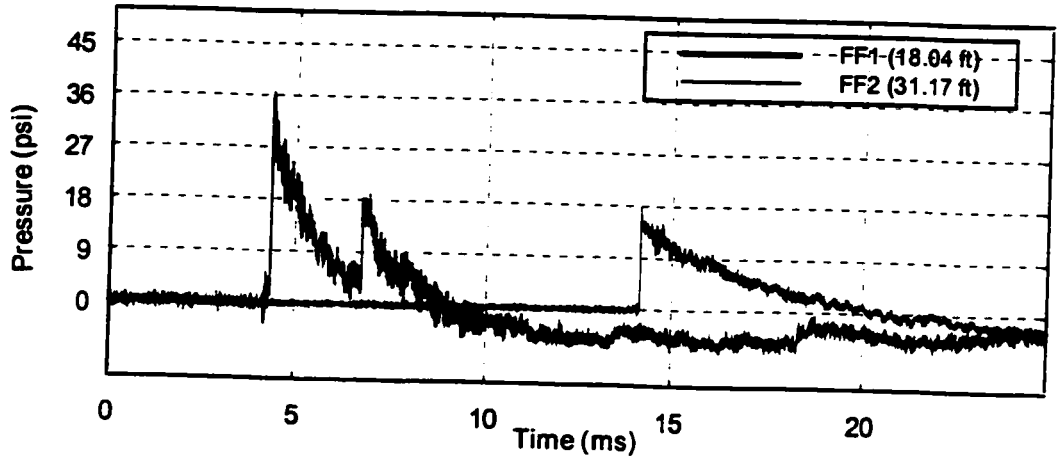

(a): Incident (free field) pressure-time profiles

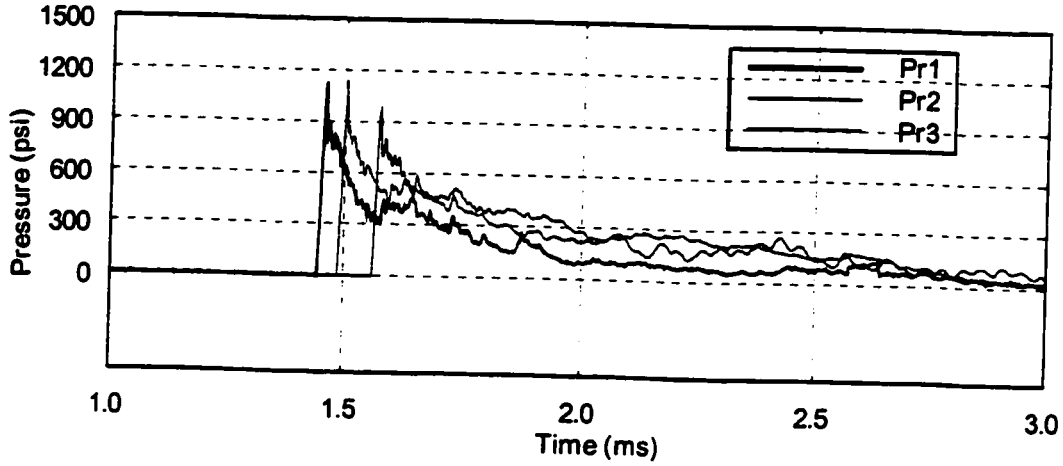

(b): Reflected pressure-time profiles

Figure C.8: Pressure-time profile for blast test # 15 (Panel CS3)

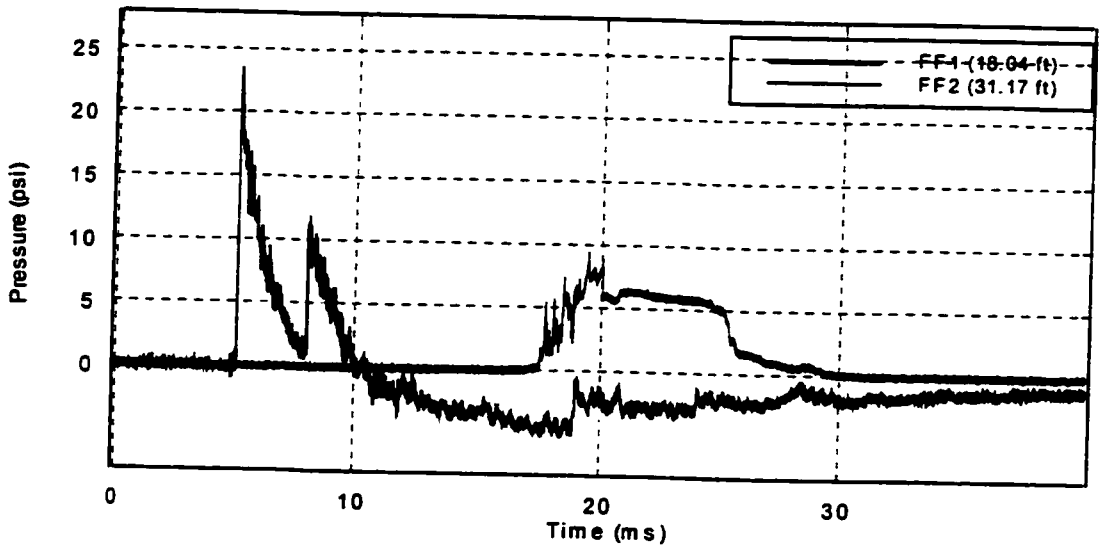

(a): Incident (free field) pressure-time profiles

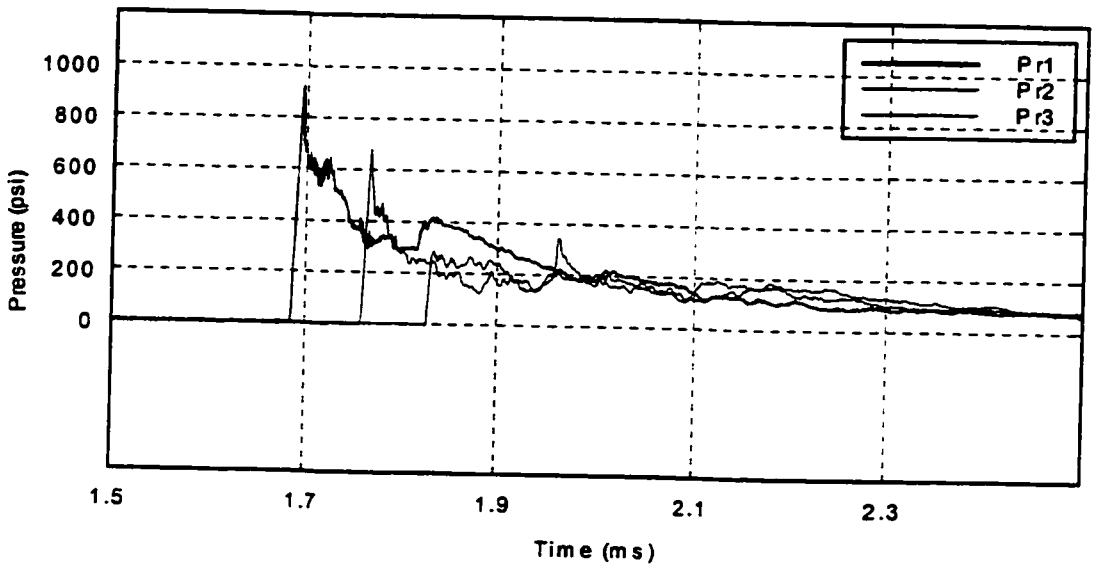

(b): Reflected pressure-time profiles

Figure C.9: Pressure-time profile for blast test # 17 (Panel CS4)

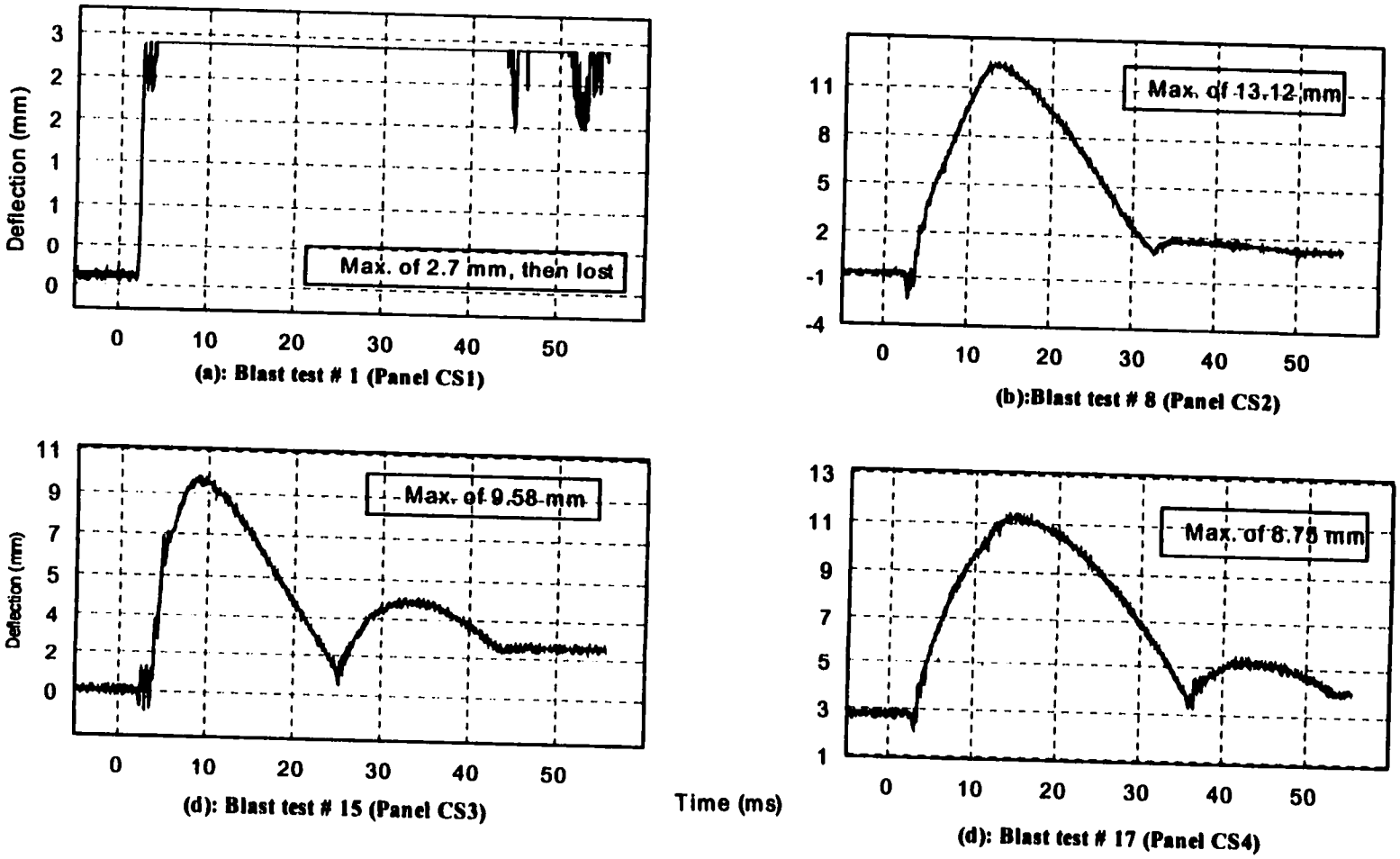

Figure C. 10: Mid-span deflection time histories of Group (1)

Group (2)

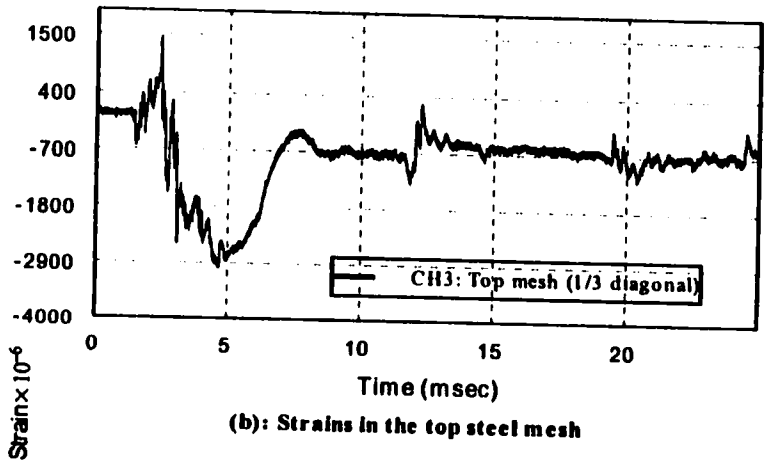

(b): Strains in the top steel mesh

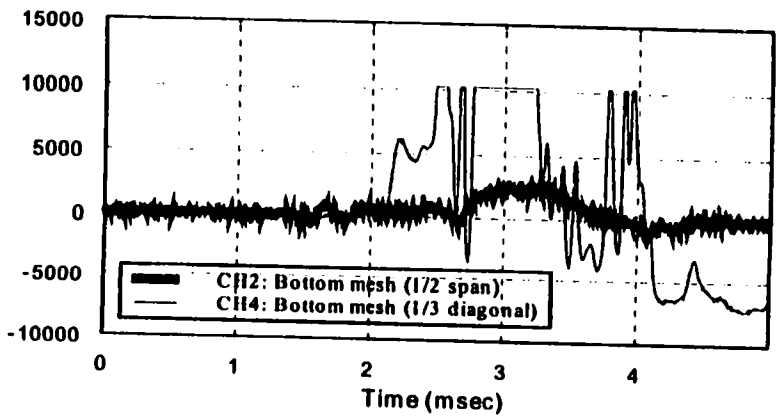

(b): Strains in the bottom steel mesh

Figure C.11: Strain-time profiles in steel (Blast test # 4: Panel GSS1)

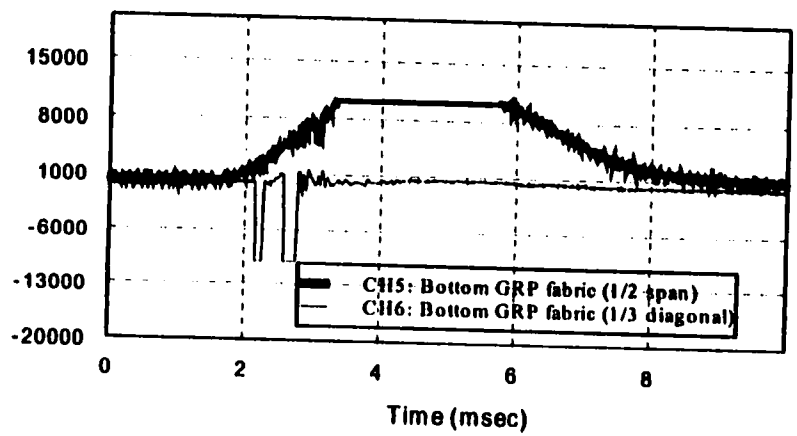

(b): Strains at the bottom GRP fabric

Figure C.12: Strain-time profiles on concrete surfaces (Blast test # 4: Panel GSS1)

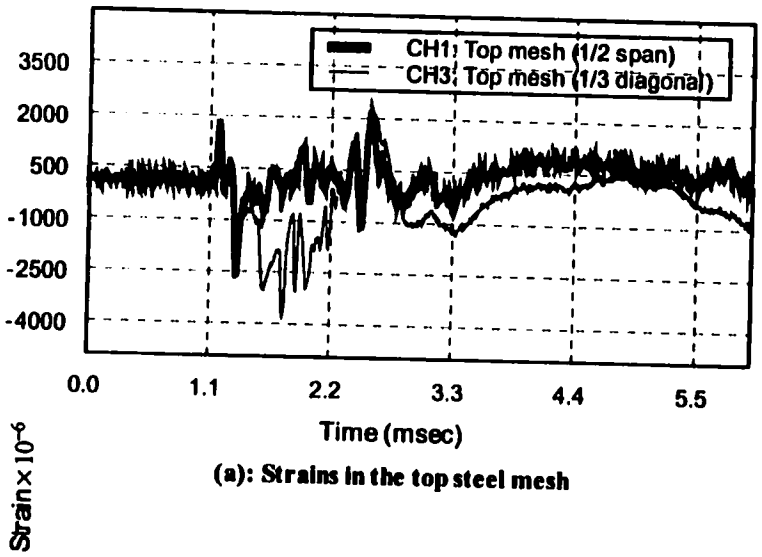

(a): Strains in the top steel mesh

Figure C.13: Strain-time profiles in steel
(Blast test # 7: Panel GSS2)

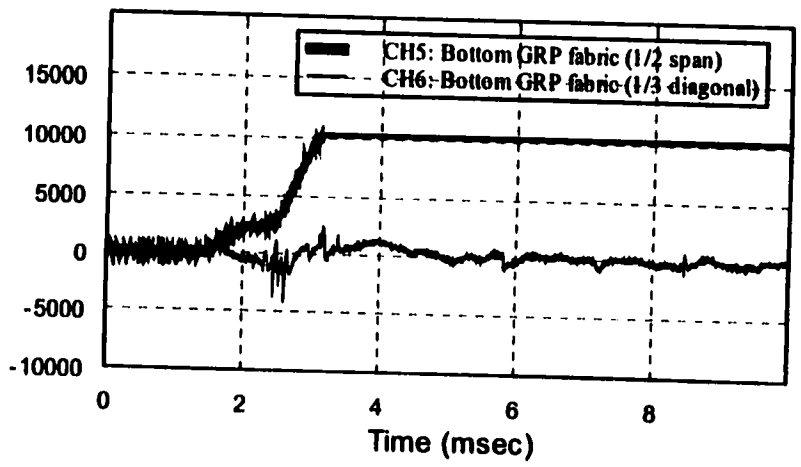

(b): Strains at the bottom GRP fabric

Figure C.14: Strain-time profiles in GFRP fabric
(Blast test # 7: Panel GSS2)

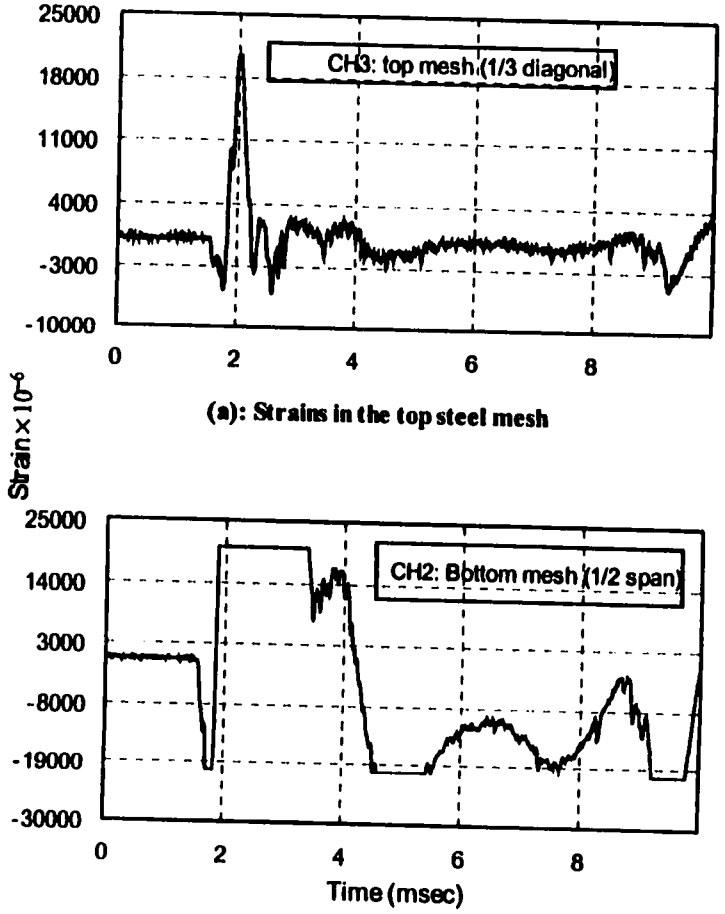

(a): Strains in the top steel mesh

(b): Strains in the bottom steel mesh

Figure C.15: Strain-time profiles in steel (Blast test # 12: Panel GSS3)

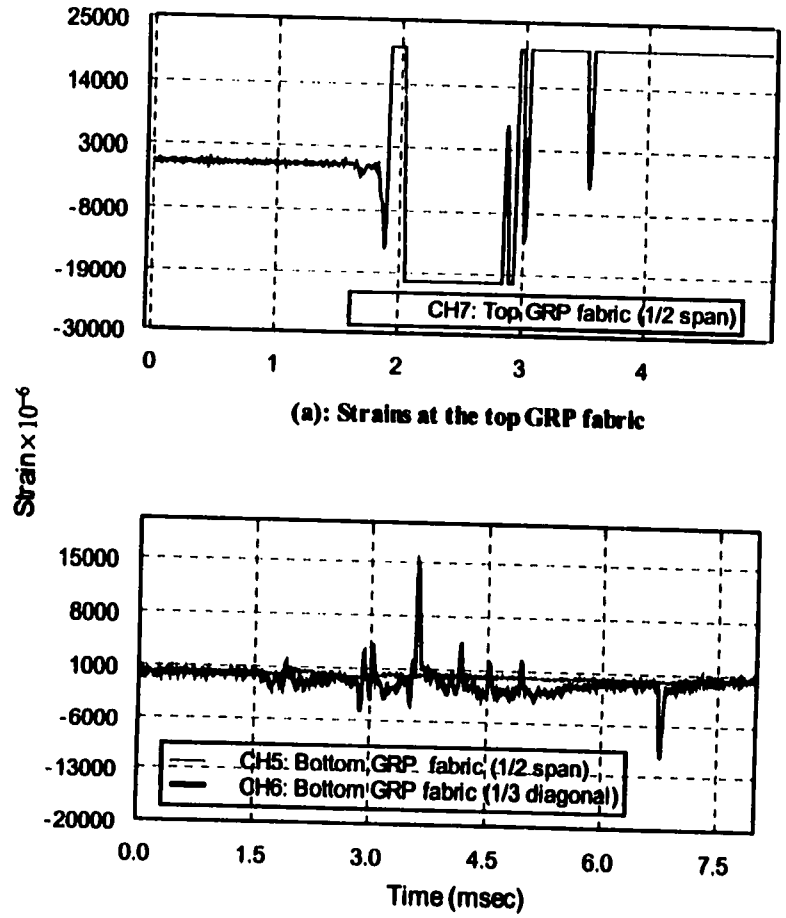

(a): Strains at the top GRP fabric

(b): Strains at the bottom GRP fabric

Figure C.16: Strain-time profiles in GFRP fabric (Blast test # 12: Panel GSS3)

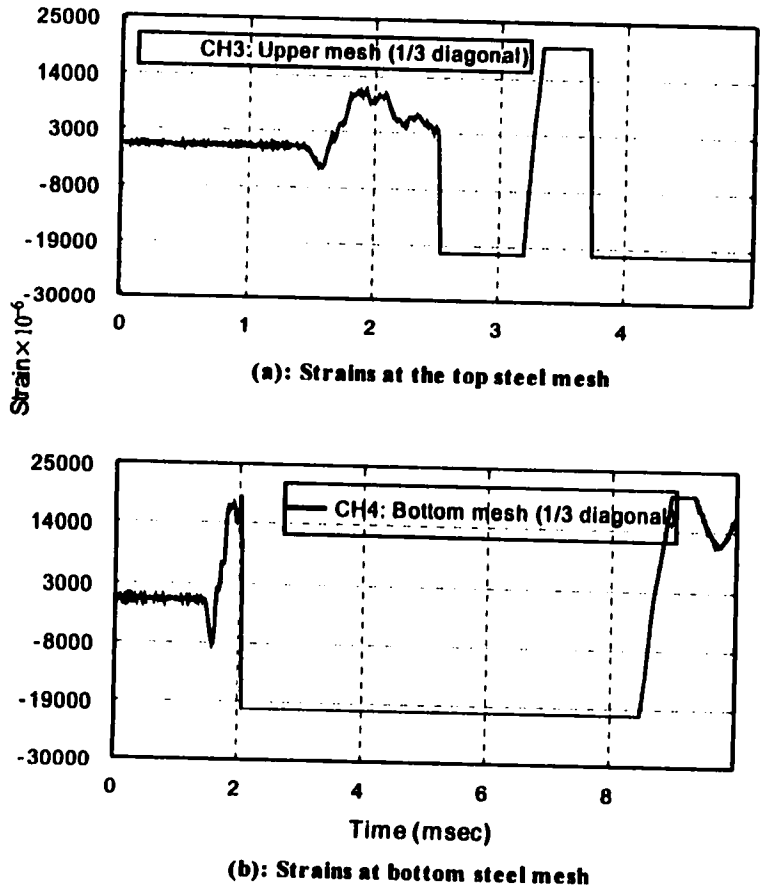

Figure C.17: Strain-time profiles in steel (Blast test # 14: Panel GSS4)

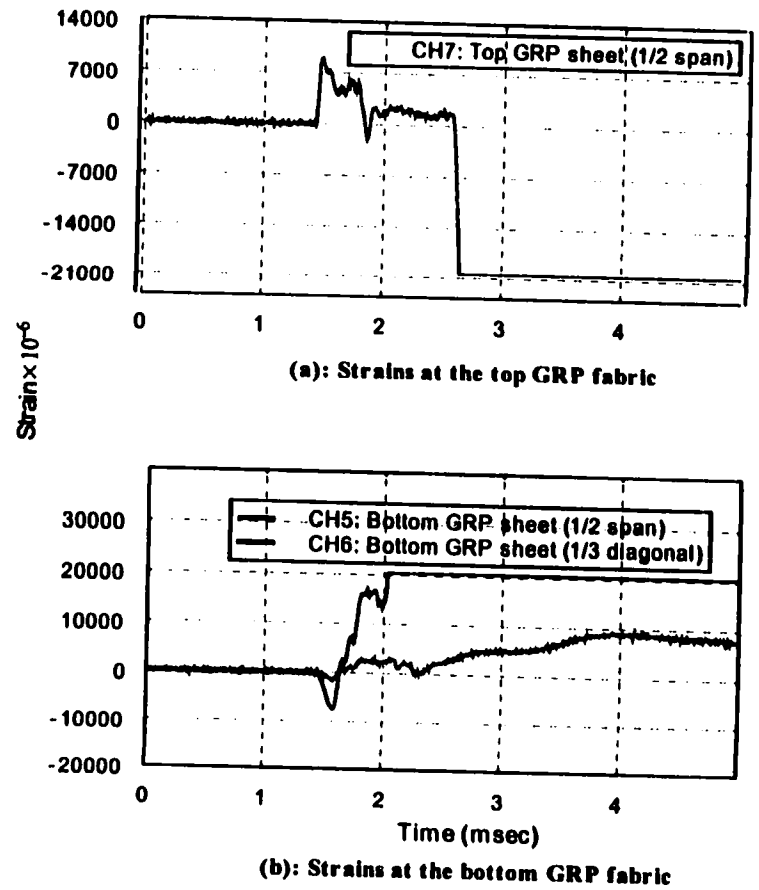

Figure C.18: Strain-time profiles in GFRP fabric (Blast test # 14: Panel GSS4)

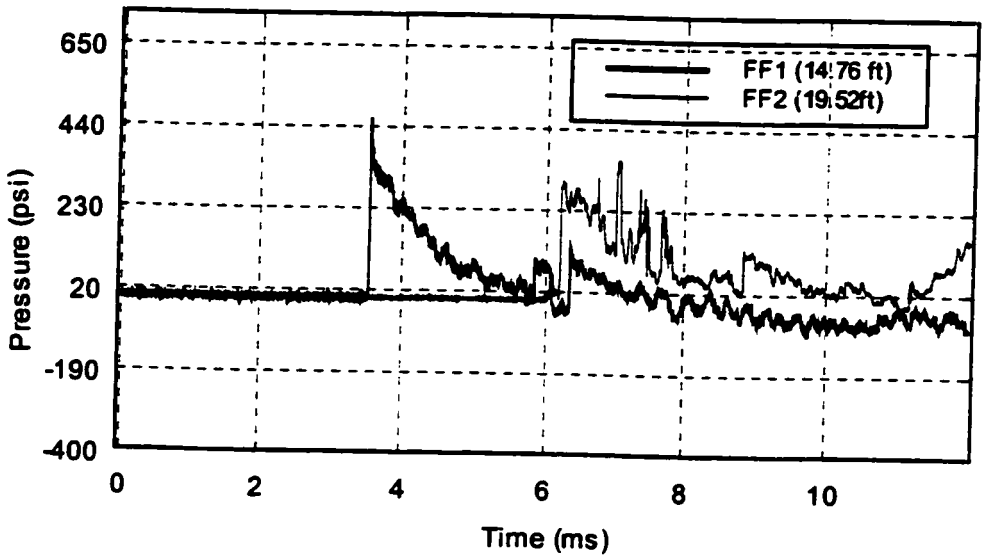

(a): Incident (free field) pressure-time profiles

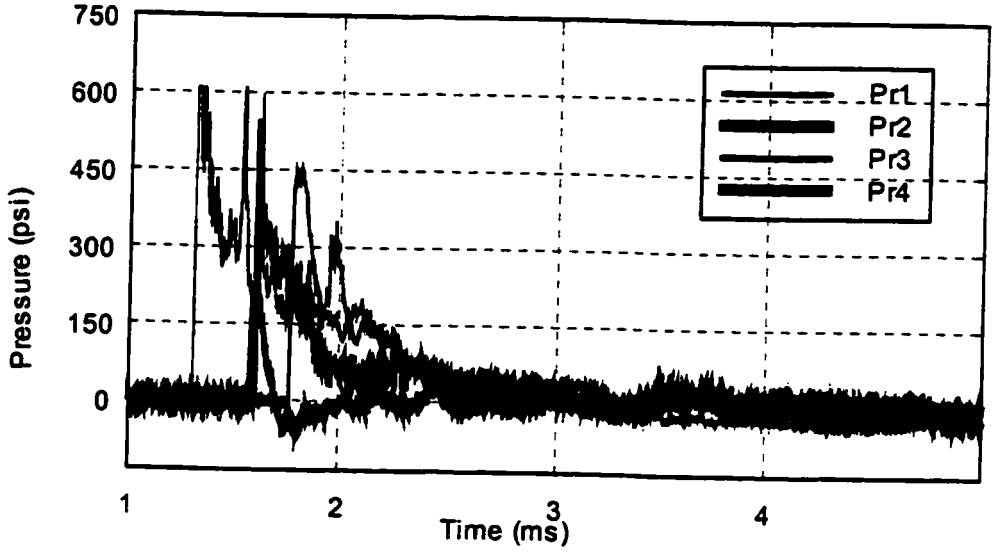

(b): Reflected pressure-time profiles

Figure C.19: Pressure-time profile for blast test # 4 (Panel GSS1)

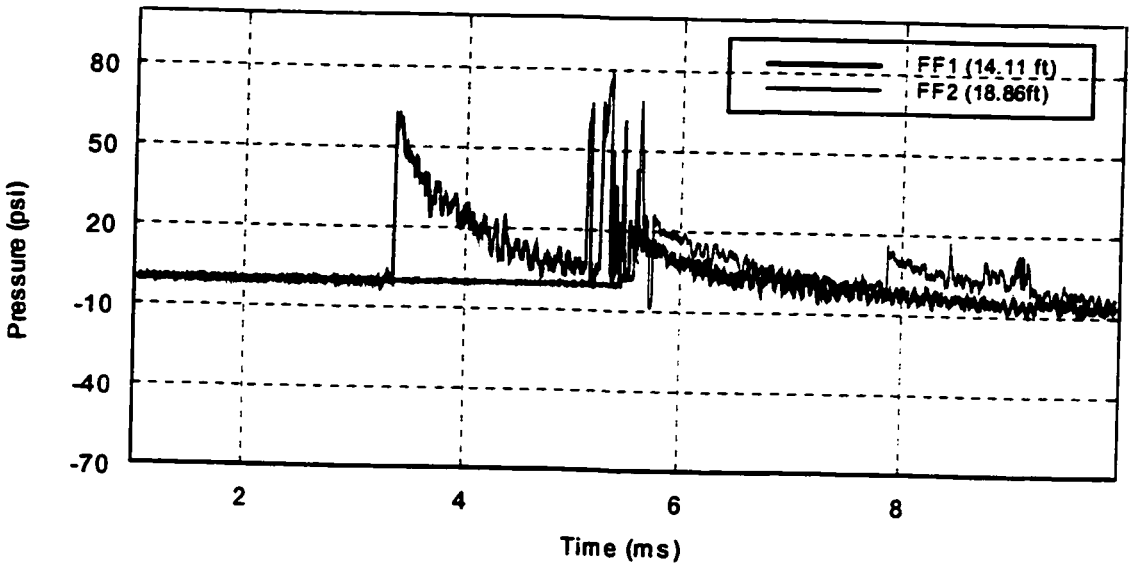

(a): Incident (free field) pressure-time profiles

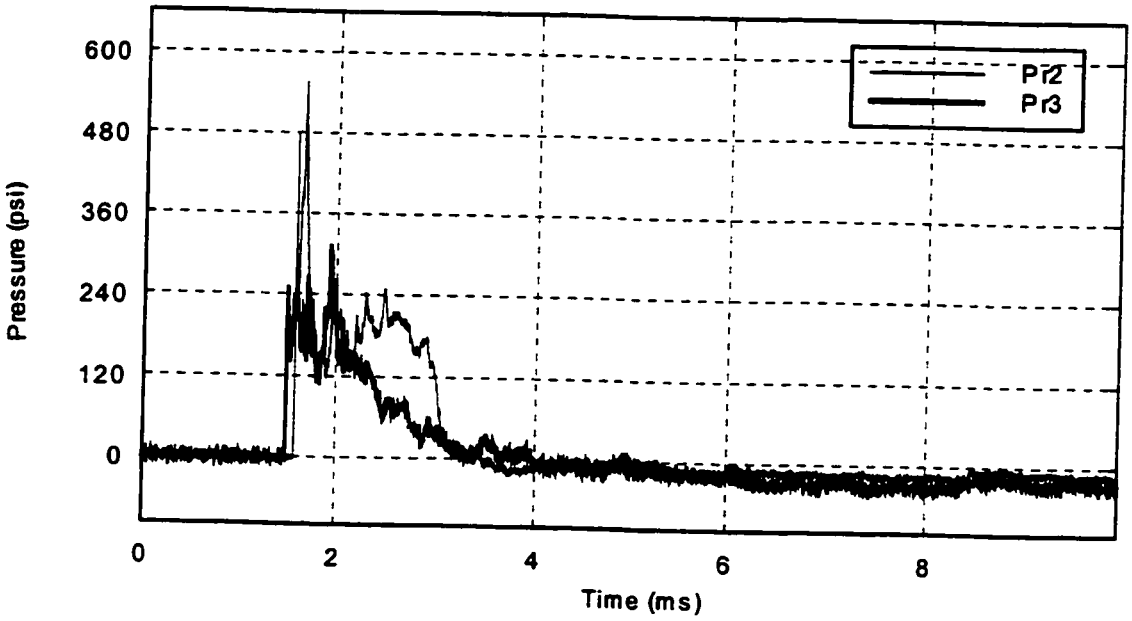

(b): Reflected pressure-time profiles

Figure C.20: Pressure-time profile for blast test # 7 (Panel GSS2)

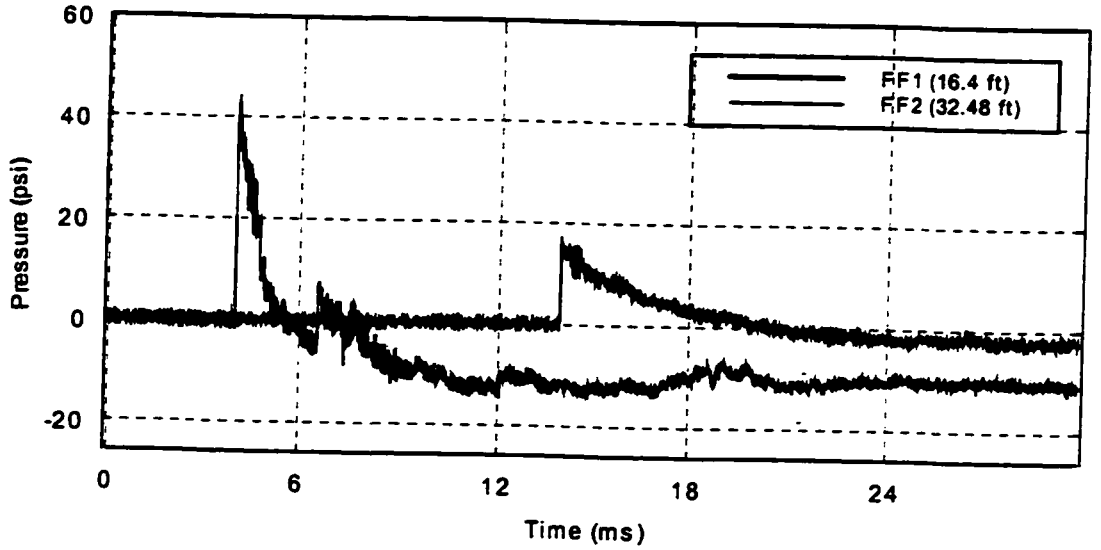

(a): Incident (free field) pressure-time profiles

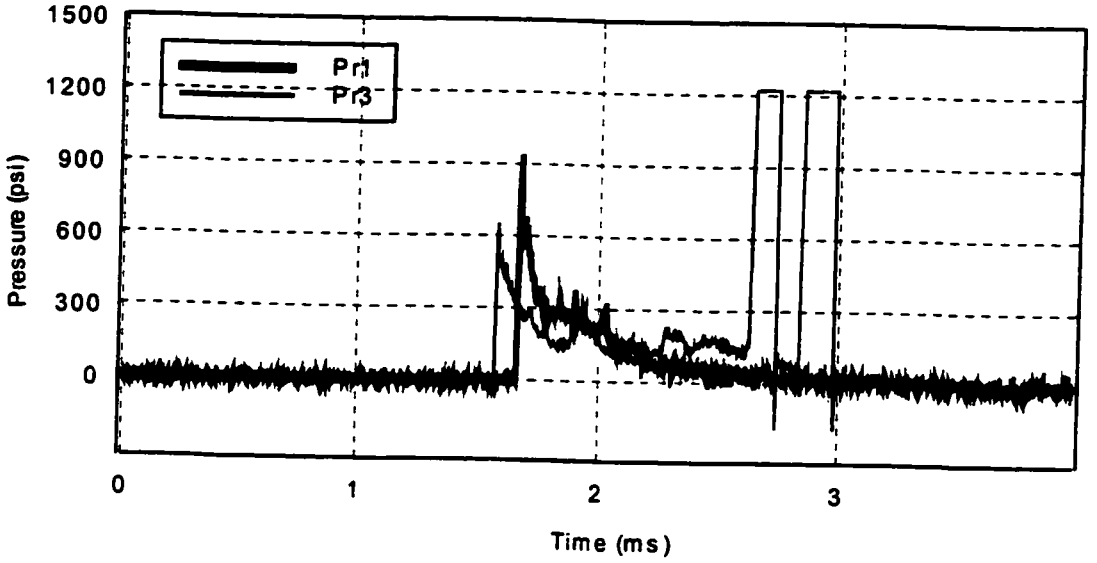

(b): Reflected pressure-time profiles

Figure C.21: Pressure-time profile for blast test # 12 (Panel GSS3)

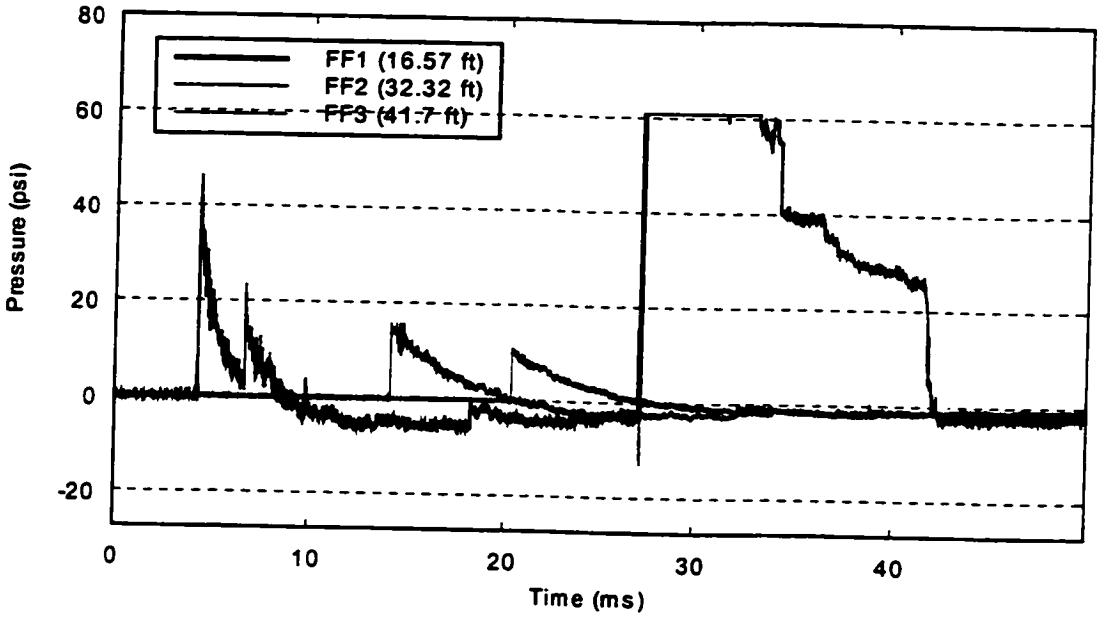

Free Field Pressure-Time Profile

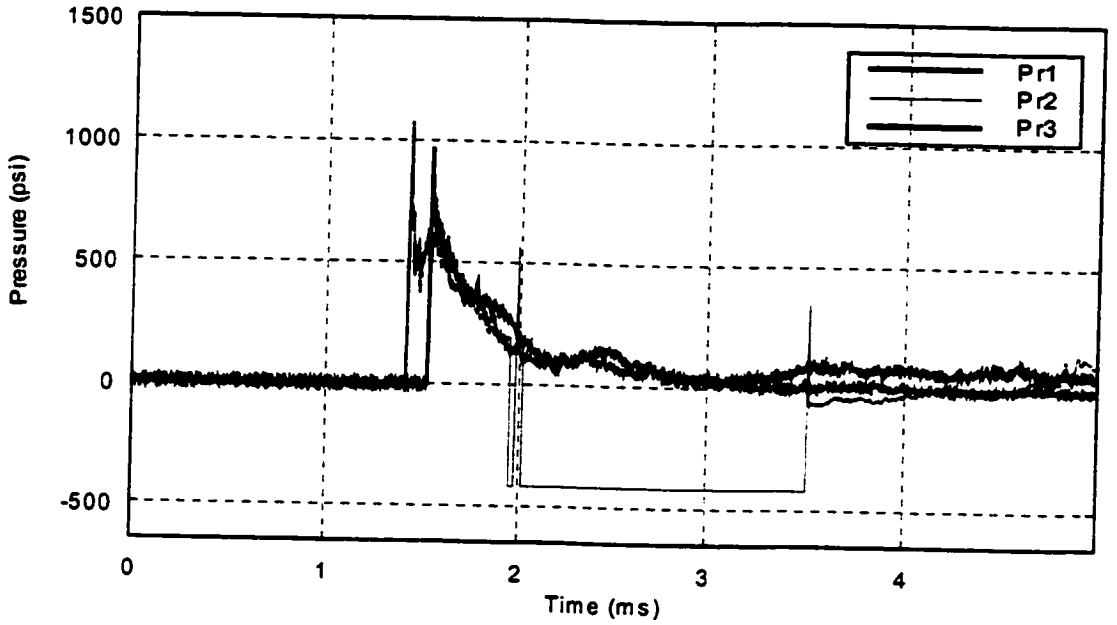

Reflected Pressure-Time Profile

Figure C.22: Pressure-time profile for blast test # 14 (Panel GSS4)

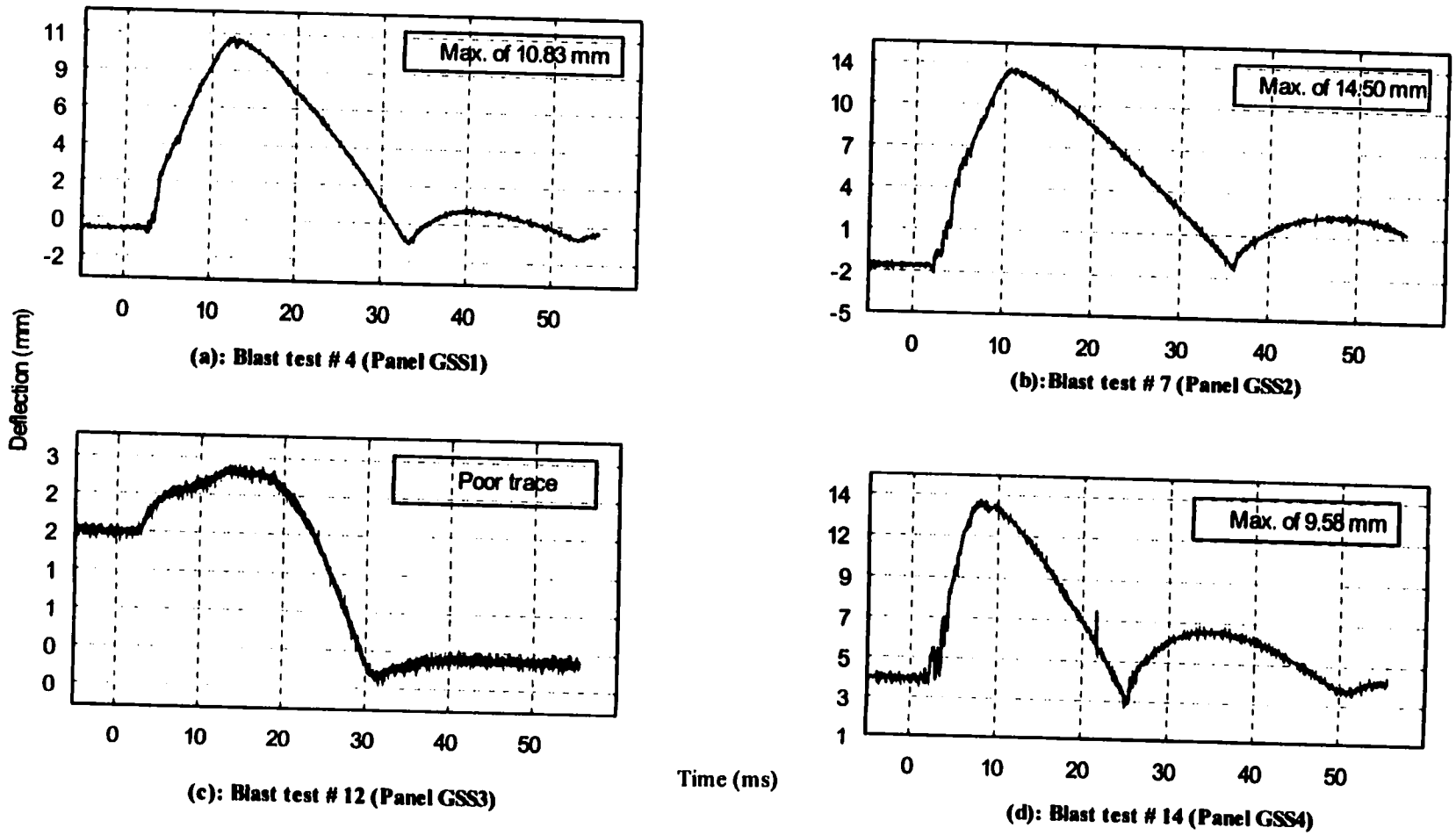

Figure C.23: Mid-span deflection time histories of Group (2)

Group (3)

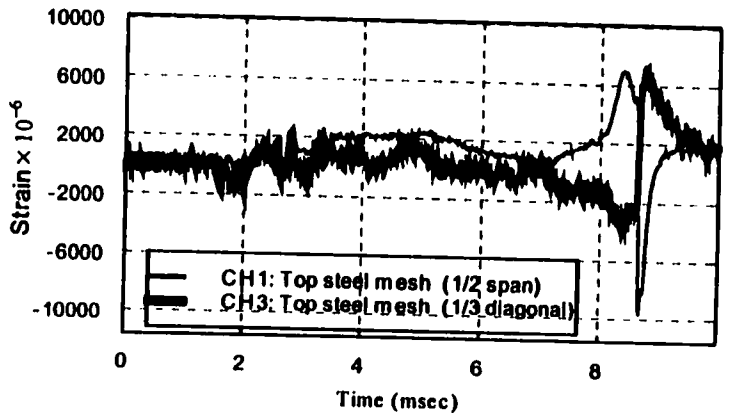

(a): Strains in the top steel mesh

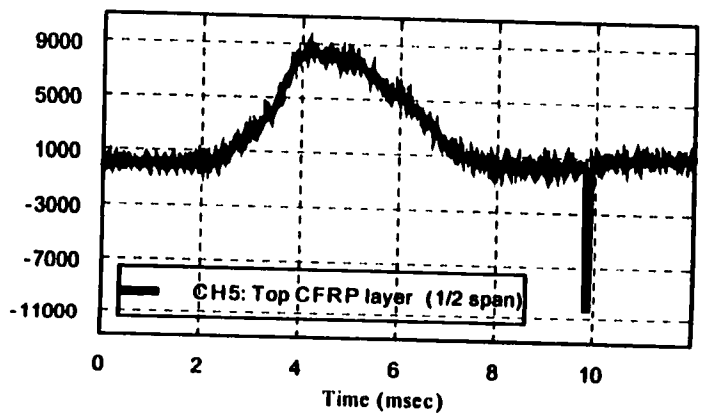

(a): Strains in the top Carbon layers

Figure C.24: Strain-time profiles in steel (Blast test # 5: Panel CSS1)

Figure C.25: Strain-time profiles in CFRP sheet (Blast test # 5: Panel CSS1)

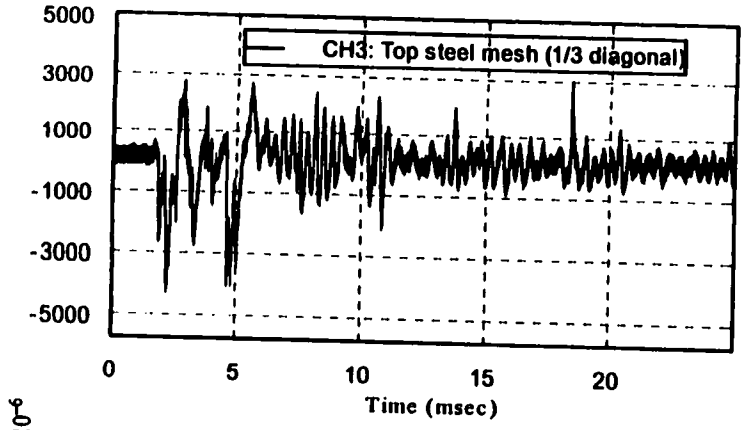

(a): Strains in the top steel mesh

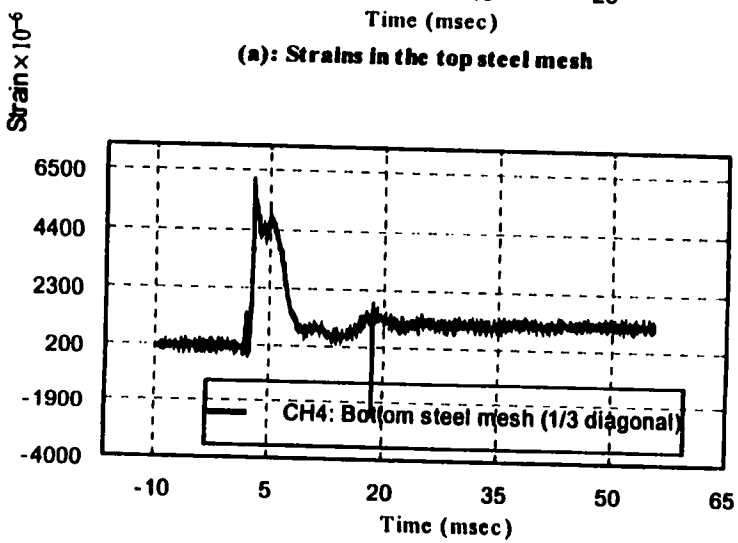

(b): Strains in the bottom steel mesh

Figure C.26: Strain-time profiles in steel (Blast test # 9: Panel CSS2)

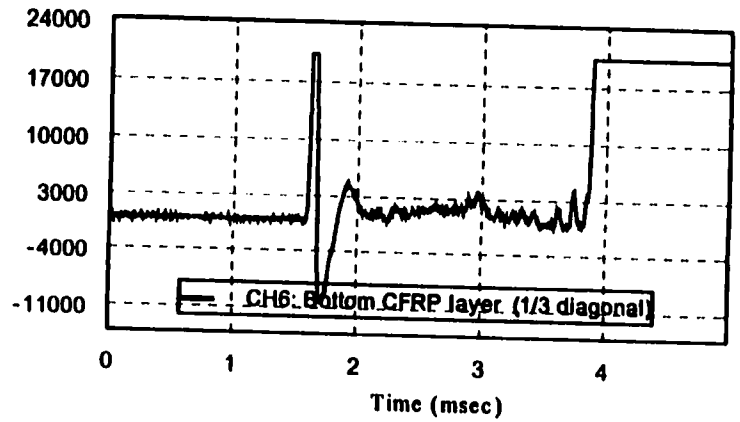

(b): Strains in the Bottom Carbon layers

Figure C.27: Strain-time profiles in CFRP sheet (Blast test # 9: Panel CSS2)

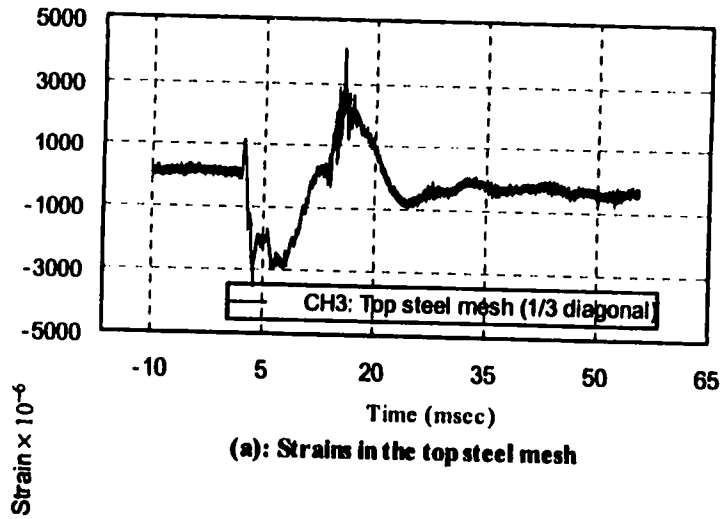

(a): Strains in the top steel mesh

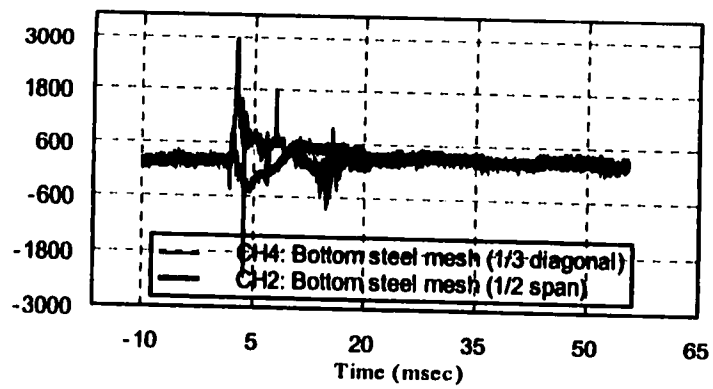

(b): Strains in the bottom steel mesh

Figure C.28: Strain-time profiles in steel (Blast test # 11: Panel CSS3)

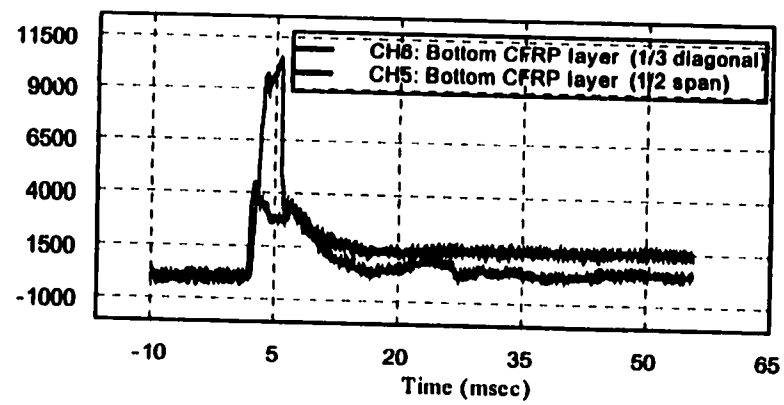

(b): Strains on the Bottom Carbon layers

Figure C.29: Strain-time profiles in CFRP sheet (Blast test # 11: Panel CSS3)

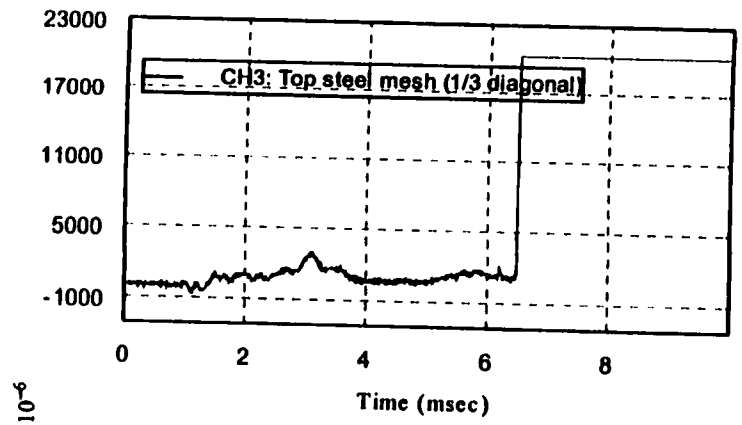

(a): Strains in the top steel mesh

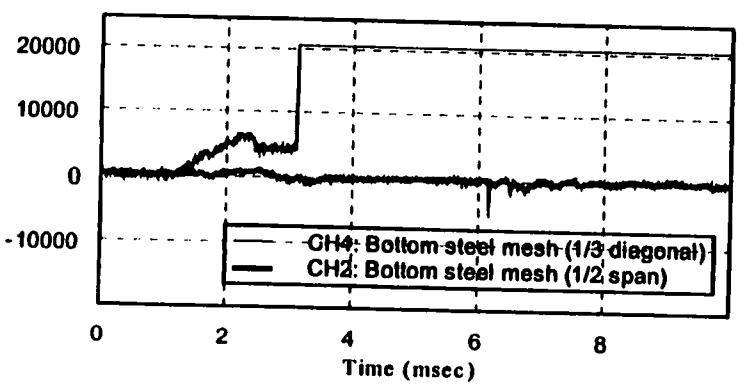

(b): Strains in the bottom steel mesh

Figure C.30: Strain-time profiles in steel (Blast test # 13: Panel CSS4)

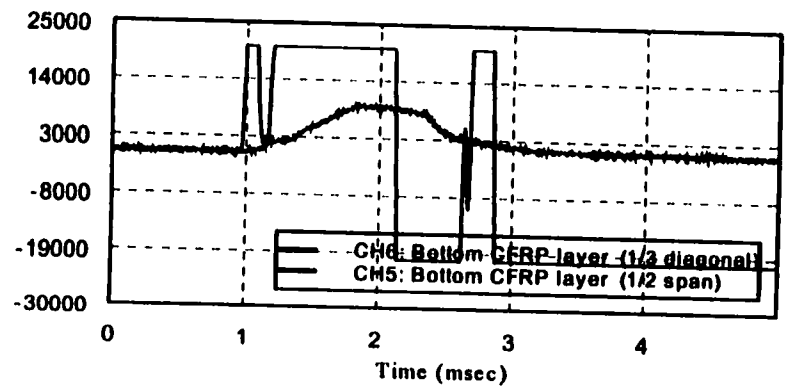

(b): Strains in the Bottom Carbon layers

Figure C.31: Strain-time profiles in CFRP sheet (Blast test # 13: Panel CSS4)

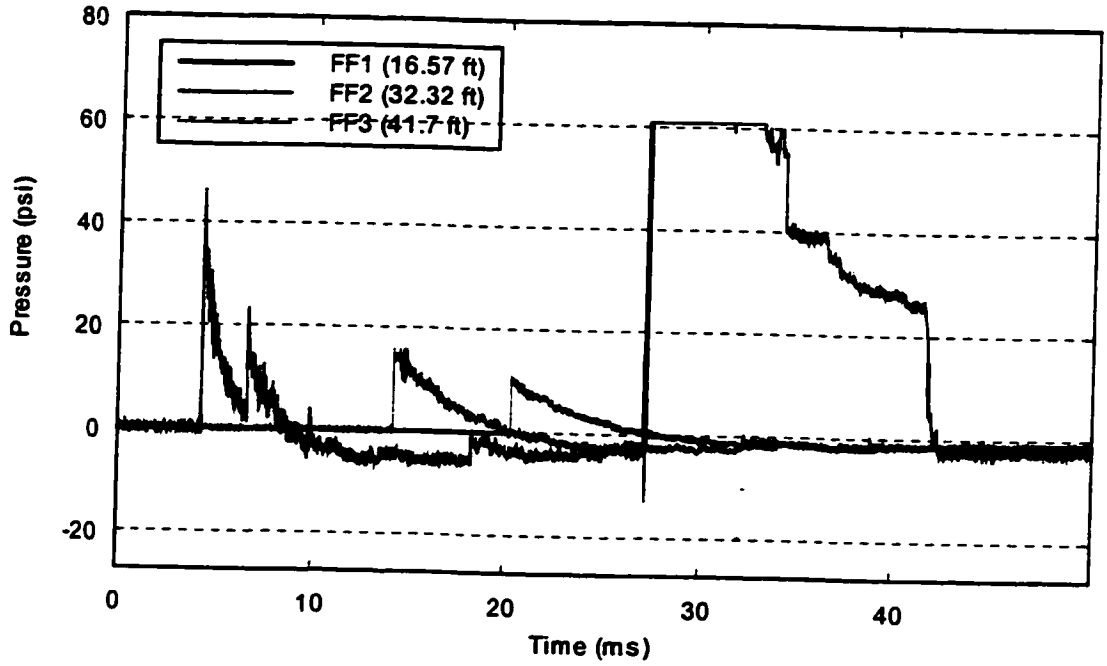

Free Field Pressure-Time Profile

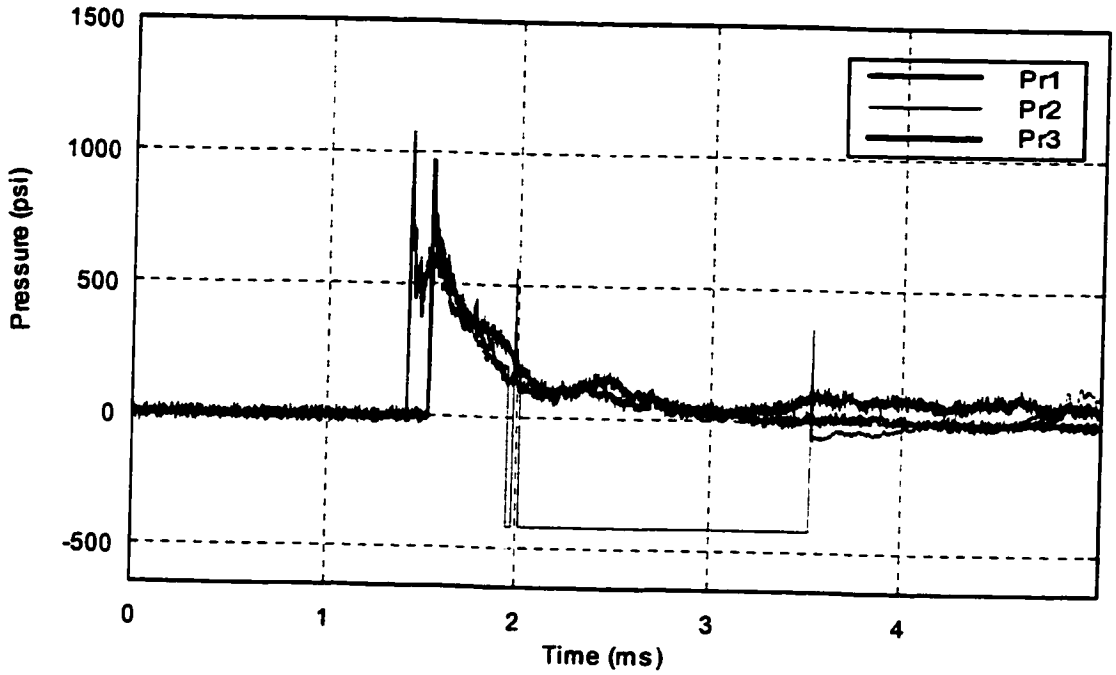

Reflected Pressure-Time Profile

Figure C.32: Pressure-time profile for blast test # 5 (Panel CSS1)

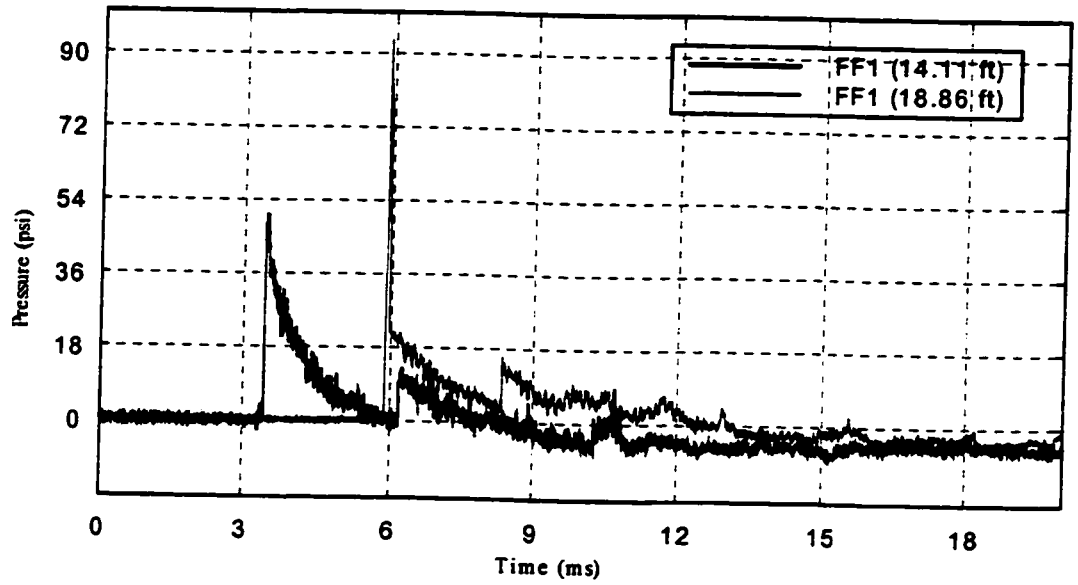

(a): Incident (free field) pressure-time profiles

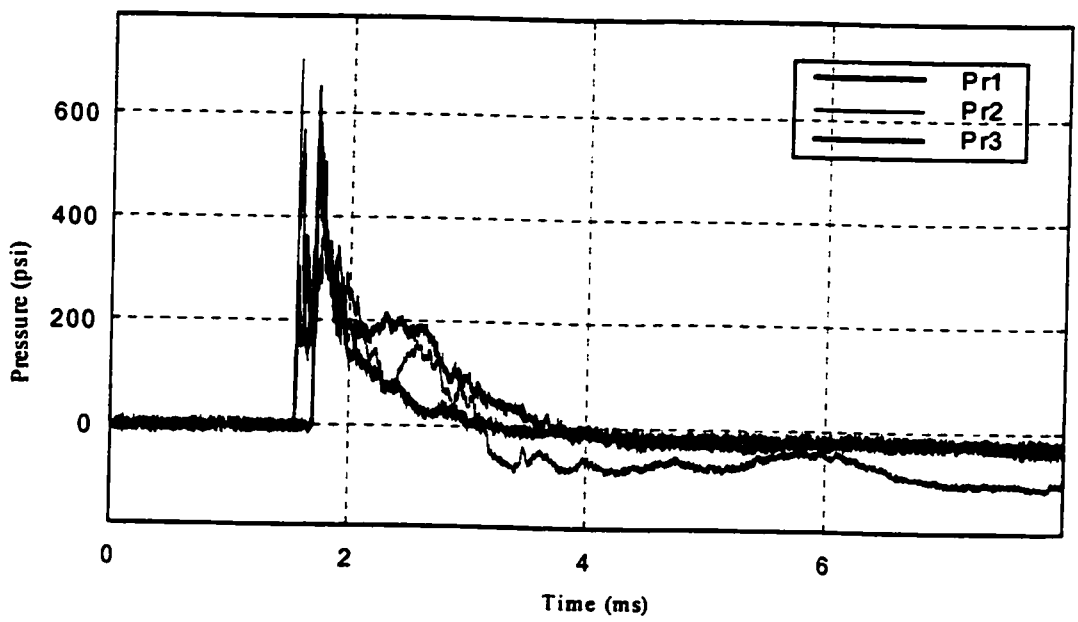

(b): Reflected pressure-time profiles

Figure C.33: Pressure-time profile for blast test # 9 (Panel CSS2)

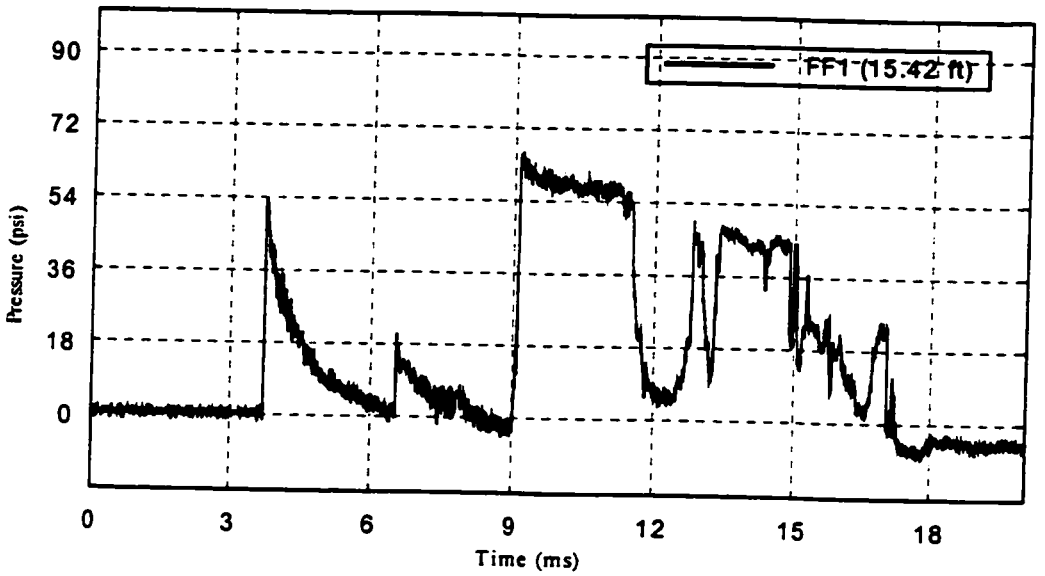

(a): Incident (free field) pressure-time profiles

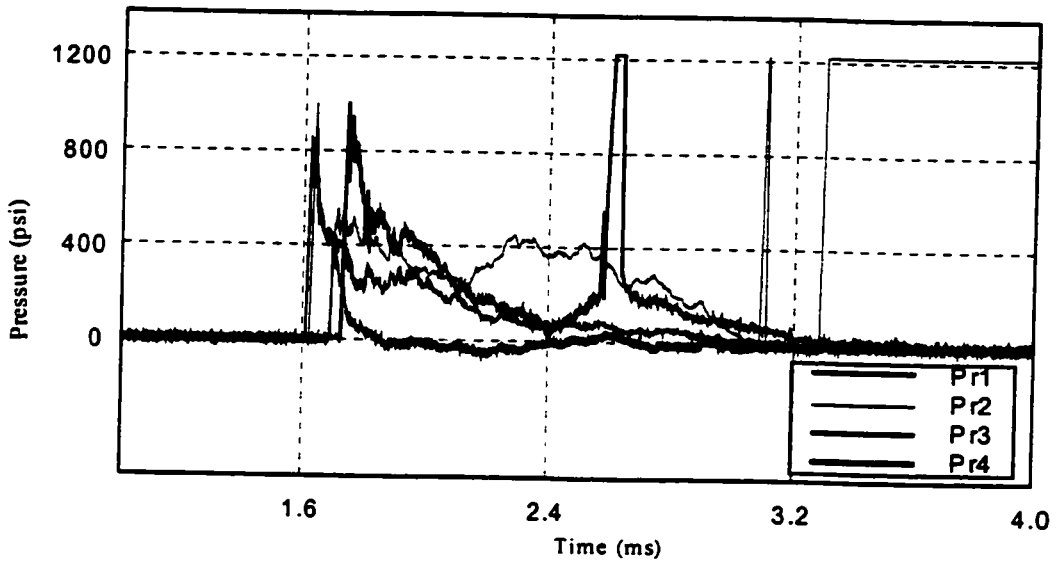

(b): Reflected pressure-time profiles

Figure C.34: Pressure-time profile for blast test # 11 (Panel CSS3)

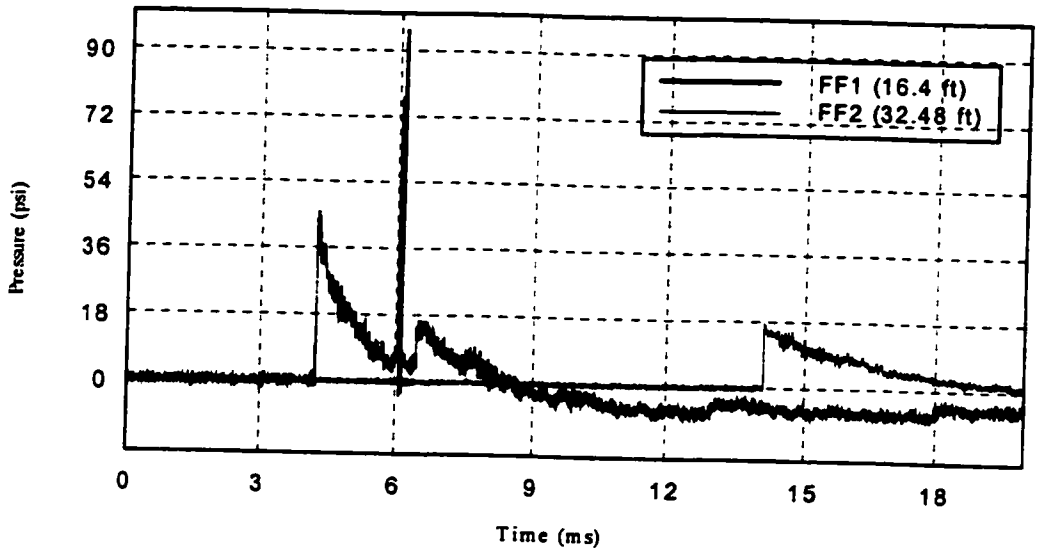

(a): Incident (free field) pressure-time profiles

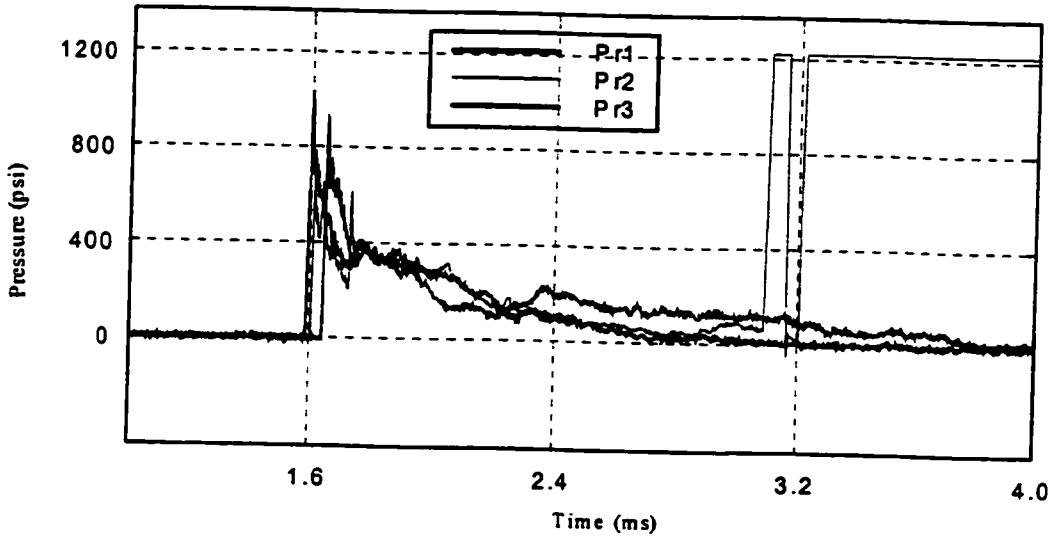

(b): Reflected pressure-time profiles

Figure C.35: Pressure-time profile for blast test # 13 (Panel CSS4)

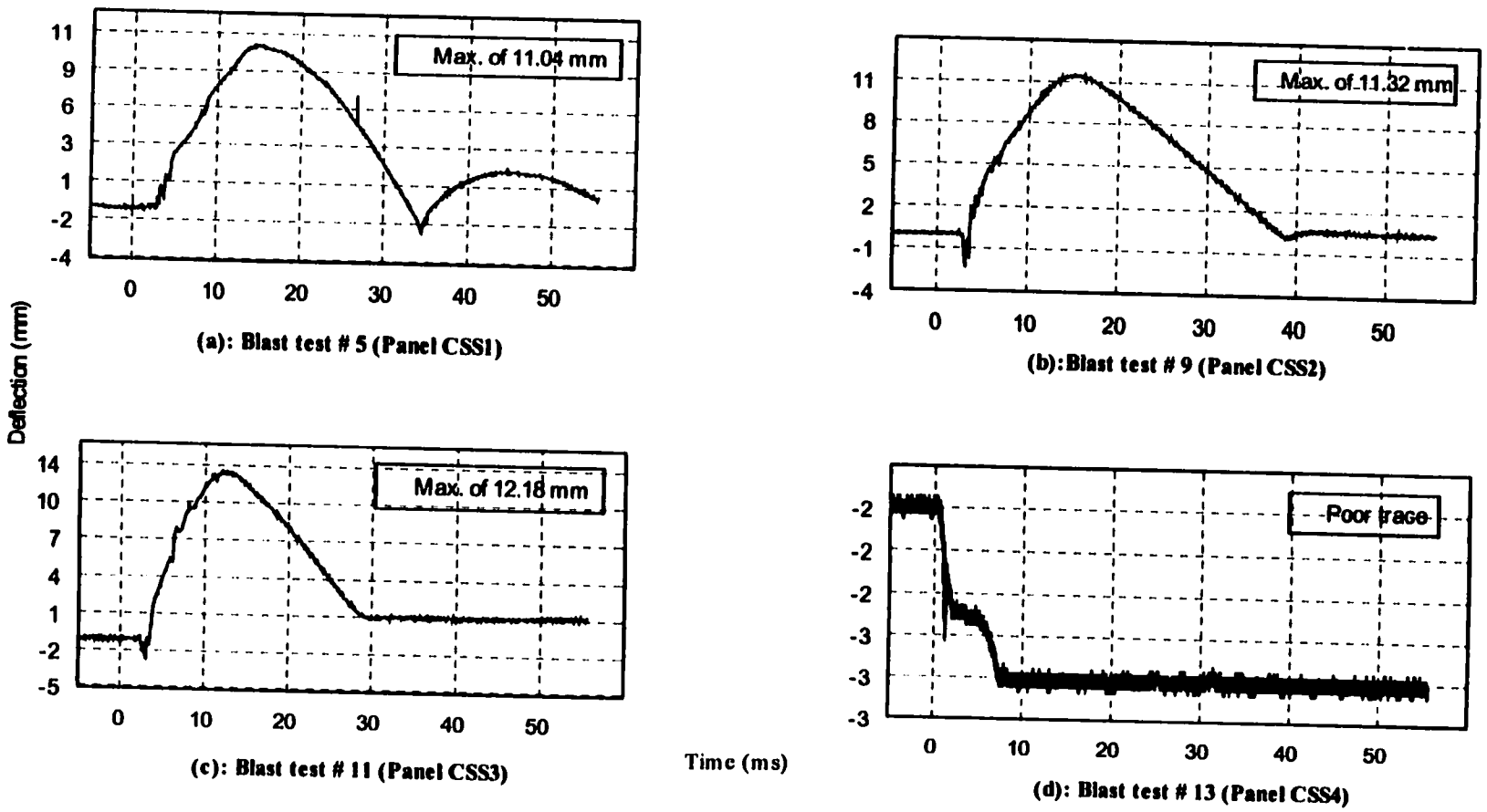

Figure C.36: Mid-span deflection time histories of Group (3)

Group (4)

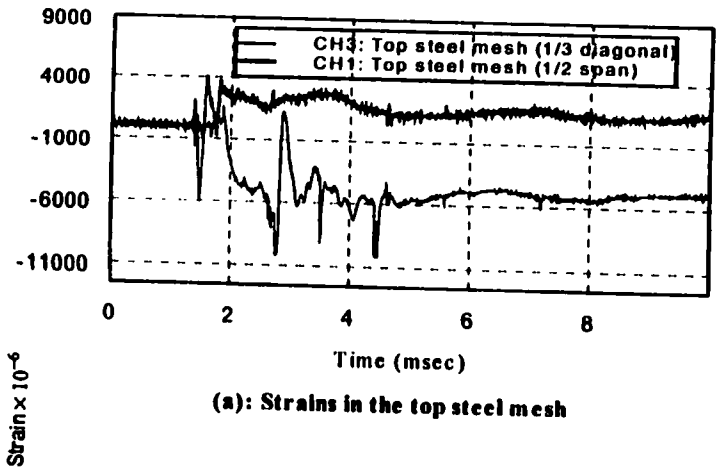

(a): Strains in the top steel mesh

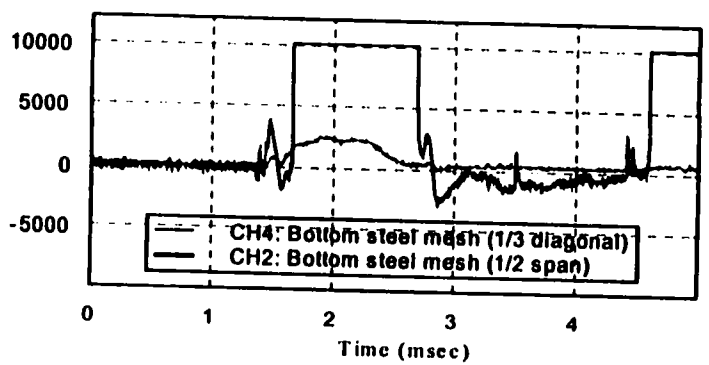

(b): Strains in the bottom steel mesh

Figure C.37: Strain-time profiles in steel (Blast test # 3: Panel CLS1)

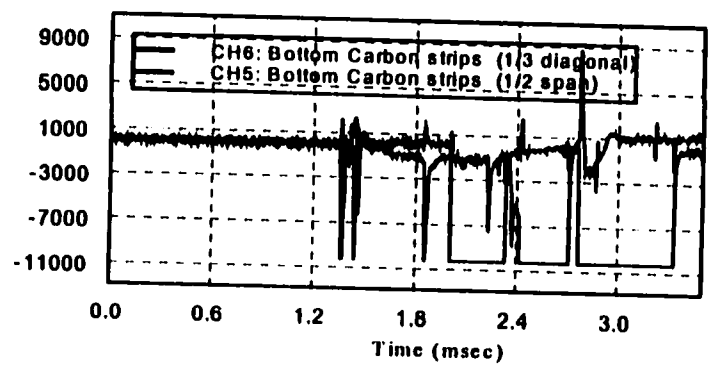

(b): Strains in the Bottom Carbon layers

Figure C.38: Strain-time profiles in CFRP strips (Blast test # 3: Panel CLS1)

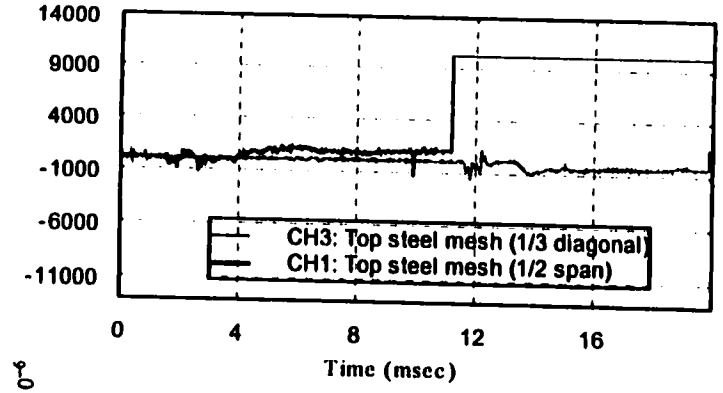

(a): Strains in the top steel mesh

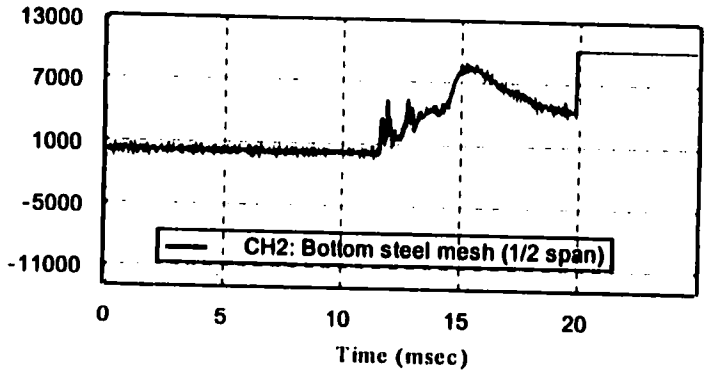

(b): Strains in the bottom steel mesh

Figure C.39: Strain-time profiles in steel (Blast test # 6: Panel CLS2)

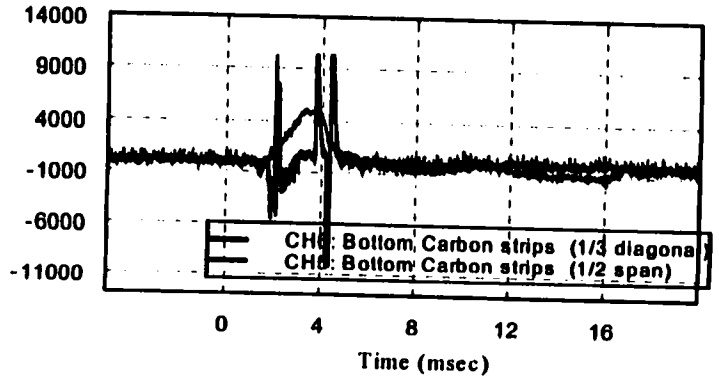

(b): Strains in the bottom Carbon layers

Figure C.40: Strain-time profiles in CFRP strips (Blast test # 6: Panel CLS2)

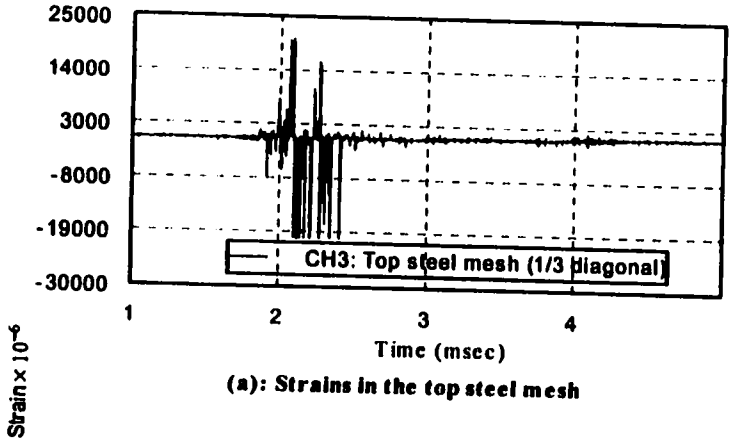

(a): Strains in the top steel mesh

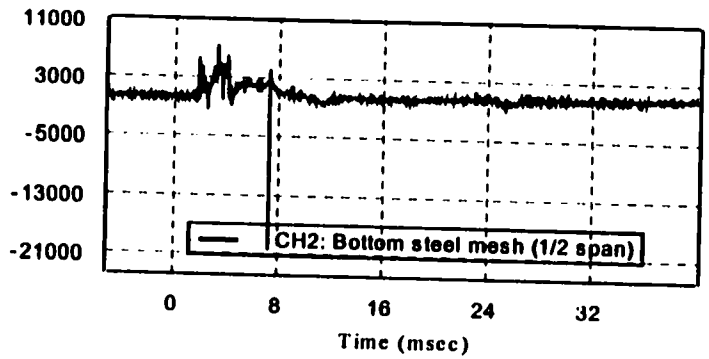

(b): Strains in the bottom steel mesh

Figure C.41: Strain-time profiles in steel (Blast test # 10: Panel CLS3)

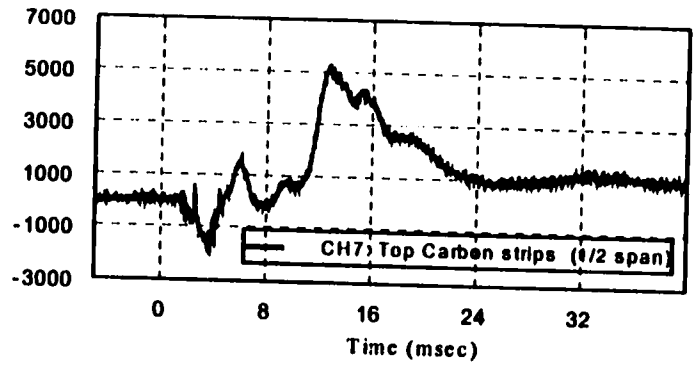

(a): Strains in the top Carbon strips

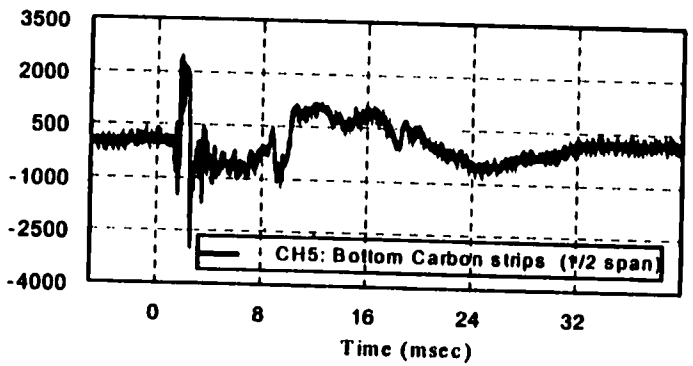

(b): Strains in the bottom Carbon strips

Figure C.42: Strain-time profiles in CFRP strips (Blast test # 10: Panel CLS3)

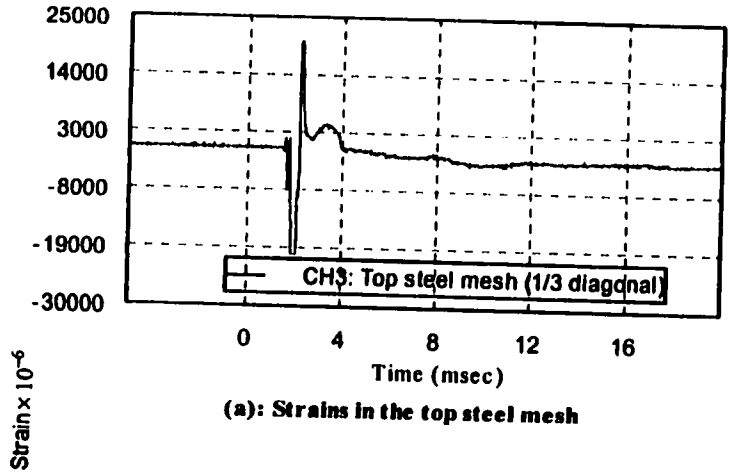

(a): Strains in the top steel mesh

Figure C.43: Strain-time profiles in steel
(Blast test # 16: Panel CLS4)

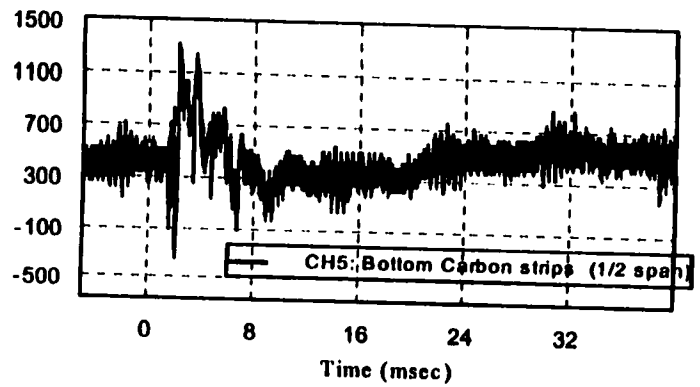

(b): Strains in the bottom Carbon strips

Figure C.44: Strain-time profiles in CFRP strips
(Blast test # 16: Panel CLS4)

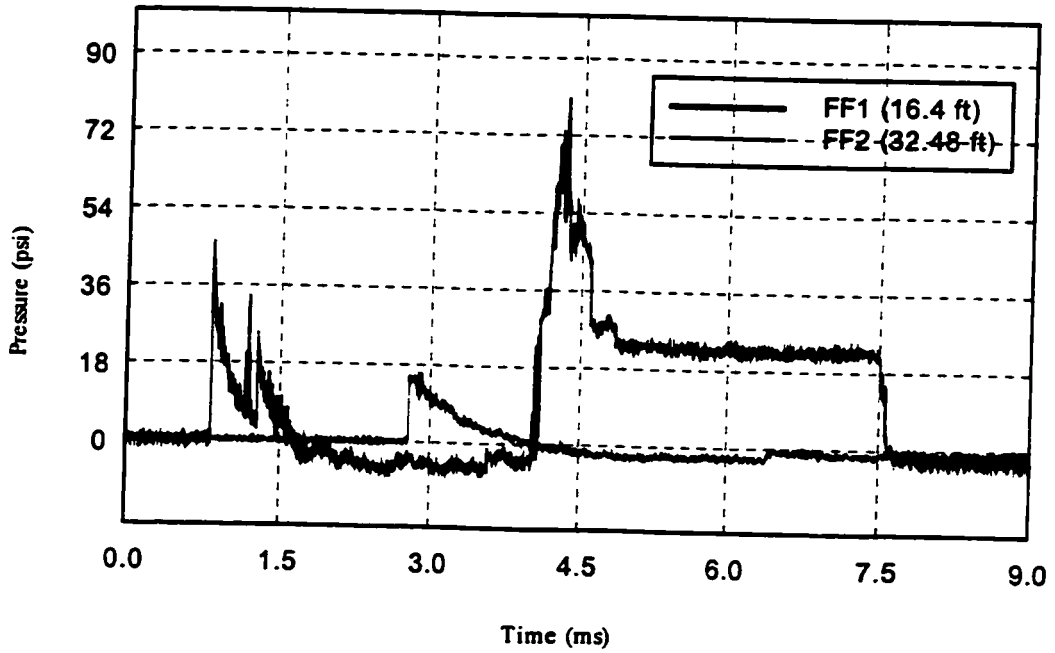

(a): Incident (free field) pressure-time profiles

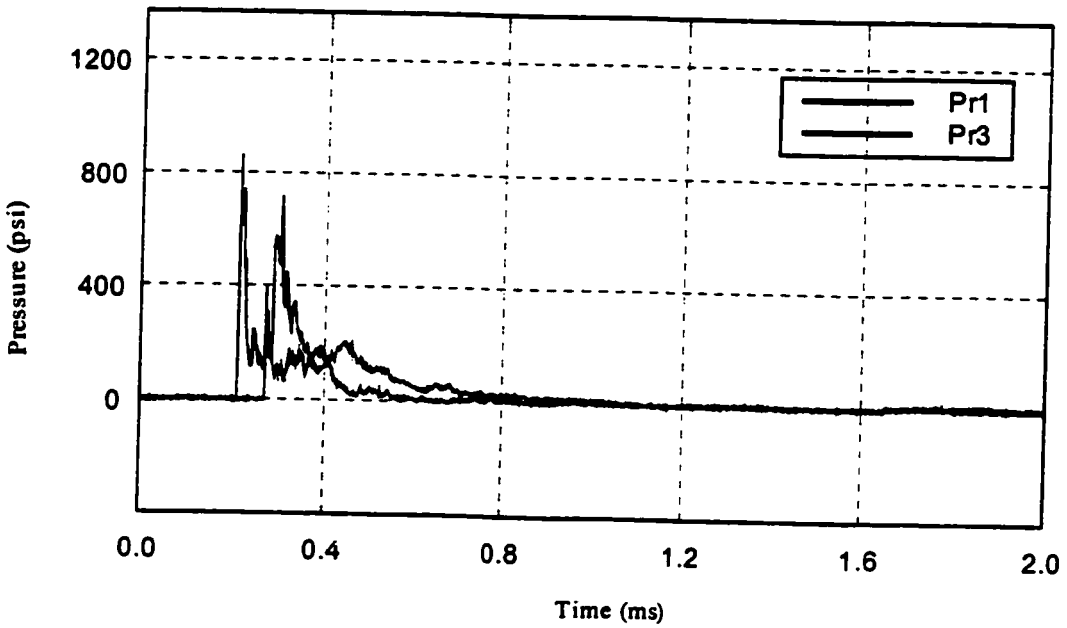

(b): Reflected pressure-time profiles

Figure C.45: Pressure-time profile for blast test # 3 (Panel CLS1)

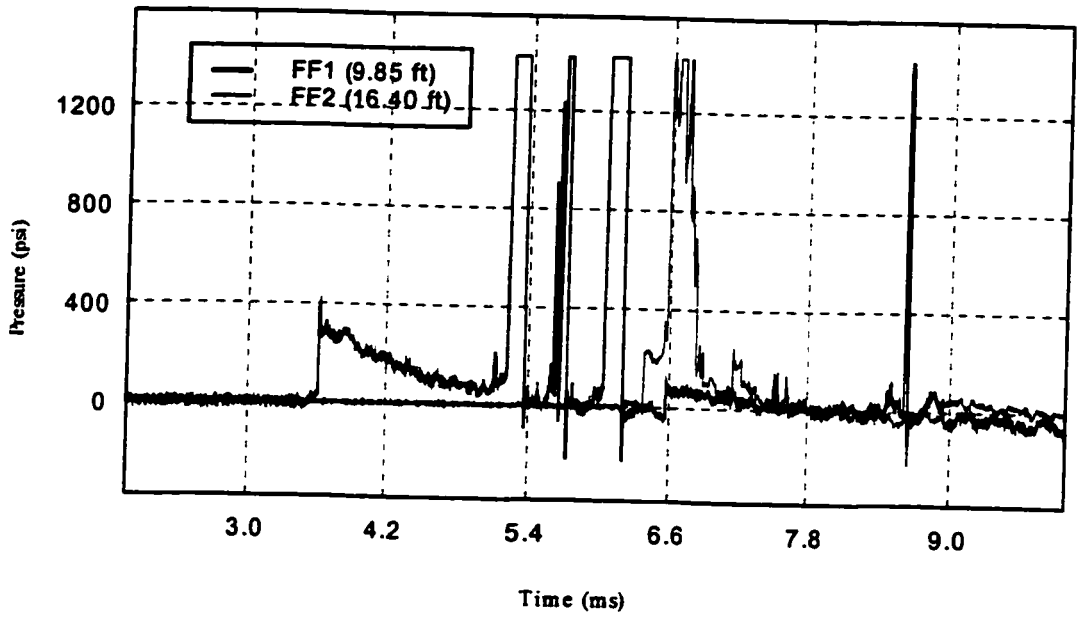

(a): Incident (free field) pressure-time profiles

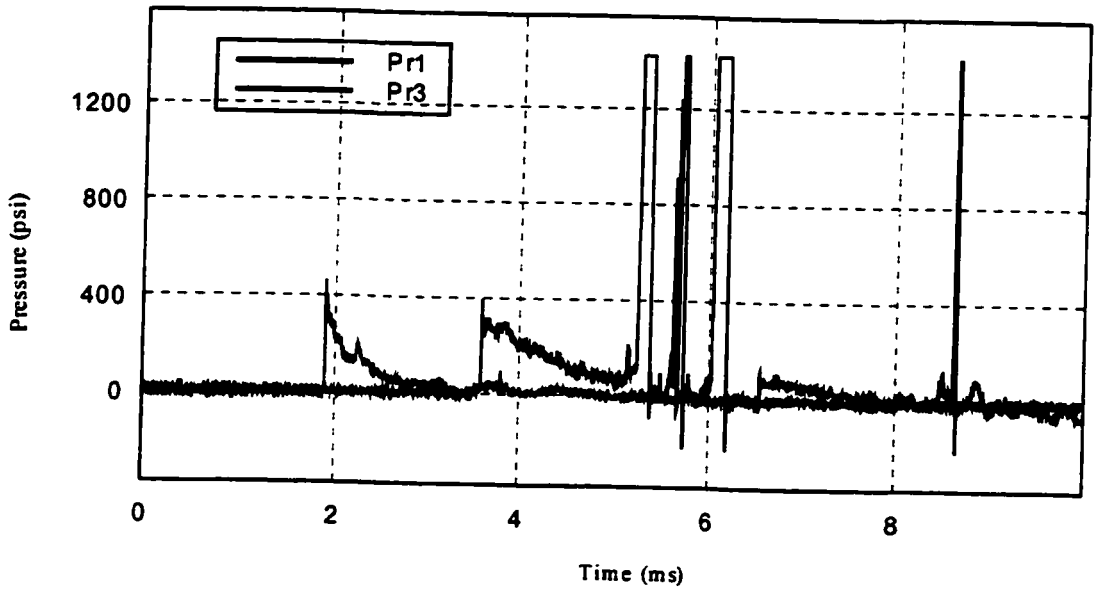

(b): Reflected pressure-time profiles

Figure C.46: Pressure-time profile for blast test # 6 (Panel CLS2)

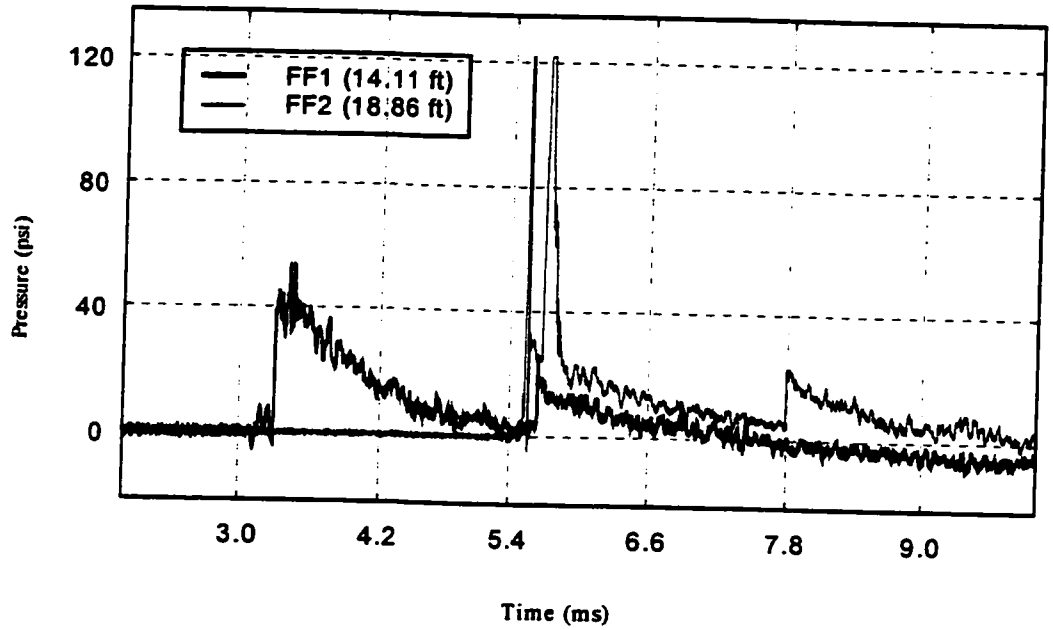

(a): Incident (free field) pressure-time profiles

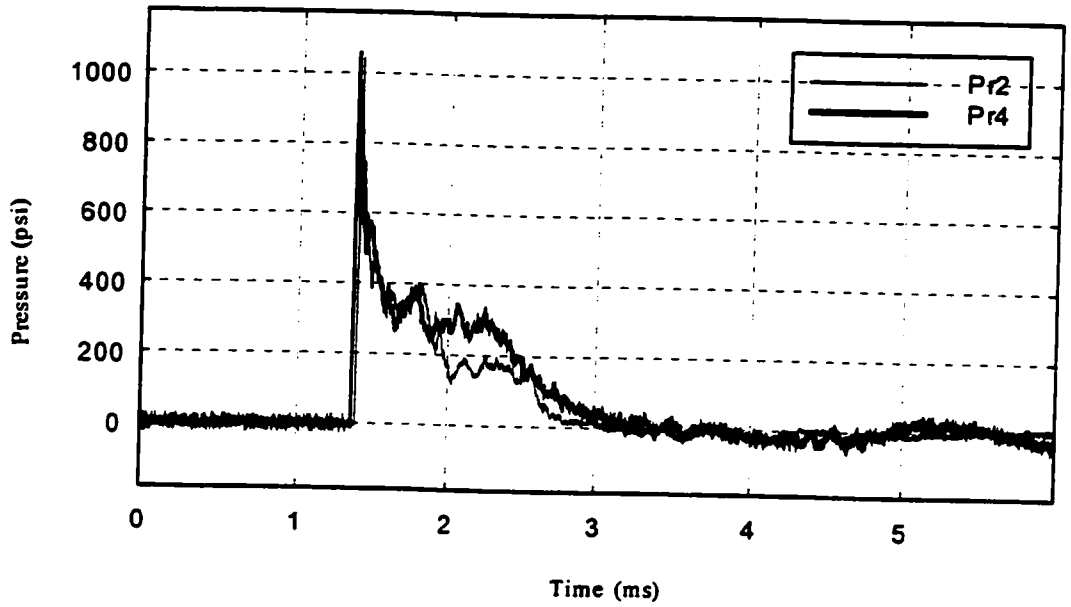

(b): Reflected pressure-time profiles

Figure C.47: Pressure-time profile for blast test # 10 (Panel CLS3)

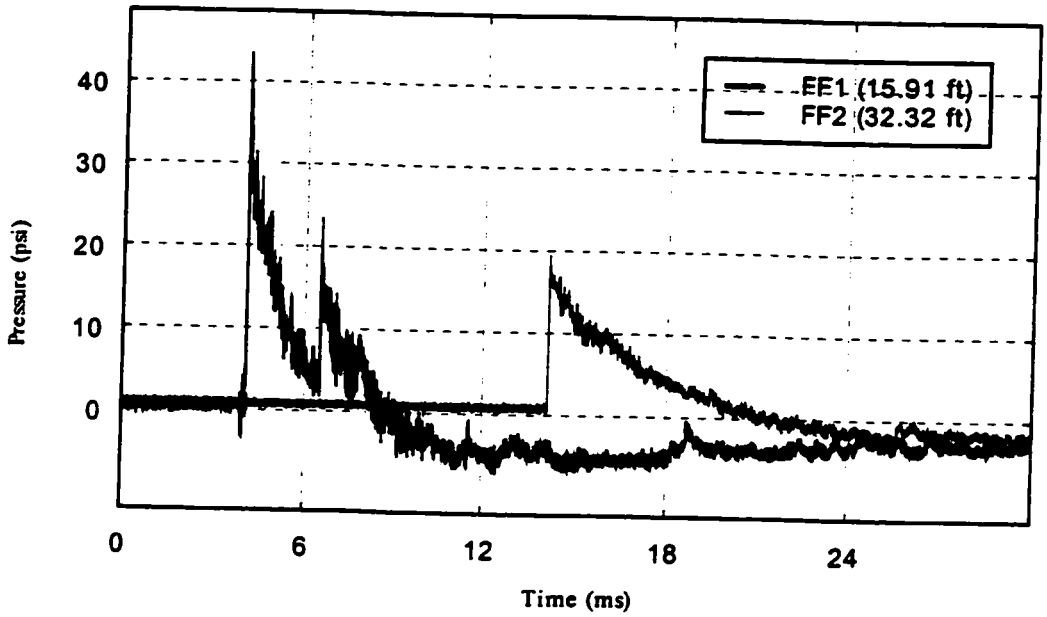

(a): Incident (free field) pressure-time profiles

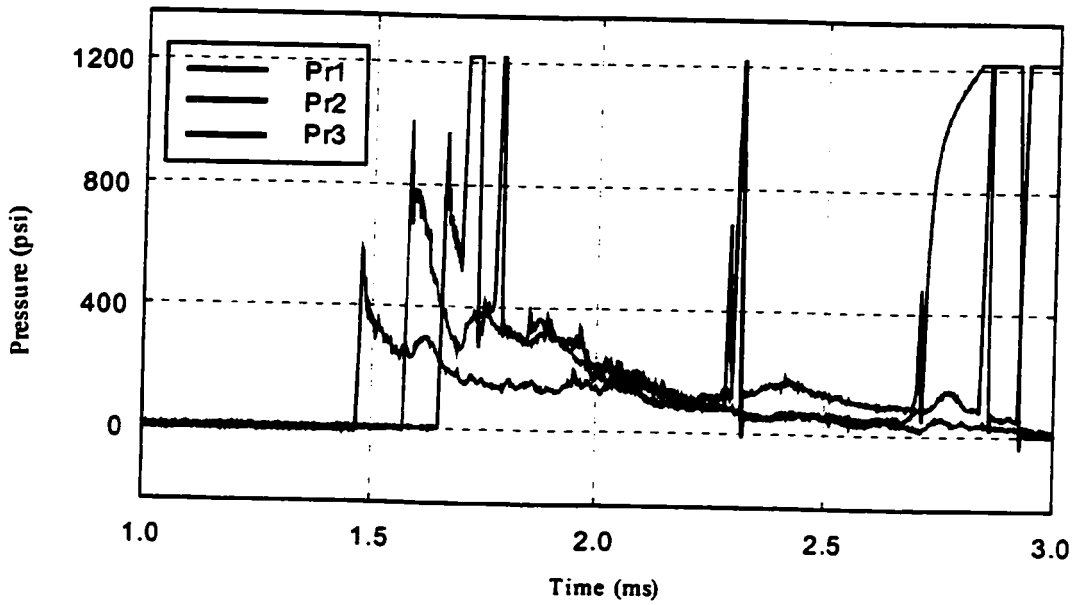

(b): Reflected pressure-time profiles

Figure C.48: Pressure-time profile for blast test # 16 (Panel CLS4)

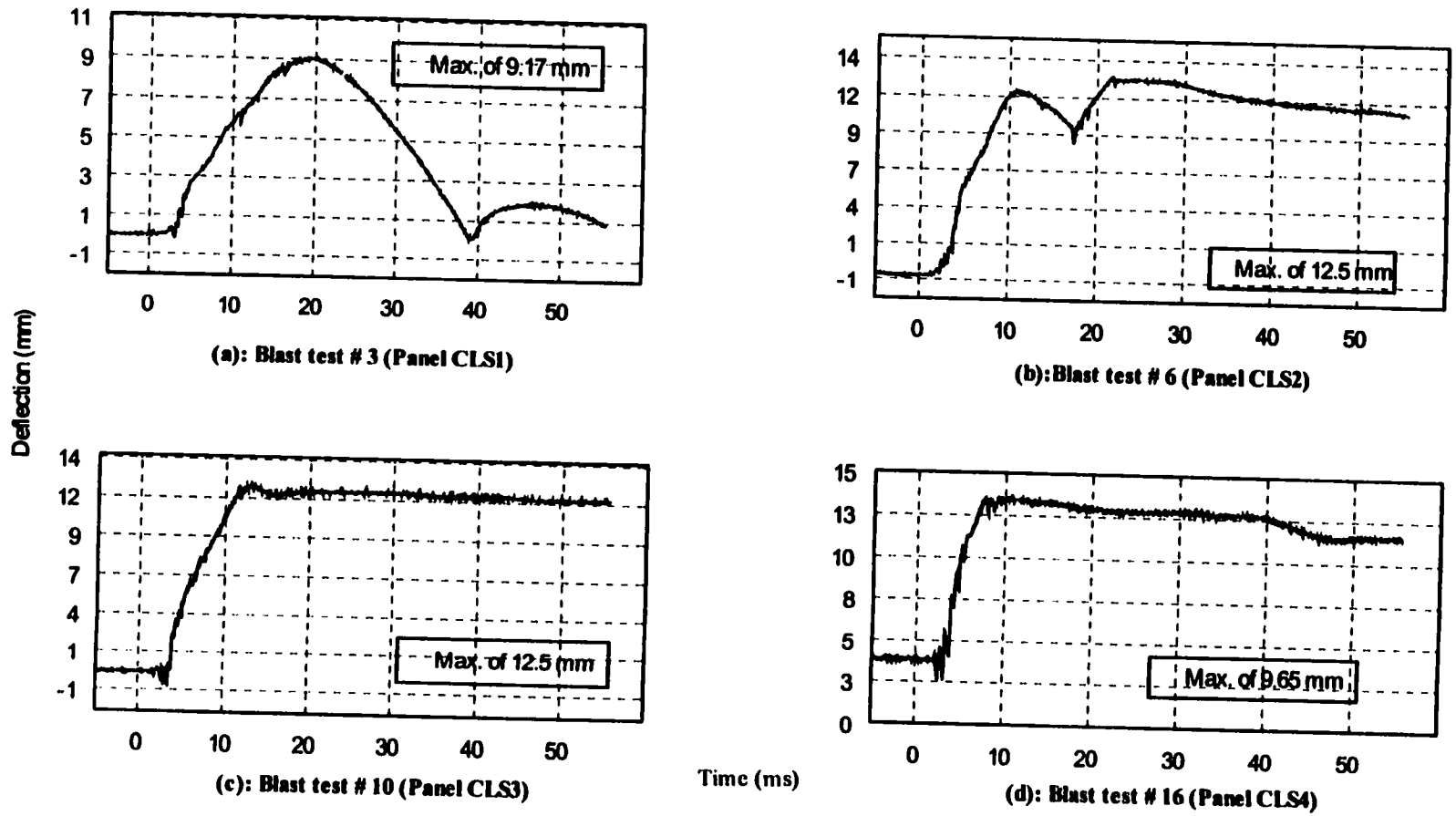

Figure C.49: Mid-span deflection time histories of Group (4)